Studying translation by Cryo-Electron Microscopy

Investigating intact mitochondria and isolated ribosomes of humans, algae and plants by cryoEM

Robert Daniel Englmeier

Doctoral thesis
Studying translation by cryo-electron microscopy
Robert Daniel Englmeier
Structural Biochemistry
Bijvoet Centre for Biomolecular Research, Faculty of Science
Utrecht University, the Netherlands

Studying translation by Cryo-Electron Microscopy

Investigating intact mitochondria and isolated ribosomes of humans, algae and plants by cryoEM

Studie van translatie door cryo-elektronenmicroscopie

(met een samenvatting in het Nederlands)

Proefschrift

ter verkrijging van de graad van doctor aan de
Universiteit Utrecht
op gezag van de
rector magnificus, prof.dr. H.R.B.M. Kummeling,
ingevolge het besluit van het college voor promoties
in het openbaar te verdedigen op

woensdag 8 februari 2023 des ochtends te 10.15 uur

door

Robert Daniel Englmeier

geboren op 25 mei 1990
te München, Duitsland

Promotor:

Prof. dr. Friedrich Förster

Beoordelingscommissie:

Prof. dr. P. Gros
Prof. dr. M. Baldus
Prof. A. Briegel
Dr. A.I.P.M. de Kroon
Prof. dr. J. Lipfert

Table of Contents

Chapter 1

General Introduction

Robert Englmeier

Structural Biochemistry group, Bijvoet Centre for Biomolecular Research, Utrecht University,
Universiteitsweg 9, 3584 CG Utrecht, The Netherlands

Modified from

Cryo-electron tomography for the structural study of mitochondrial translation
Robert Englmeier & Friedrich Förster
Tissue & Cell (2018), Volume 57, p. 129- 138
DOI: https://doi.org/10.1016/j.tice.2018.08.009

1. Ribosomes - the birthplace of all proteins

Ribosomes are the protein factories of the cell. During the process of translation, ribosomes engage with mRNA transcripts to translate the genetic information encoded as nucleic acids into a chain of amino acids (peptide). Upon emergence from the ribosome, the nascent peptides folds into functional proteins, and embark upon a journey of potential modifications, protein complex formation and intracellular sorting before arriving to their final destinations within the cell, where they fulfill a myriad of functions. Notably, eukaryotic cells possess two separate translation machineries: cytosolic ribosomes residing in the cytosol, and mitochondrial ribosomes residing inside mitochondria.

Mitochondria are organelles that play a central role in cellular energy conversion and health, and are a hallmark of the eukaryotic cell. All mitochondria originate from a bacterial cell that was engulfed by an archaea more than 2 billion years ago. Termed the endosymbiotic event, this was a defining point in the history of life that gave rise to the eukaryotic cell with its compartmentalized interior[1]. Importantly, mitochondria have maintained their own genome and translation machinery of bacterial origin, respectively the mitoribosomal DNA and the mitoribosome.

In this thesis, I investigate the structure of mitoribosomes from human and algae in their native environment by cryo-electron tomography. In the last chapter, I apply cryo-electron microscopy (cryoEM) single particle analysis (SPA) to study an example of metabolite-induced translational regulation of cytosolic ribosomes in plants.

1.1 CryoEM enables high-resolution structure determination of proteins

The visualization of biological structures is key to the mechanistic understanding of cellular processes. The development of the first light microscopes by Leeuwenhoek and Hooke led to the discovery of cellular structures and established the field of microbiology [2]. Almost 300 years later, the invention of the transmission electron microscope (TEM) [3] increased the resolution for imaging cellular structures by more than one order of magnitude, enabling the discovery of subcellular structures [4]. The seminal studies by Palade and others that shaped our current view of eukaryotic cells as heavily compartmentalized, sophisticated machines were carried out on chemically fixed, dehydrated, stained and resin-embedded samples to allow imaging inside the vacuum of the instrument. While this type of specimen preparation is sufficient to distinguish different lipid-enclosed organelles in a cell, it does not allow higher-resolution interpretation of protein complexes, because in particular dehydration alters the molecular structure of proteins and lipids. Moreover, the signal mostly stems from heavy metal salts as opposed to the biological material itself,

which is problematic for quantitative interpretation. It is often not even clear if the organic material itself (positive staining) or its direct environment (negative staining) generates the signal. Thus, these classical preparation methods used in cell biology are not suitable for analyzing the structure of the cell in molecular detail.

The development of cryofixation through rapid cooling [5], which transforms aqueous samples into a vitreous state, established the field of cryo-electron microscopy (cryo-EM). Cryo-preparation enables imaging of biological samples in their frozen-hydrated, physiological context and extended the range of structural analysis from morphological features to macromolecular complexes. In cryo-EM, the density differences in the biological material itself generate contrast, as opposed to stain in the case of conventional cell biology preparation [6]. However, only very weak signal is generated by the few electrons that image the sample prior to onset of substantial beam damage (typically ~20 electrons/Å^2). Accordingly, the signal-to-noise ratio (SNR) of images from cryo-prepared samples is dramatically worse than that of EM images from conventionally prepared samples. Due to this low SNR, the image of an individual molecule provides little reliable (i.e., statistically significant) structural detail. Thus, cryo-EM typically relies on extensive statistical analysis of images of many copies of a molecule. The addition of these noisy individual images provides higher level of detail [7]. Decades of development in most efficient data acquisition and detector technology eventually enabled capture of almost every imaging electron, leading to increased popularity of cryo-EM in the life sciences.

Cryo-EM is nowadays mostly used in conjunction with two different approaches in order to determine the three-dimensional (3D) structures of biological specimens: single particle analysis (SPA) and cryo-electron tomography (cryo-ET). In SPA, thousands of two-dimensional (2D) images of purified macromolecules are acquired [8]. From typically hundreds of thousands 2D projections, the 3D density that explains these observations best is computationally reconstructed. For macromolecules greater than 100 kDa, near-atomic resolution is increasingly routine. The 2017 Nobel prize in Chemistry awarded to Jacques Dubochet, Joachim Frank and Richard Henderson for SPA acknowledges this revolutionary development.

1.2 Cryo-ET enables structural studies of protein complexes in their native environment

In cryo-ET, the sample itself is imaged in 3D. The underlying data is a series of 2D EM images of the sequentially tilted specimen[9] (Figure 1A). The subsequent 3D reconstruction of the imaged region is obtained by computational methods that are similar to those used in computed tomography and magnetic resonance imaging in medical imaging (Figure 1B). Compared to SPA, cryo-ET is more time-consuming: whereas in SPA each particle is imaged

once, in the case of cryo-ET many 2D images at different angles, typically 40 – 100, are acquired. Such acquisition of a 'tilt series', which requires the precise interaction of microscope optics and mechanics, typically extends the acquisition time per particle by almost 2 orders of magnitude compared to the single shot in SPA. Hence, cryo-ET is usually applied to complex, pleiomorphic samples, where the 3D context is of interest.

Contextual information is important when studying membrane-associated complexes, for example those residing in cellular compartments [10]. Biochemical isolation would disrupt them from their native membrane environment, potentially causing the dissociation of low-affinity components or altering the conformation [11]. Here, cryo-ET is beneficial because it allows for the visualization of complexes in their near-native, membrane-associated state, omitting their solubilization and further biochemical isolation. Examples of membrane-associated complexes studied using cryo-ET include the nuclear pore complex [12–14], the Endoplasmic reticulum-associated ribosome [15], flagellar motors of bacteria [16] and viral complexes [17,18].

The resolution of a single macromolecule in a raw tomogram is limited to roughly 30-50 Å [19]. However, averaging of subvolumes extracted from the full-size tomogram, each depicting the same type of complex (subtomogram averaging, STA) increases the SNR and hence makes higher resolution details distinguishable from the noise. Similar to SPA, up to hundreds of thousands of subvolumes [18] containing the macromolecule of interest are iteratively aligned with respect to each other and averaged to obtain a higher resolution map. For big or rigid protein complexes, sub-nanometer resolution can be achieved, as demonstrated in the case of the ribosome-bound translocon complex [15,20], the COPI coat [21] or the HIV1 Gag polyprotein capsid [18], which even exceeded 4 Å resolution. Achieving subnanometer resolution is challenging and has so far only been achieved either for large (e.g., ribosome) or macromolecular complexes embedded in supramolecular lattices (e.g., viral and vesicular coats). In general, high molecular weight of complexes is advantageous for STA because these provide a large amount of signal, which is required for aligning the volumes to a common coordinate system. While SPA increasingly addresses structures of molecules <100 kDa, the weight of structures imaged by STA exceeds 200 kDa in most cases because the more complex samples studied by cryo-ET tend to be thicker, lowering the SNR of the raw data. The bulk of structures determined by STA are still in the resolution range of 1-4 nm, in most cases due to the limited copy number of the molecule of interest in the available data.

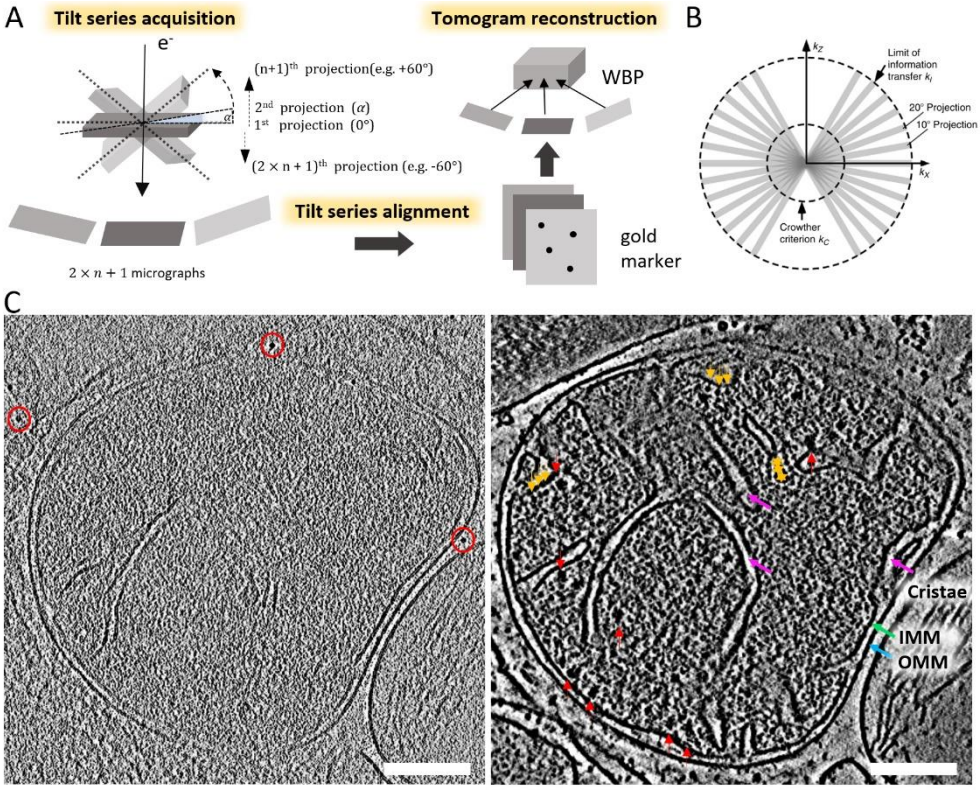

Figure 1: Workflow for tilt series acquisition, alignment and tomogram reconstruction. A) Within a defined tilt range, the stage of the electron microscope is sequentially tilted *n* times (typically *n* = 20-30) in each direction by a defined tilt increment α prior to acquiring a projection. This spatial sampling results in a 'tilt series', which contains $2 \times n + 1$ micrographs. Prior to tomogram reconstruction, the acquired tilt series must be aligned precisely to a common 3D coordinate system, compensating shifts and rotations occurring during data acquisition. The alignment is usually based on previously added gold markers (red circles in C)) serving as fiducials. The 3D tomogram can be reconstructed from the aligned tiltseries by different reconstruction methods, e.g. by weighted backprojection (WBP). B) The underlying principle for reconstructing a 3D volume from 2D images is the projection-slice theorem: the 2D projections from the 3D object correspond to slices in the 3D Fourier space of the object. C) Comparison of a 2D projection (left) to a z-slice of the reconstructed 3D tomogram (right). In the resulting tomogram of the mitochondrion, the outer mitochondrial membrane (OMM, green arrows), inner mitochondrial membrane (IMM, cyan arrows) and cristae (pink arrows), as well as membrane-associated mitoribosomes (red arrows) and ATP synthases (yellow arrows) can be identified. The scale bars correspond to 150 nm.

Cryo-ET is a suitable tool for the structural study of mitoribosomes due to their membrane-association

Cryo-ET is a suitable method to study the molecular architecture of the mitochondrion, due to the relatively inaccessible nature of this organelle. Mitochondria are difficult to study

because their disruption, which is a prerequisite for most analytical methods, affects their biochemical micro-environment and hence their function. To date, most cryo-EM studies of mitochondria used isolated mitochondrial vesicles[22–24]. The mitochondrion is characterized by a complex morphology of two membranes (outer and inner mitochondrial membrane, OMM and IMM, respectively) that enclose the intermembrane space (IMS) and the mitochondrial matrix (Figure 1C). This intricate membrane architecture enables the generation and maintenance of the proton gradient required for ATP synthesis by oxidative phosphorylation (OXPHOS). In every known organism, the mitochondrion has retained its own, albeit reduced, genome and associated translation machine, the mitoribosome.

The mitoribosome synthesizes only very few proteins (13 in humans), typically highly hydrophobic subunits of complexes of the membrane-embedded OXPHOS machinery [25]. This translation process is temporally and spatially coordinated with nuclear-encoded OXPHOS subunits[26,27]. The mitochondrial translation products are co-translationally inserted into the IMM by membrane-embedded accessory factors [28], and assemble with nuclear encoded subunits into the OXPHOS machinery (Figure 2). Due to the high hydrophobicity of the synthesized peptides and the interaction with membrane-embedded accessory factors, mitoribosomes reside at the IMM. The structures of the OXPHOS complexes, namely the respirasome and the ATP synthase, have been determined to high resolution by cryo-EM SPA [29–31] (Figure 2). While these studies have provided high-resolution models of the major complexes synthesized by the mitoribosomes, the structural mechanism for the insertion of the mitochondrially encoded subunits into the IMM remains unknown.

Structural studies of mitoribosomes by cryoEM

The structures of the mammalian and yeast mitoribosomes have been recently determined by cryoET and SPA[32–36], and revealed the vast structural differences that arose during eukaryotic evolution. Compared to the yeast mitoribosome, the rRNA fraction of the human mitoribosome is drastically reduced and was substituted by nuclear encoded proteins[37]. This resulted in a decreased sedimentation coefficient (~55 S in human vs. ~72 S in yeast), an inverted rRNA-to-protein ratio and smaller mitoribosome diameter (Figure 3). The yeast mitoribosome on the other hand is characterized by additionally acquired expansion segments absent in humans, as well as a shifted peptide exit tunnel compared to humans and bacteria[38,39]. Another noteworthy example to highlight the drastic structural impacts on the mitoribosome over the course of evolution is the green algae *Chlamydomonas reinhardtii.* Here, the small and large ribosomal subunits (SSU & LSU) do not contain one continuous rRNA each, as it is the case in humans and yeast, but 4 and 9 rRNA fragments respectively [40]. How the various fragments are recruited and assembled into the

mitoribosome remains enigmatic, as the structure of the *C.reinhardtii* mitoribosome has previously not been resolved (**see chapter 5**).

The only previous *in organello* study of a mitoribosome was performed for yeast mitochondria [41], identifying the mitoribosome's membrane association via two contact sites (Figure 3A). One of them is constituted by an rRNA expansion segment (96-ES), which is lacking for the human mitoribosome. The second contact site was shown to be Mba1, a structural homologue of the human mL45. How the membrane association of the human mitoribosome is mediated and whether the absence of a second contact site is compensated remained unresolved (**see chapter 2**). The map obtained by cryoET also showed density for the insertase adjacent to the Mba1 membrane contact site, presumably aligning the exit tunnel with the insertase but the details of the interaction could not be resolved at the limited 23 Å resolution.

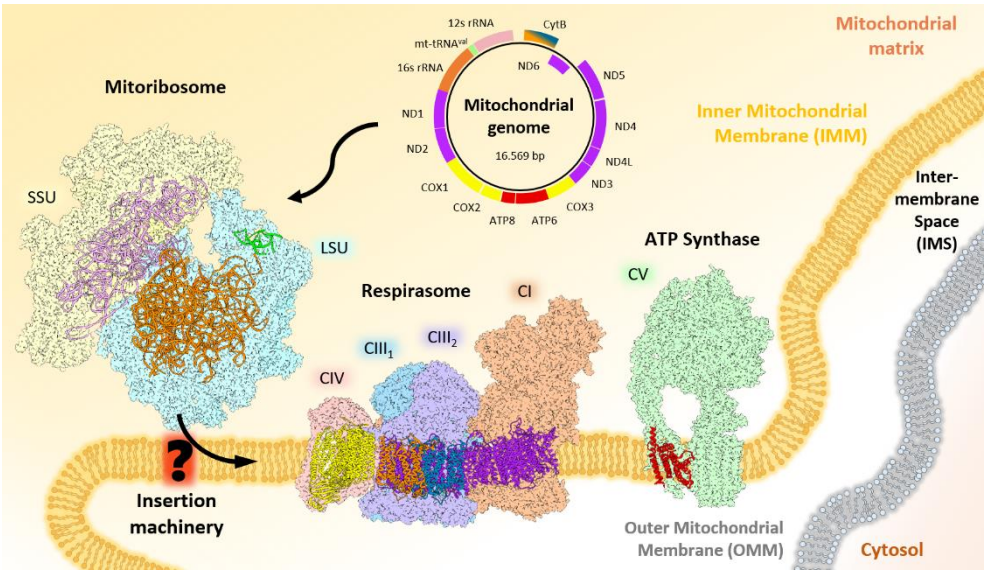

Figure 2: Mitochondrial gene expression. Throughout evolution mitochondria have kept their own genome and translation machinery, the mitoribosome (PDB 3J9)[34]. The human mitochondrial genome codes for 13 hydrophobic proteins, which are membrane-embedded subunits of the OXPHOS machinery. The mitochondria-encoded OXPHOS subunits are co-translationally inserted into the IMM by a structurally poorly-defined insertion machinery. The mitoribosome and the OXPHOS machinery are composed of subunits encoded in both the nuclear (isosurface representations) and mitochondrial genome (ribbons representations, color coded as in the mitochondrial genome). The mitoribosomal RNA of the large and small subunit (LSU and SSU, respectively) are displayed as ribbons in orange and pink, respectively, overlaid on the isosurface representation of the nuclear-encoded proteins (blue and yellow, respectively). The mitochondria-encoded $tRNA^{val}$ which is integrated into the mitoribosome is shown in green. The OXPHOS machinery, composed of the respirasome (PDB 5GUP) [29] and the ATP synthase, (PDB 6CP6) [30] contains mitochondrial encoded subunits (ribbons) for each of the major complexes (CI, CIII, CIV and CV).

Mitochondrial proteins are co-translationally inserted into the membrane by Oxa1

Because the previous high-resolution structures of the human and yeast mitoribosomes were determined from isolated mitoribosomes[32–35], their interaction with the IMM and their associated protein insertion machinery could only be addressed to a limited extent. Oxa1, a 40 kDa membrane protein which is highly conserved among eukaryotes[42,43], is the main insertase for the co-translational membrane insertion of the substrates synthesized by the mitoribosome [44]. Oxa1 is a homolog of bacterial YidC and consists of a conserved fold of five transmembrane helices, a helical-hairpin domain and a flexible c-terminal domain (CTD), both exposed to the mitochondrial matrix[45]. The structure of Oxa1 remains elusive, and our structural understanding of Oxa1 is limited to crystal structures of the bacterial homologue YidC[46] as well as a low resolution cryoEM map of YidC bound to the bacterial ribosome[47]. The most recent study to structurally investigate Oxa1 used a cross-linking reagent to stabilize the association of the Oxa1L insertase to the human mitoribosome prior to structure determination by cryoEM SPA[36] (Figure 3B-C), which gave new insights into the interaction of the mitoribosome with Oxa1. The CTD of Oxa1, which was previously shown to enhance the association of Oxa1 to the mitoribosome[44], could be resolved bound to the mitoribosome (Figure 3C). The Oxa1 CTD extends towards the back of mitoribosome (with L7/L12 as front reference point, Figure 3B), where it mainly interacts with the membrane-facing mitoribosomal protein uL24 – which also forms part of the peptide exit site. From there, an unstructured loop extends upwards towards a small helical section which interacts with the rRNA, uL29m and bL28m. The study thus revealed an important aspect of the Oxa1 binding to the mitoribosome and provides the best model of the mitoribosome-Oxa1 interaction to date. However, the mechanism of membrane-tethered mitochondrial protein synthesis which this study claimed to have resolved remains far from being elucidated. Since nearly all translation products of the mitoribosomes are very hydrophobic membrane proteins, the long-standing question of how they are co-translationally guided to, inserted into, and folded inside the IMM has remained unanswered. In particular, how the 32 Å gap between the peptide exit site and the insertase is bridged and aligned, and how the protein is correctly handed over to the insertase for proper insertion, remains unclear despite the recent complex structure (Figure 3C). Importantly, the structure and role of the helical-hairpin domain of Oxa1 (**see chapter 4)**, a highly conserved structure within the oxa1 superfamily[21], as well as the architecture of the transmembrane domains, remain unresolved.

Even upon the future determination of the structure and association of the Oxa1 insertase at high detail, the spatio-temporal coordination of co-translational protein insertion, i.e. the dynamics and interaction of the mitoribosome-insertase complex with different co-factors and chaperones, will pose further questions. Recent studies have also shown tissue-specific rescue of lethal Oxa1 mutations, possibly indicating an alternative pathway for protein

insertion[48]. Due to the complex interaction of mitoribosomes with various IMM-residing factors responsible for insertion of nascent peptides into the IMM, and its coordination of OXPHOS complex assembly, mitochondrial translation is likely best investigated in the native environment.

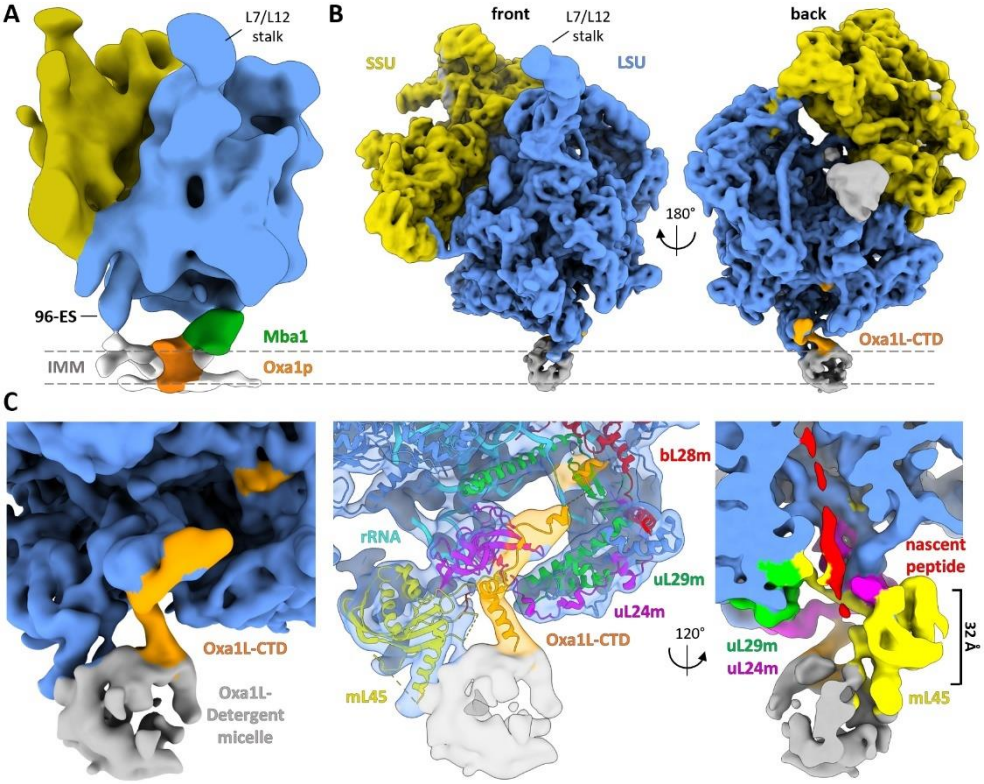

Figure 3: Structures of the yeast and human mitoribosomes determined by cryoET and SPA. A) - B) Maps of the 73S yeast mitoribosome (EMD-2826, A)) and the 55S human mitoribosome (EMD-11278, filtered to 8 Å, B)), determined respectively *in organello* by cryo-ET or from isolated mitoribosomes by SPA. Maps are aligned and shown at the same scale, inner mitochondrial membrane (IMM) plane is indicated by dashed line. C) Close-up view of the map from focusing on Oxa1L-CTD B), overlapped with the atomic model (PDB 6zm5, middle) to show Interaction of the Oxa1L-CTD with the human mitoribosome.

1.3 Metabolite-induced translational regulation of cytosolic ribosomes

Regulation of gene expression is central to all organisms and a precondition for cellular growth, division and response to changing environments. Many processes rely on the regulation of gene expression by transcriptional regulation, in which transcription factors turn the transcription of genes on or off[49]. An alternative regulatory mechanism to transcriptional regulation is translational regulation, where protein synthesis is either enhanced or stalled while the transcript is translated by the ribosome. In contrast to transcriptional regulation, translational regulation provides a faster modulation: it acts immediately on the last step of gene expression and does not rely on a cascade of actions involving transcription factors or RNAses to regulate the synthesis or degradation of a transcript. Translation regulation can be modulated by the rate of translation initiation, elongation or termination[50,51]. This can either be achieved by protein binding partners targeting the specific transcripts[52] or regulatory elements within the mRNA itself[53]. One specific example is metabolite-induced translational regulation, during which the ribosome acts as a metabolite sensor to stall or proceed with translation of a specific transcript depending on the binding of a metabolite. The TnaC operon in E.coli is probably one of the best characterized examples: in the presence of tryptophan, the ribosome stalls on the stop codon and blocks the rho utilization site, which prevents the binding of the rho transcription termination factor and therefore permits the continuous transcription of the downstream tryptophanase gene TnaA[54]. The detailed mechanism of tryptophan-induced translational stalling of TnaC was recently determined by cryoEM[55]: the TnaC peptide forms two short α-helices close to the peptidyl transferase center (PTC) when the ribosome reaches the stop codon, which together induce a tryptophan-independent pause and contribute to the formation of a ligand-binding site that accommodates a single tryptophan molecule (Figure 4). Translation termination is prevented by the two ultimate residues of TnaC which prevent the formation of the GGQ loop of RF2 and the placement of the catalytic water from adopting their active conformation, thus keeping the ribosome in a locked state.

uORFS are widespread in eukaryotes but their regulatory mechanism remains enigmatic

TnaC is a prokaryotic example of an upstream operon affecting the downstream TnaA operon. In eukaryotes, upstream regulatory elements can be harbored as upstream open reading frames (uORFs): 5' leader sequences upstream of the main gene on the mRNA, that engage with the ribosome and allows for initiation of translation. The expression of the downstream main ORF is then either negatively regulated by premature release of the ribosome upon reaching the stop codon or stalling of the ribosome before it can reach the main ORF. Bioinformatic analysis of eukaryotic genomes predicted that 20 to 50% of all eukaryotic genes harbor an uORF[56], yet the role of most of them is unknown or their mechanism of action remains elusive. The fungal arginine attenuator peptide (AAP) represents the only eukaryotic example of metabolite-induced translational regulation that

has been structurally investigated, but only a low resolution structure of the stalled yeast ribosome engaged with the peptide could be determined [57]. The binding site of arginine, and the structural dynamics of stalling were not resolved. In plants, many metabolite-controlled uORFs have been characterized that exhibit metabolite-induced regulation and are sensitive to different molecules such as sucrose, polyamines or ascorbate[58]. Many of them are conserved across the plant kingdom, and are referred to as conserved peptide uORFs (CPuORFS)[59]. The *Arabidopsis* S1-group bZIP transcription factors represent a prominent group of genes that harbors CPuORFs[60]. While the bZIP transcription factors regulate amino acid and sugar metabolism, their translation is regulated by their CPuORFs in a sucrose-dependent manner with high sucrose concentrations resulting in translational stalling on the CPuORF, preventing expression of the main ORF[61]. Single amino-acid mutations revealed that almost all C-terminal residues are important for stalling[61], but the binding mode of sucrose and the detailed mechanism of regulation is not known.

Whether metabolite induced stalling in eukaryotes functions in a similar manner to that in prokaryotes therefore remains unknown. The lack of any structural information on metabolite-induced stalling in eukaryotes presents a significant knowledge gap for the understanding of translational regulation, and calls for further investigation due to wide implications of uORFS for the regulation of cellular protein expression[62,63].

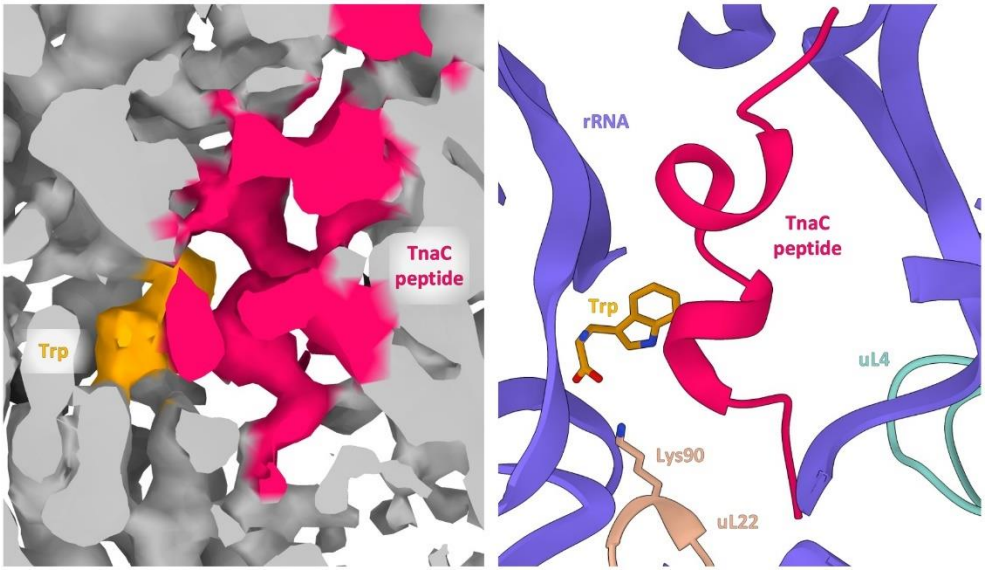

Figure 4: Mechanism of tryptophan-induced TnaC-mediated ribosome stalling in *E.coli*. Structure of the tryptophan-stalled *E.coli* ribosome translating TnaC, showing the binding of one tryptophan molecule (orange) inside the exit tunnel (grey) and in close proximity to the TnaC peptide (pink). cryoEM map on the left, atomic model on the right (PDB 7o19).

Scope of the thesis

This thesis aims to investigate the molecular mechanisms of protein synthesis within the dynamic framework of ribosomes, mRNA, nascent peptides, protein co-factors and small molecules. We combine different molecular and structural biology methods to elucidate the structures of mitoribosomes from different species within their native environments, and structurally characterize a eukaryotic example of metabolite-induced translational regulation. These results contribute to our understanding of the final step of gene expression and its intricate relation to evolution, metabolism and health.

In **chapter 2**, we apply cryoET to isolated human mitochondria to study the membrane association and distribution of mitoribosomes in their native environment, and identify how the absence of the fungal 96-ES affects the membrane association of the human mitoribosome.Our findings show that mitoribosomes predominantly associate with the membrane, and reveal that human mitoribosomes a mL45 acts as the major membrane anchor that mediates the association of the human mitoribosome to the membrane.

In **chapter 3** we provide a detailed protocol for the image analysis workflow performed in chapter 2.

In **chapter 4**, we develop an optimized protocol for the isolation of human mitochondria, which allows for the high-throughput data acquisition of a large tomogram dataset. Employing the latest advances in cryoET image analysis, we visualize the actively translating mitoribosomes inside human mitochondria at sub-nanometer resolution. These findings indicate the presence of an alternative membrane-insertase complex, and the subtomogram average of the Oxa1-mitoribosome complex allows us to identify a novel binding interface of the Oxa1-insertase and present a model for the mechanism of co-translational protein insertion in mitochondria.

Chapter 5 provides a detailed protocol for the optimized mitochondrial isolation developed in chapter 4 for human mitochondria as well as for yeast mitochondria.

In **chapter 6**, we apply cryoET to whole cells of the algae *Chlamydomonas reinhardtii* thinned by focused-ion beam milling. Combining the resulting *in situ* subtomogram with high-resolution structures of the small and large mitoribosomal subunits obtained by SPA allows for the determination of an atomic model of the *C. reinhardtii* mitoribosome. The structure reveals how the 13 mitoribosomal rRNA fragments are stabilized and assembled into the mitoribosome.

In **chapter 7**, we determine the structures of sucrose-stalled wheat germ ribosomes engaged with bZIP11-uORF2 by cryoEM SPA. The structures reveal that sucrose enriches the ribosome into two different translational states and binds to a >3 billion years-old binding pocket is that is functionally conserved and exploited across several kingdoms of life.

References

1. Sagan, L. On the origin of mitosing cells. *J. Theor. Biol.* **14**, 255–74 (1967).
2. van Leewenhoeck, A. Observations, Communicated to the Publisher by Mr. Antony van Leewenhoeck, in a Dutch Letter of the 9th of Octob. 1676. Here English'd: concerning Little Animals by Him Observed in Rain-Well-Sea. and Snow Water; as Also in Water Wherein Pepper Had Lain In. *Philos. Trans. R. Soc. London* **12**, 821–831 (1677).
3. Knoll, M. & Ruska, E. Das Elektronenmikroskop. *Zeitschrift für Phys.* **78**, 318–339 (1932).
4. Palade, G. E. & Porter, K. R. Studies on the endoplasmic reticulum. I. Its identification in cells in situ. *J. Exp. Med.* **100**, 641–56 (1954).
5. Dubochet, J. & McDowall, A. W. VITRIFICATION OF PURE WATER FOR ELECTRON MICROSCOPY. *J. Microsc.* **124**, 3–4 (1981).
6. Dubochet, J. *et al.* Cryo-electron microscopy of vitrified specimens. *Q. Rev. Biophys.* **21**, 129 (1988).
7. Henderson, R. The potential and limitations of neutrons, electrons and X-rays for atomic resolution microscopy of unstained biological molecules. *Q. Rev. Biophys.* **28**, 171–93 (1995).
8. Frank, J. Single-particle reconstruction of biological macromolecules in electron microscopy--30 years. *Q. Rev. Biophys.* **42**, 139–58 (2009).
9. Lučić, V., Förster, F. & Baumeister, W. Structural studies by electron tomography: from cells to molecules. *Annu. Rev. Biochem.* **74**, 833–65 (2005).
10. Förster, F. & Hegerl, R. Structure determination in situ by averaging of tomograms. *Methods Cell Biol.* **79**, 741–67 (2007).
11. Beck, M. & Baumeister, W. Cryo-Electron Tomography: Can it Reveal the Molecular Sociology of Cells in Atomic Detail? *Trends Cell Biol.* **26**, 825–837 (2016).
12. Mahamid, J. *et al.* Visualizing the molecular sociology at the HeLa cell nuclear periphery. *Science (80-.).* **351**, 969–972 (2016).
13. Kosinski, J. *et al.* Molecular architecture of the inner ring scaffold of the human nuclear pore complex. *Science (80-.).* **352**, 363–365 (2016).
14. Beck, M. *et al.* Nuclear Pore Complex Structure and Dynamics Revealed by Cryoelectron Tomography. *Science (80-.).* **306**, 1387–1390 (2004).
15. Pfeffer, S. *et al.* Structure of the native Sec61 protein-conducting channel. *Nat. Commun.* **6**, 8403 (2015).
16. Beeby, M. *et al.* Diverse high-torque bacterial flagellar motors assemble wider stator rings using a conserved protein scaffold. *Proc. Natl. Acad. Sci. U. S. A.* **113**, E1917-26 (2016).
17. Förster, F., Medalia, O., Zauberman, N., Baumeister, W. & Fass, D. Retrovirus envelope protein complex structure in situ studied by cryo-electron tomography. *Proc. Natl. Acad. Sci. U. S. A.* **102**, 4729–34 (2005).
18. Schur, F. K. M. *et al.* An atomic model of HIV-1 capsid-SP1 reveals structures regulating assembly and maturation. *Science (80-.).* **353**, 506–508 (2016).
19. Asano, S. *et al.* Proteasomes. A molecular census of 26S proteasomes in intact neurons. *Science* **347**, 439–42 (2015).
20. Braunger, K. *et al.* Structural basis for coupling protein transport and N-glycosylation at the mammalian endoplasmic reticulum. *Science* **360**, 215–219 (2018).
21. Dodonova, S. O. *et al.* 9Å structure of the COPI coat reveals that the Arf1 GTPase occupies two contrasting molecular environments. *Elife* **6**, e26691 (2017).
22. Nicastro, D., Frangakis, A. S., Typke, D. & Baumeister, W. Cryo-electron Tomography of Neurospora Mitochondria. *J. Struct. Biol.* **129**, 48–56 (2000).
23. Davies, K. M. *et al.* Macromolecular organization of ATP synthase and complex I in whole mitochondria. *Proc. Natl. Acad. Sci.* **108**, 14121–14126 (2011).
24. Davies, K. M., Anselmi, C., Wittig, I., Faraldo-Gómez, J. D. & Kühlbrandt, W. Structure of the yeast F1Fo-ATP synthase dimer and its role in shaping the mitochondrial cristae. *Proc. Natl.*

Acad. Sci. U. S. A. **109**, 13602–7 (2012).
25. Ott, M., Amunts, A. & Brown, A. Organization and Regulation of Mitochondrial Protein Synthesis. *Annu. Rev. Biochem.* **85**, 77–101 (2016).
26. Couvillion, M. T., Soto, I. C., Shipkovenska, G. & Churchman, L. S. Synchronized mitochondrial and cytosolic translation programs. *Nature* **533**, 499–503 (2016).
27. Richter-Dennerlein, R. *et al.* Mitochondrial Protein Synthesis Adapts to Influx of Nuclear-Encoded Protein. *Cell* **167**, 471-483.e10 (2016).
28. Ott, M. & Herrmann, J. M. Co-translational membrane insertion of mitochondrially encoded proteins. *Biochim. Biophys. Acta* **1803**, 767–75 (2010).
29. Wu, M., Gu, J., Guo, R., Huang, Y. & Yang, M. Structure of Mammalian Respiratory Supercomplex I1III2IV1. *Cell* **167**, 1598-1609.e10 (2016).
30. Srivastava, A. P. *et al.* High-resolution cryo-EM analysis of the yeast ATP synthase in a lipid membrane. *Science* **360**, eaas9699 (2018).
31. Zhou, A. *et al.* Structure and conformational states of the bovine mitochondrial ATP synthase by cryo-EM. *Elife* **4**, e10180 (2015).
32. Desai, N., Brown, A., Amunts, A. & Ramakrishnan, V. The structure of the yeast mitochondrial ribosome - Supplementary Material. *Science (80-.).* **355**, 528–531 (2017).
33. Greber, B. J. *et al.* Ribosome. The complete structure of the 55S mammalian mitochondrial ribosome. *Science* **348**, 303–8 (2015).
34. Amunts, A., Brown, A., Toots, J., Scheres, S. H. W. & Ramakrishnan, V. The structure of the human mitochondrial ribosome. *Science* **348**, 95–8 (2015).
35. Desai, N. *et al.* Elongational stalling activates mitoribosome-associated quality control. *Science (80-.).* **370**, 1105–1110 (2020).
36. Itoh, Y. *et al.* Mechanism of membrane-tethered mitochondrial protein synthesis. *Science (80-.).* **371**, 846–849 (2021).
37. van der Sluis, E. O. *et al.* Parallel Structural Evolution of Mitochondrial Ribosomes and OXPHOS Complexes. *Genome Biol. Evol.* **7**, 1235–51 (2015).
38. Amunts, A. *et al.* Structure of the yeast mitochondrial large ribosomal subunit. *Science* **343**, 1485–9 (2014).
39. Desai, N., Brown, A., Amunts, A. & Ramakrishnan, V. The structure of the yeast mitochondrial ribosome. *Science (80-.).* **355**, 528–531 (2017).
40. Boer, P. H. & Gray, M. W. Scrambled ribosomal RNA gene pieces in Chlamydomonas reinhardtii mitochondrial DNA. *Cell* **55**, 399–411 (1988).
41. Pfeffer, S., Woellhaf, M. W., Herrmann, J. M. & Förster, F. Organization of the mitochondrial translation machinery studied in situ by cryoelectron tomography. *Nat. Commun.* **6**, 6019 (2015).
42. Borowska, M. T., Dominik, P. K., Anghel, S. A., Kossiakoff, A. A. & Keenan, R. J. A YidC-like Protein in the Archaeal Plasma Membrane. *Structure* **23**, 1715–24 (2015).
43. Wang, P. & Dalbey, R. E. Inserting membrane proteins: the YidC/Oxa1/Alb3 machinery in bacteria, mitochondria, and chloroplasts. *Biochim. Biophys. Acta* **1808**, 866–75 (2011).
44. Szyrach, G., Ott, M., Bonnefoy, N., Neupert, W. & Herrmann, J. M. Ribosome binding to the Oxa1 complex facilitates co-translational protein insertion in mitochondria. *EMBO J.* **22**, 6448–6457 (2003).
45. McDowell, M. A., Heimes, M. & Sinning, I. Structural and molecular mechanisms for membrane protein biogenesis by the Oxa1 superfamily. *Nature Structural and Molecular Biology* vol. 28 234–239 (2021).
46. Kumazaki, K. *et al.* Structural basis of Sec-independent membrane protein insertion by YidC. *Nature* **509**, 516–519 (2014).
47. Kedrov, A. *et al.* Structural Dynamics of the YidC:Ribosome Complex during Membrane Protein Biogenesis. *Cell Rep.* **17**, 2943–2954 (2016).
48. Thompson, K. *et al.* OXA1L mutations cause mitochondrial encephalopathy and a combined

oxidative phosphorylation defect. *EMBO Mol Med* **10**, 9060 (2018).
49. Cramer, P. Organization and regulation of gene transcription. *Nature* vol. 573 45–54 (2019).
50. Hinnebusch, A. G. & Lorsch, J. R. The mechanism of eukaryotic translation initiation: new insights and challenges. *Cold Spring Harb. Perspect. Biol.* **4**, (2012).
51. Hershey, J. W. B., Sonenberg, N. & Mathews, M. B. Principles of Translational Control: An Overview. *Cold Spring Harb. Perspect. Biol.* **4**, a011528–a011528 (2012).
52. Gebauer, F., Preiss, T. & Hentze, M. W. From cis-regulatory elements to complex RNPs and back. *Cold Spring Harb. Perspect. Biol.* **4**, 1–14 (2012).
53. Zhang, G., Hubalewska, M. & Ignatova, Z. Transient ribosomal attenuation coordinates protein synthesis and co-translational folding. *Nat. Struct. Mol. Biol.* **16**, 274–280 (2009).
54. Konan, K. V. & Yanofsky, C. Regulation of the Escherichia coli tna operon: Nascent leader peptide control at the tnaC stop codon. *J. Bacteriol.* **179**, 1774–1779 (1997).
55. van der Stel, A. X. *et al.* Structural basis for the tryptophan sensitivity of TnaC-mediated ribosome stalling. *Nat. Commun.* **12**, (2021).
56. Kochetov, A. V. Alternative translation start sites and hidden coding potential of eukaryotic mRNAs. *BioEssays* **30**, 683–691 (2008).
57. Bhushan, S. *et al.* Structural basis for translational stalling by human cytomegalovirus and fungal arginine attenuator peptide. *Mol. Cell* **40**, 138–146 (2010).
58. Van Der Horst, S., Filipovska, T., Hanson, J. & Smeekens, S. Metabolite control of translation by conserved peptide uORFs: The ribosome as a metabolite multisensor. *Plant Physiol.* **182**, 110–122 (2020).
59. Vaughn, J. N., Ellingson, S. R., Mignone, F. & Von Arnim, A. Known and novel post-transcriptional regulatory sequences are conserved across plant families. *RNA* **18**, 368–384 (2012).
60. Weltmeier, F. *et al.* Expression patterns within the Arabidopsis C/S1 bZIP transcription factor network: Availability of heterodimerization partners controls gene expression during stress response and development. *Plant Mol. Biol.* **69**, 107–119 (2009).
61. Yamashita, Y. *et al.* Sucrose sensing through nascent peptide-meditated ribosome stalling at the stop codon of Arabidopsis bZIP11. **591**, 1266–1277 (2017).
62. Calvo, S. E., Pagliarini, D. J. & Mootha, V. K. Upstream open reading frames cause widespread reduction of protein expression and are polymorphic among humans. *Proc. Natl. Acad. Sci. U. S. A.* **106**, 7507–7512 (2009).
63. Takahashi, H. *et al.* Exhaustive identification of conserved upstream open reading frames with potential translational regulatory functions from animal genomes. *Sci. Rep.* **10**, 16289 (2020).

Chapter 2

Structure of the human mitochondrial ribosome studied *in situ* by cryoelectron tomography

Robert Englmeier[1], Stefan Pfeffer[2], Friedrich Förster[1,2,3*]

[1] Cryo-Electron Microscopy, Bijvoet Center for Biomolecular Research, Utrecht University, 3584 CH Utrecht, The Netherlands

[2] Max-Planck Institute of Biochemistry, Department of Molecular Structural Biology, 82152 Martinsried, Germany

[3] Lead contact

Published in Structure, Volume 25, Issue 10, p.1574-1581.E2; October 03, 2017;

DOI: https://doi.org/10.1016/j.str.2017.07.011

Summary

Mitochondria maintain their own genome and its corresponding protein synthesis machine, the mitochondrial ribosome (mitoribosome). Mitoribosomes primarily synthesize highly hydrophobic proteins of the inner mitochondrial membrane. Recent studies revealed the complete structure of the isolated mammalian mitoribosome, but its mode of membrane association remained hypothetical. In this study, we used cryoelectron tomography to visualize human mitoribosomes in isolated mitochondria. The subtomogram average of the membrane-associated human mitoribosome reveals a single major contact site with the inner membrane, mediated by the mitochondria-specific protein mL45. A second rRNA-mediated contact site that is present in yeast is absent in humans, resulting in a more variable association of the human mitoribosome with the inner membrane. Despite extensive structural differences of mammalian and fungal mitoribosomal structure, the principal organization of peptide exit tunnel and the mL45 homolog remains invariant, presumably to align the mitoribosome with the membrane-embedded insertion machinery.

Introduction

Mitochondria are organelles originating from bacteria that have been incorporated into eukaryotic cells in an endosymbiotic process. Throughout evolution, mitochondria maintained their own genome and protein synthesis machinery, including mitochondrial ribosomes (mitoribosomes). The human mitoribosome synthesizes 13 highly hydrophobic subunits of the oxidative phosphorylation (OxPhos) complexes I, III, IV, and V, which are co-translationally inserted into the inner mitochondrial membrane (IMM) (Ott and Herrmann, 2010). Mutations in these proteins are implicated in several diseases. Despite their importance for cellular function, little is known about the biogenesis of mitochondria-encoded proteins, e.g., their synthesis, concomitant membrane integration, and subsequent assembly into complexes.

Like their bacterial relatives, mitoribosomes are assembled from rRNA and ribosomal proteins. Throughout evolution the mitochondrial genome and, consequently, the mitochondrial rRNA changed drastically. Upon an initial constructive phase in protozoa characterized by the expansion of rRNA and the acquisition of novel proteins, metazoans went through a ‘‘destructive phase’’ with strong mitochondrial rRNA reduction and recruitment of further mitoribosome-specific proteins, giving rise to an inverted rRNA/protein ratio compared with bacterial ribosomes (van der Sluis et al., 2015). Recent studies of the mammalian and yeast mitoribosome by cryoelectron microscopy (cryo-EM) single-particle analysis (SPA) provided highresolution insights into their structures and drastic variation throughout evolution. For example, the 73S yeast mitoribosome exhibits a completely remodeled peptide exit tunnel (Amunts et al., 2014), while this feature does not differ significantly between the bacterial ribosome and the mammalian mitoribosome (Greber et al., 2014). The consequences of the extensive mitoribosome evolution for the mechanism of translation, IMM association, and protein insertion remain unclear.

Co-translational insertion of nascent peptides into the IMM is most extensively studied in yeast. Genetic and biochemical studies identified two components of this process: the integral membrane protein Oxa1, which is thought to insert newly synthesized proteins into the IMM (Hell et al., 2001), and the IMM-associated mitoribosome receptor Mba1 (Lorenzi et al., 2016; Ott et al., 2006). Both proteins have homologs in mammals, Oxa1L and mL45, respectively. While Mba1 is absent in purified yeast mitoribosomes, mL45 is a constitutive mitoribosomal subunit in mammals, and its atomic structure in the context of the isolated human mitoribosome has been determined by cryo-EM SPA (Brown et al., 2014; Greber et al., 2014).

The association of the yeast mitoribosome with the native IMM has been studied in situ using cryoelectron tomography (CET) and subtomogram analysis (Pfeffer et al., 2015). The yeast mitoribosome associates with the IMM via two major contact sites, identified as the

rRNA expansion segment 96-ES1 and Mba1, which binds near the ribosomal peptide exit tunnel (PET). In the mammalian 55S mitoribosome, 96-ES1 is absent and the PET has moved dramatically during evolution in yeast (Amunts et al., 2014, 2015; Greber et al., 2015; Pfeffer et al., 2015). Thus, the mode of membrane association remains to be addressed for the mammalian mitoribosome.

Visualization of mitoribosomes within intact mitochondria is more challenging for mammals than for other previously studied organisms such as Saccharomyces cerevisiae (Pfeffer et al., 2015). The mammalian mitoribosome's low RNA/protein ratio and its smaller size causes comparably low contrast in the dense mitochondrial matrix, preventing their accurate detection in tomograms acquired using conventional defocus-induced phase-contrast CET. Here, we made use of the recently developed Volta phase plate (VPP) (Khoshouei et al., 2017) to increase contrast in CET and study the mammalian mitoribosome in situ. Using CET and subtomogram analysis, we studied the distribution and structure of human mitoribosomes in the context of the native IMM.

Results

Distribution of Mitoribosomes in Human Mitochondria

Mitochondria were isolated from HEK cells in the logarithmic growth phase, vitrified by plunge freezing, and imaged using VPP-CET. Due to the high density of the mitochondrial matrix in mammals, we mostly acquired tomograms of thin mitochondria, which had sufficient contrast for identification of mitoribosome particles with high specificity. Typically, imaged mitochondria measured approximately 200 nm along the beam direction and up to 800 nm in the perpendicular plane. In the reconstructed tomograms, mitoribosomes can be distinguished clearly from the mitochondrial matrix (Figure 1A).

To generate an unbiased template for subsequent automatic search, 231 subtomograms depicting putative mitoribosomes were interactively located in two tomograms and iteratively aligned using a sphere as an initial reference (Chen et al., 2013). The resulting subtomogram average is highly similar to cryo-EM SPA reconstructions of the mammalian mitoribosome (Figure S1A). This subtomogram average was used as a template for a six-dimensional cross-correlation search (''template matching'') in 51 acquired tomograms (Lucic et al., 2005). Areas corresponding to peaks of the cross-correlation function were visually inspected to remove obvious false positives from the set of candidate particles, resulting in 7,796 subtomograms that were individually reconstructed and iteratively aligned. Using classification based on constrained principal component analysis (CPCA) (Fo¨ rster et al., 2008) of the mitoribosome particles, false positives and low-quality particles were removed, resulting in 2,592 well-defined particles (Figure S1B). To identify

mitoribosomes in a homogeneous state, the particles underwent a second round of CPCA classification, focusing on the small subunit (SSU) of the mitoribosome particles (Figure S1B). The class averages indicate that the SSU is present in all particles, but in approximately 10% of particles the SSU is less defined, probably due to structural variability. In total, 2,343 mitoribosome particles were retained for further analysis.

Most of the identified mitoribosomes appear to reside near the cristae or on the top and the bottom surface of the imaged mitochondria, all in close proximity to the IMM (Figure 1A). To quantify the spatial distribution, we computed the Euclidean distance between the center of detected mitoribosomes and the surface of the IMM for two representative tomograms. Indeed, the resulting distribution of distances suggests that the vast majority of mitoribosomes is directly adjacent to the IMM (Figure 1B), as also observed for the yeast mitoribosome (Pfeffer et al., 2015). The median distance between the center of the mitoribosome and the IMM is approximately 15 nm.

In our tomograms, mitoribosomes typically appear in clusters on the IMM. Ribosome particles that are engaged in translation of the same mRNA molecule (polysome) tend to adopt specific three-dimensional (3D) organizations (Brandt et al., 2010; Pfeffer et al., 2012, 2015). To analyze the 3D organization of human mitoribosomes, we determined the relative positions and orientations of its next neighbor within a maximum center-to-center distance of 40 nm. To exclude particles from different membranes from the analysis, we removed those pairs from the dataset that had a relative membrane inclination of more than 35 (Figures S2A and S2B). The plot of the relative positions and orientations of these neighbors yielded two distinct clusters (Figures S2C and S2D). When visualizing the arrangements represented by these two populations using the average positions and orientations, we observed that these clusters likely correspond to the left and the right neighbor within the same polysomal arrangement (Figure S2E).

This arrangement of mitoribosomes in a polysome results in a curved path of mRNA (Figure 1C). This arrangement minimizes unoccupied mRNA stretches, and we have previously observed it at the ER (Pfeffer et al., 2012) and also in yeast mitochondria (Pfeffer et al., 2015). However, compared with the 3D organization of yeast mitoribosomes (Pfeffer et al., 2015), the plot of relative positions and orientations shows less-defined clusters for human mitoribosomes. This indicates an increased variability of adjacent polysomal mitoribosomes or clusters of adjacent mitoribosomes not engaged in translation of the same mRNA molecule.

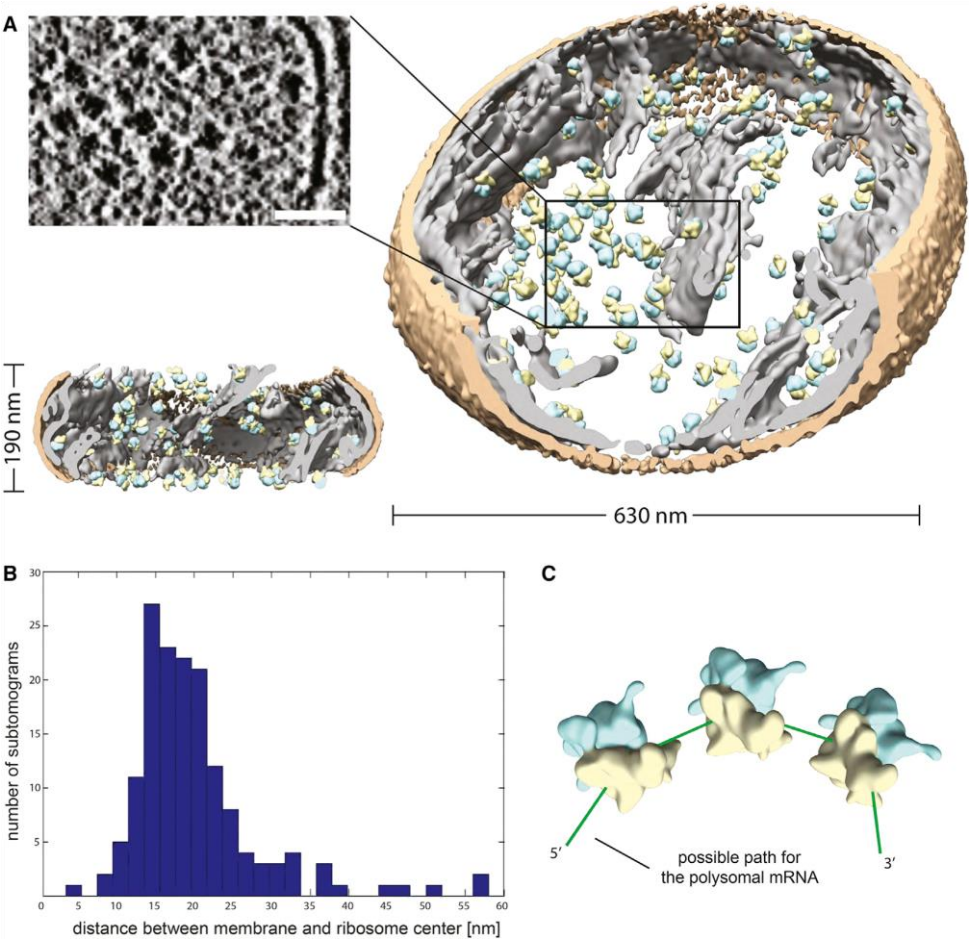

Figure 1: Distribution of mitoribosomes inside a human mitochondrion. A) Distribution of mitoribosomes (LSU: blue, SSU: yellow) within a segmented mitochondrion (outer mitochondrial membrane, OMM: orange, IMM: grey). The slice of a tomogram (top left) depicts a cluster of mitoribosomes (scale bar: 50nm). B) Distribution of the centre-to-membrane distances of 155 mitoribosomes from two tomograms. C) Average 3D arrangement of mitoribosomes in membrane-bound human mitochondrial polysomes, with a possible pathway for polysomal mRNA depicted in green. The membrane resides in the paper plane. See also Figures S1 and S2.

In Situ Structure of the Human Mitoribosome

The 2,343 subtomograms depicting well-defined mitoribosomes were subjected to a second round of classification focusing on the membrane region (Figure S1B), resulting in 663 particles with clear density for the IMM. This low proportion of particles with clear membrane density mainly results from the geometry of imaged mitochondria: the majority of particles reside at the top or the bottom of the flattened mitochondria (‘‘top views’’), where the mitochondrial membrane is not resolved due to the limited tilt range

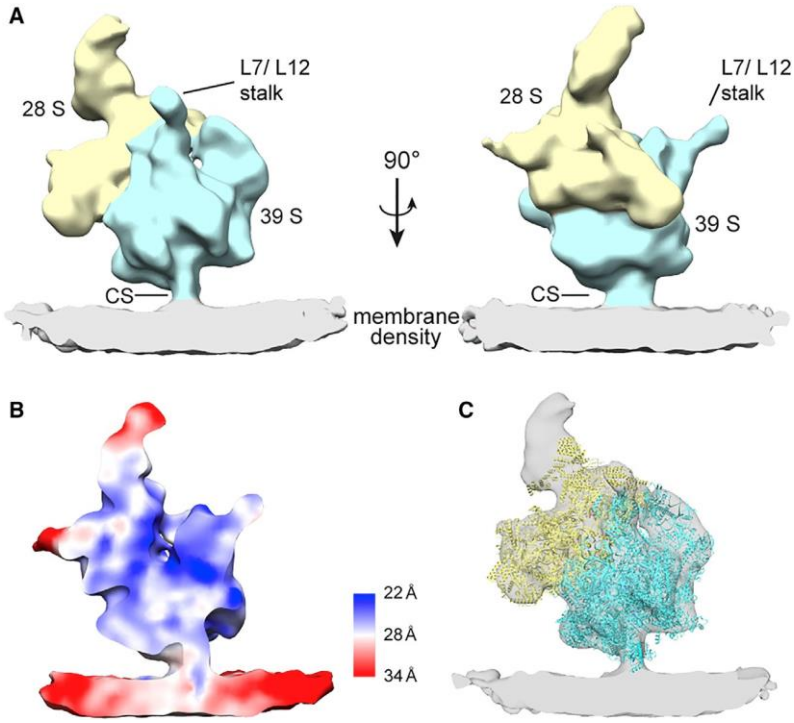

Figure 2: Structure of the membrane-bound human mitoribosome. A) Subtomogram average of the human mitoribosome filtered to 25 Å (SSU: yellow, LSU: blue, IMM: gray). The contact site (CS) tethering the mitoribosome to the IMM is indicated. B) Local resolution map**.** C) Atomic model of the human 55S mitoribosome (PDB 3j9m) fitted into the subtomogram average. See also Figure S1 and S3.

in CET (‘‘missing wedge effect’’). We decided to exclude these top views from further analysis, (1) because over-representation of one particular view in the dataset results in anisotropic resolution and artificial elongation of the averaged density along the imaging direction (as illustrated in Figure S1C) and (2) because including the top views resulted in only an insignificant improvement of the overall resolution, indicating that the sample and raw data quality rather than the particle number limit the obtainable resolution.

The remaining 663 subtomograms were iteratively aligned and averaged, resulting in a structure with well-defined SSU and large subunit (LSU) as well as pronounced density for the IMM (Figure 2A). Fourier shell cross-resolution against a cryo-EM single-particle reconstruction of the human mitoribosome (Amunts et al., 2015) (EMDataBank: EMD-2876) yielded a resolution of 25 A˚ (Fourier shell correlation [FSC] = 0.33). FSC of two independently aligned averages from each half of the data indicated a resolution of 26 A˚

(FSC = 0.143) (Figure S3). Local resolution varies between 22 and 28 A˚ for the mitoribosome and up to 34 A˚ for the peripheral membrane regions (Figure 2B).

For molecular interpretation, an atomic model of the human mitoribosome (PDB: 3j9m) was fitted into the subtomogram average (Figure 2C). Most of the density is explained well by the fitted atomic model. However, unexplained density is present in proximity to the head of the SSU. This uncovered density associates with mS39 (Figure 3A), which is positioned at the mRNA entry site of the SSU and supposedly guides the mRNA into the mitoribosomal mRNA channel (Greber et al., 2015). The size of the density suggests a mass of approximately 100 kDa. The resolution within this region is lower than for the core of the mitoribosome (Figure 2B), indicating compositional or conformational heterogeneity, which could not be disentangled using subtomogram classification (Figure S1B).

In the subtomogram average, membrane association of the human mitoribosome is mediated by a single contact site, which co-localizes with mL45 in the fitted atomic model (Figure 3B). Thus, similar to its yeast homolog Mba1 (Pfeffer et al., 2015), mL45 mediates the IMM association of the mammalian mitoribosome. Compared with the atomic model of the human mitoribosome (PDB: 3j9m), a larger part of the N-terminal domain of mL45 was modeled in the atomic model of the porcine mitoribosome (Greber et al., 2015) (PDB: 5Aj4); toward the C terminus of mL45 it contains an additional a helix h2 (S101-K114; considering a predicted, unresolved helix h1 from E53-K62). To analyze the interaction of mL45 with the membrane in detail, we thus fitted the model of the porcine mitoribosome into the subtomogram average. h2 and h3 (V116-S128) of the fitted mL45 model are positioned directly on the membrane, suggesting that they mediate the interaction with the IMM (Figure 3B). Mitoribosomal membrane attachment by h2 of mL45 was already suggested previously (Greber et al., 2014) due to its positioning at the PET and the structural homology to the C-terminal domain of Tim44.

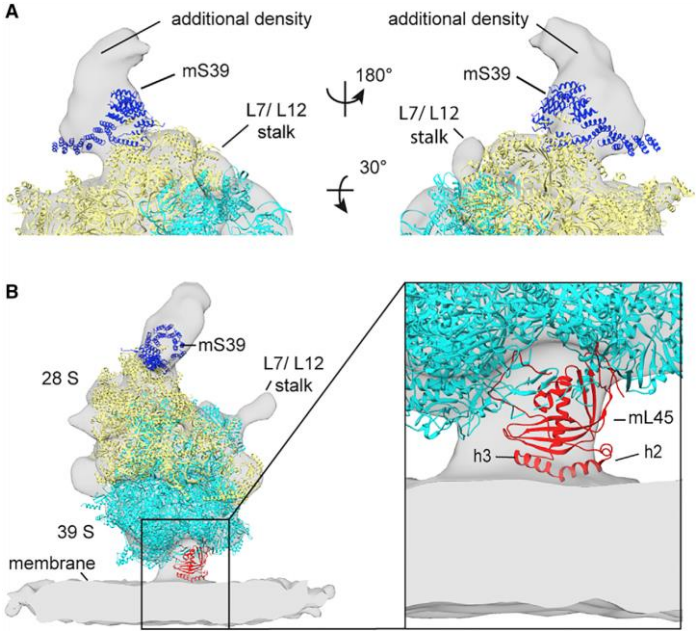

Figure 3: Features of the *in situ* mitoribosome structure. A) Density of roughly 100 kDa, unexplained by the atomic model near mS39 (dark blue). B) The mitoribosome is attached to the membrane via mL45 (red, PDB 5aj4). Its amphipathic α-helices h2 and h3 are positioned on the membrane surface. See also Figure S5.

Comparison with the Yeast Mitoribosome

While the yeast mitoribosome associates with the IMM via two contacts, mediated by the mL45 homolog Mba1 and the long rRNA expansion segment 96-ES1, the in situ structure of the human mitoribosome reveals only one mL45-mediated contact site (Figure 4A). Thus, mitoribosomal proteins do not compensate for the absence of 96-ES1 in mammals. On both the human and yeast mitoribosome, mL45/Mba1 is positioned directly beneath the PET, bridging the 30-A˚ gap between the ribosomal surface and the IMM (Figure 4A). Due to the strongly remodeled pathway of the PET in yeast, the absolute position of mL45/Mba1 on the mitoribosome differs between the human and yeast systems (Figure 4A), but with respect to the PET the position remains essentially invariant.

To analyze how the absence of the second contact site affects the arrangement of mitoribosome and membrane in humans, the subtomogram averages of the human and yeast mitoribosome (EMDataBank: EMD-2826) were aligned based on the conserved cores of their LSU rRNA (Figures 4B and S4A). The global arrangement of mitoribosome and membrane is defined by two main parameters: (1) the distance between the mitoribosomal core and the membrane surface, and (2) the orientation of the mitoribosome with respect to the IMM plane. The distance between a common reference point (ribosomal peptidyl-transferase center) and the surface of the IMM indicates that the catalytic core of the human mitoribosome resides approximately 15 A˚ closer to the membrane than that of the yeast mitoribosome (Figure 4B). This is in agreement with the decreased size of the human

mitoribosome. The orientation of the mammalian mitoribosome core, however, is strikingly similar to that of the yeast mitoribosome: the orientations of the membrane planes differ by no more than approximately 5°.

The presence of only one major membrane association site for the human mitoribosome suggests that its relative orientation with respect to the membrane might be more flexible than for its yeast counterpart. Subtomogram classification focused on the membrane region of the average consistently yielded classes depicting a range of different membrane inclinations with respect to the mitoribosome. To analyze the flexibility of mitoribosome orientation with respect to the IMM, we fitted atomic models into these class averages as rigid bodies and determined the positions of three reference points (located on mL45, the SSU, and LSU) in a common coordinate system. Difference vectors between mL45 and the reference points on the SSU and LSU reveal orientation variability of the mitoribosome on the IMM (Figure S4B). Classes with maximal membrane inclination tilt approximately ±10 with respect to the average orientation (Figure S4B). High variability of mitoribosome association to the IMM is consistent with the decreasing local resolution observed for the membrane region of the subtomogram average and might also explain why polysomal mitoribosome arrangements are less defined in human mitochondria compared with yeast (Figure S2D).

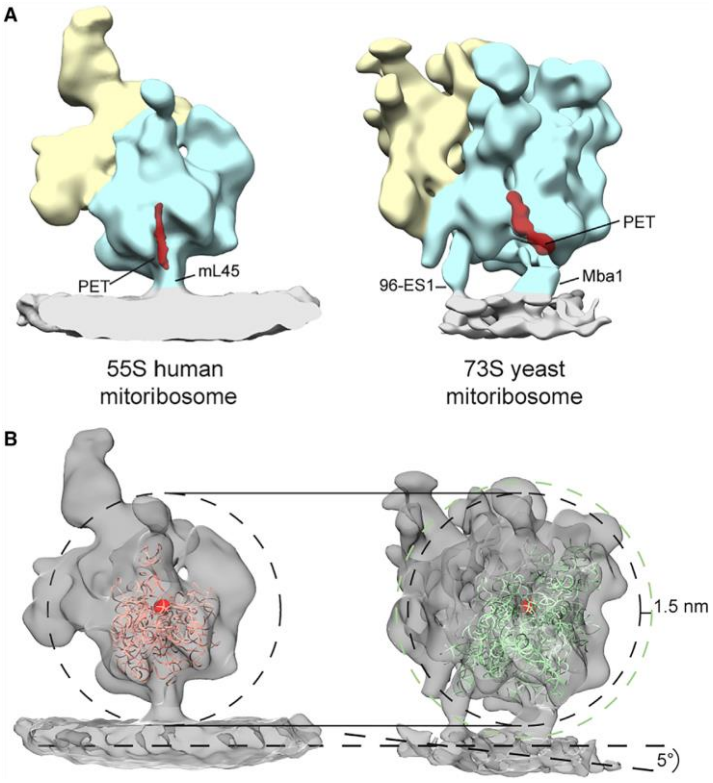

Figure 5: Comparison of IMM interaction between the human and the yeast mitoribosome. A) *In situ* structures of the human and yeast mitoribosomes, with the contact sites and the peptide exit tunnel (PET, red) highlighted. B) I*n situ* structures aligned to each other based on their LSU rRNA (PDB 3J9M rRNA: salmon, PDB 3J6B rRNA: green). Membrane planes are indicated by dashed lines and shown in the view with maximum tilt difference. Dashed circles (black: human, green: yeast) indicate distance between peptidyl transferase center (red sphere) and IMM. See also Figure S4.

Discussion

In Situ Structure of the Human Mitoribosome

Here, we studied the structure and distribution of human mitoribosomes in their native microenvironment using CET and subtomogram analysis. By imaging intact human mitochondria, extensive purification procedures were circumvented and the IMM association of the mitoribosome was preserved. Comparison of the in situ subtomogram average with high-resolution structures of the isolated mitoribosome reveals an additional density on the small mitoribosomal subunit (Figure 3A). This density might represent a weakly bound cofactor, which dissociates upon solubilization and purification. The additional density associates with mS39, which forms parts of the ribosomal mRNA entry site and interacts with mitochondrial mRNAs (Davies et al., 2009). The spatial proximity between the unexplained density and mS39 as well as the mRNA channel may hint at its involvement in translation regulation.

Association with the Inner Mitochondrial Membrane

In our subtomogram average, membrane association of the 55S mitoribosome is mediated by only a single contact site, involving mL45 (Figure 3B). Fitting of the high-resolution structure of the isolated porcine mitoribosome suggests that the amphipathic helices h2 and h3 of mL45 establish contact with the IMM. The lipid composition of the mammalian IMM, mainly consisting of negatively charged cardiolipin and zwitterionic phosphatidylethanolamine (Daum, 1985), potentially supports electrostatic interactions of the helices h2 and h3, which contain several charged amino acids pointing toward the membrane surface (Figure S5). However, considering the high protein-to-lipid ratio of the IMM (3:1) (Daum, 1985), it cannot be ruled out that mL45 additionally interacts with membraneembedded proteins that could not be resolved. A second contact site, which has previously been hypothesized to be mediated by the IMM proteins MPV17L2 or LetM1 (Mai et al., 2017) serving as ribosome recruitment factors (Dalla Rosa et al., 2014; Piao et al., 2009), was not observed. Consequently, MPV17L2 and LetM1 either must contribute to the mL45-mediated contact site or they associate only transiently during mitoribosome recruitment.

Another factor, which is likely to be involved in the visualized IMM contact site, is the membrane insertase Oxa1L. Its C-terminal domain was shown to bind to the ribosome (Haque et al., 2010; Keil et al., 2012; Szyrach et al., 2003), and the matrix-exposed loops of its bacterial homolog YidC serve functional roles in ribosome recruitment and subsequent protein insertion into the membrane (Geng et al., 2015). In the light of the large body of biochemical studies indicating cooperativity of Mba1 and Oxa1p in yeast (Keil et al., 2012; Lorenzi et al., 2016; Ott et al., 2006; Preuss et al., 2001; Szyrach et al., 2003) and the association of human mitoribosomes with Oxa1L (Haque et al., 2010; Richter-Dennerlein et

al., 2016), it appears likely that Oxa1L is involved in the contact site. A higher-resolution in situ structure of the mitoribosome attached to the IMM could further clarify permanent and transient components of the co-translational insertion machinery and reveal their molecular architecture.

Evolution of Mitoribosomal Membrane Association

The conserved molecular architecture of the Mba1/mL45-mediated contact site suggests a general role for mL45 and its homologs in mitochondrial membrane protein biogenesis. Based on its position close to the mitoribosomal PET in yeast, Mba1 was previously proposed to guide the highly hydrophobic nascent polypeptides from the tunnel exit to the associated membrane protein insertase (Pfeffer et al., 2015), which was further supported by crosslinking experiments (Lorenzi et al., 2016). Interestingly, the C-terminal domain of Tim44, which is structurally related to mL45 (Greber et al., 2014), also was recently shown to directly interact with peptides during their translocation from the mitochondrial intermembrane space to the mitochondrial matrix (Banerjee et al., 2015). These findings, together with the identification of mL45 as the major constituent of the single contact site between mitoribosome and IMM, suggest a conserved role of the Mba1/mL45 contact site in peptide transfer. A systematic structural analysis of membraneassociated mitoribosomes from various evolutionarily distant mitochondria-containing organisms will have to show whether the molecular architecture of the Mba1/mL45-mediated contact site is indeed universally conserved. The investigation of additional contacts from an evolutionary perspective, such as the one formed by the expansion segment 96-ES1 in yeast, could provide clues about their function.

Our structure of the human mitoribosome, studied in situ using CET, reveals that the human mitoribosome shares a conserved IMM contact site with the yeast mitoribosome, despite the vast structural rearrangements throughout evolution. Still, many mechanistic details, in particular regarding the transfer of highly hydrophobic nascent polypeptides from the PET to the IMM and their subsequent membrane insertion as well as the precise molecular organization of membrane association, remain to be investigated. Recent advances in mitoribosome purification protocols (Couvillion et al., 2016) and electron microscopic imaging technology (Bai et al., 2015) provide promising tools to address these open questions in further detail in the future.

STAR Methods

Contact for Reagent and Resource Sharing

Further information and requests for resources and reagents should be directed to and will be fulfilled by the Lead Contact, Friedrich Förster (f.g.forster@uu.nl).

Experimental Model and Subject Details

HEK cells were grown in suspension to a cell density of 1.1 x10^6/ ml at 37 °C in FreeStyle™ 293 Expression Medium (ThermoFisher), pelleted at 600g and washed once with PBS. Cell viability was determined to 98.4% by trypan blue staining.

Method details

Isolation of Mitochondria from HEK Cells

All subsequent steps were performed at 4 C. The cell pellet from 1 Liter of cell culture was resolved in 15 ml of isolation buffer (10 mM Tris, 150 mM sucrose, 1 mM EGTA, pH 7.4) and homogenized in a Potter-Elvehjem homogenizer for 10 minutes at 1,200 rpm by continuous up- and downstrokes. The resulting lysate was centrifuged for 10 minutes at 800 g, the supernatant was collected and centrifuged at 9,000 g for 10 minutes. The resulting supernatant was decanted and the pellet washed once with buffer, prior to a last centrifugation step at 9,000 g for 10 minutes. The supernatant was discarded and the final pellet was resuspended in 1.5 ml of isolation buffer, aliquoted and flash-frozen in liquid nitrogen. The samples were stored at -80C.

Cryoelectron Tomography

Quantifoil holey carbon coated copper grids (R 2/1) were glow discharged for 60 seconds before 3 ml of diluted mitochondria were applied to the grid and mixed with 3ml gold fiducial markers in 10mM Tris, pH 7.4 by pipetting. Grids were then manually blotted with filter paper from the back for 3 seconds and plunged into a liquid ethane-propane mixture using a custom-built guillotine plunger. The grids were mounted on autogrids (FEI). Tiltseries were recorded on a FEI Titan Krios operated at 300 kV equipped with the Volta Phase Plate, a Gatan K2 summit direct electron detector (3838x3710 pixel) and a Gatan Quantum Imaging Filter. For each half of a tiltseries (0 to -60 and 2 to +60, respectively, with an increment of 2), a new position on the phase plate was used, which was pre-irradiated with 30 nC on a trial area prior to data acquisition (Danev et al., 2014). The pixel size corresponded to 2.62 A˚ on the specimen level and the nominal defocus was set to 500 nm (26 tiltseries) or 3 mm (25 tiltseries). The electron dose did not exceed

100 $e^-/A^{\circ 2}$ per tiltseries. Data acquisition was performed with the SerialEM software (Mastronarde, 2005).

Data Processing

Tiltseries were aligned based on the fiducial markers using the TOM toolbox in MATLAB (Nickell et al., 2005). For tomograms with an insufficient number of gold markers, tilt image alignment was performed by patch tracking with the IMOD software package (Kremer et al., 1996). For the projections acquired at 3 mm defocus, phase reversals due to the contrast transfer function (CTF) were corrected using MATLAB scripts and PyTom (Hrabe et al., 2012) on single projections by strip-based periodogram averaging (Eibauer et al., 2012), accounting for a cosine shaped CTF as an effect of the phase plate. The aligned and weighted projections were downscaled in Fourier space from 3696x3696 to 462x462 pixels and tomograms were reconstructed in TOM (resulting voxel size 2.096 nm). Using reference-free spherical harmonics based subtomogram alignment (Chen et al., 2013) an initial structure for template matching was generated from 231 manually selected particles from two tomograms. To localize particles automatically in the complete set of tomograms template matching was performed with this reference using PyTOM (Hrabe et al., 2012). Peaks of the resulting 6-D cross-correlation function localized in the mitochondrial matrix were manually inspected in UCSF Chimera (Pettersen et al., 2004) to discard false-positive matches. For the retained coordinates, subtomograms were individually reconstructed (voxel size 0.524 nm) and subjected to subtomogram alignment using rotation sampling in real space with PyTom. Aligned subtomograms were classified using constrained principle component analysis (Fo¨ rster et al., 2008) in PyTOM and TOM to enrich subtomograms with clear density for the IMM and the small ribosomal subunit (SSU). The subtomograms were then iteratively aligned until convergence in PyTOM using a gold-standard procedure (two independent half-sets) (Scheres, 2012). Resolution of the subtomogram average was determined by Fourier shell cross-resolution against a cryo-EM single particle reconstruction of the human mitochondrial ribosome (EMDataBank: EMD-2876, FSC = 0.33) and half-set resolution (FSC = 0.143). For local resolution estimation the Bsoft software package was used (Cardone et al., 2013).

Ribosome Distribution Analysis

For analyzing the distribution of distances between located mitoribosomes and the membrane, the outer and inner mitochondrial membranes of two tomograms were segmented with Amira (FEI) (voxel size of 2.1 nm). The Euclidean distance between

the centres of mass of 155 classified mitoribosomes and the IMM was calculated in MATLAB (Mathworks, USA). The 3D distribution analysis was carried out as previously described for the yeast mitoribosome (Pfeffer et al., 2015). In brief, the coordinate system of the mitoribosome was chosen such that the IMM was perpendicular to the z-axis. The analysis was restricted to the neighbourhood of the 2,343 mitoribosomes obtained after two rounds of classification described in Figure S1. The next-neighbour analysis was restricted to only the next neighbour within a distance of 20 nm to 40 nm and a relative membrane inclination of 0 to 35. Two angles describing the relative position (a) and orientation (b) of the next neighbour were defined (Figure S2C), plotted against each other and hierarchically clustered in these two dimensions in MATLAB using the 'single' linkage and 'distance' clustering criteria. For each cluster, the average positions, determined using spherical coordinates and the CircStat toolbox (Berens, 2009), and the average orientations were used for generating the polysome models.

Molecular Weight Estimation of the Extra Density

The density of the subtomogram average was determined by manually removing the membrane density, measuring the volume in UCSF chimera at the same density threshold depicted in the figures and normalizing it to the 2.7 MDa of the 55 S mitoribosome. The density was determined to 0.61 Da/ A^3. The extra density was then manually segmented, its volume measured at the same density threshold as the subtomogram average and the mass was determined to 110 kDa by using the determined density.

Analysis of the Flexibility of the Mitoribosome

The 909 subtomograms with a clear membrane-density, obtained after focused classification with a spherical mask and a mask encompassing the SSU (Figure S1), were separated into 17 classes with varying membrane inclinations. The atomic model of the 55S mitoribosome (PDB3j9m) was fitted into the class averages with UCSF Chimera's ''Fit in Map'' function. Reference points were chosen on the small (uS2m, L293) and large subunits (mL38, E181) and the membrane contact (mL45, Q119) in the atomic model (3j9m) with Chimeras Volume Tracer. The coordinates of the markers were then extracted and difference vectors between the membrane contact and the reference points on the small and large subunit were calculated in MATLAB. The average reference point positions were determined using spherical coordinates and the resulting vectors were used as reference to calculate the angular distance of each class. Rotation matrices describing the transformation between the average reference point positions and the maximum outlier positions

- for which only the two thirds of datapoints with the smallest angular distance was considered - were determined in MATLAB (vrrotvec, vrrotvec2mat) and applied to the subtomogram average using TOM (tom_rotate) for the purpose of visualization (Figure S4B).

Data and software availability

A subtomogram average of the membrane-associated human mitoribosome has been deposited in the EMDataBank with accession code EMD-3784. All remaining relevant data are available from the authors. Correspondence and requests for data should be addressed to FF (f.g.forster@uu.nl).

AUTHOR CONTRIBUTIONS

R.E. prepared the sample, acquired tomography data, and, together with S.P. and F.F., carried out analysis of CET data. S.P. and F.F. planned and supervised the experiments and, together with R.E., wrote the manuscript.

ACKNOWLEDGMENTS

This work was supported by grants from the Deutsche Forschungsgemeinschaft to F.F. (FO 716/4-1 and the German Research Council GRK1721), as well as the Nederlandse Organisatie voor Wetenschappelijke Onderzoek (Vici 724.016.001). We thank Sabine Suppmann and Melanie Ried of the core facility of the Max Planck Institute of Biochemistry for suspension culture of HEK cells. The authors declare no competing financial interests.

References

Amunts, A., Brown, A., Bai, X., Llácer, J.L., Hussain, T., Emsley, P., Long, F., Murshudov, G., Scheres, S.H.W., and Ramakrishnan, V. (2014). Structure of the yeast mitochondrial large ribosomal subunit. Science *343*, 1485–1489.

Amunts, A., Brown, A., Toots, J., Scheres, S.H.W., and Ramakrishnan, V. (2015). Ribosome. The structure of the human mitochondrial ribosome. Science *348*, 95–98.

Bai, X., McMullan, G., and Scheres, S.H.. (2015). How cryo-EM is revolutionizing structural biology. Trends Biochem. Sci. *40*, 49–57.

Banerjee, R., Gladkova, C., Mapa, K., Witte, G., and Mokranjac, D. (2015). Protein translocation channel of mitochondrial inner membrane and matrix-exposed import motor communicate via two-domain coupling protein. Elife *4*, e11897.

Berens, P. (2009). CircStat : A MATLAB Toolbox for Circular Statistics. J. Stat. Softw. *31*, 1–21.

Brandt, F., Carlson, L.-A., Hartl, F.U., Baumeister, W., and Grünewald, K. (2010). The three-dimensional organization of polyribosomes in intact human cells. Mol. Cell *39*, 560–569.

Brown, A., Amunts, A., Bai, X., Sugimoto, Y., Edwards, P.C., Murshudov, G., Scheres, S.H.W., and Ramakrishnan, V. (2014). Structure of the large ribosomal subunit from human mitochondria. Science *346*, 718–722.

Cardone, G., Heymann, J.B., and Steven, A.C. (2013). One number does not fit all: mapping local variations in resolution in cryo-EM reconstructions. J. Struct. Biol. *184*, 226–236.

Chen, Y., Pfeffer, S., Hrabe, T., Schuller, J.M., and Förster, F. (2013). Fast and accurate reference-free alignment of subtomograms. J. Struct. Biol. *182*, 235–245.

Couvillion, M.T., Soto, I.C., Shipkovenska, G., and Churchman, L.S. (2016). Synchronized mitochondrial and cytosolic translation programs. Nature *533*, 499–503.

Dalla Rosa, I., Durigon, R., Pearce, S.F., Rorbach, J., Hirst, E.M.A., Vidoni, S., Reyes, A., Brea-Calvo, G., Minczuk, M., Woellhaf, M.W., et al. (2014). MPV17L2 is required for ribosome assembly in mitochondria. Nucleic Acids Res. *42*, 8500–8515.

Danev, R., Buijsse, B., Khoshouei, M., Plitzko, J.M., and Baumeister, W. (2014). Volta potential phase plate for in-focus phase contrast transmission electron microscopy. Proc. Natl. Acad. Sci. U. S. A. *111*, 15635–15640.

Daum, G. (1985). Lipids of mitochondria. Biochim. Biophys. Acta - Rev. Biomembr. *822*, 1–42.

Davies, S.M.K., Rackham, O., Shearwood, A.-M.J., Hamilton, K.L., Narsai, R., Whelan, J., and Filipovska, A. (2009). Pentatricopeptide repeat domain protein 3 associates with the mitochondrial small ribosomal subunit and regulates translation. FEBS Lett. *583*, 1853–1858.

Eibauer, M., Hoffmann, C., Plitzko, J.M., Baumeister, W., Nickell, S., and Engelhardt, H. (2012). Unraveling the structure of membrane proteins in situ by transfer function corrected cryo-electron tomography. J. Struct. Biol. *180*, 488–496.

Förster, F., Pruggnaller, S., Seybert, A., and Frangakis, A.S. (2008). Classification of cryo-electron sub-tomograms using constrained correlation. J. Struct. Biol. *161*, 276–286.

Geng, Y., Kedrov, A., Caumanns, J.J., Crevenna, A.H., Lamb, D.C., Beckmann, R., and Driessen, A.J.M. (2015). Role of the Cytosolic Loop C2 and the C Terminus of YidC in Ribosome Binding and Insertion Activity. J. Biol. Chem. *290*, 17250–17261.

Greber, B.J., Boehringer, D., Leitner, A., Bieri, P., Voigts-Hoffmann, F., Erzberger, J.P., Leibundgut, M., Aebersold, R., and Ban, N. (2014). Architecture of the large subunit of the mammalian mitochondrial ribosome. Nature *505*, 515–519.

Greber, B.J., Bieri, P., Leibundgut, M., Leitner, A., Aebersold, R., Boehringer, D., and Ban, N. (2015). Ribosome. The complete structure of the 55S mammalian mitochondrial ribosome. Science *348*, 303–308.

Haque, M.E., Elmore, K.B., Tripathy, A., Koc, H., Koc, E.C., and Spremulli, L.L. (2010). Properties of the C-terminal tail of human mitochondrial inner membrane protein Oxa1L and its interactions with mammalian mitochondrial ribosomes. J. Biol. Chem. *285*, 28353–28362.

Hell, K., Neupert, W., and Stuart, R.A. (2001). Oxa1p acts as a general membrane insertion machinery for proteins encoded by mitochondrial DNA. EMBO J. *20*, 1281–1288.

Hrabe, T., Chen, Y., Pfeffer, S., Cuellar, L.K., Mangold, A.-V., and Förster, F. (2012). PyTom: a python-based toolbox for localization of macromolecules in cryo-electron tomograms and subtomogram analysis. J. Struct. Biol. *178*, 177–188.

Keil, M., Bareth, B., Woellhaf, M.W., Peleh, V., Prestele, M., Rehling, P., and Herrmann, J.M. (2012). Oxa1-ribosome complexes coordinate the assembly of cytochrome C oxidase in mitochondria. J. Biol. Chem. *287*, 34484–34493.

Khoshouei, M., Pfeffer, S., Baumeister, W., Förster, F., and Danev, R. (2016). Subtomogram analysis using the Volta phase plate. J. Struct. Biol.

Kremer, J.R., Mastronarde, D.N., and McIntosh, J.R. (1996). Computer visualization of three-dimensional image data using IMOD. J. Struct. Biol. *116*, 71–76.

Lorenzi, I., Oeljeklaus, S., Ronsör, C., Bareth, B., Warscheid, B., Rehling, P., and Dennerlein, S. (2016). Ribosome-Associated Mba1 Escorts Cox2 from Insertion Machinery to Maturing Assembly Intermediates. Mol. Cell. Biol. *36*, 2782–2793.

Lučić, V., Förster, F., and Baumeister, W. (2005). Structural studies by electron tomography: from cells to molecules. Annu. Rev. Biochem. *74*, 833–865.

Mai, N., Chrzanowska-Lightowlers, Z.M.A., and Lightowlers, R.N. (2016). The process of mammalian mitochondrial protein synthesis. Cell Tissue Res.

Mastronarde, D.N. (2005). Automated electron microscope tomography using robust prediction of specimen movements. J. Struct. Biol. *152*, 36–51.

Nickell, S., Förster, F., Linaroudis, A., Net, W. Del, Beck, F., Hegerl, R., Baumeister, W., and Plitzko, J.M. (2005). TOM software toolbox: acquisition and analysis for electron tomography. J. Struct. Biol. *149*, 227–234.

Ott, M., and Herrmann, J.M. (2010). Co-translational membrane insertion of mitochondrially encoded proteins. Biochim. Biophys. Acta *1803*, 767–775.

Ott, M., Prestele, M., Bauerschmitt, H., Funes, S., Bonnefoy, N., and Herrmann, J.M. (2006). Mba1, a membrane-associated ribosome receptor in mitochondria. EMBO J. *25*, 1603–1610.

Pettersen, E.F., Goddard, T.D., Huang, C.C., Couch, G.S., Greenblatt, D.M., Meng, E.C., and Ferrin, T.E. (2004). UCSF Chimera - A visualization system for exploratory research and analysis. J. Comput. Chem. *25*, 1605–1612.

Pfeffer, S., Brandt, F., Hrabe, T., Lang, S., Eibauer, M., Zimmermann, R., and Förster, F. (2012). Structure and 3D arrangement of endoplasmic reticulum membrane-associated ribosomes. Structure *20*, 1508–1518.

Pfeffer, S., Woellhaf, M.W., Herrmann, J.M., and Förster, F. (2015). Organization of the mitochondrial translation machinery studied in situ by cryoelectron tomography. Nat. Commun. *6*, 6019.

Piao, L., Li, Y., Kim, S.J., Byun, H.S., Huang, S.M., Hwang, S.-K., Yang, K.-J., Park, K.A., Won, M., Hong, J., et al. (2009). Association of LETM1 and MRPL36 contributes to the regulation of mitochondrial ATP production and necrotic cell death. Cancer Res. *69*, 3397–3404.

Preuss, M., Leonhard, K., Hell, K., Stuart, R.A., Neupert, W., and Herrmann, J.M. (2001).

Mba1, a novel component of the mitochondrial protein export machinery of the yeast Saccharomyces cerevisiae. J. Cell Biol. *153*, 1085–1096.

Richter-Dennerlein, R., Oeljeklaus, S., Lorenzi, I., Ronsör, C., Bareth, B., Schendzielorz, A.B., Wang, C., Warscheid, B., Rehling, P., Dennerlein, S., et al. (2016). Mitochondrial Protein Synthesis Adapts to Influx of Nuclear-Encoded Protein. Cell *167*, 471–483.e10.

Scheres, S.H.W. (2012). RELION: Implementation of a Bayesian approach to cryo-EM structure determination. J. Struct. Biol. *180*, 519–530.

van der Sluis, E.O., Bauerschmitt, H., Becker, T., Mielke, T., Frauenfeld, J., Berninghausen, O., Neupert, W., Herrmann, J.M., and Beckmann, R. (2015). Parallel Structural Evolution of Mitochondrial Ribosomes and OXPHOS Complexes. Genome Biol. Evol. *7*, 1235–1251.

Szyrach, G., Ott, M., Bonnefoy, N., Neupert, W., and Herrmann, J.M. (2003). Ribosome binding to the Oxa1 complex facilitates co-translational protein insertion in mitochondria. EMBO J. *22*, 6448–6457.

Supplementary Materials

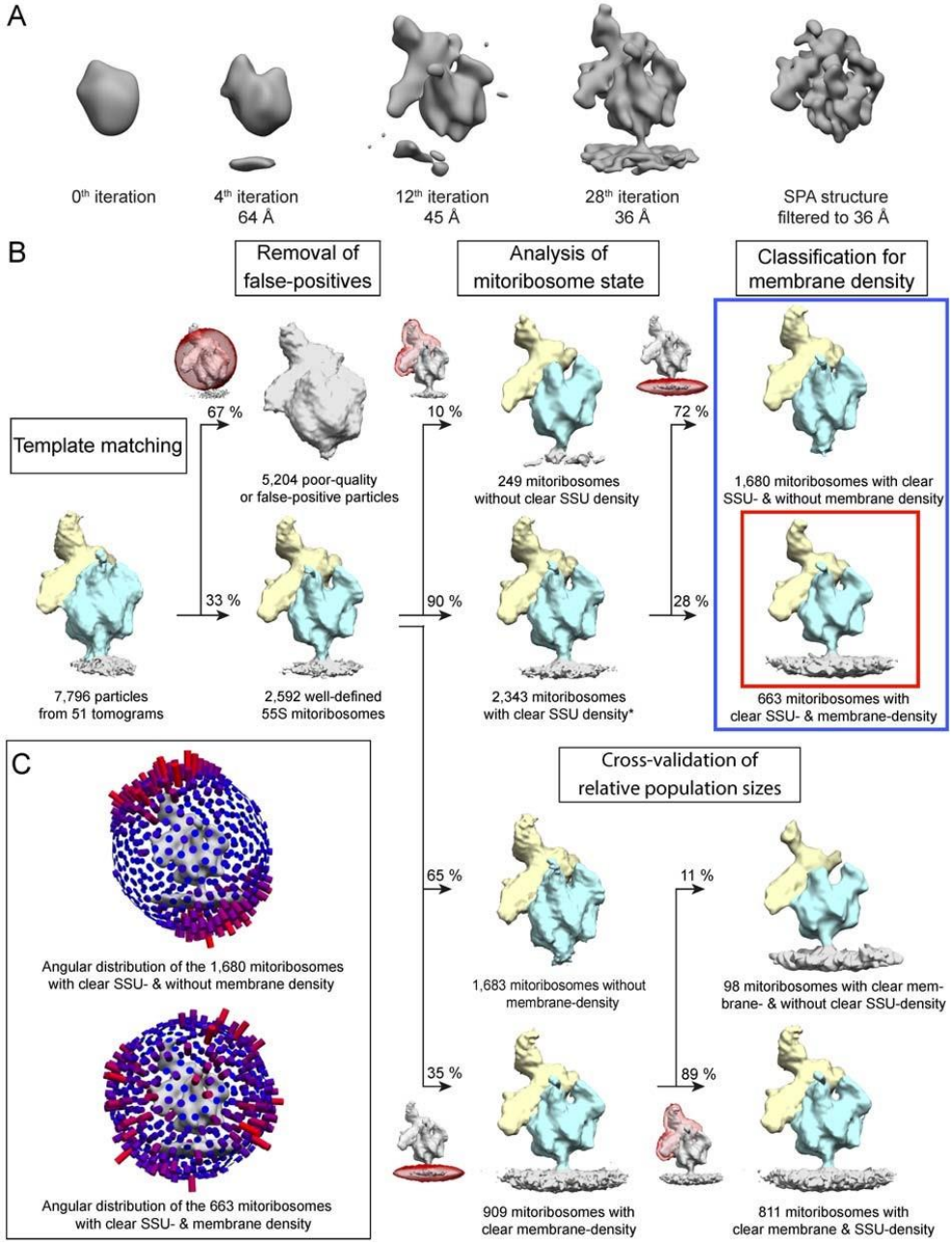

Figure S1. Related to Figure 1 and Figure 2. Reference free Template generation a**nd extended classification procedure**. A) 231 interactively located particles from two tomograms were aligned without prior structural information using fast rotational matching (Chen et al., 2013). The final average is very similar to the single particle analysis (SPA) structure (EMDB 2876) filtered to the same resolution. Resolution of the averages from each iteration was determined by Fourier shell correlation

of two halves of the data (FSC criterion = 0.5). B) An initial round of classification using a spherical mask (depicted in red) was performed to obtain well-defined particles from a set of candidate particles retrieved by template matching and manual inspection. Two additional rounds of classification were then performed to identify mitoribosomes with a clear membrane and SSU density, either focusing first on the SSU and then on the membrane region (top), or the other way round (bottom). The sequence of these two classification rounds does not affect the relative size of the subpopulations. The dataset used for the analysis of the polysomal organization is marked with an asterisk. The dataset used for averaging is highlighted by a red box. C) Angular distribution of subtomograms contributing to the two classes (blue box) without (top) and with a clear membrane density (bottom). Length and color of spikes indicate abundance.

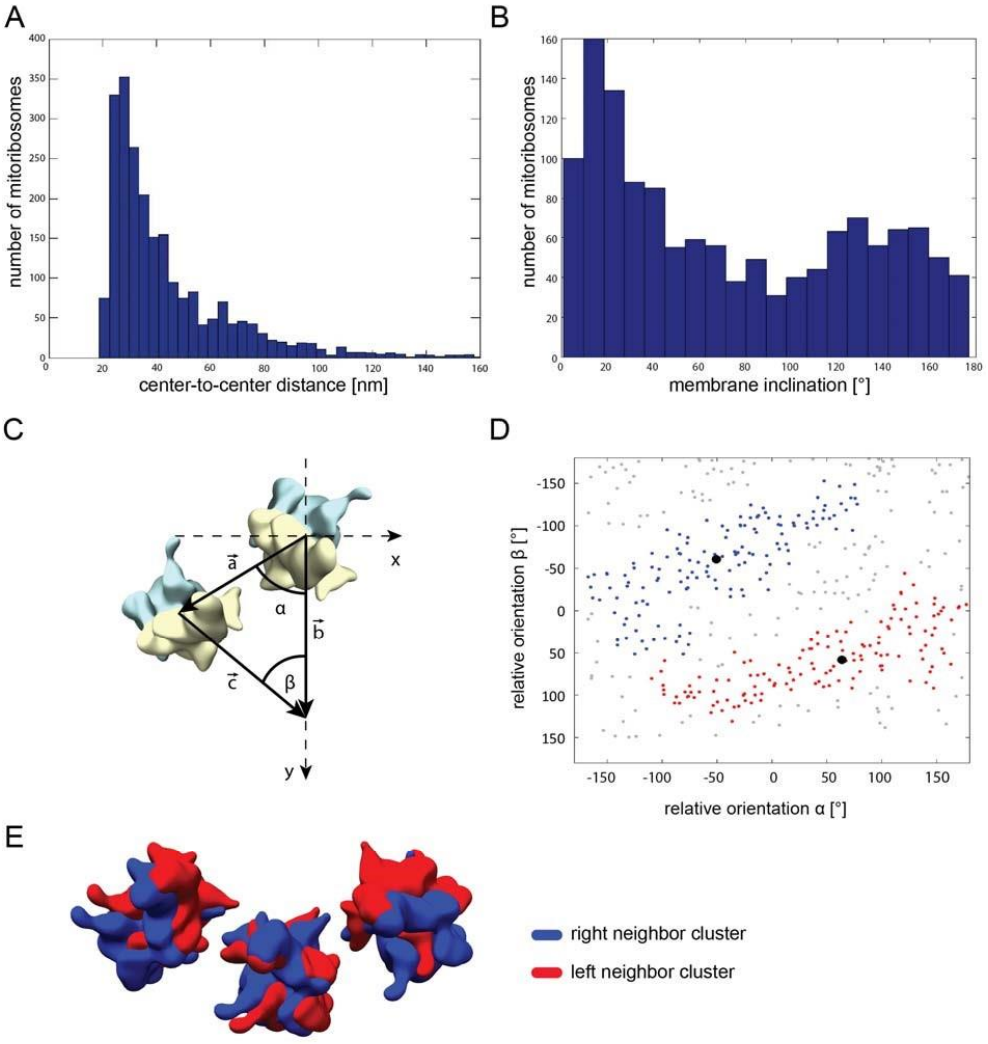

Figure S2. Related to Figure 1. 3D arrangement of membrane-bound human mitochondrial polysomes. A) Center-to-center distances between a mitoribosome and its next neighbor. B) Relative membrane inclination between a mitoribosome and its next neighbor within a distance range of 20nm

to 40nm. C) The relative positions and orientations of next neighbors were defined using two angles (α, β), as depicted. D) Relative positions (α) and orientations (β) of next neighbors within a distance of 20nm to 40nm, and a membrane inclination of 0° to 35° were plotted against each other. Hierarchical clustering identified two classes (blue and red) with the class centers depicted (black points). E) 3D organization of the polysomes, corresponding to the left and right neighbor (respectively the red and blue cluster in D)) .

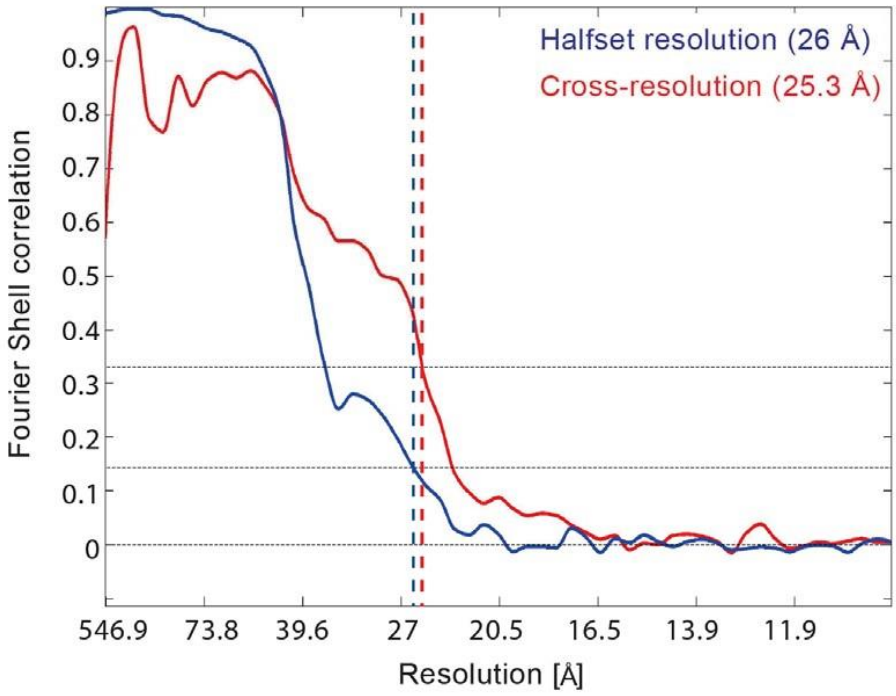

Figure S3. Related to Figure 2. Resolution assessment. Using a spherical mask encompassing the complete mitoribosome, Fourier shell cross-resolution against a single particle cryo-EM density (EMDB 2876, FSC criterion 0.33) and Fourier shell correlation of two independent halves of the data (FSC criterion 0.143) indicate resolutions of
25.3 Å and 26 Å, respectively.

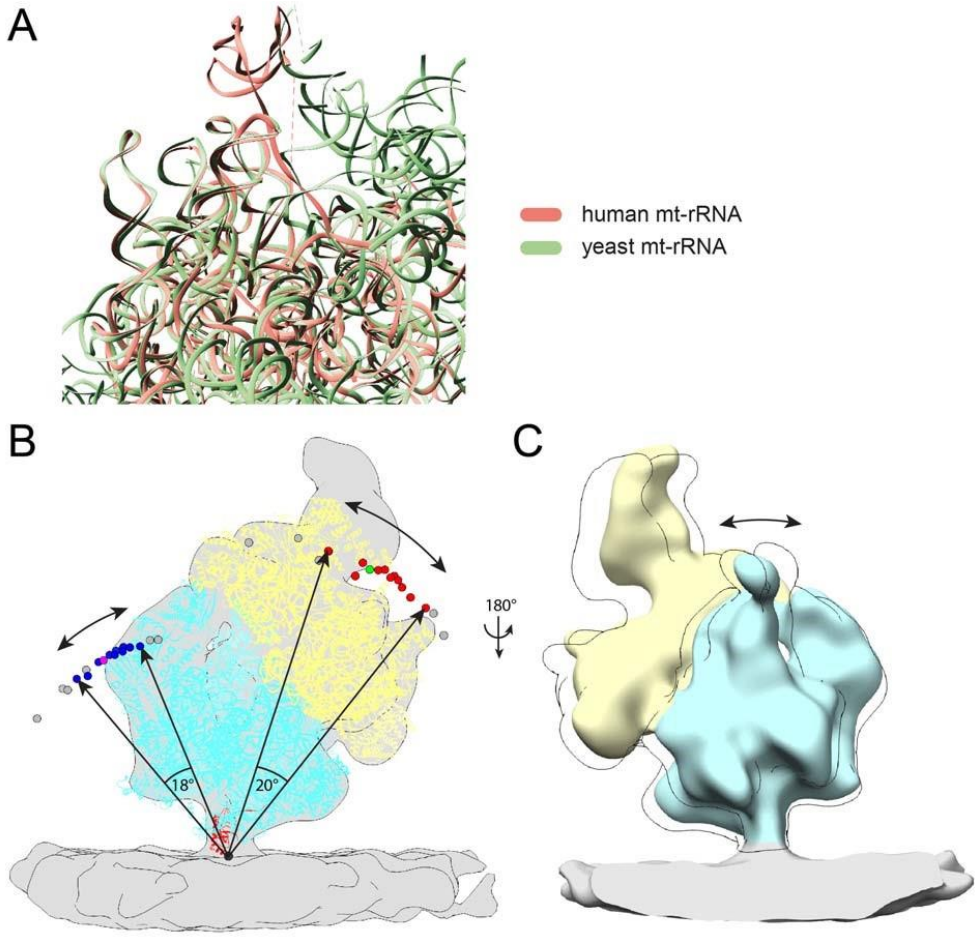

Figure S4. Related to Figure 4. Structure-based alignment of the human (PDB 3j9m) and yeast (PDB 3j6b) mitoribosomal large subunit rRNAs and flexibility of the human mitoribosome on the membrane. A) Superposition of the aligned rRNAs shows little displacement of the conserved parts. B) Three reference points were positioned on mL45 (black point), the large (blue points) and the small subunits (red points) of the atomic model for the human mitoribosome (LSU: cyan, SSU: yellow, mL45: red). The model was fitted into the class averages with different membrane inclinations. Endpoints of difference vectors between mL45 and the other two reference points scatter around the average reference point positions (magenta and green). The angular distances between the maximum outliers of the two individual reference point groups are 18° and 20°, respectively (the 33% of datapoints with the highest angular distance to the mean (grey points) were not considered). Contours of the subtomogram averages with maximal membrane inclination visualize movement of the ribosome on the membrane (right panel).

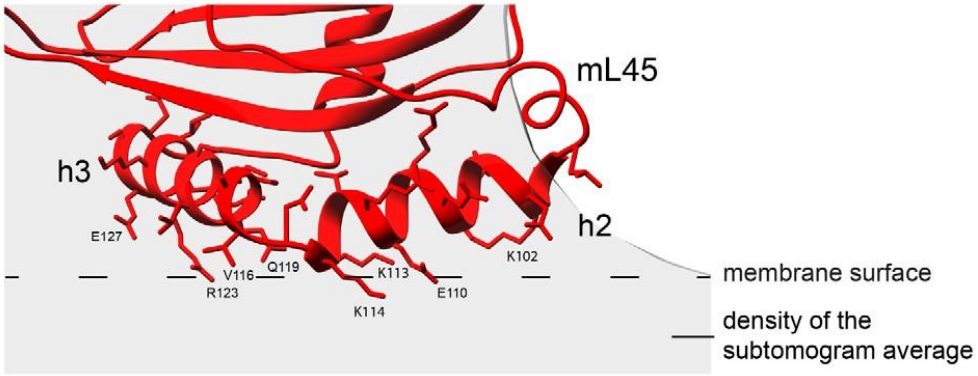

Figure S5. Related to Figure 3. Membrane interaction of mL45 helices h2 and h3. Atomic model of porcine mL45 (PDB 5aj4, red) fitted into the subtomogram average (grey). Several of the charged residues of helices h2 and h3 (K102/113/114, R123, E110/127) are facing the membrane surface.

Chapter 3

In situ studies of mitochondrial translation by cryoelectron tomography

Robert Englmeier[1], Friedrich Förster[1,2]

[1] Cryo-Electron Microscopy, Bijvoet Center for Biomolecular Research, Utrecht University, 3584 CH Utrecht, The Netherlands

2: Correspondence to: f.g.forster@uu.nl

Published in Mitochondrial Gene Expression. Methods in Molecular Biology, vol 2192. Humana, New York;

DOI: https:/doi.org/10.1007/978-1-0716-0834-0_18

Abstract

Cryoelectron tomography (cryo-ET) enables the three-dimensional (3D) visualization of macromolecular complexes in their native environment (*in situ*). The ability to visualize macromolecules *in situ* is in particular advantageous for complex, membrane-associated processes, such as mitochondrial translation. Mitochondrial translation occurs almost exclusively associated with the inner mitochondrial membrane, giving rise to the mitochondrial DNA-encoded subunits of oxidative phosphorylation machinery. In cryo-ET, the 3D volume is reconstructed from a set of 2D projections of a frozen-hydrated specimen, which is sequentially tilted and imaged at different angles in a transmission electron microscope. In combination with subtomogram analysis, cryo-ET enables the structure determination of macromolecular complexes and their 3D organization. In this chapter, we summarize all steps required for structural characterization of mitochondrial ribosomes *in situ*, ranging from data-acquisition to tomogram reconstruction and subtomogram analysis.

1 Introduction

Cryo-electron tomography (cryo-ET) enables the three-dimensional (3D) visualization of frozen-hydrated biological specimens in a close-to-native state at molecular resolution [1]. In order to obtain a 3D image, the sample is sequentially tilted in the transmission electron microscope (TEM) and projection images are acquired, resulting in a tilt series. In contrast to classical electron microscopy (EM) of dehydrated, heavy metal stained and plastic-embedded specimens, vitrification by rapid cooling (cryo-preparation) preserves the molecular structure of the specimen and enables the detailed analysis of macromolecular complexes [2].

While cryo-EM single particle analysis (SPA) allows for the structure determination of macromolecular complexes at atomic resolution, this method requires purification of the respective molecules, thus isolating them from their native context. In contrast, cryo-ET can be applied to isolated organelles or even whole cells, enabling the visualization of macromolecules *in situ*. Therefore, this imaging modality is suitable for the structural analysis of membrane-associated processes. Mitochondrial translation belongs to this category: mitochondrial mRNA is translated by the membrane-bound mitochondrial ribosome (mitoribosome), and the product is typically co-translationally inserted into the inner mitochondrial membrane (IMM) [3].

Application of cryo-ET to isolated mitochondria can visualize mitoribosomes *in organello*. Due to the beam sensitivity of vitrified biological samples tomograms are acquired with low doses (typically < 100 $e^-/Å^2$). The resulting low signal-to-noise ratio (SNR) limits the resolution of the tomograms to approximately 5 nm [4]. Key to quantitative analysis of mitoribosomes in noisy tomograms is a process called template matching, which can localize and identify copies of the target macromolecule based on its known structural signature. By aligning and averaging multiple copies of the macromolecule, i.e. subtomogram averaging, the SNR improves, allowing subnanometer and even atomic resolution in selected cases [5] [6]. Classification allows for disentangling different conformational or compositional states, e.g. separating fully-assembled mitoribosomes from smaller species.

In this this method chapter we cover cryo-ET sample preparation, data acquisition and processing in the context of mitochondrial translation. For data processing we also describe the software packages TOM [7] and PyTom [8].

2. Materials

2.1 Isolation of mitochondrial vesicles

The precise purification protocol will ultimately depend on the biological question, which may require different levels of enrichment or ultrastructural preservation. We achieved a

fairly pure sample of yeast mitochondria with a previously described protocol [9]. For human mitochondria, we previously used a protocol [10] adapted from Frezza *et al.* [11]. Both protocols employ differential centrifugation, and show sufficient enrichment for cryo-ET analysis despite notable contamination by multivesicular vesicles and ER. Here, the protocol that we employed for the purification of mitochondria from Freestyle™ 293-F cells grown in suspension is described [10].

1. Freestyle™ 293-F cells grown in Freestyle medium.
2. PBS buffer: Dissolve 8 g of NaCl, 0.2 g of KCL, 1.44 g of Na_2HPO_4 and 0.2 g of KH_2PO_4 in 800 ml of H_2O. Adjust pH to 7.4 with HCl and fill up to 1 liter with H_2O.
3. Isolation buffer: 10 mM Tris, 150 mM sucrose, 1 mM EGTA, pH 7.4. Prepare 200 mM Tris stock solution by resolving 2.64 g of Trizma HCl and 0.38 g of Trizma Base in 100 ml. Prepare 0.5 mM EGTA stock solution by resolving 1.9 g EGTA in 8 ml. Adjust pH to 8.0 with KOH and fill up to 10ml. Prepare 2 M Sucrose stock solution by resolving 18g in 35ml H20. Fill up to 50 with H2O. Pipette 5ml of the 200 mM Tris stock solution with 100 µl of 0.5 M EGTA solution, 3.85 ml of the 2 M sucrose solution and 41.15 ml of H_2O
4. Glass-Teflon homogenizer.

2.2 Preparation of cryoEM grids

1. Mechanical or automated grid-plunger (Vitrobot™, Thermo Fisher Scientific) including all the required accessories, i.e. container with separate cup for liquid nitrogen and cryogen and a tweezer-mount with appropriate tweezer.
2. Ethane or Ethane-Propane mixture as a cryogen.
3. Ice-free liquid nitrogen.
4. Holey or lacey carbon coated grids (Quantifoil).
5. Glow discharger (e.g. Pelco Easiglow).
6. Filter paper (Whatman, Grade 595).
7. 10 nm BSA-coated gold beads (e.g., UMC Utrecht). Dilute them at the half of the recommended value (usually 1:40 to 1:50) in 20 mM Hepes pH 7.4 buffer to achieve a 2x gold buffer for on-grid dilution.
8. EM grid storage boxes (e.g., Ted Pella).

2.3 Electron microscopy

The crowded environment of the mitochondrial matrix as well as the thickness of mitochondria both result in low contrast in tomograms and make the identification of mitoribosomes difficult. The minimum requirement to obtain interpretable data of the interior of isolated mitochondria is a 200 kV cryo-TEM, equipped with a field-emission gun, energy-filter and direct electron detector. With this equipment, the vitrified mitochondria should not exceed 200 nm thickness along the normal of the EM grid. A 300 kV TEM in

combination with a phase plate maximizes penetration depth of electrons and hence the resulting contrast.

2.4 Software

The following software is required to perform the protocols described in this method chapter:

- Current version of SerialEM [12] for tilt series acquisition (here we use version 3.6) (http://bio3d.colorado.edu/SerialEM/).
- motioncor2 [13], for alignment of dose-fractionated movies.
- TOM and AV3 toolbox [5], [7]; for localization of gold markers required for tilt series alignment (https://bitbucket.org/FridoF/av3).
- Matlab R2014a or earlier; to run the TOM/ AV3 toolbox. Add TOM and av3 directories to the Matlab search path, i.e. by the "`Set path`" button or the '`addpath`' command.
- PyTOM v0.971 [8]; for tomogram reconstruction, template matching, subtomogram alignment and classification (http://pytom.org).
- UCSF Chimera 1.10 or higher [14]; for data visualization.
- "Chooser" plugin for Chimera; available on the PyTom website [15].

Regarding the processing of tomographic data, the TOM/AV3 toolbox is only required for the gold marker clicking. It includes all required functions for the processing of 2D and 3D images (e.g. filtering, downscaling, cropping, reconstruction of tomograms and averaging of subtomograms) and enables the integration of standard Matlab functions and external Matlab packages for data analysis. Template matching, subtomogram alignment and classification are implemented in PyTOM, which provides more functionalities for subtomogram processing, higher interpolation accuracy and higher computational speed. We will therefore focus on the application of PyTom and mention the usage of TOM/ AV3 functions where required.

3 Methods

3.1 Purification of crude mitochondrial vesicle from human suspension cells

1. Grow the cells to a cell density of approximately 1x 10^6 cells/ ml.
2. Collect the cells by centrifugation for 5 minutes at 360 g and 4 °C. All subsequent steps should be carried out at 4 °C.
3. Wash the cells twice by resuspending the cell pellet in 1x PBS buffer and repeating the centrifugation from step 2.
4. Resuspend the cell pellet in homogenization buffer (5 ml/g cell pellet).
5. Transfer the cell suspension to a Glass-Teflon Potter and homogenize it by 120 up- and downstrokes (see **Note 1**).
6. Clear the lysate for 10 minutes at 800 g.
7. Transfer the supernatant to a new tube and centrifuge for 10 minutes at 9,000 g.
8. Resuspend the mitochondrial pellet in 1ml/ g homogenization buffer and centrifuge it again at 9,000 g for 10 min.
9. Resuspend the mitochondrial pellet to a concentration of 10 mg/ml in homogenization buffer. Store it at -80 ° upon flash-freezing in liquid nitrogen or use it directly for grid preparation by diluting it to 1.5 mg/ ml (see **Note 2**).

3.2 CryoEM grid preparation of mitochondrial vesicles

To analyze purified biological sample in the cryo-TEM, the sample needs to be applied to a specimen carrier, the EM grid, and vitrified by plunge-freezing into a cryogen (ethane or ethane-propane). The EM grid is a thin, circular (Ø 3 mm) specimen container with a regular grid-mesh (e.g. copper or molybdenum), and a support film (usually carbon) to accommodate the sample. Due to the hydrophobicity of carbon, EM grids are generally made hydrophilic by a plasma treatment in a glow-discharger just prior to grid preparation. Due to the relatively short inelastic mean free path of electrons in vitreous ice (~400 nm at 300 kV [16], ~250 nm at 120 kV [17]), the EM grid is blotted after applying the sample and just prior to plunge-freezing resulting in a thin the water-film containing the sample (~200 nm).

1. Glow discharge an adequate amount of Quantifoil holey or lacey carbon coated grids.
2. Cool the container down with liquid nitrogen.
3. Make sure that the container is dry and condense the cryogen in the cooled container (*see* **Note 3**).

4. Pick up the glow discharged grid with the tweezers and mount it on the manual or automated grid-plunger.

5. Pipette 3 μL of your mitochondrial sample (1.5 mg/ml) on to the EM grid, followed by 3 μL of the 2x gold buffer (*see* **Note 4**).

6. Blot the EM grid, either one-sided with a manual plunger or from both sides with an automated plunger.

7. Plunge the grid into the cryogen.

8. Transfer the grid into a grid storage box, repeat for the desired number of grids and store them in liquid nitrogen.

3.3 Data acquisition with SerialEM

SerialEM is an open-source, academic software, which includes all functionalities required for cryo-ET data acquisition [12]. In addition to a low-dose mode that allows the setup of five different imaging modes and the exposure of separate areas to minimize radiation damage during acquisition, it has an implemented mapping functionality ("Navigator"), supports the execution of scripts, and provides control over all the necessary detector and energy filter parameters. We will briefly cover the data acquisition with SerialEM, but the considerations of imaging parameters apply to any cryo-ET data acquisition irrespective of the software. Before starting, make sure to optically align the TEM and perform all essential calibrations in SerialEM (e.g. pixel size on specimen level, image-, beam-, stage-shift, beam-tilt, etc.; see Serial EM home page [18] for detailed instructions on installation and calibration). Here we will focus on using the Navigator to acquire grid montages and multiple tilt series. For additional details concerning the operation of SerialEM, the reader is referred to the SerialEM documentation.

3.3.1 Fast and systematic: Using the Navigator and montage-maps in SerialEM

The initial parameters that need to be defined are the magnifications at which the sample will be screened (View and Search modes), as well as the magnification at which tilt series will be recorded (Record, Focus and Trial modes). The lateral size of mitochondrial vesicles ranges from 300 nm to 800 nm (depending on the isolation conditions). The field of view (FOV) in Record mode should cover that area. Once the settings are defined, it is useful to map the entire EM grid to obtain a low magnification overview that will aid targeting regions of appropriate ice thickness. SerialEM provides the option to acquire montage maps (i.e. stitched images), at an intermediate magnification that minimizes the electron dose applied to the sample

and can be used to interactively select features and move to them from the Navigator window. This function expedites the screening process and also helps to document samples, facilitating the identification of mitochondria within heterogenous samples.

1. Set up the magnification of the five modes (View, Search, Focus, Trial, Record) to cover the useful ranges (the values in the brackets correspond to the approximate pixel sizes of the K2 Summit Direct Electron Detector): View: ~5 µm FOV (~1.5 nm/pixel), Search: ~500 µm FOV (~120 nm/pixel), Record/ Focus/ Trial: ~700 nm FOV (~0.22 nm/pixel) (*see* **Note 5**).
2. Adjust the exposure time and acquisition mode of the detector (Super-resolution mode, Dose fractionation and frame rate) for your five acquisition modes, and the file options for your record parameter ("`Setup`" in the Camera control panel) so that they match your requirements (*see* **Note 6**).
3. For a full grid montage, open the navigator and go to "`Navigator/ Montage/ Full Grid montage`". Make sure to have the desired low magnification settings (~500 µm FOV) saved to the View parameters. If calibrated correctly, SerialEM will automatically choose the correct number of patches to acquire a full grid montage and the covered area will be displayed below (~2.5x2.5 mm^2).
4. To map the area around the current location (adjust to above magnification for the View mode if you have changed it for a full grid montage), select "`File/ New Montage`". The number of tiles which also defines the covered area can be specified.
5. Start the acquisition of the map from the "`Montage`" floating window by clicking "`Start`".
6. After the acquisition, load the map into the Navigator window by clicking "`New map`".
7. To add points of interest to the navigator, click on "`Add points`" in the navigator floating window and then click on the area of interest on the map. You can add comments to the points in the Navigator and assign them different colors for easy identification on the map.

3.3.2 Tilt series acquisition

During the tilt series acquisition, the specimen is sequentially tilted, and projection movies are acquired. Despite high mechanic accuracy of the stage, the sample is never completely eucentric during the tilt. To compensate for the residual lateral and horizontal motion, tracking and focusing are usually performed after each tilt.

In order to prevent the sample from unnecessary exposure both are performed on user-defined areas that are translated with away from the exposure area along the tiltaxis ('low dose').

1. Once you have found and centered a suitable region at intermediate magnification (View mode), move the sample to eucentric height by running the routine "`Tasks/ Eucentric rough`". For high magnification also run "`Tasks/ Eucentric fine`".
2. Define the position of the Focus and Trial area in the "Low Dose" control panel (*see* **Note 7**).
3. Open the Tilt series dialog box.
4. Check and define all the parameters of the tilt series. The major parameters are the tilt scheme (uni-, bidirectional or dose-symmetric), tilt range, tilt increment, starting angle, settling time and criteria for tracking and focusing (*see* **Note 8**).
5. Press "`GO`" to start the acquisition of the tilt series.

3.3.3 Setting up a batch acquisition

The option to set up a batch acquisition is implemented via the Navigator window. SerialEM requires two maps per position, one at low (View mode) and one at high magnification (Record mode). The reference maps are stored in two different files, and the function "Realign to Item" is used by SerialEM to find back areas of interest based on the stored stage coordinates and by cross-correlation of the images.

1. Open two new files for the high and low magnification maps (e.g. "`maps.mrc`" and "`anchors.mrc`") by clicking "`File/ Open New`".
2. Navigate to the area of interest. If you have stored them in the navigator, locate them using the "`Go To XYZ`" button.
3. Acquire a preview picture of the feature of interest. If necessary, center it and acquire another preview picture. Make sure that the image shift is low (<0.5 FOV).
4. Toggle to the "`maps.mrc`" file from the "`Buffer Control`" panel and click "`New Map`".
5. Acquire a View image.
6. Toggle to the "`maps.mrc`" file from the "`Buffer Control`" panel and click "`New Map`".
7. Check the boxes "`Acquire at position`" and "`New file at item`" for the high magnification? item in the navigator window.
8. Repeat this procedure for all your points/ areas of interest.

9. After having created high and low magnification maps at all points, open the batch acquisition window by "`Navigator/ Acquire at points…`".
10. Select the desired operations to execute at each point. If the eucentricity has not been refined at all points, this option should be checked.
11. Start the batch acquisition by pressing "`GO`".

3.4 Reconstructing a 3D tomogram from 2D micrographs

In order to reconstruct a 3D tomogram from the 2D projections of a tilt series, several mechanical and optical distortions that arise during the acquisition of a projection at near-atomic resolution have to be corrected for. The first major step is the alignment of the subframes, to account for mechanical and beam induced motion of the sample during the exposure. For this task we recommend motioncor2 [13]. The second major step is the alignment of the tilted images to a common 3D coordinate system. If the images contain gold beads (following section 3.1), the following steps will cover the tilt series alignment with TOM/ PyTOM. If this is not the case, we recommend IMOD for alignment by patch tracking (not covered here, see IMOD web site for more information [19]).

1. Run motioncor2 by executing the following command in the terminal (*see* **Note 9**):

   ```
   motioncor2 -InTif 'path to your frames' -OutMrc 'targetpath' -Patch 5 5
   ```

2. PyTOM and TOM read projections in the *.em format based on a base-name followed by an index ascending according to the tilt angle (i.e. projection1.em corresponds to -60 °, the maximum negative tilt). To sort the motion-corrected frames according to the tilt-series and the tilt angle in ascending order (e.g. "`tomogram1/sorted/sorted[1- 61].em`", run `av3_sortTSbymdoc` (see **Note 10**):

   ```
   av3_sortTSbymdoc(numtomo, mdocdir, mdocprefix, rawframesuffix, framedir, projdir, dim, scale)
   ```

   The information of the corresponding angles is derived from the SerialEM *.mdoc file. Here, `numtomo` is the index of the tomogram (in the above example 1), `mdocdir` and `mdocprefix` specify the mdoc logfile, `rawframesuffix` and `framedir` the raw frames, `projdir` the location of the sorted and aligned projections and `dim` the lateral size of the generated images (in pixels). Define a

downscaling factor (e.g. 4: scale=4) to generate downscaled projections, which will will accelerate and facilitate the tilt series alignment.

3. Start the GUI for gold marker by typing '`tom_setmark`' in the Matlab shell.
4. Load the tilt series by clicking '`New`' and selecting the last projection in the directory of the scaled projections (Fig 1, label 1). Four new windows will open.
5. Choose the first gold marker by clicking '`ADD`' in the main panel (Fig 1, label 2), and then clicking on your desired gold marker in the working images (Fig 1, label 3) and the magnified image (Fig 1, label 4).
6. Check the "`Turbo`" box (Fig 1, label 5) to automatically load the next projection, and click the marker for all projections of the tilt series.
7. After clicking one marker for the whole tilt series, add new markers by clicking '`NEW`' and adding them as before. Click at least 3 gold markers in all projections and compute the alignment. The residual error should ideally be below 1.5 pixels.
8. Write a markerfile corresponding to the full-sized images by multiplying the values in the created markerfile with the previously applied downscaling factor from step 4 of this section (e.g. factor 2).
9. Refine the marker positions using `av3_finelocate` (matlab) using the full-sized projections and write out the corresponding markerfile.
10. Run the function '`reconstructTomogram.py`' with the desired parameters to align the projections and reconstruct the tomogram by weighted backprojection. Type '`reconstructTomogram.py --help`' to display all parameters. Choose the 0° projection as the reference index, the refined markerfile as markerfile ('`markerfile_refined.em`') and the most central marker as reference marker (see **Note 11**).

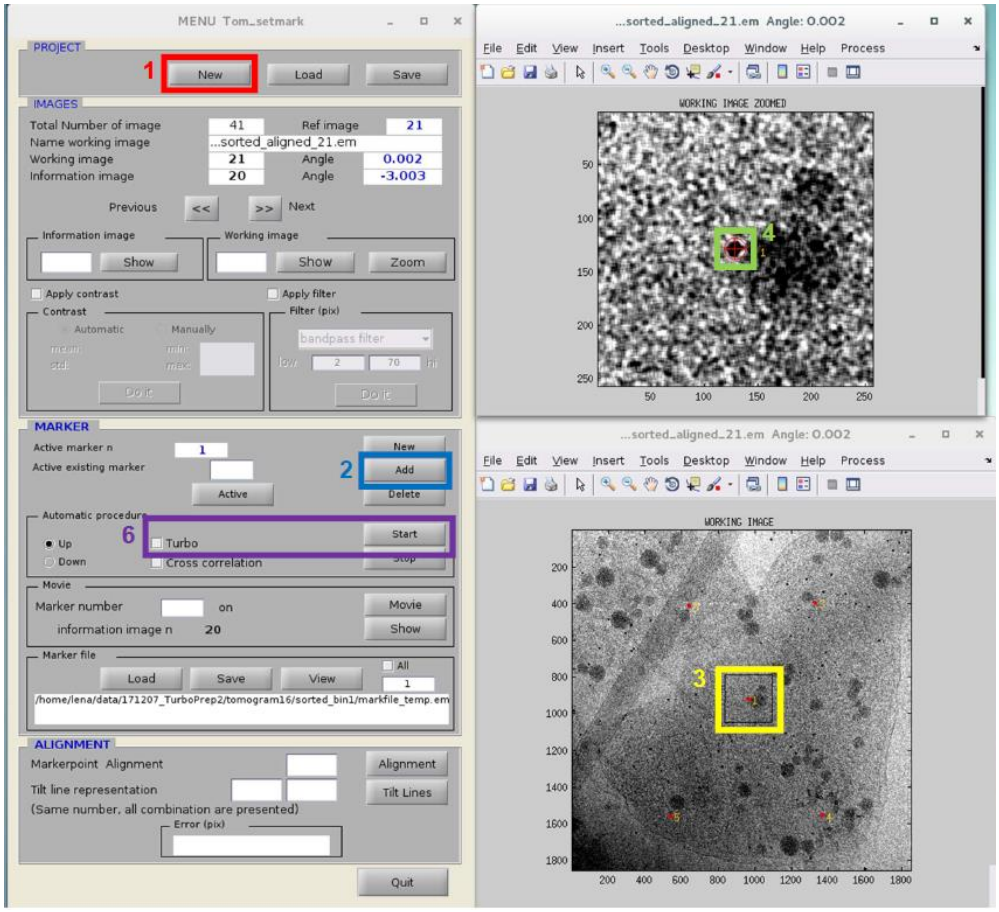

Fig 1: Interface of the tom_setmark GUI. Load a new tilt series from the Project tab (1). Add the first marker by clicking 'ADD' (2), and then selecting the area containing your first marker in the working image (bottom right, 3). Then click on the gold marker in the zoomed image (top right, 4). Check the box 'Turbo' (5) and click 'Start'.

3.5 Subtomogram averaging

The resolution of a tomogram is typically not limited by the sampling (=voxel size on specimen level), but rather by the SNR. Similar to SPA, subtomogram averaging (STA) enables the reconstruction of a high-resolution density by aligning and averaging multiple subtomograms each depicting copies of the macromolecule. A common approach to STA is to (*i*) interactively localize copies of the macromolecule of interest in a few tomograms, (*ii*) to align and average the corresponding subvolumes by fast rotational matching allowing exhaustive orientation sampling [20], (*iii*) to localize more copies in the remaining datasets by template matching, and (*iv*) to determine a higher resolution average of different classes of the molecule using real-space methods. In order to select initial candidates, exclude

template bias and select for true positives, the complex of interest should be visible in the tomogram. For mitochondria, the ATP synthases and mitoribosomes can be identified in a high-quality tomogram (Fig 2).

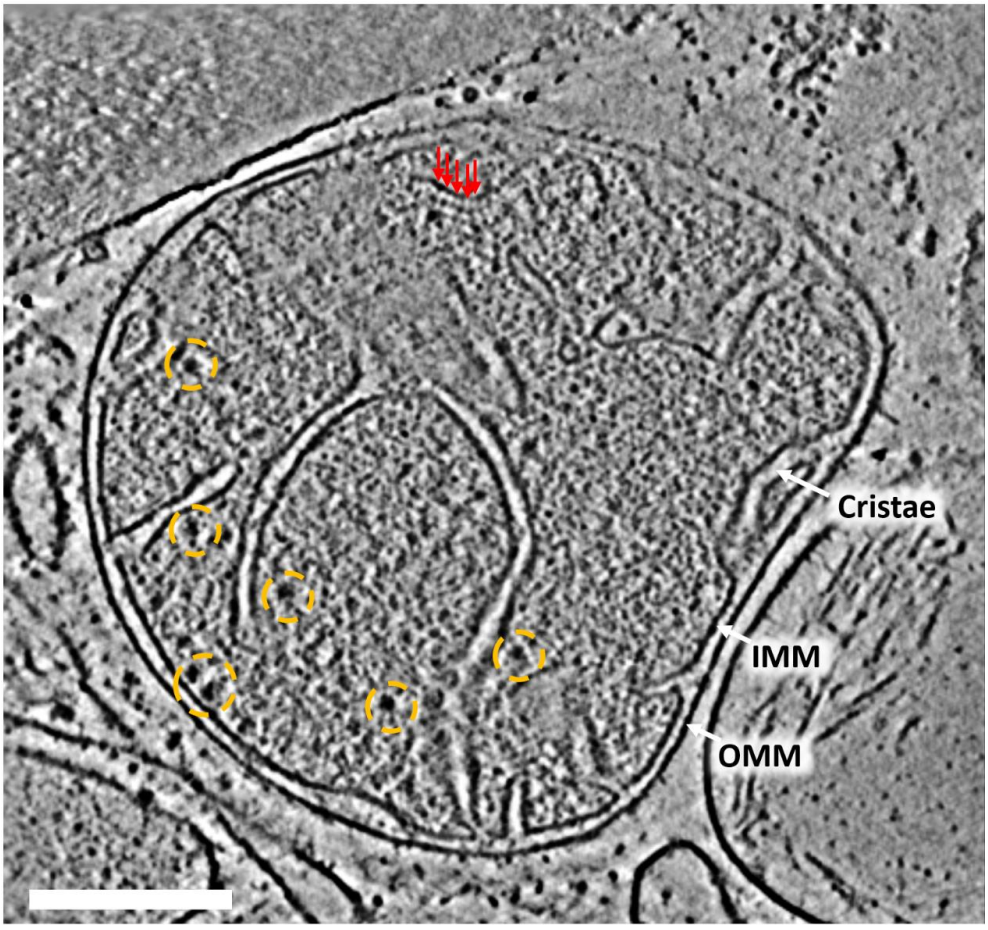

Fig 2: Slice from a reconstructed tomogram of a human mitochondrion (data acquired with the Volta Phase Plate at 300 kV). In the resulting tomogram of the mitochondrion, the outer and inner mitochondrial membranes (OMM and IMM), as well as cristae, membrane-associated mitoribosomes (yellow) and ATP synthases (red) can be identified. Scale bar: 200nm.

3.5.1 Creating an initial, reference-free average from manually picked particles by FRM alignment

1. Open chimera and load the reconstructed tomogram (*see* **Note 12**).
2. Open the Volume tracer in the Volume Viewer Panel ('Tools / Volume Tracer', Fig 3).

3. Choose how to place a marker (e.g. using middle + control button).
4. Set the color of the marker by clicking on it and choose an opacity of 0.1 to 0.2 to facilitate particle selection. Make sure that within the Viewing panel (Favorites/ Side View/ Effects), the box '`single layer`' (under transparency) is unchecked.
5. Use the slider to go through your z-slices to locate your particles. For each particle you wish to pick, place a marker on top of it to record its location. When you are done, save the marker file ('File/ Save current marker set as', e.g., `tomogram1/reconstruction/man_picked.cmm`).
6. Use the matlab script av3_cmm2particlelist to read the xyz-coordinates from the '`.cmm`' marker file (textfile) and write a Pytom compatible particle list in `.xml` format (see **Note 13**).
7. Run the `reconstruct_subtomos_INFR.py` function to reconstruct subvolumes with the INFR method (see **Note 14**). In this example full-magnification subvolumes of 256x256x256 voxels are reconstructed:
   ```
   pytom
   PathToPytom/reconstruction/reconstruct_subvolumes_INFR.py -d [Path_to_unweighted_projections/] -s 256 -b 1 -o 0,0,0 -p path_to_particleList.xml
   ```
8. Check that your subtomograms indeed depict particles using `with tom_dspcub (matlab) or` Chimera. In case of a mitoribosome, you should clearly see a central density in the lowpass-filtered subtomogram.
9. Make a directory for your FRM alignment.
10. For an initial alignment, it is advisable to scale down the subvolumes to 5- 10 Å voxel size. Use either `tom_rescale` (matlab) or `resize` (pytom) to write downscaled versions of the reconstructed full-size subtomograms (see point 7.).
11. Generate a particleList for your resized particles (see step 6.)
12. `Create an average from your particles created with tom_average (matlab) or average.py (pytom). Display the average with tom_dspcub (matlab) or in Chimera and check that there is a clear density in the center.`
13. Generate a mask with `tom_spheremask` (matlab) or `initSphere.py` (pytom). Check that the mask encompasses the structure of interest (Fig 3).
14. The FRM alignment requires a jobfile (e.g., "`job.xml`") format specifying the parameters (**bold** parameters need to be adjusted to your environment and data). (see **Note 15**). To this end execute 'av3_createFRMjobfile' in the matlab shell to create the jobfile with the respective parameters. These are the lower (here: 8) and upper (64) limits of spherical harmonics, lowpass for initial iteration (6), number of iterations (30), maximum offset of peaks (30), name of

resulting average (‘`average.em`'), mask (‘`maskfile.em`’), pixelsize (5.24 Å), particle diameter (250 Å) and particlelist (‘`particleList.xml`’):

```
av3_createFRMjobfile(‘job.xml’, 8, 64, 6, 30, 30, ‘average.em’, ‘maskfile.em’, 5.24, 250.0, ‘particleList.xml’)
```

15. Run the FRM alignment:

    ```
    pytom PathToPytom/frm/FRMAlignment.py -j job.xml -v
    ```

    After each iteration, an unfiltered average, as well as an average filtered to the determined resolution and an updated particleList will be written out (see **Note 16**).

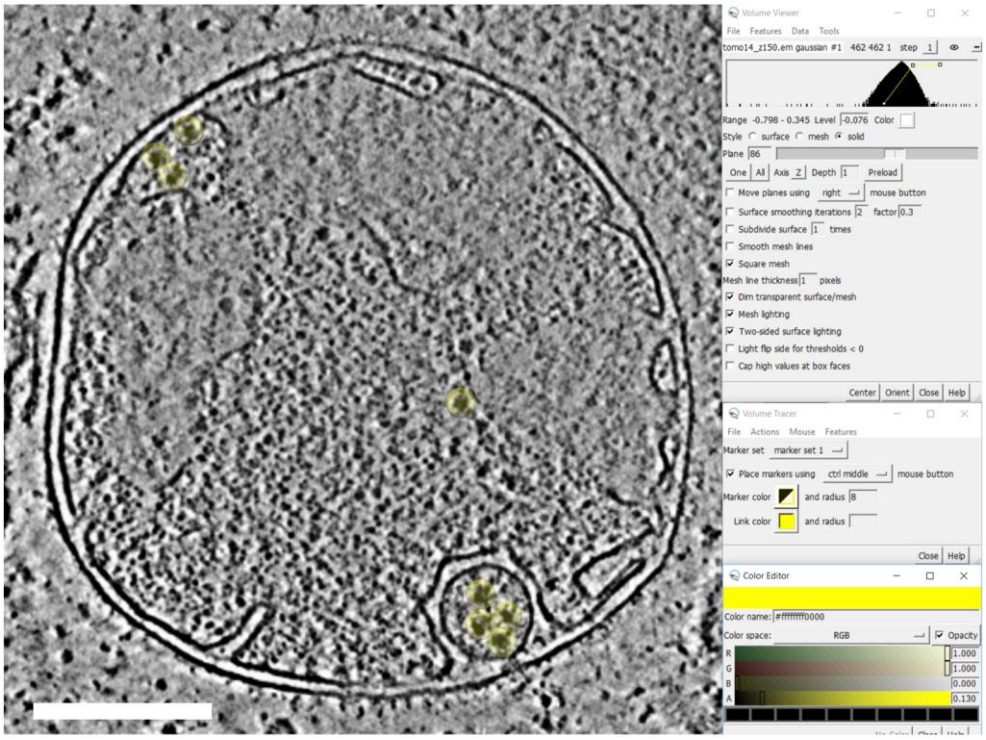

Fig 3: Manual particle picking in Chimera. Use the Volume filter and/ or adjust the histogram to get sufficient contrast. Open the Volume Tracer dialog box (bottom right) and choose the color and radius of your marker. Place markers by clicking on the data planes. Scale bar: 200nm.

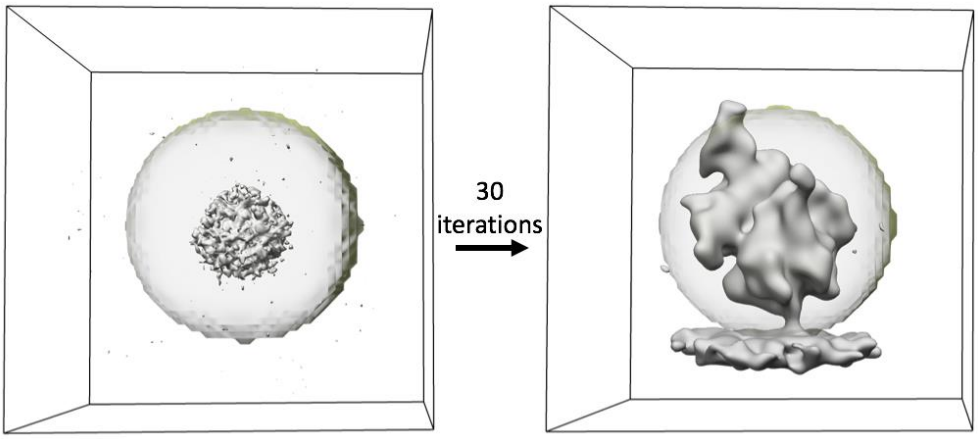

Fig 4: FRM alignment of manually picked particles. a) The average of the subtomograms (grey) with randomly assigned angles should have a spherical shape, and the mask (yellow) should encircle it. b) After 30 rounds of alignment, the spherical shape should ideally converge to a structure resembling your molecule of interest, a human mitoribosome computed from 231 subtomograms in this case.

3.5.2 Template matching

During the template matching, the cross-correlation of a masked template structure is computed at different orientations and at each voxel coordinate. Therefore, the tomographic volume, a template, a mask and a list of rotations are required. Due to the noise within the tomogram and to speed up the computation, template matching is usually performed on downscaled tomograms. Depending on the macromolecule of interest, we recommend an effective voxel size of 1 - 2nm (the example of the human Mitoribosome was performed at 2 nm).

1. Generate a template by applying the appropriate scaling factor to either your reference-free average or external structure (see step 10, 3.4.1) (see **Note 17**).
2. Generate a mask with same dimensions as the template (see step 12, 3.5.1).
3. If computational time is scarce, crop the tomogram in z to only capture the sample (note down the z offset!). Use either `read` (pytom) or `tom_emread` (matlab) to read and write a subvolume of the tomogram.
4. Execute `av3_createTMjobfile` in the matlab shell to create the jobfile with the respective parameters (tomogram '`tomogram.em`', template '`template.em`', mask '`mask.em`', missing wedge of 30°, 7112 angles specified in '`angles_12.85_7112.em`') (see **Note 18**):

```
av3_createTMjobfile('JobInfo.xml', 'tomogram.em',
'template.em', 'mask.em', 30, 'angles_12.85_7112.em')
```

5. Start the Job with the following function that supports message passing interface (MPI). The precise MPI syntax might vary depending on your system (see **Note 19**):

```
mpiexec --tag-output -n 16 pytom
/path_to_pytom/bin/localization.py JobInfo.xml 4 4 1
```

6. Inspect the resulting correlation function by opening the "`scores.em`" file and superimposing it with your tomogram. Adjust the histogram to show the highest scores (Fig 5) (see **Note 20**).

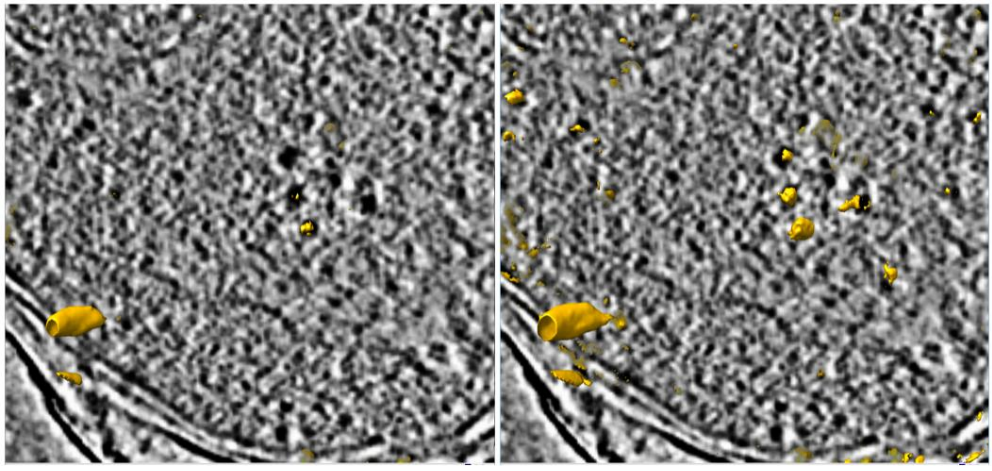

Fig 5: Tomogram with superimposed cross-correlation peaks from template matching. The volume file containing the scores ("scores.em", orange density) obtained by template matching was superimposed with the tomogram (shown as slice). At a high threshold (left), the most significant correlation peaks superimpose with mitoribosomes (center) as well ice contamination (left). Reducing the threshold reveals less significant correlation peaks that superimpose with mitoribosomal densities (right image; center and top left part), as well as false positive matches with the membrane (edges).

3.5.3 Particle extraction and subtomogram reconstruction

Prior to subtomogram reconstruction, the resulting correlation ("`scores.em`") and angle ("`angles.em`") volumes obtained by template matching need to be converted into a list (paricleList in PyTom, motiflist in TOM) containing the particle coordinates, orientation and correlation values. During the particle extraction step, the voxels around the high correlation peaks are zeroed within a defined radius to

exclude multiple entries of the same particle. To separate false-positives from true-positives particles in your template matching results, it is usually necessary to manually filter the identified correlation peaks. This can be done with “Chooser”, a Chimera plugin available on the PyTom website.

1. Extract the particle coordinates into an .xml-file and a motiflist with the following function (see **Note 21**):

```
pytom PathToPyTom/bin/extractCandidates.py -j job.xml
-n 700 -s 8 -r scores.em -o angles.em -p pl.xml -m
targetpath.em -t pathToNewParticles
```

2. Open Chimera and load the tomogram that was used for template matching. Load the corresponding particlelist with the Chooser.
3. The Chooser will display all the entries from the particlelist, starting from the highest correlation values. Inspect all the correlation peaks and assign class indices (e.g. 1 for correct and 0 false-positive matches; more than two class labels can be assigned if desired)see **Note 22**).

4. Save the class labels by clicking “Save” and close the Chooser. Each line in the resulting text file corresponds to the respective entry in the particle-/motifList.

5. Filter the particle-/ motifList by excluding the entries according to the assigned classLabels by executing `av3_filterClassLabels` (see **Note 23**):

```
av3_filterClassLabels(motlin, labelfile, class,
motlout, zheight, scaling, rawsize)
```

6. Run the INFR subtomogram reconstruction (see step 7, 3.4.1), or use the weighted back projection algorithm with the filtered particleList as input (see **Note 24**):

```
reconstructWB.py -p particleList.xml --
projectionDirectory
../reconstructTomo/alignedProjections/ -s 128 -b
1 -o 0,0,192
```

7. Check the correct reconstruction by looking at the subtomograms. Depending on the downscaling factor and pixel size, it might be necessary to apply a strong filter to see features (see **Note 25**).

8. Average the particles with the following function (see **Note 26**):

```
pytom PathToPyTom/bin/average.py -p
particleList.xml -a Average.em
```

3.5.4 Gold standard subtomogram alignment in real space

In addition to the FRM alignment (see 3.4.1), PyTom also provides the option to perform the subtomogram alignment in real space. The real space alignment tends to be more accurate because it simultaneously samples rotational and translational degrees of freedom, but due to the higher computational requirements the rotational search is restricted. Thus, the method requires initial starting angles, which were at this point either determined from the template matching or by a previous round of FRM alignment. The following steps will cover the gold standard real space alignment, which splits the dataset into two independent halves used for the alignment against independent references to reduce over-fitting.

1. Create a directory for the real space alignment.
2. For an initial alignment, it is advisable to downscale the particles to 5 - 10 Å voxel size. Use either `tom_rescale` (matlab) or `resize` (pytom) to write downscaled particles (see 3.3, step 4), or use a downscaling parameter ("`-b`") for reducing volumes on the fly during the alignment (see step 6).
3. Generate a particleList for your resized particles (see 3.4.1, step 6)
4. Create an average from your particles with tom_average (matlab) or average.py. Open the average and check that there is a clear density in the center (see 3.4.1, step 12).
5. Generate a spherical mask (see step 13, 3.4.1). Check that the mask encompasses the structure of interest (Fig 3).
6. Run the 'gold-standard' Real Space local alignment. In this example, 10 iterations of alignment are performed with the data downscaled on the fly by a factor of 2 using an initial rotational sampling of 3 degrees increment (subsequently adjusted according to resolution) in 3 shells:

```
mpirun -n numberOfCPUs pytom
PathToPytom/bin/GLocalJob.py -p particleList.xml -r
Reference.em -m Mask.em --SphericalMask --angleShells
3 --angleIncrement 3. -d ./ -n 10 -b 2 --pixelSize 2.62
--particleDiameter 250
```

3.5.5 Classification

Subtomograms with differing structural features, e.g. due to a particular conformational state or different composition, can be disentangled during subsequent classification. This is usually done by constrained principle component analysis (CPCA), where a pair-wise cross-correlation matrix of the subtomograms is computed and subsequently grouped by principle component analysis and k-means clustering. This allows for the removal of false positives from the dataset, as well as the enrichment of subtomograms showing distinct pronounced structural features such as the small ribosomal subunit or the membrane (Fig. 6A).

1. Generate a mask encompassing the feature of interest within your initial average (Fig. 6A), either with Chimera (shape mask), or with `initSphere` (pytom) for a spherical mask (see 3.4.1, step 13).
2. Compute a cross-correlation matrix of all particles by running the following command (see **Note 27**):

   ```
   mpiexec --tag-output -n numberOfCPUs pytom PathToPytom/calculate_correlation_matrix.py -p particleList.xml -m Mask.mrc -f 10 -b 1
   ```

3. Group the data based on the output '`correlation_matrix.csv`' using CPCA and k-means clustering (see **Note 28**). Here, the data are projected to 5 principal components and grouped 7,800 subtomograms into 67 classes (Fig 6A):

   ```
   pytom path_to_pytom/bin/classifyCPCA.py -p particleList.xml -o pL_classified.xml -c correlation_matrix.csv -e 5 -n 67 -a "Average"
   ```

4. Open and inspect all the classes (here "`Average1-67.em`") in Chimera (Fig 6B) and note down the class numbers that you would like to merge for your further analysis.
5. Filter the particleList to include only the classes that you have picked using the pytom function `splitByClass`:
   Load the pytom module and open the interactive shell by typing '`ipytom`'. Then run the following lines to split the particlelist '`pL_classified.xml`':

   ```
   pl=ParticleList()
   pl.fromXMLFile('pL_classified.xml')
   lists=pl.splitByClass()
   ```

Specify the desired classes in the square brackets and write them out to a new particlelist by running the following lines:

```
ribos=lists[1] + lists[2]
ribos.toXMLFile('pickedClasses.xml')
```

For convenience, you can also use the provided bash script `merge_pl_classes.sh` which also allows merging of classes from several particleLists and contains explanations.

6. If desired, apply further rounds of classification with different masks to separate the subtomograms according to variations in specific areas, e.g., membrane density (Fig 6A). Alternatively, repeat the alignment with the filtered set of subtomograms.

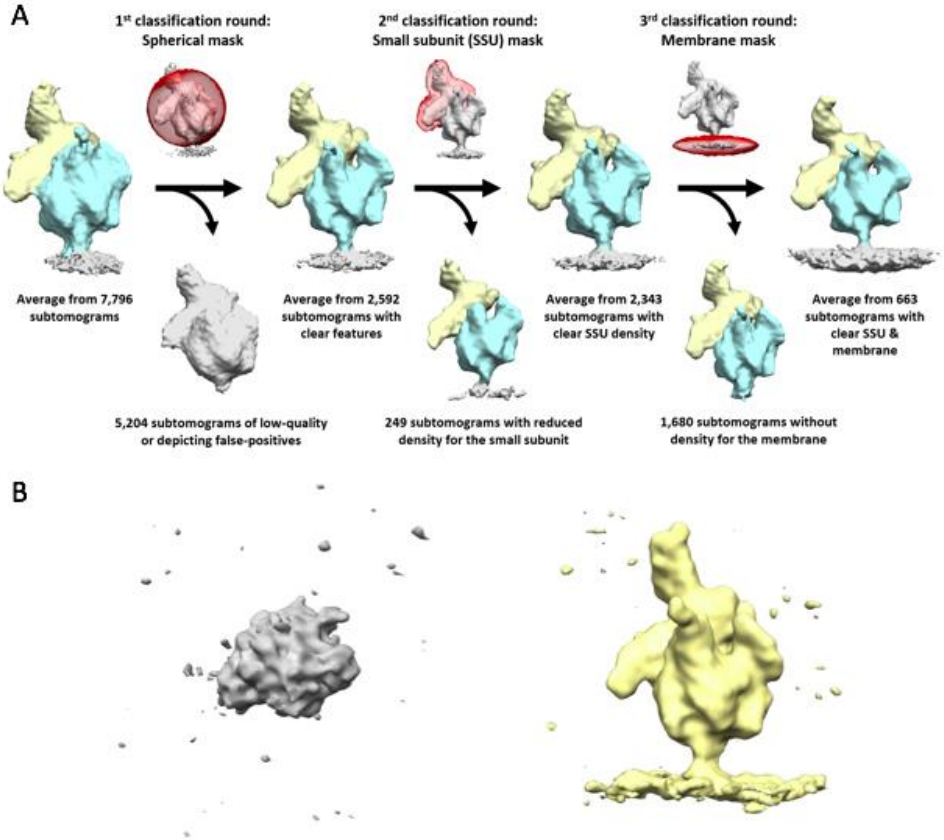

Fig 6: Classification scheme to enrich mitoribosomes with a clear membrane density. A) By performing multiple rounds of classification with different masks (red), subtomograms with a clear membrane density can be separated from subtomograms depicting noise or lacking a clear density for

small subunit or membrane. B) Class averages computed from ~100 subtomograms upon the initial classification of 7,796 subtomograms with a spherical mask. The left class-average (grey) represents a class of false-positives matches, e.g. ice, gold markers, or membrane densities that should be discarded. The right class-average (yellow) already shows clear mitoribosomal features, i.e. the small and large subunit as well as the membrane. (both averages were filtered in Chimera with a Gaussian filter of 1.2).

4 Notes

1. Lysis efficiency will slightly differ depending on the tightness of the individual Glass-Teflon-Potter. Monitor the cell lysis in a light microscope and adjust the number of strokes to achieve of roughly 60 %.

2. Test at least two dilutions of your sample (e.g. undiluted and 1:3). In the case where you characterize your purification protocol for the first time sample a wider range of concentrations. We found that Nanodrop measurements at 280 nm provide reproducible results with regards to mitochondria and vesicle densities and recommend the following conditions for the mitochondrial sample: 1.5 mg/ mL in 20 mM Hepes pH 7.4 and 150 mM Sucrose (human) or 600 mM Sorbitol (yeast). The concentration of the mitochondrial sample is a critical parameter to achieve high-quality tomograms since it affects the ice thickness. Plunge freezing of four grids roughly takes 30 min, so the handling time is neglectable compared to mitochondrial isolation protocols, but mitochondria should be kept on ice.

3. Make sure to not contaminate the ethane or ethane-propane with any liquid nitrogen or water, e.g. from your breath. Try to maintain a protective atmosphere of cold nitrogen vapor in your container at all time to prevent contamination of your sample by ice crystals from the air humidity.

4. For iso-osmotic conditions, mitochondria require 150 to 300 mM sucrose (human) and ~600 mM sorbitol (yeast) in the isolation buffer (see 2.1). However, the sugar concentration should be as low as possible in the vitrified sample to provide a good contrast and to prevent beam damage in the TEM.

5. The choice of the magnification is a tradeoff between FOV and the pixel size. A large FOV enables covering large or even multiple vesicles, while the pixel size puts an upper limit to the maximum resolution. In practice, the maximum resolution is limited to approximately 50% of the Nyquist frequency, i.e. the minimal distinguishable distance is four times the pixelsize on the specimen level. For *in organello* studies of mitochondrial translation a pixel size of ~2 Å does not limit the

resolution, which is rather restricted by the low contrast arising from the sample thickness and the crowded environment of the mitochondrion.

6. It is recommended to test the beam and detector settings in a region of the grid that does not contain useful mitochondrial vesicles, or on a completely different grid to avoid unnecessary radiation damage to the sample. The exposure times for your View/ Search/ Focus/ Trial mode should be adjusted as low as possible but high enough to yield sufficient signal in the resulting image. For your record parameter, the exposure time should be adjusted so that the accumulated dose does not exceed 80 e^-/A^2 for 200 kV respectively 120 e^-/A^2 for 300 kV EM for thinner samples (accumulated dose = dose per tiltangle * number of images). Saving record frames in super-resolution takes slightly longer than in simple counting, and the files are four times bigger. However, these considerations are negligible for tomography, and more critical for SPA data acquisition, where the fairly small gain in detector quantum efficiency often does not outweigh the lower throughput. Regarding the file options, it is advisable to save the files as .tif files with LZW compression as one stack, which yields compression factors of ~40. Including the tilt angle in the filename is also recommended.

7. The position of the Focus/ Trial area should differ from the Exposure area by more than the beam diameter. To measure the beam diameter, you can over-expose carbon to the beam by putting the screen down with the Record mode settings. If possible, try to have some carbon or other features in your Focus/ Trial area, since discrete, high-contrast features facilitate the focusing and tracking.

8. For initial or standard data-acquisition, we recommend the following settings: bi-directional tilt scheme, tilt range -60° to +60°; starting angle -20°, tilt increment of 2° or 3°. The settling time strongly depends on the stage of the microscope, but 15 sec is a good starting value that can be increased if blurring is observed in the Trial image, or reduced otherwise for higher throughput. For all other parameters the provided standard settings are a good starting point. We routinely employ a dose-symmetric tilt scheme [21], which has been recently implemented in the SerialEM tilt series dialog box. It requires slightly more time per tilt series but provides a better dose distribution and is advantageous for high resolution subtomogram averaging.

9. These are the minimum input requirements for both global and local motion, with the standard patch size of 5 x 5. For more information, e.g. on how to apply gain normalization, see the motioncor2 user manual or type “motioncor2” into your terminal.

10. `av3_sortTSbymdoc(numtomo, mdocdir, mdocprefix, rawframesuffix, framedir, projdir, dim, scale)`: `numtomo` defines the number of tomograms and corresponding mdoc files, `mdocdir` the path to your mdoc file, `mdocprefix` the prefix of the mdoc file, `rawframesuffix` the filesuffix of the unaligned frames (e.g. '.tif' or '.mrc'), `framedir` the directory containing the aligned frames, `projdir` directory of projections, `dim` the desired dimension (cut to square) scale the desired scaling factor. The function will create the number of folders defined by `numtomo`, sort the corresponding tiltseries according to the tiltangles into the folder defined in `projdir` and scale and cut the projections.
11. Choose a downscaling factor between 4 to 8 to increase the signal in the resulting volume and keep the file size reasonable for subsequent template matching. Pytom also provides an alternative tomogram reconstruction method, called INFR [22]. It requires aligned but unweighted projections, which can also be obtained using `reconstructTomogram.py` with `—weightingType 0`. Run `reconstruct_INFR.py` to perform the tomogram reconstruction with INFR. The resulting tomogram will have better contrast, which facilitates the manual and automated picking (template matching) of particles.
12. Depending on the data quality and binning, it might be necessary to filter the volume. Go to 'Tools/ Volume Filter' and apply a Gaussian filter with width 0.5 to 0.9 to your volume. It might also be necessary to select solid rendering and adjust the histogram for a good contrast.

13. Check the XYZ coordinates in your generated particleList. They should be positive values corresponding to the dimension of the tomogram you have picked. If the tilt range is different than -60° to +60°, define the opening angle of the missing wedge respectively.

14. `reconstruct_subtomos_INFR.py`: The subtomograms will be written into the specified path in the `particleList.xml`. The option `-d` specifies the input projections, `-s` specifies the box size, `-b` the downscaling factor (be sure to use the same the downscaling factor that corresponds to the tomogram you used for picking your coordinates), and `-o` the offset of the coordinate system in case the positions were picked on cropped tomograms. The function does not have the option to apply a downscaling to the subtomograms. If downscaled subtomograms are intended, create downscaled projections and use them as an input for the subtomogram reconstruction (see 3.3, step 4).

15. The parameter "`Frequency`" defines the starting spatial frequency (in inverse pixels) for the lowpass filter in the first iteration of alignment, and

"`BandwidthRange`" the bandwidth range that is used throughout all iterations (i.e., a highpass filter is effectively used). 30 iterations should usually result in a converging average.

16. Ideally, the resolution will increase and meaningful structural features will manifest themselves. However, for small particle sizes, the structure can align structures according to the missing wedge than their structures. Nevertheless, for large complexes such as the ribosome this reference-free FRM alignment typically succeeds. If the FRM alignment results in a subtomogram average with distinctive features and details, the gold standard real space alignment with the angles from the FRM alignment might improve the result even further (see 3.3.4)

17. If an external structure as a template is intended, apply the correct scaling and have matching density values (i.e. both positive/ negative values for the electron-density). Also, make sure that handedness corresponds your reference system (left- or right-handed). To generate a template for the human mitoribosome you can use the EMDB structure EMDB-2876. Load it in Chimera ('`File/Fetch by ID`'), and save the density map as an mrc density file ('`2876.mrc`'). Determine the scaling factor to de-magnify from 1.34 Å/vox to the desired voxel size (e.g. 20 Å/vox) and divide the box size by that factor to yield your final box size (e.g. 16). Then run the following command with the value in the square brackets to rescale it:

```
map=tom_mrcread('2876.mrc')

map=tom_rescale(map.Value,[16,16,16])
```

If the map needs to be mirrored or inverted, use the following commands (otherwise skip them):

```
map=tom_mirror(map,'x')

map=map*-1
```

Save the map by executing the following line:

```
tom_emwrite('5aj4_scaled.mrc',map)
```

18. The angular search of 7,112 angles (12.85° increment) is a good standard parameter. The different angle files are located within `PathtoPytom/angles/angleLists/`.

19. The last three numbers indicate the splitting of the volume in x, y and z. This should ideally correspond to the number of nodes. The division of the volume by the provided factor has to result in full integers.

20. If the results do not correspond to the features, make sure to have checked all the requirements mentioned in note 14. Especially for small, elongated particles, template matching might fail. In this case, apply a higher downscaling to the tomogram.

21. `extractCandidates.py`: Option `-n` defines the number of particles ,`-s` defines the radius around the peak which will be zeroed to exclude multiple picking of the same particle, `-p` defines the path to the particle list and `-m` defines the path to write out the results in TOM-compatible motiflist format. A good template matching result will show a gaussian distribution for the determined cross-correlation peaks ("`Value`" in `particleList.xml` (PyTom), column 1 in AV3-motiflist). However, within the crowded mitochondrial matrix the results of the template matching often show false-positive matches (Fig. 5). In order to filter the template matching results, multiply the correlation volumes prior to particle extraction with a binary mask encompassing the mitochondrion (e.g. by generating the mask with Chimera Volume Tracer). If the particle list is to be used directly for subtomogram reconstruction (see step 7, 3.4.1), provide an option `-t` with an argument, which defines the target directory for the reconstructed subtomograms.
22. At this step it is beneficial to exclude as many false-positives as possible. However, this is not absolutely critical since a classification will also help in removing false-positives (Fig 6B).

23. `av3_filterClassLabels`: `motlin` defines the input motiflist file, `labelfile` the file containing the manual classifications from the Chooser, `class` defines the class index that will be included (e.g. 1) and `motlout` the name of the filtered output motifllist. The last three parameters - `z_height` (defines the z position at which, if applicable, the downscaled tomogram was cropped), `scaling` (scaling factor of the tomogram) and `rawsize` (dimension of the non-downscaled projections) - are optional, and used for the generation of a non-scaled motiflist with the coordinate system of the aligned raw projections.

24. The argument of option `-s` defines the box size, `-b` the downscaling factor of the particle coordinates compared to the projection, and `-o` the offset of the particle coordinates from the coordinate system chosen for the reconstruction, which is used in the .xml file, if any.

25. If the box is empty, make sure that the supplied coordinates in the .xml file correspond to your tomogram dimension. (0 to 3838/3710 for full-size data from a K2 detector)

26. The resulting average should show distinctive structural features if the template matching and reconstruction have worked. If this is not the case, the template-matching probably resulted in a considerable number of false-positives which have to be removed by repeating steps 2. to 5., checking the template matching results or repeating the template matching. If the results do not improve, manual particle selection might be the only option (see 3.4.1). Mitoribosomes are reliably detected by template matching in very thin tomograms (< 150 nm) with good contrast but are hardly detected in thicker tomograms where they can still be identified by eye.

27. `calculate_correlation_matrix.py`: Option `-f` represents a low-pass filter, and `-b` a downsampling factor to be applied to the subtomograms.

28. `classifyCPCA.py`: Option `-p` defines the path to the particlelist (make sure that the path to the subtomograms within the particlelist is correct), `-o` the targetpath for the output-particlelist that will include the classlabels, `-c` filename of the correlation matrix, `-e` number of eigenvectors; `-n` the number of classes; `-a` basename of the class-averages. Five eigenvectors are usually sufficient to represent the main features of the subtomograms. On the one hand side, the number of classes should be chosen as high as possible in order to separate subtomograms depicting different conformations. On the other hand, the number should be chosen sufficiently small, such that a class-average contains enough subtomograms to yield sufficient SNR to distinguish features. For mitoribosomes, 100 subtomograms/ class should yield enough signal for the reliable assessment of class-averages (Fig. 6B).

5 References

[1] V. Lucić, F. Förster, and W. Baumeister, "Structural studies by electron tomography: from cells to molecules.," *Annu. Rev. Biochem.*, vol. 74, pp. 833–65, Jan. 2005.

[2] J. Dubochet *et al.*, "Cryo-electron microscopy of vitrified specimens," *Q. Rev. Biophys.*, vol. 21, no. 02, p. 129, Mar. 1988.

[3] M. Ott and J. M. Herrmann, "Co-translational membrane insertion of mitochondrially encoded proteins.," *Biochim. Biophys. Acta*, vol. 1803, no. 6, pp. 767–75, Jun. 2010.

[4] S. Asano *et al.*, "Proteasomes. A molecular census of 26S proteasomes in intact neurons.," *Science*, vol. 347, no. 6220, pp. 439–42, Jan. 2015.

[5] F. Förster and R. Hegerl, "Structure determination in situ by averaging of tomograms.," *Methods Cell Biol.*, vol. 79, pp. 741–67, Jan. 2007.

[6] W. Wan and J. A. G. Briggs, "Cryo-Electron Tomography and Subtomogram Averaging," *Methods Enzymol.*, vol. 579, pp. 329–367, Jan. 2016.

[7] S. Nickell *et al.*, "TOM software toolbox: acquisition and analysis for electron tomography.," *J. Struct. Biol.*, vol. 149, no. 3, pp. 227–34, Mar. 2005.

[8] T. Hrabe, Y. Chen, S. Pfeffer, L. K. Cuellar, A.-V. Mangold, and F. Förster, "PyTom: a python-based toolbox for localization of macromolecules in cryo-electron tomograms and subtomogram analysis.," *J. Struct. Biol.*, vol. 178, no. 2, pp. 177–88, May 2012.

[9] G. Daum, P. C. Böhni, and G. Schatz, "Import of proteins into mitochondria. Cytochrome b2 and cytochrome c peroxidase are located in the intermembrane space of yeast mitochondria.," *J. Biol. Chem.*, vol. 257, no. 21, pp. 13028–33, Nov. 1982.

[10] R. Englmeier, S. Pfeffer, and F. Förster, "Structure of the Human Mitochondrial Ribosome Studied in Situ by Cryoelectron Tomography," *Structure*, vol. 25, no. 10, p. 1574–1581.e2, 2017.

[11] C. Frezza, S. Cipolat, and L. Scorrano, "Organelle isolation: functional mitochondria from mouse liver, muscle and cultured fibroblasts.," *Nat. Protoc.*, vol. 2, no. 2, pp. 287–95, Jan. 2007.

[12] D. N. Mastronarde, "Automated electron microscope tomography using robust prediction of specimen movements.," *J. Struct. Biol.*, vol. 152, no. 1, pp. 36–51, Oct. 2005.

[13] S. Q. Zheng, E. Palovcak, J.-P. Armache, K. A. Verba, Y. Cheng, and D. A. Agard, "MotionCor2: anisotropic correction of beam-induced motion for improved cryo-electron microscopy," *Nat. Methods*, vol. 14, no. 4, pp. 331–332, Apr. 2017.

[14] E. F. Pettersen *et al.*, "UCSF Chimera - A visualization system for exploratory research and analysis," *J. Comput. Chem.*, vol. 25, no. 13, pp. 1605–1612, Oct. 2004.

[15] "PyTom | Python and Tomography." [Online]. Available: http://pytom.org/. [Accessed: 22-

Oct-2018].

[16] K. Yonekura, M. B. Braunfeld, S. Maki-Yonekura, and D. A. Agard, “Electron energy filtering significantly improves amplitude contrast of frozen-hydrated protein at 300 kV,” *J. Struct. Biol.*, vol. 156, no. 3, pp. 524–536, Dec. 2006.

[17] R. Grimm, D. Typke, M. Bärmann, and W. Baumeister, “Determination of the inelastic mean free path in ice by examination of tilted vesicles and automated most probable loss imaging,” *Ultramicroscopy*, vol. 63, no. 3–4, pp. 169–179, Jul. 1996.

[18] “SerialEM Home Page.” [Online]. Available: http://bio3d.colorado.edu/SerialEM/. [Accessed: 22-Oct-2018].

[19] “Patch Tracking Example Data Set.” [Online]. Available: http://bio3d.colorado.edu/imod/doc/patchTrackExample.html. [Accessed: 22-Oct-2018].

[20] Y. Chen, S. Pfeffer, T. Hrabe, J. M. Schuller, and F. Förster, “Fast and accurate reference-free alignment of subtomograms,” *J. Struct. Biol.*, vol. 182, no. 3, pp. 235–245, 2013.

[21] W. J. H. Hagen, W. Wan, and J. A. G. Briggs, “Implementation of a cryo-electron tomography tilt-scheme optimized for high resolution subtomogram averaging,” *J. Struct. Biol.*, vol. 197, no. 2, pp. 191–198, 2017.

[22] Y. Chen and F. Förster, “Iterative reconstruction of cryo-electron tomograms using nonuniform fast Fourier transforms,” *J. Struct. Biol.*, vol. 185, no. 3, pp. 309–316, 2014.

Acknowledgement

We would like to thank Dr. Stuart Howes for critical comments on the manuscript. This work was supported by funding from the Nederlandse Organisatie voor Wetenschappelijke Onderzoek (Vici 724.016.001), the European Research Council under the European Union's Horizon2020 Programme (ERC Consolidator Grant Agreement 724425 - BENDER) and the Deutsche Forschungsgemeinschaft (FO 716/3-2).

Chapter 4

Visualizing actively translating mitoribosome-insertase complexes inside human mitochondria

Robert Englmeier[1], Kerem Can Akkaya[2], Cong Wang[2], Fan Liu[2], Friedrich Förster[1]

[1] Structural Biochemistry group, Bijvoet Centre for Biomolecular Research, Utrecht University, Padualaan 8, 3584 CG Utrecht, The Netherlands

[2] Department of Chemical Biology, Leibniz-Forschungsinstitut für Molekulare Pharmakologie (FMP), 13125 Berlin, Germany

manuscript in preparation

Abstract

Mitoribosomes synthesize mitochondrially-coded transmembrane subunits of the respiratory chain-complexes, which are essential for cellular metabolism and health. However, the mechanism that guides hydrophobic nascent peptides to the insertase Oxa1L and into the inner mitochondrial membrane (IMM) remains elusive. Here, we use cryo-electron tomography (cryoET) to visualize the mitoribosome inside isolated human mitochondria at sub-nanometer resolution, and provide the structures of a previously uncharacterized mitoribosome-insertase complex as well as the insertase Oxa1L bound to the mitoribosome in the native IMM. Oxa1L engages with the mitoribosomal membrane-facing proteins via two luminal, amphipathic helices in addition to its C-terminal domain. These helices form a helical hairpin above the hydrophobic core of Oxa1L, bridge the gap between the exit tunnel and the membrane, align the insertase with the exit tunnel, and guide the nascent peptide into the membrane. Our data provides a model for the insertion of the hydrophobic respiratory-chain subunits into the membrane and shows the potential of cryoET to elucidate the interactions of protein complexes with miniscule membrane proteins in their native environment.

Introduction

Mitochondria are a hallmark of eukaryotic cells and play a central role in cellular energy conversion and health. Throughout evolution, mitochondria have maintained their own genome as well as their own protein synthesis machinery, the mitoribosome[1]. In human cells, mitoribosomes synthesize a small but essential set of 13 transmembrane proteins, which are all subunits of respiratory chain complexes. During protein synthesis, mitoribosomes associate with the membrane and the nascent proteins are co-translationally guided into the lipid membrane by the insertase Oxa1L[2], the eponymous 40kDa protein of the Oxa1-superfamily of protein insertases [3]. Mutations of mitoribosomal proteins and its cofactor Oxa1L can result in diseases such as congenital encephalopathy and Leigh's disease[4,5].

Previous studies used cryo-electron microscopy single particle analysis (cryoEM SPA) to determine the structure of the mitoribosome at near atomic resolution[6,78]. These studies revealed extensive remodeling of the mitoribosome throughout eukaryotic evolution resulting in an inverted RNA and protein composition between yeast and human, and even a displacement of the exit tunnel in yeast. A recent high-resolution structure of the solubilized mitoribosome and its associated insertion machinery obtained by cryoEM SPA revealed the interaction of the C-terminal domain of Oxa1 with the mitoribosome. However, the architecture of the Oxa1's transmembrane parts and its highly conserved helical hairpin domain, as well as their interaction with the mitoribosome were not resolved. Furthermore, the interaction of Oxa1 with the mitoribosomal protein mL45 also remains unclear.

Despite these structural insights into the mitoribosome, its interaction with the insertion machinery remains poorly understood due to the nature of SPA requiring solubilization resulting in removal of the mitoribosome-insertase complex from its native membrane environment. In contrast to SPA, cryo-electron tomography (cryoET) enables the three-dimensional visualization of complexes *in situ*, i.e., in their native environment and can be applied to study viruses, organelles and even thinned cells [9]. Compared to SPA, however, cryoET has the limited possibility to enrich protein complexes of interest, a lower throughput, increased sample thickness and lower contrast resulting from the crowded, native environment, which all make it more challenging to obtain high resolution. Previous cryoET studies visualized yeast and human mitoribosomes *in organello*, revealing their native organization into polysomes and predominant association with the membrane [10,11]. They also revealed a ~25 Å gap between the exit tunnel and the membrane, a striking difference to cytosolic ER-associated ribosomes that reside closely to the membrane. This gap raises the question how the highly hydrophobic nascent peptides are guided to the lipid membrane, prior to their insertion. However, the resolution of 20-30 Å did not allow distinguishing the protein-protein interactions that mediate the mitoribosomal membrane interaction. The alignment of the mitoribosomal exit tunnel with the insertase, and how the the gap between the two is bridged so that the hydrophobic nascent peptides are reliably guided via the insertase into the membrane, remains unresolved.

Thus, the currently available high-resolution structures of isolated mitoribosomes by SPA and low-resolution *in situ* structures by cryoET leave a knowledge gap in the mechanistic understanding of the membrane insertion machinery and its interaction with the

mitoribosome. Here, we present the structures of actively translating human mitoribosome-insertase complexes imaged inside isolated mitochondria by CET at sub-nanometer resolution. The results provide structural evidence for a previously uncharacterized mitoribosome-insertase complex and resolve the helical hairpin domain of Oxa1 engaged with the mitoribosome.

Results

Low speed centrifugation enables cryo-ET studies of intact mitochondria

Previous studies of isolated mitochondria using cryoET were limited to few tomograms and therefore delivering relatively low-resolution structures[11–13]. To facilitate the acquisition of a large dataset enabling higher resolution, we have screened several parameters to optimize the quality and quantity of mitochondria enriched from HEK cells: (*i*) cell lysis, (*ii*) differential centrifugation and (*iii*) cryoEM grid preparation (Fig. 1A). For cell lysis, we tested douncing and nitrogen cavitation. While nitrogen cavitation lysed cells more efficiently (Fig. S1A), histone and cytochrome C release into the supernatant indicated undesired rupturing of the nucleus and outer mitochondrial membrane, which was not observed for douncing (Fig. S1b). Thus, douncing yielded superior conservation of organelle structure compared to nitrogen cavitation.

Many isolation protocols apply forces of 9,000 - 12,000g for 10 minutes to sediment mitochondria in an isotonic buffer [11,14]. However, we previously observed that these forces result in damage to mitochondria and contamination arising from the endoplasmic reticulum[12]. To optimize the centrifugation speed for mitochondria sedimentation, we performed Western blot analysis of supernatant fractions of HEK cell lysates after sequential centrifugation at increasing centrifugal forces. Already after centrifugation at 4,000 g for 5 minutes we observed a strong reduction of mitochondrial marker (Hsp60) in the supernatant fraction, and almost no further reduction in mitochondrial signal past 5,600g (Fig. 1B). These findings indicate that centrifugation forces below ~5,000 g are sufficient for to enrich mitochondria. Indeed, cryo-EM imaging of a sample obtained after sedimentation at 3,000g confirms the sedimentation of mitochondria, showing a high density of intact mitochondria with clearly discernable inner and outer membranes and internal features (Fig. S1C). Differential centrifugation of cell lysates from yeast and S2 insect cells also show sedimentation of mitochondria at 3,000 g after 5min, with the supernatant nearly completely depleted of mitochondria after 5min at 6,000g (Fig. S1C). Interestingly, pioneering studies of organelle isolation from mammalian cells also applied low centrifugal forces (2,500 g) for mitochondrial sedimentation[15]. Compared to isolation using high centrifugal forces[12], the concentration of intact mitochondria on the cryoEM grid was considerably higher when lower forces were applied. The higher forces presumably lead to the rupture of mitochondria during centrifugation and pellet resuspension.

Lastly, we tested different methods for grid preparation. Compared to automated two-sided blotting, one-sided manual blotting resulted in a higher density of mitochondria (Fig. S1D, E). Combining the optimized isolation and grid preparation parameters resulted in a

protocol requiring less than 30 minutes and yielded a sample that allowed for the high-throughput acquisition of 368 tilt-series in 8 microscopy days, highlighting the feasibility of our isolation protocol to achieve both a high quality and quantity of mitochondria on cryoEM grids.

Structure of the actively translating human mitoribosome at sub-nanometer resolution

Due to the relatively large size of mitochondria gold beads, which are typically used as fiducials for tilt-series alignment, position relatively peripheral compared to the mitoribosomes resulting in a suboptimal tilt series alignment. Feature-based tilt-series alignment[16] is an alternative alignment method but is usually less accurate. To improve the accuracy of feature tracking the signal-to-noise ratio of the tilt series was increased by deconvolution[17], which reduced the alignment residual of the tilt series by approximately 20% compared to the unprocessed images (Fig. S4). In the resulting tomograms, mitoribosomes could be clearly identified (Fig. 1C).

Particle localization by template matching is prone to false positives at the low signal-to-noise ratio of mitochondria tomograms. In previous *in organello* studies of mitoribosomes, true positive mitoribosome hits were manually identified among candidates from template matching[11,12] – a time-intensive and cumbersome procedure, which is not feasible for large datasets. Here, we applied template matching followed by the extraction of >400,000 candidate subtomograms of mitoribosomes from the 368 tomograms and subsequent 3D classification in RELION to exclude likely false positives. This protocol resulted in 27,983 subtomograms that were classified as 55S mitoribosomes (Fig. S3). Alignment and averaging of the subtomograms yielded a map with sub-nanometer resolution ($FSC_{0.143}$ = 8.47 Å) and local resolution reaching 6.5 Å (Figs. 1D, S4). Consistent with the reported resolution of 7-10 Å, the rRNA, peptidyl -tRNA and protein α-helices are clearly defined for both central and peripheral regions, such as the α-helices of mL40 and mL48 that contact the P-site tRNA and of the membrane anchor mL45 (Fig. 1F-E).

The pronounced, well-defined density corresponding to the peptidyl (P) site tRNA indicates that the vast majority of mitoribosomes are translationally active. Indeed, density explained by the nascent peptide can be traced inside the peptide exit tunnel in line with the local resolution and demonstrating translational activity of the mitoribosomes (Fig. 1F). To assess whether different translation states are present in our sample, we performed classification focusing on the ribosome cleft, where the aminoacyl (A), P and exit (E) sites for the tRNAs locate and accessory factors bind. We obtained four classes which can all be assigned to actively elongating states (Fig. 1G & S5). The majority of mitoribosome particles are present in the accommodated states with tRNAs occupying the A, P and E site (59.4%) (Figure S5). This ratio of mitoribosomes in the accommodated state is considerably higher compared to previous study of isolated mitoribosomes that used non-hydrolizable GTP analogue and knockdown of the mt-tRNA processing factor Pde12 (28.4 %)[18] (Fig. S5). Notably, the majority of ribosomes (43.8 %) in intact cells of the prokaryote *M. pneumoniae* were also found in the accommodated state[19]. The different abundance of the accommodated state

observed for the mitoribosomes in comparison to previous studies might therefore be a result of mitoribosome isolation or the use of translation inhibitors. In addition to the accommodated state, we observe classes for the rotated state (8.8 %), the post-translocation state (7.1 %) and one class with bound elongation factors (24.7 %) (Fig. 1G). For the latter class, subsequent classification focusing on the elongation factor yielded class averages with too low resolution to reliably discern between mtEF-G and mtEF-Tu bound states. A previous publication using a non-hydrolizable GTP analogue found mtEF-G to be eight times more abundant than mtEF-Tu[20], indicating that a considerable larger dataset would be required to separate the two states. For all classes, we observe various interactions between the tRNAs and densities corresponding to mL64, mL40 and mL48 (Fig. 1G, S5A). These proteins were previously shown to bind the A, P and E-site tRNAs and were suggested to assist in tRNA translocation by undergoing conformational changes[21]. In subclasses obtained for the accommodated state, we observe subtle differences for the densities for the E-site tRNA which correlates with the binding of those proteins to the tRNAs and supports the previously suggested role in coordinating translation (Fig. S5). Taken together, our rapid isolation protocol does not impede mitochondrial translation and allows for high-resolution structural investigations at near-native conditions.

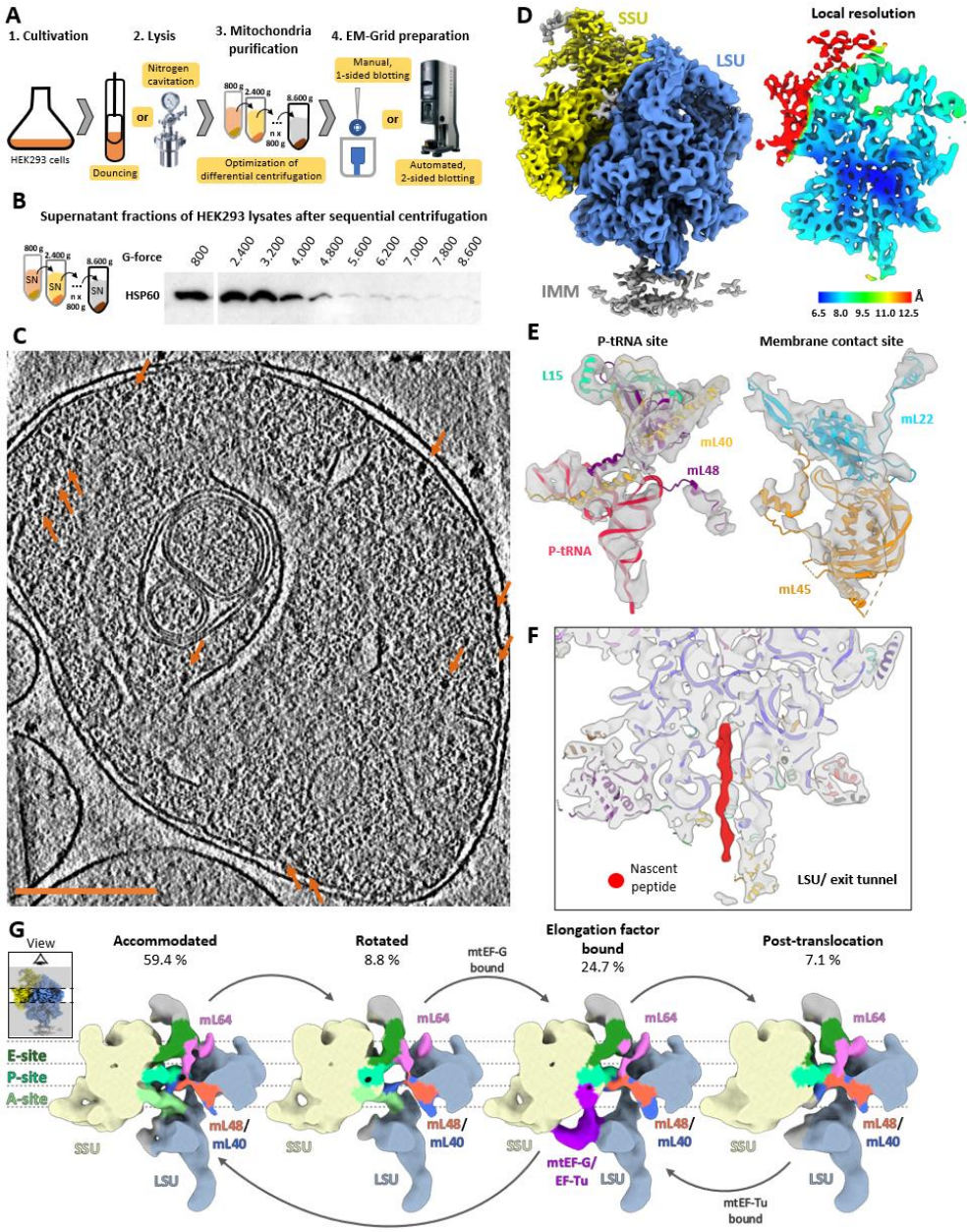

Figure **1: *In organello* structure of the actively translating human mitoribosome at sub-nanometer resolution.** A) Overview of mitochondria purification protocol, with the screened parameters highlighted in yellow**.** B) Western blot of supernatant fractions of cell lysates from after sequential centrifugation at increasing centrifugal force, using HSP60 as mitochondrial marker. C) Tomogram slice of mitochondria (thickness: 1 voxel/ 1.7nm) enriched from HEK cells by differential centrifugation at 3,000 g. Mitoribosomes are indicated by orange arrows. Scale bar 500 nm. D) *In organello* subtomogram average (STA) of translating mitoribosome at overall resolution of 8.5 Å (left) and local

resolution map (right), obtained after local refinement on the large subunit. E- F) Map of subtomogram average (grey) overlayed with atomic model (PDB 6ZM5) highlighting structural details around central P-site tRNA (left), peripheral membrane contact site (right) and the peptide exit tunnel (slice), with the nascent peptide highlighted in red (bottom). G) Translation states of the mitoribosome obtained after classification focusing on the mitoribosome cleft.

Mitoribosomes associate with two different membrane protein complexes

Oxa1 is a major factor responsible for co-translational membrane insertion[22]. The Oxa1 C-terminal domain (CTD) was shown to bind to the mitoribosome using cryoEM SPA[20,23], but aside from the CTD the structure of Oxa1's and its interaction with the mitoribospome remains elusive. To analyze the structure of the mitoribosome-associated insertase machinery in its native environment we applied 3D classification focusing on the membrane region to separate mitoribosome particles with a clearly resolved membrane from those without discernable membrane density near the exit tunnel (Fig. S3). Surprisingly, this 3D classification yielded two classes of different complexes associated with the mitoribosome, which were present in a ratio of approximately 1:1 (Fig. 2A). The complexes are both positioned under the peptide exit tunnel and next to the membrane anchor mL45. The shape and size of complex 2 is consistent with a predicted Alphafold[24] model of Oxa1L (AF-Q15070) containing five transmembrane helices and three luminal helices, including Oxa1L's CTD (Fig. S5 & Fig. 4). One of those three luminal helices is in excellent agreement with the previously assigned C-terminal domain of Oxa1 (Fig S5). Additionally, cross-linking mass-spectrometry confirmed the proximities of several adjacent residues Oxa1L model (see below). Therefore we conclude that complex 2 represents Oxa1.

In contrast to Oxa1L which shows a connective density towards the exit tunnel as well as density for its CTD, C1 does not show any luminal densities (Fig. 2B). We observe eight tubular densities for C1 which are adjacent to helix 2 of mL45 and placed directly under the peptide exit tunnel (Fig. 2B). With dimensions of 54 x 45 Å in the membrane plane, complex 1 (C1) is considerable larger compared to the cylindrical shape of Oxa1L with a diameter of 25 Å (Fig. 2B, 3A). We also measured a significantly larger volume and surface area for C1 compared to Oxa1L (89.5 nm^3 and 210 nm^2, vs. 50.5 nm^3 and 10.2 nm^2). Based on this we estimate a molecular mass of roughly 75 kDa for C1. Importantly, we also observe density for the nascent chain inside the peptide exit tunnel as well as density for the P-site tRNA, indicating that the complex 1 represents a translationally active complex (Fig. 2D). A small additional density can also be observed adjacent to the density of the nascent peptide in the exit tunnel and in contact with complex 1 (Fig. 2C,D). Despite the detection of inter-protein crosslinks between Oxa1L and mitoribosomal exit tunnel proteins, we could not detect other crosslinks that could give an indication on the identity of C1. It might therefore represent an alternative insertase, the folded substrate, or chaperons associated to Oxa1. The absence of the connective density observed for Oxa1L, and the presence of nascent density suggest that this complex represents a co-translationally active alternative insertase rather than a heteromeric complex containing Oxa1L or a pre-/ post-translational complex.

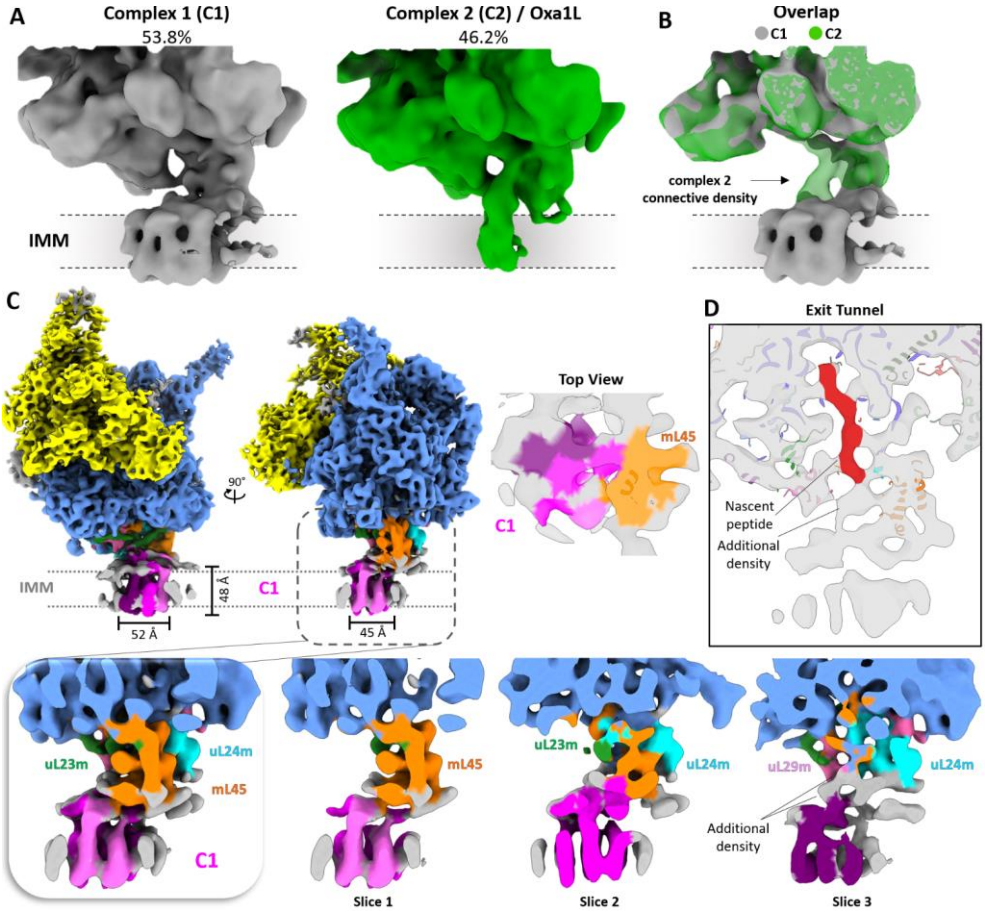

Figure 2: Membrane-bound human mitoribosomes associate with two different membrane protein complexes. A) Maps of the two classes obtained after focused classification. Inner mitochondrial membrane (IMM) plane is indicated in orange. **B)** Clipped overlap of both maps showing a connective density unique to complex 2. **C)** Composite structure of 55S and C1 subtomogram averages after refinement (shades of purple), with map of C1 and slices through it shown on the bottom and on the right (top view of membrane plane). Additional density adjacent to the tunnel exit is shown in slice 3. Surfaces of mL45, uL24m and uL23 were coloured within a 6 Å radius of the fitted atomic model. D) Slice through subtomgoram average of C1 showing the exit tunnel region with a nascent chain density (red) and the observed additional density.

Oxa1L guides the nascent peptide via its helical hairpin domain

To obtain structural information on the interaction of the complete Oxa1L with the mitoribosome we focused the refinement on the membrane region of the mitoribosome-Oxa1L complex, resulting in a map with a resolution of approximately 12 Å (Figure S4C). The membrane-associated density is explained well by an AlphaFold [24] model of Oxa1L consistent with the assignment of the density to this protein (Fig. 3A & Fig. S5). The previously modelled Oxa1 C-terminal domain (CTD) overlaps with our density and was used for the initial fitting of the predicted model followed by minor refinement (Fig. S6). The density overlapping with the CTD further extends towards the membrane region, covering previously unresolved stretch of the Oxa1 CTD (Fig 3A & S5). In the mitochondrial lumen, we can resolve a density that fits the two predicted helices h3 and h4 that form a helical hairpin (Fig 3A & S5). The reported local resolution of ~9- 10 Å for the luminal regions in our map supports the assignments of the CTD and the helical hairpin, while the limited resolution of ~13- 17 Å within the TM region does not allow for verification of Oxa1's transmembrane secondary structure (Fig S5C).

To validate our model, we performed cross-linking mass-spectrometry which resulted in three detected cross-links for the predicted helices h3 and h4 to the mitoribosomal proteins uL23 and mL45, as well as another crosslink between mL45 and a short α-helical stretch between the last TM helix of Oxa1 and its CTD, which is closely located to mL45 (Fig 3B). The Cα-Cα distance for the reported crosslinks range from 17- 30 Å in our model, in agreement with the crosslinker length of 14 Å and a length of ~6 Å for each lysine. These inter-protein cross-links confirm the proximity of helices h3 and h4 to mL45 and uL23m observed in our model.

Helices h3 and h4 position below the peptide exit tunnel, in close proximity to mL45, uL23m and the nascent peptide. Notably, h3 and h4 are positioned close to three stretches of mL45 and uL23m that could not be modelled previously: residues 95- 109 and 201- 205 for mL45 and residues 113- 133 for uL23m (Figure 3B). Three of the four cross-links for mL45 and uL23m to Oxa1 were detected within these unmodelled stretches. The subtomogram average also shows additional density at the binding interface of helices h3 and h4 with mL45 and uL23m (Fig. 3B), which could potentially accommodate the unmodelled stretches of uL23m and mL45. The map also shows another additional density between uL29m and the CTD of Oxa1L (Fig 3B). Based on these findings, we suggest an interaction between Oxa1L, mL45 and uL23m via Oxa1's helical hairpin domain, as well as a previously unobserved interaction between the Oxa1L CTD and uL29m.

In the fitted model, the Oxa1L helical hairpin projects towards the exit tunnel and contacts the nascent peptide (Fig. 3C). Our subtomogram average shows density for the nascent peptide reaching from the exit tunnel towards h3 and h4, as well additional density adjacent to the peptide and in between the helical hairpin and Oxa1L-CTD (Fig 3C), extending towards the core of the insertase. A surface representation of our Oxa1L model colored by hydrophobicity demonstrates that, while the top of the hairpin is hydrophilic, its underbelly

is strongly hydrophobic (Fig. 3D). Between the helices h3 and h4, a hydrophobic cleft extends from the tip into the core of the membrane-embedded part of Oxa1L, likely aiding insertion of the hydrophobic nascent chain. In addition, together with the CTD and the surrounding mitoribosomal exit tunnel proteins mL45, uL24m and uL23m, the helical hairpin forms a funnel that shields the gap between the exit tunnel and the membrane. Our structure therefore provides a model of how the exit tunnel is aligned with Oxa1L, and how the hydrophobic nascent peptide is guided into the membrane.

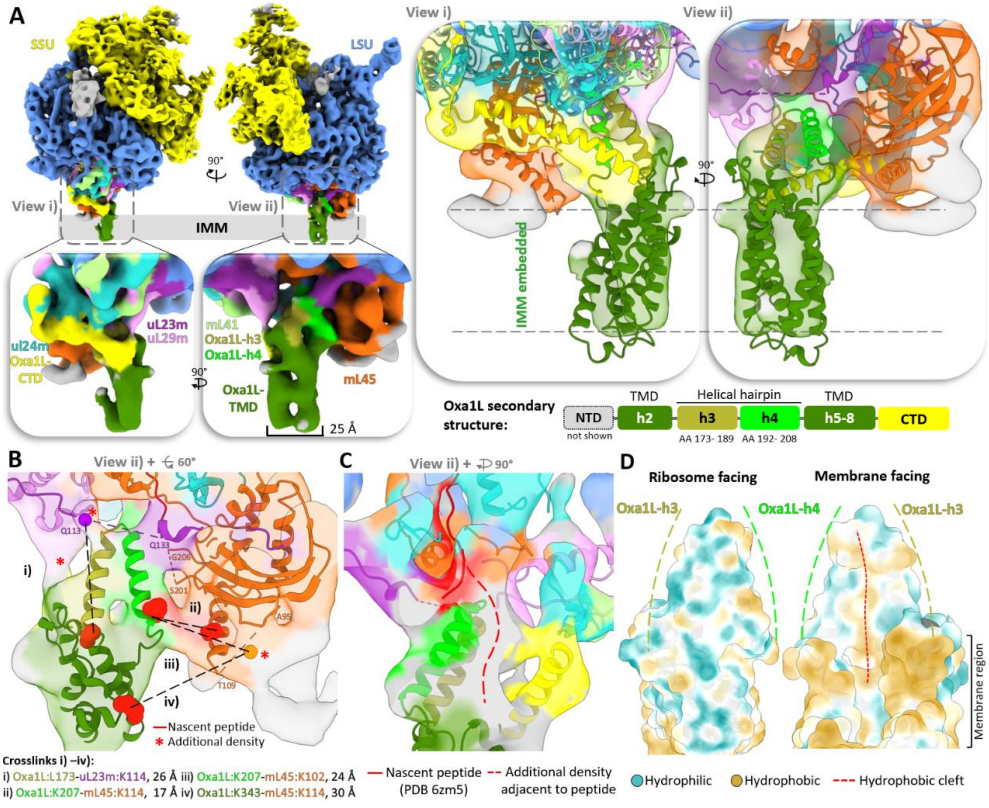

Figure 3: Structure of the human Oxa1L-mitoribosome complex. A) Composite structure of the 55S and Oxa1L subtomogram averages (top), with panels showing the Oxa1L-subtomogram average with (right) and without the fitted atomic model (bottom). Secondary structure of Oxa1L according to predicted model shown on bottom right. Surface are colored according to the atomic model within 6 Å radius. B) Oxa1L-mitoribosome crosslinks. Crosslinks are indicated by black dashed lines and red spheres (modelled region), or purple/ orange spheres for crosslinks within the unmodelled region of uL24m or mL45. Additional densities not explained by the atomic model are marked with red asterisks. C) Clipped overlap of the STA and model focusing on the interface between peptide exit and Oxa1L. Surface of STA was colored according to the atomic model within a radius of 3 Å, grey densities therefore represent regions with a distance greater than 3 Å from the model. Red dashed line indicates additional density and suggested insertion path of the nascent peptide. D) Surface of Oxa1 colored by hydrophobicity viewed from the top (left) and the bottom (right).

Discussion

After ~3 billion years of eukaryotic evolution, nearly all genes of the mitochondrial ancestor were shifted to the nucleus in most species[25]. Only a small subset of extremely hydrophobic proteins of the respiratory chain remained in the mitochondrial genome, raising questions about this peculiar partitioning and their precise mechanisms of insertion into the membrane. Here, applying cryoET we provide structural insights into co-translationally active mitoribosome-insertase complexes inside human mitochondria. Our data provides a model for the highly conserved helical hairpin domain of Oxa1L[3,26]. The reported interactions between the helical hairpin and the mitoribosome provide a mechanism for aligning Oxa1L's transmembrane domain with the mitoribosomal exit tunnel – a critical aspect considering the flexible nature of the CTD, the only previous structurally characterized interaction site between Oxa1L and the mitoribosome[23]. Additionally, together with the CTD and the tunnel exit proteins, the hairpin domain forms a funnel that shields the hydrophobic nascent peptide and guides it to the core of Oxa1L. Based on our model and the identified crosslinks, we hypothesize that the unstructured loops of mL45 and ul23m, which are in close proximity to the helical hairpin of Oxa1, act as a binding site and could previously not be resolved by SPA due to their flexibility presumably complex disruption resulting from isolation of the mitoribosome. The hydrophobic cleft on the belly of the helical hairpin potentially acts as a slide to guide nascent hydrophobic peptides into the membrane. Therefore, in addition to aligning Oxa1L with the mitoribosome together with the CTD, the helical hairpin likely provides a critical role in closing the ~25 Å gap between the exit tunnel and the membrane and targeting the nascent peptide into the latter.

The helical hairpin domain of Oxa1 or its related protein family members has previously not been resolved in its substrate-bound state[3]. In contrast to our model where the helical hairpin of Oxa1L points upwards to the mitoribosome, in a crystal structure of the bacterial YidC the helical hairpin was in a downward conformation[27]. A previous study of YidC showed a high degree of flexibility for this domain[26]. The helical hairpin domain of Oxa1L and its homologues might therefore undergo a conformational change from the downward to the upward conformation prior to co-translational insertion, possibly triggered by its binding to the ribosome.

The importance of the helical hairpin domain is supported by previous findings on the Oxa1 homologue YidC which showed reduced insertion efficiency upon mutations of domain[27–29]. A role of the helical hairpin domain in guiding the peptide via its hydrophobic cleft is also in agreement with the step-wise insertion along the greasy slide formed by the TMD's 3 and 5, which line up with the cleft of the helical hairpin domain [29,30]. Importantly, the first case of a mitochondrial disease caused by mutations in Oxa1L was recently characterized, identifying two lethal mutations in one patient within and directly adjacent to the helical hairpin domain of Oxa1L[4]. This finding supports a critical physiological role of the helical hairpin. Our results visualize the context of this domain and provide a hypothesis for the

observed deleterious consequences of mutations in this region. The structure suggests that the mutations may either i) disrupt the helix-helix interaction of the helical hairpin domain, ii) disrupt the interaction of the helical hairpin with mL45 and uL23m and thus impair he binding to the mitoribosome, iii) disrupt the proper alignment of Oxa1L to the mitoribosome or iv) perturb the membrane insertion of the nascent peptides.

Furthermore, we here present the first structural evidence for an alternative insertase complex. This alternative insertase complex also functions co-translationally as the P-site is occupied in the associated ribosomes. The complex is notably larger than the Oxa1L insertase and the Oxa1 helical hairpin is not visible. The fact that the observed second complex is translationally active and lacks density for the Oxa1L helical hairpin suggests that C1 contains an alternative insertase. An alternative insertase has recently been speculated to explain the tissue-specific phenotype of lethal Oxa1L mutations, which are compensated for in some tissues[4]. In addition, an alternative insertase would also explain why the different OxPhos subunits are affected to different extent by mutation or knockdown of Oxa1 [4,22,31]. While we obtained several crosslinks between the CTD and the helical hairpin domain of Oxa1 to mL45, uL23m and uL24m, we did not obtain any crosslinks between those proteins and other potential insertase candidates. Its identification might therefore be challenging due to the seeming lack of luminal densities. Our results provide a starting point for its further characterization which would be critical for our understanding of mitochondrial gene expression.

This study provides a proof of concept for structural characterization of miniscule binding partners of large mitochondrial complexes *in organello* by overcoming previous limitations of low throughput analyses, and demonstrating potential to resolve the binding interface between Oxa1L and the mitoribosome at subnanometer resolution. This is an important resolution range as it allows for the validation of protein secondary structures from promising new structure predictions tools[24]. Of the ~1,500 proteins constituting the mitochondrial proteome, hundreds of these are at least temporarily associated with large complexes that carry out fundamental functions such as oxidative phosphorylation, mitochondrial DNA replication, transcription, or energy conversion. Using the latest developments in structure prediction and subtomogram averaging, we show that cryoET proves a powerful tool for their structural characterization and will further contribute to our understanding of the powerhouse of the cell.

Material and Methods

Cell lysis and western blot analysis

HEK293 cells were grown in FreeStyle medium to a density of 1- 2 x 10^6 cells ml, harvested by centrifugation at 500g and washed twice in cold PBS. All subsequent steps were at 4 C or on ice. Cells were resuspended in lysis buffer (250mM Sucrose, 20mM Tris pH 7.4, 1mM EGTA, 1mM PMSF, 0.2 % BSA) to a density of 10^6 cells/ ml and lysed by either 60 up and downstrokes using a glass-teflon douncer or by 2 rounds of nitrogen cavitation (Parr Instruments) using an incubation period of 10min at 450 psi. Lysis efficiency was determined with a TC20 cell counter (Bio-Rad) using a 9 µm cutoff. Western blot analysis was performed using antibodies against Histon H3 (Abcam ab1191, diluted 1:3,000), cytochrome C (Tebubio E90050, diluted 1:3,000) or mt-CO2 (Abcam ab110271, diluted 1:2,000).

Isolation of Mitochondria

Cell lysates were spun down for 5 minutes at 800 g and 4 °C to remove unlysed cells. The supernatant was taken and applied to a second round of centrifugation at 800 g, followed by centrifugation of the resulting supernatant fraction at 3,000 g for 5 minutes. The supernatant was discarded and the pellet washed, followed by resuspension of the pellet in EM buffer **(**250mM Sucrose, 20mM Tris pH 7.4, 0.5% BSA).

Grid Preparation

Resuspended mitochondria were diluted to a concentration of 1.5- 3 mg/ml determined by absorption at 280nm using a Nanodrop. Lacey Carbon coated Cu 200 Mesh grids (Quantifoil) were glow-discharged for 25 seconds at 20 mA and 0.39 bar using a glow discharger (Pelco easiglow). 2ul of the sample were applied onto the glow-discharged grids and diluted on the grid with 4ul of gold buffer (100mM Sucrose, 20mM Tris pH 7.4, 0.2% BSA, 10 nm BSA-coated gold beads (UMC Utrecht, diluted 1:30)), resulting in a final concentration of 0.5- 1 mg/ ml. Grids were then blotted either manually from one side or using a ThermoFisher Vitrobot and plunged into a mixture of liquid ethane-propane.

CryoEM data acquisition

Tilt-series were acquired with SerialEM v3 on a ThermoFisher Titan Krios equipped with a Gatan energy filter (GIF) and K3 detector. A pixel-size of 2.17 Å/ pixel, a dose of ~15 e^-/ pixel/ sec, a grouped dose-symmetric tilt scheme with a tilt-increment of 2°, a group size of 5 tilts and a tilt-range of +50° to -50° degrees were used, resulting in 51 projections and a total cumulative dose of ~135 e^-/ $Å^2$. As

Subtomogram analysis

Motion- and CTF-correction were performed in Warp. Tilt-series were deconvolved using Dimitry Tegunov's tom_deconv and stacks aligned in imod using batchruntomo using the patch tracking for tilt series alignment. Deconvolved tomograms were reconstructed with Warp at a voxel size of 17.36 Å. An initial reference was created from 302 manually picked particles that were aligned using Relions Class3D without a reference, followed by refinement yielding 39 Å. The resulting average was subsequently used for template matching in pytom. Coordinates of the highest 1,000 or 1,200 cross-correlation peaks were

extracted for each tomogram and sub-tomograms were reconstructed with Warp at a voxel-size of 8.68 Å / pixel. The subtomograms were subjected to 3D classification in Relion v3.1.2 using a spherical mask with a diameter of 350 Å, an initial reference filtered to 60 Å and batch-sizes of 40,000 to 60,000 subtomograms per classification job. From the total of 441,600 subtomograms, 31,699 were classified as mitoribosomes. Subsequent classification using a mask encompassing the SSU and followed by a mask around the LSU resulted in 27,938 subtomograms. All mitoribosomes were refined to a resolution of 9 Å using relion and M prior to subsequent classification. For the classification of the translational states, a mask encompassing the ribosome cleft including A, P and E-site as well as translation elongation factors was created from PDB7A5G and PDB7A5I with UCSF ChimeraX. For classification of the insertase-complexes, subtomograms were recentered on the membrane and classification performed with an oval mask encompassing the membrane density associated to the mitoribosomal contact site. Classes of the translational states or the different mitoribosome-insertase complexes were individually refined in relion and M.

Model Building

For model building of the Oxa1L-mitoribosome complex, a model of Oxa1L from the AlphaFold database (AF-Q15070) was fitted into the map of the Oxa1L-mitoribosome subtomogram average. The initial model was then locally refined for the CTD and the helical hairpin in COOT[32] to maximize the overlap. In detail, the CTD was slightly bent and the helical hairpin domain was lifted to match the observed density. For complex 1, helical poly-alanine helices were generated in COOT and then rigid body fitted into the subtomogram average in ChimeraX[33].

Molecular weight estimation

Molecular weight of complex one was estimated by segmenting the corresponding density of C1 and the Oxa1L subtomogram average and measuring its volume using ChimeraX.

Visualization

Visualizations were prepared using UCSF ChimeraX 1.4[33].

Cross-linking and digestion

Mitochondria from HEK293T cells were isolated and washed twice with PBS, pH 7.4 (Gibco). TH buffer (300 mM Trehalose, 10 mM KCl, 10 mM HEPES, pH 7.4) supplemented with 0.1 mg/ml BSA was used for homogenization. Homogenization was performed 25 times at 1,000 rpm on ice. Cell debris was removed by centrifugation at 400 g for 10 min. The supernatant was collected and subjected to a second centrifugation step at 800 g for 10 min to further remove cell debris. The supernatant was collected and mitochondria in the supernatant were pelleted at 11,000 g for 10 min. Mitochondria were washed three times with TH buffer without BSA. All centrifugation steps were performed at 4°C. Cross-linking was carried out by incubating sample twice with 0.5 mM DSBSO (resuspended in DMSO to 50 mM) for 30 minutes each at room temperature. The cross-linking reaction was subsequently quenched by adding 30 mM TrisHCL buffer (pH 7.4 - 8) at room temperature for 20 minutes. Cross-linked samples were centrifuged, the supernatant removed and the

sample was washed once with cross-linking buffer. Afterwards, samples were denatured with lysis buffer (8 M urea in 50 mM ammonium bicarbonate), reduced with 5 mM dithiothreitol at 56°C for 30 min, and alkylated with 15 mM iodoacetamide for 30 min in the dark at room temperature. Cross-linked proteins were digested with Lys-C for 4 hours at 37°C and subsequently digested by trypsin overnight. The resulting peptide mixture was desalted using Sep-Pak C18 cartridges (Waters). Cross-linked peptides were enriched with DBCO beads and the elution was subjected to size exclusion chromatography and high pH reverse phase fractionation for further fractionation. Fractions were subjected to LC-MS analysis.

LC-MS analysis

LC-MS analysis was performed using an UltiMate 3000 RSLC nano LC system coupled on-line to an Orbitrap Fusion Lumos mass spectrometer (Thermo Fisher Scientific). Reversed-phase separation was performed using a 50 cm analytical column (in-house packed with Poroshell 120 EC-C18, 2.7µm, Agilent Technologies) with a 180 min gradient. Cross-link acquisition was performed using a LC-MS2 method. The following parameters were applied: MS resolution 120,000; MS2 resolution 60,000; charge state 4-8 enable for MS2.

LC-MS data analysis

Data analysis was performed using XlinkX standalone[34] with the following parameters: minimum peptide length=6; maximal peptide length=35; missed cleavages=3; fix modification: Cys carbamidomethyl=57.021 Da; variable modification: Met oxidation=15.995 Da; DSSO cross-linker=308.0388276 Da (short arm = 54.0106 Da, long arm = 236.01770 Da); precursor mass tolerance = 10 ppm; fragment mass tolerance = 20 ppm. Results were reported at 1% FDR at CSM level.

Acknowledgements

We would like to thank NeCEN and NEMI for their support in acquiring the dataset. We thank Stefan Pfeffer, Sebastian Filbeck (both University of Heidelberg) and Mihajlo Vanevic for their support and discussion on subtomogram analysis using M. This research was funded by the Dutch Research Council (NWO, Vici 724.016.001) and the Netherlands Electron Microscopy Infrastructure, project number 184.034.014 of the National Roadmap for Large-Scale Research Infrastructure of the Dutch Research Council (NWO).

Author contributions

R.E., F.F. and F.L. designed experiments. R.E. performed mitochondrial isolation, cryoEM grid preparation, cryoET data acquisition and data analysis. K.C.K., C.W. and F.L. performed cross-linking mass spectrometry (XL-MS) and XL-MS data analysis. R.E. prepared all figures and wrote the initial draft of the manuscript, which was edited by F.F. and F.L.

References

1. O'Brien, T. W. & Kalf, G. F. Ribosomes from Rat Liver Mitochondria. *J. Biol. Chem.* **242**, 2172–2179 (1967).

2. Szyrach, G., Ott, M., Bonnefoy, N., Neupert, W. & Herrmann, J. M. Ribosome binding to the Oxa1 complex facilitates co-translational protein insertion in mitochondria. *EMBO J.* **22**, 6448–6457 (2003).

3. McDowell, M. A., Heimes, M. & Sinning, I. Structural and molecular mechanisms for membrane protein biogenesis by the Oxa1 superfamily. *Nature Structural and Molecular Biology* vol. 28 234–239 (2021).

4. Thompson, K. *et al.* OXA1L mutations cause mitochondrial encephalopathy and a combined oxidative phosphorylation defect. *EMBO Mol Med* **10**, 9060 (2018).

5. Wang, F., Zhang, D., Zhang, D., Li, P. & Gao, Y. Mitochondrial Protein Translation: Emerging Roles and Clinical Significance in Disease. *Frontiers in Cell and Developmental Biology* vol. 9 1737 (2021).

6. Desai, N., Brown, A., Amunts, A. & Ramakrishnan, V. The structure of the yeast mitochondrial ribosome - Supplementary Material. *Science (80-.).* **355**, 528–531 (2017).

7. Greber, B. J. *et al.* The complete structure of the 55S mammalian mitochondrial ribosome. *Science (80-.).* **348**, 303–308 (2015).

8. Amunts, A., Brown, A., Toots, J., Scheres, S. H. W. & Ramakrishnan, V. The structure of the human mitochondrial ribosome. *Science* **348**, 95–8 (2015).

9. Mahamid, J. *et al.* Visualizing the molecular sociology at the HeLa cell nuclear periphery. *Science (80-.).* **351**, 969–972 (2016).

10. Englmeier, R., Pfeffer, S. & Förster, F. Structure of the Human Mitochondrial Ribosome Studied In Situ by Cryoelectron Tomography. *Structure* **25**, 1574-1581.e2 (2017).

11. Pfeffer, S., Woellhaf, M. W., Herrmann, J. M. & Förster, F. Organization of the mitochondrial translation machinery studied in situ by cryoelectron tomography. *Nat. Commun.* **6**, 6019 (2015).

12. Englmeier, R., Pfeffer, S. & Förster, F. Structure of the Human Mitochondrial Ribosome Studied in Situ by Cryoelectron Tomography. *Structure* **25**, 1574-1581.e2 (2017).

13. Gold, V. A., Chroscicki, P., Bragoszewski, P. & Chacinska, A. Visualization of cytosolic ribosomes on the surface of mitochondria by electron cryo-tomography. *EMBO Rep.* **18**, 1786–1800 (2017).

14. Frezza, C., Cipolat, S. & Scorrano, L. Organelle isolation: functional mitochondria from mouse liver, muscle and cultured fibroblasts. *Nat. Protoc.* **2**, 287–95 (2007).

15. Claude, A. The constitution of mitochondria and microsomes, and the distribution of nucleic acid in the cytoplasm of a leukemic cell. *J. Exp. Med.* **80**, 19–29 (1944).

16. Mastronarde, D. N. & Held, S. R. Automated tilt series alignment and tomographic reconstruction in IMOD. *J. Struct. Biol.* **197**, 102–113 (2017).

17. Tegunov, D. & Cramer, P. Real-time cryo-electron microscopy data preprocessing with Warp. *Nat. Methods* **16**, 1146–1152 (2019).

18. Desai, N. *et al. Elongational stalling activates mitoribosome-associated quality control*. http://science.sciencemag.org/.

19. Xue, L., Lenz, S., Zimmermann-kogadeeva, M., Tegunov, D. & Cramer, P. Visualizing translation dynamics at atomic detail inside a bacterial cell. 1–34 (2021).

20. Desai, N. *et al.* Elongational stalling activates mitoribosome-associated quality control. *Science (80-.).* **370**, 1105–1110 (2020).

21. Aibara, S., Singh, V., Modelska, A. & Amunts, A. Structural basis of mitochondrial translation. *Elife* **9**, 1–17 (2020).

22. Szyrach, G. *et al.* Ribosome binding to the Oxa1 complex facilitates co-translational protein insertion in mitochondria. *EMBO J.* **22**, 6448–57 (2003).

23. Itoh, Y. *et al.* Mechanism of membrane-tethered mitochondrial protein synthesis. *Science (80-.).* **371**, 846–849 (2021).

24. Jumper, J. *et al.* Highly accurate protein structure prediction with AlphaFold. *Nature* **596**, 583–589 (2021).

25. Gray, M. W., Burger, G. & Lang, B. F. Mitochondrial evolution. *Science* vol. 283 1476–1481 (1999).

26. Wickles, S. *et al.* A structural model of the active ribosome-bound membrane protein insertase YidC. *Elife* **3**, e03035 (2014).

27. Kumazaki, K. *et al.* Structural basis of Sec-independent membrane protein insertion by YidC. *Nature* **509**, 516–519 (2014).

28. Geng, Y. *et al.* Role of the Cytosolic Loop C2 and the C Terminus of YidC in Ribosome Binding and Insertion Activity. *J. Biol. Chem.* **290**, 17250–61 (2015).

29. Kedrov, A. *et al.* Structural Dynamics of the YidC:Ribosome Complex during Membrane Protein Biogenesis. *Cell Rep.* **17**, 2943–2954 (2016).

30. He, H., Kuhn, A. & Dalbey, R. E. Tracking the Stepwise Movement of a Membrane-inserting Protein In Vivo. *J. Mol. Biol.* **432**, 484–496 (2020).

31. Stiburek, L. *et al.* Knockdown of human Oxa1l impairs the biogenesis of F1Fo-ATP synthase and NADH:ubiquinone oxidoreductase. *J. Mol. Biol.* **374**, 506–16 (2007).

32. Emsley, P., Lohkamp, B., Scott, W. G. & Cowtan, K. Biological Crystallography

Features and development of Coot. (2010) doi:10.1107/S0907444910007493.

33. Pettersen, E. F. *et al.* UCSF ChimeraX: Structure visualization for researchers, educators, and developers. *Protein Sci.* **30**, 70–82 (2021).

34. Liu, F., Rijkers, D. T. S., Post, H. & Heck, A. J. R. Proteome-wide profiling of protein assemblies by cross-linking mass spectrometry. *Nat. Methods* **12**, 1179–1184 (2015).

Supplemental Material

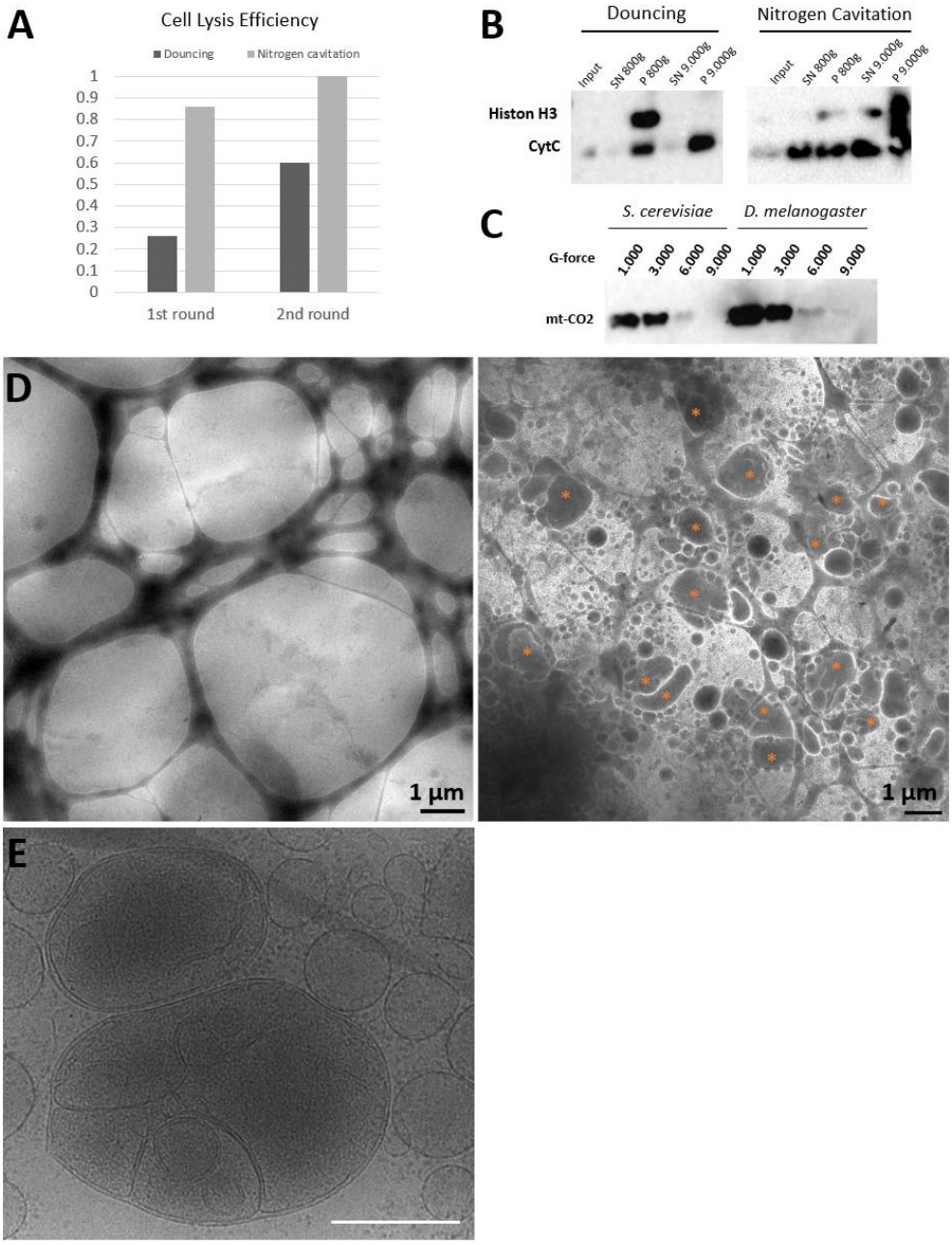

Figure S1: Optimization of Cell lysis and cryoEM grid preparation. A) Relative amount of lysed cells in resuspended 800g pellets after one or two lysis rounds by either douncing or nitrogen cavitation. B) Western blot analysis of supernatant (SN) and pellet (P) fractions obtained from cell lysates after douncing (left) or nitrogen cavitation (right). Histone H3 and

cytochrome c release in the supernatant fractions indicate damage of the nucleus and outer mitochondrial membrane. C) Western blot analysis of supernatant (SN) from yeast and S2 cell lysates after differential centrifugation. Cell lysates were obtained after douncing and clearing using the same protocol as in B). Mitochondrial cytochrome c oxidase subunit 2 (mt-CO2) was used as mitochondrial marker. D) Micrographs of cryoEM grids of an identical sample prepared by either two-sided, automated blotting with a Vitrobot (left) or a one-sided manual plunger (right). Mitochondria identified by either clear internal features (cristae) and/ or a double membrane are highlighted with and orange asterisk. E) high-resolution micrograph of sample used for data acquisition, showing two mitochondria with clear internal feature and intact double membrane. Scale bar 1 µm.

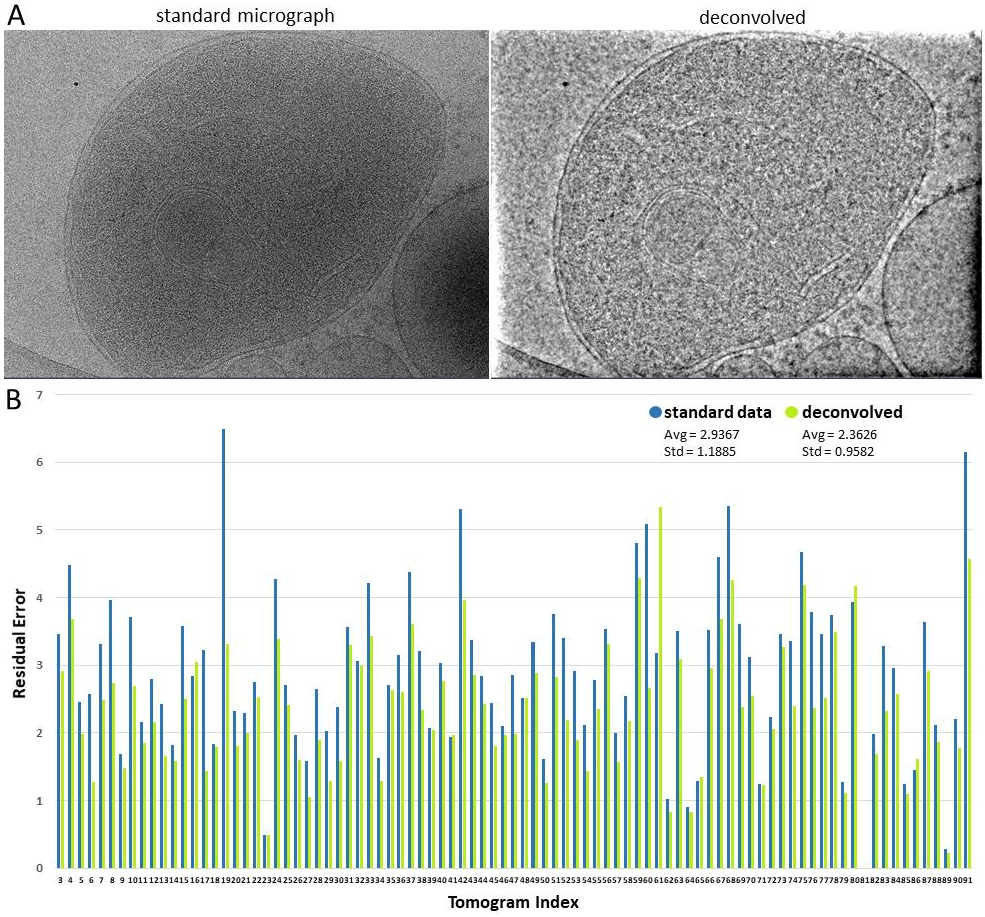

Figure S2: Deconvolution and tilt-series alignment. A) Standard micrograph (left) compared to micrograph after applying deconvolution. Scale bars 250nm. B) Residual error of a subset of 88 tilt-series after alignment using feature-based patch-tracking for standard data (blue) and deconvolved micrographs (green). Averages residual error (Avg) and standard deviation (std) are indicated.

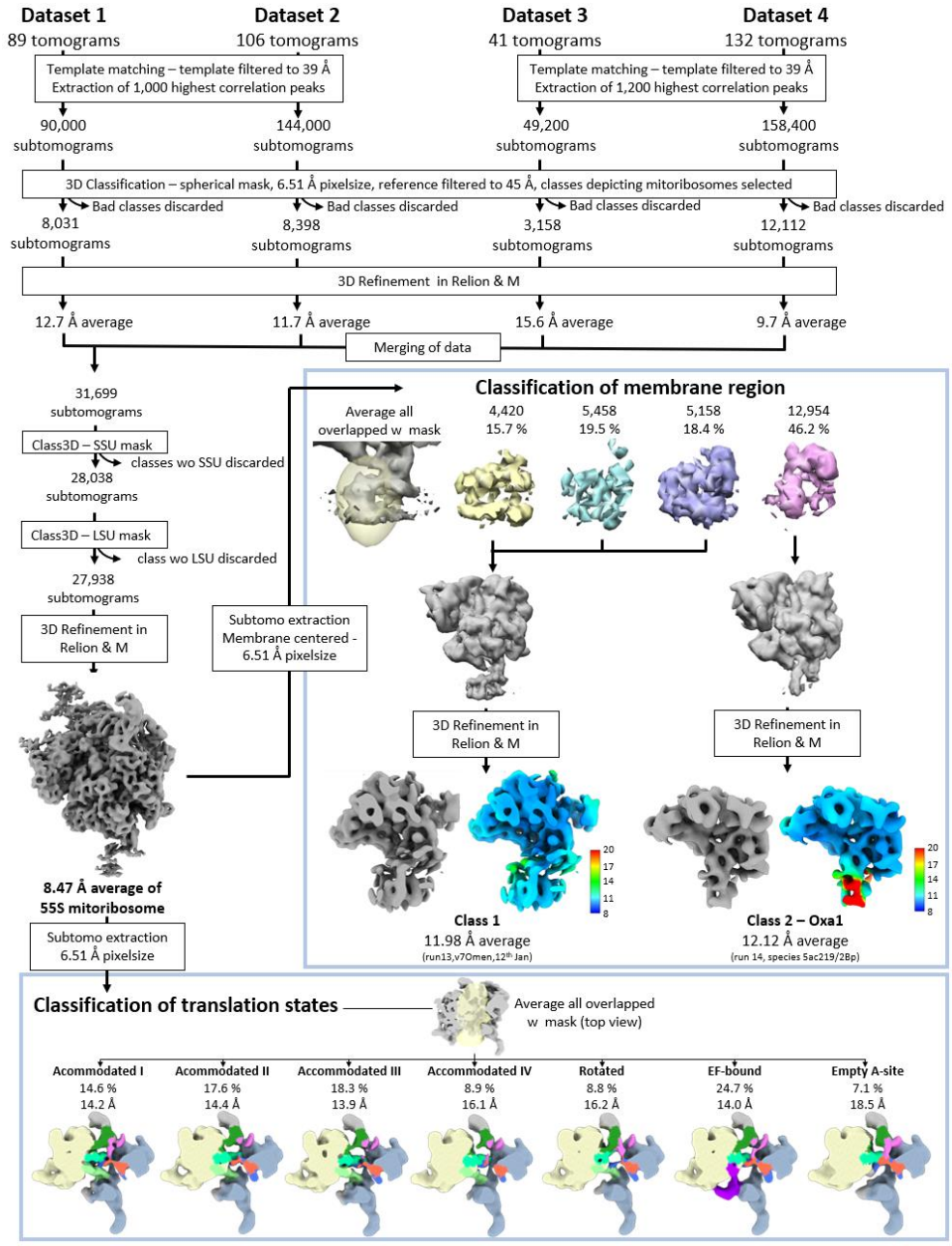

Figure S3: cryoET data processing. Four datasets containing in total 368 tilt series were first individually processed to obtain converged subtomogram averages of the 55S mitoribosome at resolutions of 9.7- 15.6 Å. Datasets were then combined for subsequent classification resulting in a 8.47 Å subtomogram average of the 55S mitoribosome ($FSC_{0.143}$ criterion) from 27,938 subtomograms. This set of subtomograms was then used for classifications focusing on the membrane or the ribosomes cleft for the determination of

translational states. Membrane classification yielded two different classes which were refined yielding subtmogram averages with global resolutions of 11.98 and 12.0 Å ($FSC_{0.143}$ criterion).

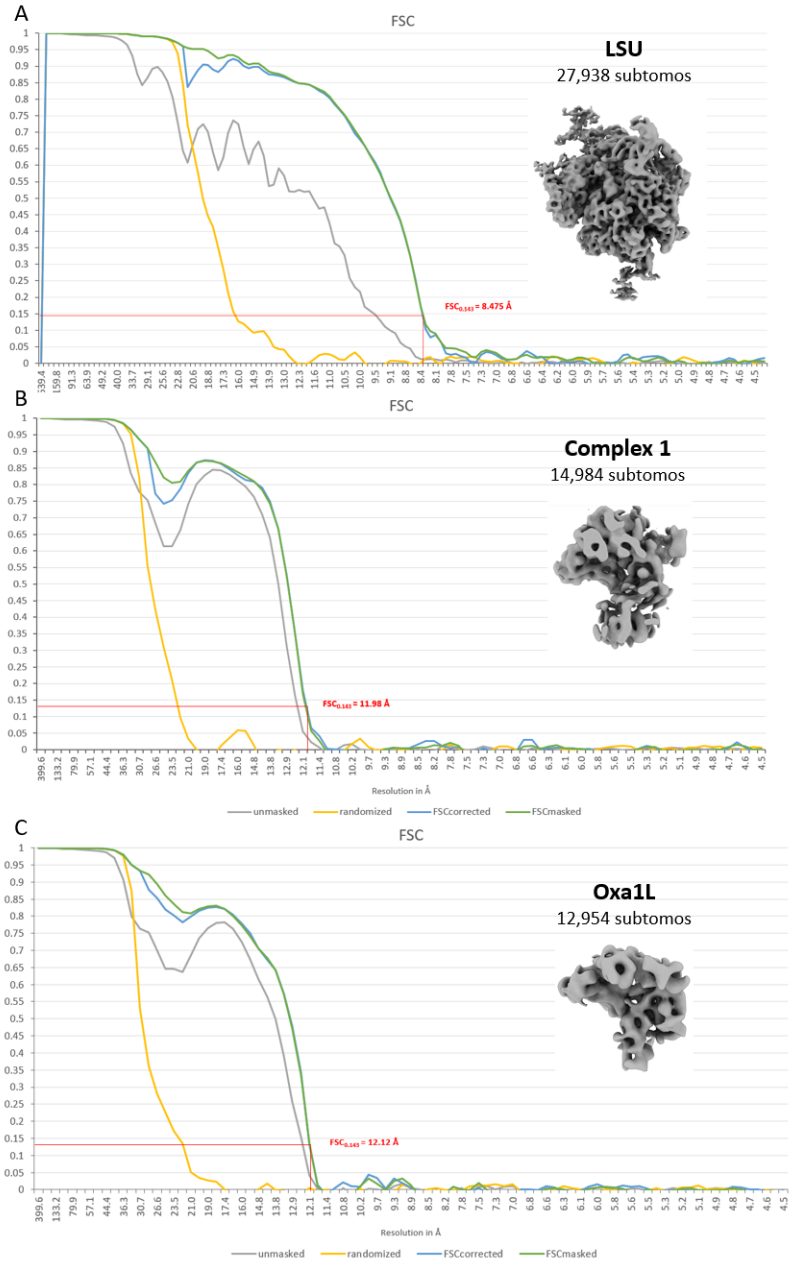

Figure S4: Fourier-shell correlations of the subtomogram averages presented in this study. A) Fourier-shell correlation (FSC) for the 55S mitoribosome map from Figure 1 b. The resolution was determined to 8.47 Å according to the $FSC_{0.143}$ criterion. B) FSC for complex 1 bound to the mitoribosome. The global resolution was determined to 11.98 Å according to the $FSC_{0.143}$ criterion. C) FSC of the mitoribosome-Oxa1L complex. The global resolution was determined to 12.1 Å according to the $FSC_{0.143}$ criterion.

A

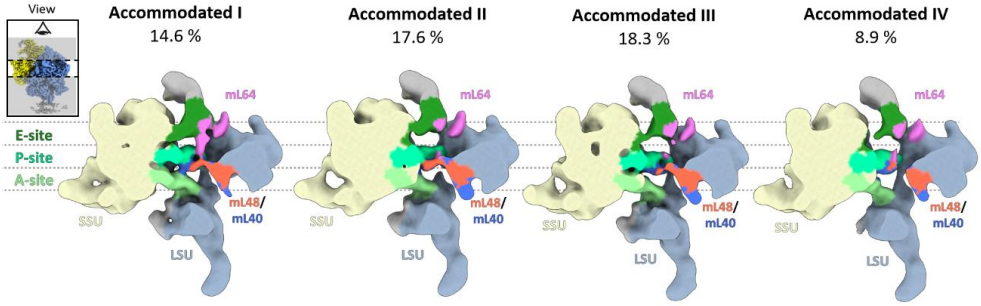

B

	Aibara et al., 2020	Desai et al., 2020	This study
Sample	Isolated mitoribosomes	Isolated mitoribosomes	Isolated mitochondria
Translation inhibitor	Quinupristin & Dalfopristin	PDE12 knockout & GMPPCP	none
Translation states			
Accommodated (A/A, P/P, E/E)	10.8 % (9 %)	28.4 % (22 %)	59.4%
A/A, P/P	12 % (10 %)	-	-
P/P, E/E	20.5 % (17 %)	4.5 % (3.5 %)	7.1%
P-only	6.0 % (5 %)	-	-
E-only	30.1 % (25 %)	-	-
Rotated	3.6 % (3%)	20.6 % (16 %)	8.8 %
P/E hybrid	16.8 % (14 %(	-	-
mtEF-G	-	41.3 % (32 %)	24.7 %
mtEF-TU	-	5.2 % (4 %)	

Figure S5: Classes of and comparison to previous studies. A) Sub-classes of accommodated state showing subtle difference for the densities observed for E-tRNA, mL64, mL48 and mL40. B) Summary of translational states that were quantified in previous and this study. For previous studies, values were normalized relative to all described translational states as reported numbers did not add up to 100% (Aibara et al.: 83%, Desai et al.: 77.5%). Values in bracket correspond to originally reported numbers in the respective studies.

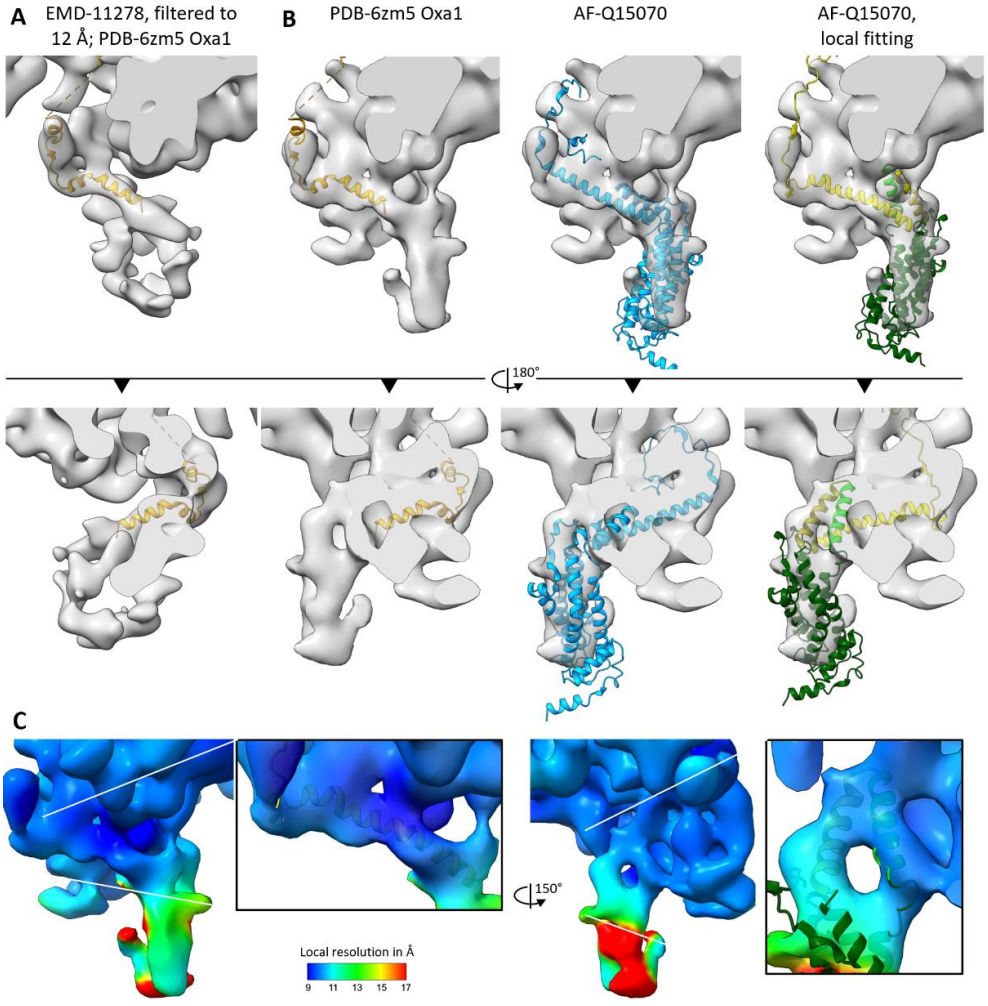

Fig S5: Overlap of Mitoribosome-Oxa1 map with atomic models Oxa1. A) Previous map of the isolated mitoribosome (EMD11278) filtered to 12 Å overlapped with atomic model of Oxa1's C-terminal domain (PDB-6zm5). B) Denoised map of subtomogram average (STA) overlapped with previously determined stretch of Oxa1's C-terminal domain (PDB-6zm5), an AlphaFold-predicted model of Oxa1L (AF-Q15070) and the AlphaFold model after local fitting in COOT (colored according to Figure 3). C) STA map colored according to local resolution (left), boxes contain clipped maps overlapped with atomic model to highlight the regions of the matrix-exposed Oxa1L helices.

Chapter 5

Sample Preparation of Isolated Mitochondria for Cryoelectron Tomography and in situ Studies of Translation

Lena Thärichen, Robert Englmeier and Friedrich Förster

Structural Biochemistry, Bijvoet Center for Biomolecular Research, Utrecht University, 3584 CG Utrecht, The Netherlands

2

The chapter has been submitted and is currently under review.

Abstract
Cryoelectron tomography is a method to image biological samples three-dimensionally at molecular resolution. This modality provides insights into intracellular processes in their physiological settings. Obtaining a high-quality sample for cryoelectron tomography on mitochondria, however, can be challenging. In this chapter we describe the crucial steps from sample preparation to data acquisition enabling studies of mitochondrial translation in situ by cryoelectron tomography. We provide detailed protocols for yeast and human mitochondria preparations yielding a high concentration of intact mitochondrial vesicles on cryo-EM grids. In addition, we describe a workflow for particle identification and spatial mapping in context of the organelle.

Key Words Mitochondria, Cryoelectron tomography, Translation, Ribosome

1 Introduction

Cryoelectron tomography (cryo-ET) has extended the scope of structural biology studies from isolated molecules to molecules in context of their physiological organellar environment and even native cellular settings allowing to study their molecular sociology [1]. Cryo-ET provides 3D density volumes of an object of interest, typically referred to as tomograms. They are calculated from a set of 2D projection images of the sequentially rotated object, which is called a tilt series. These projections are acquired using a transmission electron microscope (TEM), which provides parallel projections of the sample along the electron beam to very good approximation [2].

Prior to imaging the sample is vitrified. The transition into a vitreous phase of matter is achieved by rapid cooling via plunge freezing into a suitable cryogen like liquid ethane [3]. Importantly, cryo-ET does not involve dehydration of the sample and does not require any staining or fixation agents, enabling studies under near native aqueous conditions and avoiding preparation artifacts of EM methods relying on resin embedding. Cryo-ET relies on the contrast generated intrinsic density differences of the sample, which is relatively weak and gives rise to a low signal-to-noise ratio (SNR) of the data [2]. A further limitation of cryo-ET is that sample must not exceed few hundred nm in thickness to remain transparent to the electron beam.

The potential of cryo-ET to retain the organelle environment during structural studies makes it attractive for mitochondrial research. Due to the requirement of relatively thin samples cryo-ET has typically been applied to isolated mitochondria. Early studies revealed the ultra-structure of such isolated mitochondria with relatively modest TEM equipment

[4]. High-voltage TEMs (typically operated at 200-300 kV) and advanced direct electron detectors allow insights into the organization of specific macromolecules. Due to the low SNR of tomograms high molecular weight complexes are easier to distinguish in the data due to their larger volume. Thus, cryo-ET has primarily provided information on the intricate spatial organization of large mitochondrial complexes such as the ATP sythetase [5, 6].

Cryo-ET also enables a comprehensive understanding of mitochondrial translation with the large molecular weight mitochondrial ribosome (mitoribosome) as its centrepiece. Two routes are typically pursued to analyse specific particles depicted in tomograms. On the one hand, features of interest such as mitoribosomes can be automatically identified and traced, resulting in a segmentation, as exemplified by Pfeffer et al. and Englmeier et al. for mitochondrial polysomes *in situ* [7, 8]. On the other hand, particle volumes or subtomograms depicting the same type of macromolecule can be aligned in 3D and added up during subtomogram averaging [9]. This step significantly increases the electron density SNR, which manifests in higher resolution reconstructions of the macromolecule of interest. Thus, subtomogram averaging of yeast and human mitoribosomes *in organello*, revealed details of membrane tethering, protein insertion and translational states [7, 8, 10].

Efficient collection of high-quality data relies on a high-quality mitochondria sample. Mitochondria have been isolated from a variety of sources for decades and used in functional studies, examining respiration [11], mitochondrial translation [12] or mitochondrial import [13–15], respectively. However, these protocols include harsh centrifugation steps. For yeast mitochondria preparations additionally involve extended biochemical treatment for cell wall digestion [16]. Cryo-EM grid preparation from these samples results in a relatively low number of structurally intact mitochondria per grid area, which inevitably leads to extended search time during data collection setup at the cost of expensive and often closely calculated electron microscope time. In this chapter we describe gentle and fast protocols for mitochondria preparations from human [10] and yeast cells for the purpose of cryo-ET. Furthermore, we complement the sample preparation protocols with a data processing workflow for membrane segmentation and particle mapping in tomograms.

2 Materials

2.1 Isolation of mitochondria from HEK 293 suspension cells

This protocol is focused on obtaining a highly enriched, intact mitochondria preparation for the purpose of cryo-ET and will contain other subcellular vesicle contaminations, such as endoplasmic reticulum (ER) vesicles. The underlying procedure is differential centrifugation for separation of different subcellular vesicles after cell lysis (Fig. 1A) [11]. The

centrifugation speeds have been optimized for HEK 239 suspension cells (Fig. 1B) and might need to be optimized for other cell lines (see Note 3). Since Cytochrome C resides in the intermembrane space, its enrichment in the pellet fraction indicates outer membrane intactness (Fig. 1 B). For buffer preparations use sterile filtered (ø 0.2 µm) Hepes and Sucrose stock solutions.

1. HEK 239 suspension-adapted cells (e. g. FreeStyle™ 293-F Cells from Thermo Fisher) at 1-1.5 mio cells/ml grown in FreeStyle™ 293 Expression Medium (Thermo Fisher) for > 2 days
2. Phosphate-Buffered saline (PBS) w/o magnesium and calcium (Corning®)
3. Glass dounce homogenizer with Teflon piston
4. Homogenization buffer HEK: 20 mM Hepes pH 7.4, 250 mM Sucrose, 1 mM EGTA, 1 mM PMSF, 0.2 % fatty acid free BSA in ddH_2O.
5. 2 ml Eppendorf tubes
6. Mitochondria buffer HEK: 20 mM Hepes pH 7.4, 250 mM Sucrose.
7. UV/Vis spectrophotometer for OD_{280} measurement (Nanodrop™)

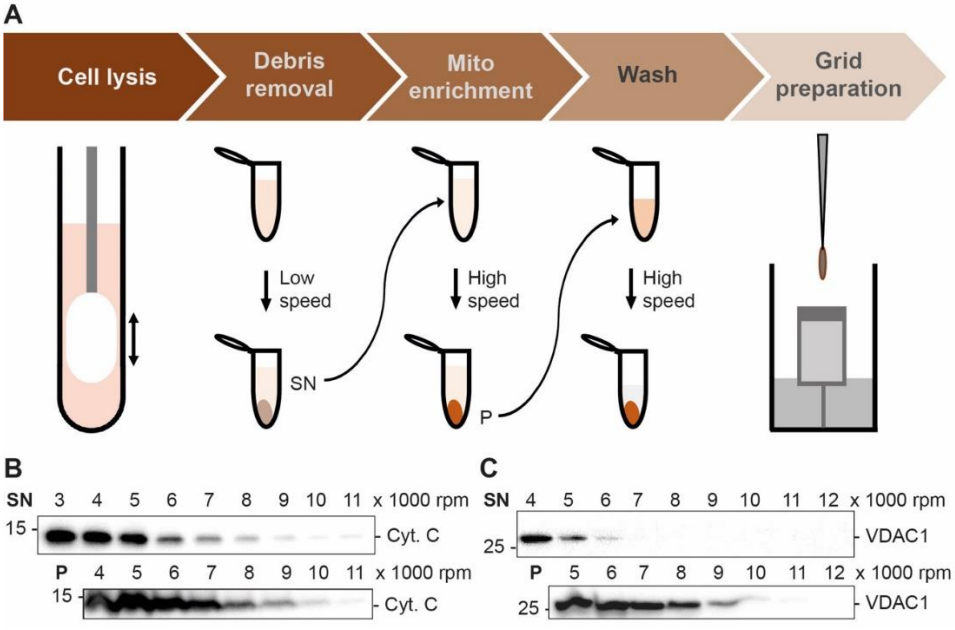

Fig. 1: Enrichment of intact mitochondrial vesicles by differential centrifugation: (A) Schematic of the sample preparation protocol ranging from cell lysis to grid preparation. (B) Western blot detection of the human mitochondrial marker Cytochrome C in supernatant (SN) and pellet (P) fractions at different centrifugation speeds after cell lysis. (C) Western blot detection of the yeast mitochondrial

marker VDAC1 in supernatant (SN) and pellet (P) fractions at different centrifugation speeds after cell lysis.

2.2 Isolation of mitochondria from yeast cells

Like the protocol for mitochondria preparations from HEK cells (Fig. 1A), this protocol has been optimized for a high abundance of intact mitochondrial vesicles for cryo-ET and will still contain other subcellular vesicles. The protocol was based on Pfeffer et al. [7] and buffers, cell wall digestion and centrifugation speeds have been optimized for *S. cerevisiae* spheroplasts (BY4742 [17]) (Fig. 1C). This yeast strain carries modifications to maximize mitochondrial biomass production and reduce loss of mitochondrial DNA that is observed in the wild type S288c background strain. For buffer preparations use sterile filtered (ø 0.2 µm) buffer, salt and Sorbitol stock solutions.

1. Yeast strain grown on a YPD agar plate for 3 days at 30 °C.
2. Semi-synthetic (SS) medium: Dissolve 0.5 g Glucose, 1.0 g H_2HPO_4, 1.05 g $MgSO_4 \bullet 7H_2O$, 1.0 g NH_4Cl, 3.0 g yeast extract, 0.3 ml 1 % w/v $FeCl_3$ in 800 ml ddH_2O. Add 22 ml 90 % lactic acid and adjust the pH to 5.5 using KOH pellets. Then add 0.5 g $CaCl_2$, fill up to 1 l with ddH_2O and sterilize by autoclaving.
3. Water bath at 30 °C
4. Wash buffer: 50 mM Hepes pH 7.4, 50 mM KOAc, 20 mM $Mg(OAc)_2$, 1 mM EGTA
5. DTT buffer: 50 mM Hepes pH 8.0, 50 mM KOAc, 20 mM $Mg(OAc)_2$, 2 mM DTT
6. Zymo buffer: 20 mM KH_2PO_4 pH 7.4, 1.2 M Sorbitol, 50 mM KOAc, 20 mM $Mg(OAc)_2$
7. Zymolyase 20T (AMSBIO)
8. Glass dounce homogenizer with teflon piston
9. Homogenization buffer yeast: 20 mM Hepes pH 7.4, 600 mM Sorbitol, 50 mM KOAc, 20 mM $Mg(OAc)_2$, 1 mM PMSF, 1 mM EGTA
10. 2 ml Eppendorf tubes
11. Mitochondria buffer yeast: 20 mM Hepes pH 7.4, 600 mM Sorbitol, 50 mM KOAc, 20 mM $Mg(OAc)_2$
12. UV/Vis spectrophotometer for OD_{280} measurement (Nanodrop™)

2.3 Grid preparation

To reduce sample viscosity and beam sensitivity while ensuring membrane intactness, mitochondria samples are diluted with the respective plunging buffer on the mounted grid immediately prior to blotting. Low concentrations of Sucrose or Sorbitol in the plunging buffer will ensure vesicle intactness. Manual one-sided blotting is used to reduce mechanical force on mitochondrial vesicles. BSA coated

gold fiducials are added for tilt series alignment during the tomogram reconstruction process [18].

1. Plunging buffer HEK: 120 mM Sucrose, 20 mM Hepes pH 7.4, 10 nm BSA-coated gold beads (e.g., UMC Utrecht diluted 1:30-1:40)
2. Plunging buffer yeast: 20 mM Hepes pH 7.4, 200 mM Sorbitol, 50 mM KOAc, 20 mM $Mg(OAc)_2$, 10 nm BSA-coated gold beads (e.g., UMC Utrecht diluted 1:30-1:40)
3. Protective googles and gloves
4. Manual plunger for single-sided blotting
5. Ice-free liquid Nitrogen
6. Pressurized ethane gas
7. Grid storage boxes for grids
8. Glow discharger
9. Quantifoil® Cu 200 Mesh Holey Carbon R2/1 or Cu 200 Mesh Lacey Carbon grids
10. Blotting filter paper Whatman® 595

2.4 Image analysis and visualization software

The workflow described here requires already reconstructed tomograms. The software packages required to perform the described segmentation protocol are the following:

- Chimera X 1.2.5 [19] for template generation, visualization, and segmentation clean-up.

- Relion image handler [20] to prepare a template for template matching.

- PyTOM v0.993 [21] for tomogram deconvolution (deconv.py), template matching, and motl file generation (pytom_xml_to_motl.py) (https://github.com/FridoF/PyTom).

- EMAN 2.31 [22] for convolutional neural network (CNN) segmentation [23].

- TOM toolbox [24]

- MATLAB vR2018a (The MathWorks Inc.): plot_particles.m and tom_classmask.m (https://bitbucket.org/FridoF/av3/src/master/utils/)

3 Methods

3.1 Mitochondria isolation human

To isolate mitochondria from HEK cells, these need to be grown to logarithmic growth phase (see Note 1 & 2). Lysis is performed mechanically while ensuring organelle intactness using a dounce-homogenizer. Gentle differential centrifugation ensures vesicle intactness during

the enrichment step (Figure 1). All buffers should be prepared and cooled prior to the lysis step and the centrifuge and other equipment should be cooled as well to ensure fast execution of the protocol.

1. Grow HEK293ES suspension cells in FreeStyle™ medium to a density of approximately 1.5 x 10^6 cells / ml. 50 mio cells are sufficient for a small-scale purification and preparation of more than 10 grids.
2. Harvest the cells by centrifugation at 400 x g for 5 min.
3. Discard the supernatant, resuspend the pellet in ice-cold PBS and repeat step 2.
4. Discard the supernatant, resuspend the pellet in ice-cold homogenization buffer and transfer the suspension to the pre-cooled dounce homogenizer.
5. Lyse the cells by douncing three times with 30 strokes. Shortly cool the lysate on ice in between sets.
6. Transfer the lysate to 2 ml Eppendorf reaction tubes and centrifuge at 3000 rpm (Heraeus Biofuge 13, corresponding to 800 x g) for 5 min at 4 °C for removal of unbroken cells, nuclei and other cellular debris.
7. Transfer the supernatant into new 2 ml Eppendorf and repeat the centrifugation as in step 6.
8. Transfer the supernatant into new 2 ml Eppendorf tubes and centrifuge at 6000 rpm (Heraeus Biofuge 13, corresponding to 3000 x g) for 5 min at 4 °C to pellet the mitochondria fraction.
9. Remove the supernatant and carefully resuspend each pellet in 1 ml ice-cold mitochondria buffer. Repeat the centrifugation as in step 8 to wash.
10. Resuspend the mitochondria pellet carefully in ice-cold mitochondria buffer to an OD_{280} of 1-1.4 for grid preparation.

3.2 Mitochondria isolation yeast

For isolation of yeast mitochondria, the same requirements apply as described under 3.1. Additionally, DTT buffer and Zymo buffer need to be pre-warmed. DTT treatment and zymolyase digestion is kept as short as possible.

1. Streak out the yeast strain onto a YPD agar plate and grow it for 3 days at 30 °C.
2. Use these cells to inoculate 20 ml of SS medium in the morning with an inoculation loop and grow the culture at 30 °C and 160 rpm for 8-10 hours.
3. In the evening, inoculate 1 l of SS medium with the pre-culture, aiming at an OD_{600} of 0.7-1.0 the next day.
4. Harvest the cells at room temperature (RT) and 4000 x g for 10 min.

5. Discard the supernatant and resuspend the cell pellet in 50 ml RT wash buffer. Transfer into a pre-weighed 50 ml Eppendorf tube and centrifuge at RT, 4000 x g for 5 min.
6. Discard the supernatant and weigh the cell pellet.
7. Per 1 g of cell pellet, add 6 ml pre-warmed DTT buffer (at 30 °C), resuspend well and incubate at 30 °C for 5 min. Then harvest the cells as in step 5.
8. Per 1 g of cell pellet add 17 mg Zymolyase20T dissolved in pre-warmed (30 °C) Zymo buffer and resuspend well. Incubate at 30 °C for 40 min and mix the suspension by inverting the tube every 15 min. Then harvest the cells as in step 5.
9. Discard the supernatant, resuspend the cell pellet in 25 ml Zymo buffer without Zymolyase20T and repeat the centrifugation as in step 5.
10. Resuspend the pellet in 2.3 ml ice-cold homogenization buffer per 1 g cell mass, transfer to the pre-cooled dounce homogenizer and lyse the cells three times with 20 strokes. Shortly cool the lysate on ice between sets.
11. Transfer the lysate into 2 ml Eppendorf tubes and centrifuge for 5 min at 4 °C and 4000 rpm (Heraeus Biofuge 13, corresponding to 1200 x g). Repeat this step two more times for the respective supernatant sample.
12. Pellet the mitochondria fraction for 5 min at 4°C and 8000 rpm (Heraeus Biofuge 13, corresponding to 5300 x g) and resuspend the pellet in mitochondria buffer to an OD_{280} of 2.5.

3.3 Grid preparation

The described procedure yields a good distribution (Fig. 2 A & B) of largely intact mitochondria (Fig. 2 C & D) on grids suitable for efficient cryoelectron tomography data acquisition.

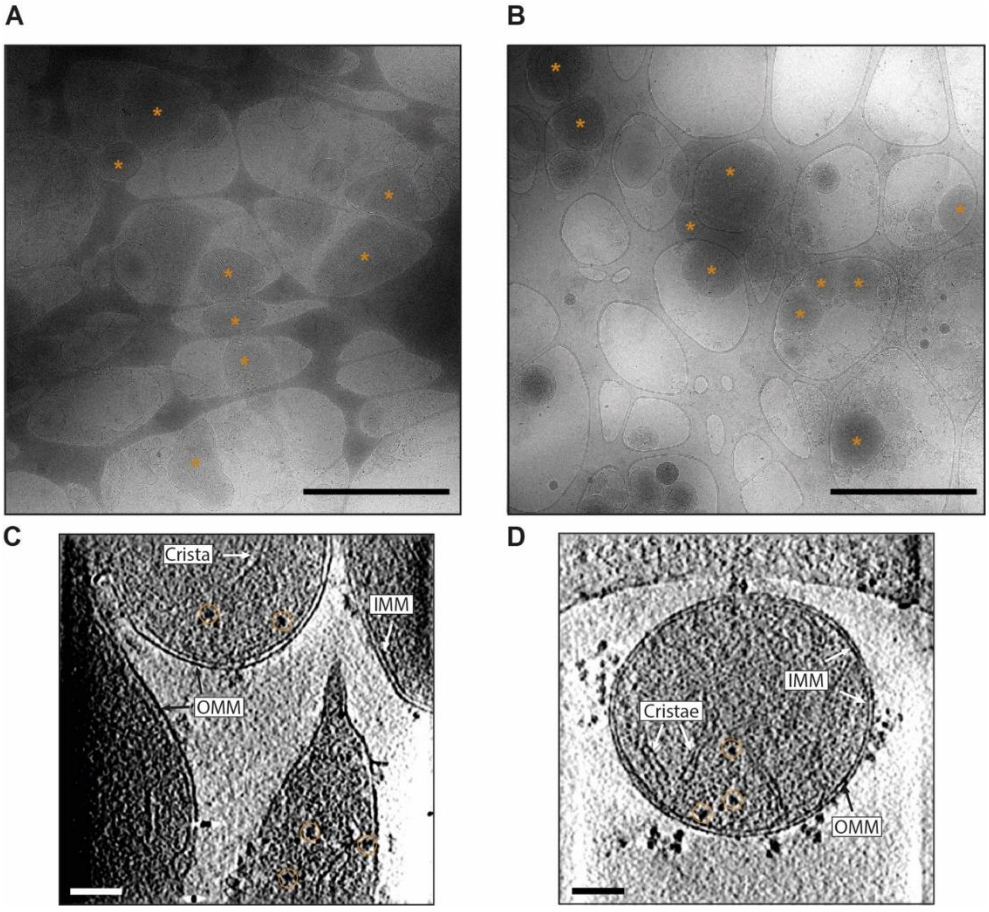

Fig. 2: Cryo-ET sample quality of isolated HEK and yeast cell mitochondria: Electron micrographs of mitochondria samples acquired on a 200 kV Talos Arctica electron microscope from (A) HEK cell or (B) yeast mitochondria preparations. Intact mitochondrial vesicles are indicated by asterisks and scale bars correspond to 2 µm. (C) Example tomogram of HEK cell mitochondria. Intact inner (IMM) and outer (OMM) mitochondrial membranes, Cristae and mitochondrial ribosomes are indicated by arrows or circles, respectively. (D) Example tomogram of a yeast mitochondrion with features indicated as in (C). Scale bars correspond to 100 nm.

1. Prepare the grid plunger with liquid nitrogen and ethane using goggles and gloves for protection.
2. Glow discharge the grids for 30 s at 20 mA and 0.39 mBar for Holey carbon grids and 25 s at 15 mA and 0.39 mBar for Lacey carbon grids (see Note 5).
3. Insert a glow discharged grid into the plunging tweezers and add 2 µl mitochondria sample onto the carbon-coated side of the grid. Then insert the tweezer into the plunging device.

4. Add 4 µl gold fiducial buffer (HEK or yeast, respectively) and carefully mix with the sample on the grid (see Note 6).
5. Immediately blot away excess sample from the back side of the grid using blotting paper and plunge the grid into liquid ethane (see Note 7).
6. Store grids in grid boxes in liquid nitrogen.

3.4 Tomogram segmentation

The following protocol describes all necessary steps to segment mitochondrial membranes using the CNN in EMAN2 and to identify molecules of interest by template matching using pyTOM, as well as plotting them back into the tomographic volume using the TOM toolbox and MATLAB. As mentioned in section 2.4, a reconstructed tomogram is required. Furthermore, we recommend working with 6-8 times down-sampled data (pixel size corresponding to approximately 15 Å). An example for a yeast mitochondrion with visualized inner and outer membranes and cytosolic, as well as mitochondrial ribosomes is shown in Fig. 3 C.

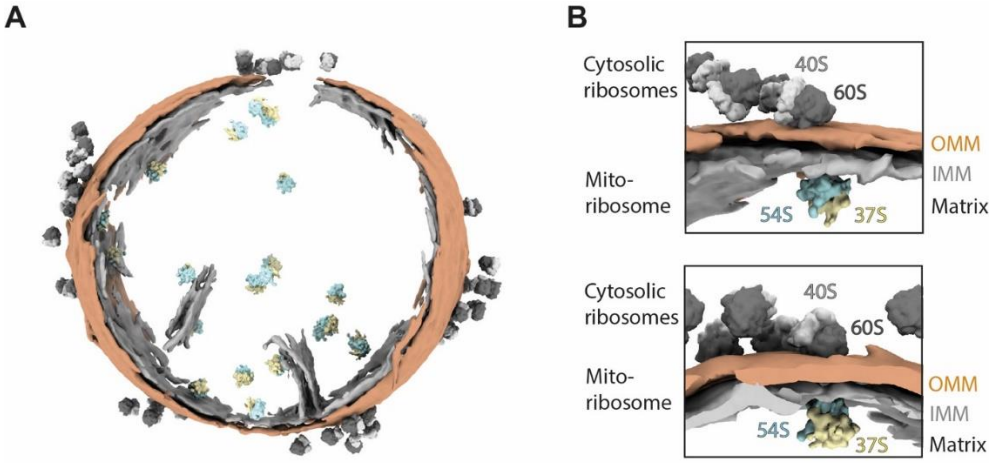

Fig. 3: Visualization of membranes and mitoribosomes in cryoelectron tomograms: (A) Tomogram segmentation of a yeast mitochondrion, visualizing cytosolic (40S in light, 60S in dark grey) and mitochondrial (37S in yellow, 54S in blue) ribosomes in the context of the mitochondrial membrane environment (OMM in orange, IMM in grey). (B) Cytosolic ribosome clusters coincide with mitochondrial ribosome positions on the IMM.

3.4.1 Tomogram segmentation

The described segmentation workflow is intended to quickly segment apparent features, such as the outer mitochondrial membrane. For features in dense environments or thick parts of a sample, additional manual segmentation in e.g. Amira (Termo Fisher) is likely necessary.

1. Make sure the tomogram is compatible with EMAN2 (see Note 9).
2. In a Linux terminal, load pyTOM 0.993 to execute deconv.py according to the described usage (deconv.py --help). The parameters provided below are an example and should be optimized for each dataset.
deconv.py -f <tomogram.mrc> -o <tomogram_deconv.mrc> -s <pixelsize> -z <defocus (positive value in µm)> --snrfalloff <1.5> --deconvstrength <0.5> --phaseflipped (in case phase-flipping was used for CTF correction).
3. Load EMAN2 and execute e2projectmanager.py in a terminal. To prevent automatic pixel addition to the tomographic volume (due to --clip option applied during import via EMAN2 Project Manager), create a folder called 'tomograms' in the EMAN2 project folder.
4. Import tomograms into that folder manually as follows:
e2proc3d.py <tomogram_deconv.mrc> <tomograms/tomogram_deconv.hdf> --process normalize
5. Go back to the EMAN2 Project Manager and follow the tutorial as described on the EMAN2 homepage (https://blake.bcm.edu/emanwiki/EMAN2/Programs/tomoseg, accessed 03/03/2022). Segment inner and outer membranes separately.
6. Create a segmentation file using the Segger tool [25] in Chimera X: Open the segmentation file obtained from EMAN2 and go to *Tools > Volume Data > Segment Map*. Under '*Segmentation Options*' in the *Segger* window '*Display at most 300 regions*' and select '*Group by smoothing 6*'. Click '*Segment*' at the bottom of *Segger* window.
7. Select all regions of interest by right clicking while pressing *Ctrl + Shift*, then group the regions via '*Group*' at the bottom of the *Segger* window.
8. Under Shortcuts Options '*Invert*' the selection, then '*Delete*' all unwanted regions and select the remaining region of interest by *right mouse clicking + Ctrl*.
9. Save the segmentation as an mrc file (*File > Save selected regions to .mrc file …*).
10. In the command line resample the segmentation onto the original volume dimensions using 'vop resample #<ID_segmentation> onGrid #<ID_CNN_hdf_file>' and save the resampled map using 'save <filename.mrc> model #<ID_segmentation_resampled.mrc>'.

11. Clean up the segmentation in Chimera X: Hide small volumes using the Hide Dust Tool under *Tools > Volume Data >Hide Dust*. Then open *Tools > Volume Data > Map Eraser*. Remove noise or falsely segmented features from the map and save it as a new file.

3.4.2 Mapping particles in the segmentation

1. Prepare templates for template matching using the Relion image handler as follows:
relion_image_handler --i <EMDBfile.mrc> --o <EMDBfile_temp.mrc> --angpix <Input pixel size(Å)> --lowpass <resolution (Å)> --rescale_angpix <Desired pixel size(Å)>
The pixel size needs to match the tomogram used for segmentation.
2. Open the templates in Chimera and if necessary, scale the density to match the tomogram density values using 'vop scale #<IDEMDBfile_temp.mrc> factor -1'.
3. Generate a spherical mask around the template in pyTOM (gen_mask.py) with the same box size as the template. To adjust the mask position with respect to the template use the 'vop resample' command in Chimera X (see 3.4.1 point 10).
4. Perform template matching and extract particles to an .xml file using pyTOM (https://github.com/FridoF/PyTom/wiki).
5. Clean up the particle lists via the pyTOM GUI (pytomGUI.py): Create a new project folder and under '*Enable Stage*' select '*Particle Picking*'. In the '*Manual Picking*' tab open the tomogram and click '*Pick*'. Apply a gaussian filter to the tomogram and select a suitable particle size, then load the particle list extracted in step 4. Use the left and right keyboard arrows to navigate and right click on particles to remove them. Then save the particle list as a new file.
6. Prepare motl files from the pyTOM particle lists as follows with pyTOM:
pytom_xml_to_motl.py <input file name>
7. In MATLAB add the path for the TOM toolbox (addpath(genpath('<path>'));), then open and execute tom_classmask.m. Set paths or add to path if required.
8. Open plot_particles.m for plotting molecule references to their positions in a tomogram, enter motl file name, the template file name, the tomogram dimensions and run the script for each molecule type to be displayed.
9. Visualize the segmentation, as well as the plotted particles in Chimera X.

4. Notes:

1. Culture cells for at least two days after thawing and do not freeze cells before mitochondria isolation. The freezing process significantly reduces the yield of intact mitochondrial vesicles.

2. Only harvest cells in logarithmic growth phase, otherwise the yield of mitochondrial vesicles is very low.

3. We recommend optimizing the sedimentation settings for differential centrifugation when applying the protocols to other cell lines, yeast strains or other sources of mitochondria.

4. Working at 4 ° C and fast preparation is crucial to yield structurally and functionally intact mitochondrial vesicles.

5. The use of Lacey carbon grids improves the vesicle distribution compared to Holey carbon grids due to a smaller carbon surface. However, holey carbon grids provide more stability during data acquisition.

6. The ratio of mitochondria sample to fiducial buffer can be varied to sample different mitochondria, sucrose/sorbitol or gold fiducial concentrations.

7. Since the sample thickness is one main limiting factor for high resolution subtomogram averaging, but mitochondrial vesicles are up to 500 nm in diameter, a balance needs to be found between vesicle intactness and sample thickness. Different sample thickness values can be sampled by varying the blotting parameters or by choosing acquisition points depending on ice thickness or vesicle size, respectively.

8. Using a dose symmetric acquisition scheme from +/- 52 ° with a 3 ° tilt increment allows a higher electron dose per tilt image and increases signal to noise ratio. However, the increased missing wedge leads to more missing information in its direction.

9. When using tomograms reconstructed with Etomo in IMOD, make sure to untick the '*convert to bytes*' option in both '*Coarse Alignment*' and '*Post-processing*' prior to reconstruction.

10. Coordinate systems can be defined differently in different software packages and need to be considered for combining e.g., membrane segmentations and back-mapped particles. Especially after a segmentation clean-up in Chimera, the original tomogram dimensions (box size) are not saved automatically and need to be manually applied prior to saving. Otherwise, Chimera automatically sets the volume dimensions depending on the cleaned segmentation, which might have a smaller box size compared to the initial tomogram.

5. Acknowledgements

We would like to acknowledge Stuart Howes and the whole EM Square facility at Utrecht University for technical support in electron microscopy as well as Mihajlo Vanevic for computational technical support. We would also like to thank Gijs van der Schot and Marten Chaillet for providing pyTOM scripts.

This work was supported by funding from Nederlandse Organisatie voor Wetenschappelijke Onderzoek (Vici 724.016.001) and NEMI.

6. References

1. Mahamid J, Pfeffer S, Schaffer M, et al (2016) Visualizing the molecular sociology at the HeLa cell nuclear periphery. Science 351:969–972

2. Lučić V, Förster F, Baumeister W (2005) Structural studies by electron tomography: From cells to molecules. Annual Review of Biochemistry 74:833–865

3. Dubochet J, Adrian M, Chang J-J, et al (1988) Cryo-electron microscopy of vitrified specimens. Quarterly Review of Biophysics 21:129–228

4. Nicastro D, Frangakis AS, Typke D, Baumeister W (2000) Cryo-electron tomography of Neurospora mitochondria. Journal of Structural Biology 129:48–56

5. Strauss M, Hofhaus G, Schröder RR, Kühlbrandt W (2008) Dimer ribbons of ATP synthase shape the inner mitochondrial membrane. EMBO Journal 27:1154–1160

6. Davies KM, Strauss M, Daum B, et al (2011) Macromolecular organization of ATP synthase and complex I in whole mitochondria. Proceedings of the National Academy of Sciences of the United States of America 108:14121–14126

7. Pfeffer S, Woellhaf MW, Herrmann JM, Förster F (2015) Organization of the mitochondrial translation machinery studied in situ by cryoelectron tomography. Nature Communications 6:1–8

8. Englmeier R, Pfeffer S, Förster F (2017) Structure of the Human Mitochondrial Ribosome Studied in Situ by Cryoelectron Tomography. Structure 25:1574–1581

9. Förster F, Hegerl R (2007) Structure Determination In Situ by Averaging of Tomograms. Methods in Cell Biology 2007:741–767

10. Englmeier R, Förster F (2021) In Situ Studies of Mitochondrial Translation by Cryo-Electron Tomography. In: Methods in Molecular Biology. Humana Press Inc., pp 243–268

11. Frezza C, Cipolat S, Scorrano L (2007) Organelle isolation: Functional mitochondria from mouse liver, muscle and cultured filroblasts. Nature Protocols 2:287–295

12. Fernández-Silva P, Acín-Pérez R, Fernández-Vizarra E, et al (2007) In Vivo and In Organello Analyses of Mitochondrial Translation. Methods in Cell Biology 80:571–588

13. Maccecchini M-L, Rudin Y, Blobelt G, Schatz G (1979) Import of proteins into mitochondria: Precursor forms of the extramitochondrially made F1-ATPase subunits in yeast. Proceedings of the National Academy of Sciences of the United States of America 76:343–347

14. Lazarou M, Smith SM, Thorburn DR, et al (2009) Assembly of nuclear DNA-encoded subunits into mitochondrial complex IV, and their preferential integration into supercomplex forms in patient mitochondria. FEBS Journal 276:6701–6713

15. Bihlmaier K, Bien M, Herrmann JM (2008) In Vitro Import of Proteins Into Isolated Mitochondria. In: Methods in Molecular Biology: Membrane Trafficking. pp 85–94

16. Meisinger Chris, Pfanner Nikolaus, Truscott Kaye N (2006) Isolation of Yeast Mitochondria. In: Yeast Protocol. pp 33–39

17. Couvillion MT, Soto IC, Shipkovenska G, Churchman LS (2016) Synchronized mitochondrial and cytosolic translation programs. Nature 533:499–503

18. Ress D, Harlow ML, Schwarz M, et al (1999) Automatic acquisition of fiducial markers and alignment of images in tilt series for electron tomography

19. Pettersen EF, Goddard TD, Huang CC, et al (2021) UCSF ChimeraX: Structure visualization for researchers, educators, and developers. Protein Science 30:70–82

20. Scheres SHW (2012) RELION: Implementation of a Bayesian approach to cryo-EM structure determination. Journal of Structural Biology 180:519–530

21. Hrabe T, Chen Y, Pfeffer S, et al (2012) PyTom: A python-based toolbox for localization of macromolecules in cryo-electron tomograms and subtomogram analysis. Journal of Structural Biology 178:177–188

22. Tang G, Peng L, Baldwin PR, et al (2007) EMAN2: An extensible image processing suite for electron microscopy. Journal of Structural Biology 157:38–46

23. Chen M, Dai W, Sun SY, et al (2017) Convolutional neural networks for automated annotation of cellular cryo-electron tomograms. Nature Methods 14:983–985

24. Nickell S, Förster F, Linaroudis A, et al (2005) TOM software toolbox: Acquisition and analysis for electron tomography. Journal of Structural Biology 149:227–234

25. Pintilie GD, Zhang J, Goddard TD, et al (2010) Quantitative analysis of cryo-EM density map segmentation by watershed and scale-space filtering, and fitting of structures by alignment to regions. Journal of Structural Biology 170:427–438

Chapter 6

How to build a ribosome from RNA fragments in Chlamydomonas mitochondria

Florent Waltz[1,2,3*], Thalia Salinas-Giegé[2*], Robert Englmeier[4], Herrade Meichel[2], Heddy Soufari[1], Lauriane Kuhn[5], Stefan Pfeffer[6], Friedrich Förster[4], Benjamin D. Engel[3], Philippe Giegé[2+], Laurence Drouard[2+], Yaser Hashem[1*]

[1]Institut Européen de Chimie et Biologie, U1212 Inserm, Université de Bordeaux, 2 rue R. Escarpit, F-33600 Pessac, France
[2]Institut de biologie de moléculaire des plantes, CNRS, Université de Strasbourg, 12 rue du général Zimmer, F-67084 Strasbourg, France
[3]Helmholtz Pioneer Campus, Helmholtz Zentrum München, Ingolstädter Landstraße 1, 85764 Neuherberg, Germany
Department of Chemistry, Technical University of Munich, 85748 Garching, Germany
[4]Structural Biochemistry, Bijvoet Centre for Biomolecular Research, Utrecht University, Universiteitsweg 99, 3584 CG, Utrecht, the Netherlands
[5]Plateforme protéomique Strasbourg Esplanade FRC1589 du CNRS, Université de Strasbourg, F-67084 Strasbourg, France
[6]Zentrum für Molekulare Biologie der Universität Heidelberg, DKFZ-ZMBH Alliance, Im Neuenheimer Feld 282, 69120 Heidelberg, Germany
[+]Corresponding authors
*Co-first authors

Published in *Nat Commun* **12**, 7176 (2021);
DOI: https:/doi.org/10.1038/s41467-021-27200-z

Abstract

Mitochondria are the powerhouse of eukaryotic cells. They possess their own gene expression machineries where highly divergent and specialized ribosomes, named hereafter mitoribosomes, translate the few essential messenger RNAs still encoded by mitochondrial genomes. Here, we present a biochemical and structural characterization of the mitoribosome in the model green alga *Chlamydomonas reinhardtii*, as well as a functional study of some of its specific components. Single particle cryo-electron microscopy resolves how the Chlamydomonas mitoribosome is assembled from 13 rRNA fragments encoded by separate non-contiguous gene pieces. Additional proteins, mainly helical repeat proteins, including OPR, PPR and mTERF proteins are found in Chlamydomonas mitoribosome, revealing the structure of an OPR protein in complex with its RNA target. Targeted amiRNA silencing indicated that these ribosomal proteins are required for mitoribosome integrity. Finally, we use cryo-electron tomography to show that Chlamydomonas mitoribosomes are attached to the mitochondrial inner membrane via two contact points mediated by Chlamydomonas-specific proteins. Our study expands our understanding of the mitoribosome diversity and the various strategies they adopt for membrane tethering.

Introduction

Mitochondria are essential organelles of eukaryotic cells that act as metabolic hubs and powerhouses, producing energy through aerobic respiration. They still possess their own genome and gene expression machineries, vestige of their once free-living bacterium ancestor[1,2]. Due to the evolutionary drift of eukaryotes, mitochondrial complexes involved in metabolism and gene expression combine features from their bacterial ancestor with traits that evolved in eukaryotes[3,4]. The final step of gene expression, translation, is carried out by specialized mitochondrial ribosomes (mitoribosomes). They synthesize the few proteins still encoded by the mitochondrial genome, most of which are hydrophobic components of the respiratory chain. Despite their shared prokaryotic origin[5], mitoribosome structure and composition were shown to be highly divergent across eukaryotes. They systematically acquired numerous additional ribosomal proteins (r-proteins), and their ribosomal RNAs (rRNAs) were either greatly reduced like in animals and kinetoplastids[6–9] or expanded like in plants and fungi[10–13].

Among the most prominent unresolved questions in the mitochondria biology field, is the long-standing debate over the peculiar organization of the mitochondrial genome in the unicellular green alga *Chlamydomonas reinhardtii* and the biogenesis of its mitoribosome. This organism is widely used to study photosynthesis and cilia/flagellar motility and function[14], but is also an excellent model to investigate mitochondrial biology. It is one of the few organisms where mitochondrial transformation is possible[15], and mitochondrial mutants are viable in photoautotrophic conditions[16]. In contrast to vascular plants, or Viridiplantae in general, which are characterized by gene-rich and largely expanded mitochondrial (mt)-genomes, *C. reinhardtii* possess a small linear mt-genome of 16kb. It only encodes eight proteins (all membrane-embedded components of the respiratory chain), three transfer RNAs (tRNAs) and, most intriguingly, non-contiguous pieces of the large subunit (LSU) and small subunit (SSU) ribosomal RNAs (rRNAs), scrambled across the genome[17–19]. The mt-genome is transcribed as two polycistronic primary transcripts synthesized from opposite strands[17,19]. Individual transcripts are then generated from the primary transcripts to produce mature, functional RNAs. When initially characterized 30 years ago[17], Chlamydomonas mitoribosome rRNA fragmentation represented the earliest example that an rRNA does not need to be continuous in order to be functional[20]. Although it was predicted that the rRNA fragments would somehow be integrated into a functional ribosome[18], it is enigmatic how these fragments are recruited, interact with each other, and are stabilized to form the 3D mitoribosome structure.

Here, we combine cryo-electron microscopy (cryo-EM) with *in situ* cryo-electron tomography (cryo-ET) to resolve the structure of a green algal mitoribosome, stunningly different from both its prokaryotic ancestor, as well as from the flowering plant

mitoribosome[11], but also from all other characterized mitoribosomes across diverse species[3]. Our structure reveals how the reduced and fragmented rRNAs are organized and stabilized in the mitoribosome via numerous Chlamydomonas-specific r-proteins. Cryo-ET reveals the native structure and organization of Chlamydomonas mitoribosomes inside mitochondria, revealing that these mitoribosomes are exclusively bound to the inner membrane of mitochondria. Our study provides an example of a mitoribosome composed of numerous rRNA fragments, revealing a strikingly divergent blueprint for building this conserved molecular machine.

Results

Isolation, mass spectrometry, and cryo-EM of mitoribosomes

To analyze the *C. reinhardtii* mitoribosome, mitochondria were purified and used for mitoribosome isolation following a procedure based on sucrose density gradient separation (see Methods) (Supplementary Fig. 1). Collected fractions were systematically analyzed by nano-LC MS/MS (Supplementary Table 1) and screened by cryo-EM to determine their composition. This approach allowed us to identify fractions containing the two mitoribosome subunits which were subsequently used for data collection (Supplementary Fig. 1). The proteomic analysis identified putative Chlamydomonas-specific r-proteins that were then confirmed by the corresponding cryo-EM reconstructions. Following image processing and extensive particle sorting, reconstructions of both dissociated subunits were obtained. The large subunit (LSU) was resolved to 2.9 Å while the small subunit (SSU) was reconstructed at 5.49 Å and further refined to 4.19 Å for the body and 4.47 Å for the head using a focused refinement approach (Supplementary Fig. 2). Fully assembled mitoribosomes were identified by nano-LC MS/MS in the cytoribosome fraction (Supplementary Fig. 1), but cryo-EM investigation revealed aggregates in this fraction, most likely corresponding to mitoribosomes. Nevertheless, the subunit reconstructions were docked into the map of the entire *C. reinhardtti* mitoribosome obtained from the subtomogram averaged mitoribosomes of the *in situ* cryo-ET data allowing accurate positioning of both subunits relative to each other in the context of a fully assembled native mitoribosome. The isolated subunit reconstructions were similar to the *in situ* subtomogram average, demonstrating that they represent the mature LSU and SSU and not assembly intermediates. Notably, all densities corresponding to Chlamydomonas specific r-proteins were present in both single particle and subtomogram average reconstructions.

Overall structure of the Chlamydomonas mitoribosome

Our cryo-EM reconstructions, along with our extensive MS/MS analyses, allowed us to build atomic models of both *C. reinhardtii* mitoribosome subunits (see Methods) (Fig.

1 and 2). The overall architecture of this mitoribosome (Fig. 1) is clearly distinct from both its bacterial ancestor and the flowering plant mitoribosome[11]. Chlamydomonas-specific proteins and domains largely reshape both subunits. Similar to all previously described mitoribosomes, the Chlamydomonas mitoribosome has more r-proteins compared to its bacterial counterpart[3,4]. These proteins include bacteria-conserved (ancestral r-proteins), r-proteins shared with other mitoribosomes (mitoribosome-specific) and Chlamydomonas-specific r-proteins. In total, the mitoribosome contains 47 r-proteins in the LSU and 36 in the SSU. These include 11 new r-proteins (not accounting for unknown densities) 8 in the LSU and 3 in the SSU, for a total of more than 80 proteins altogether compared to the 54 r-proteins in bacterial ribosomes (Fig. 2 and Supplementary Table 1). As a result, very few rRNAs are exposed to the solvent, with proteins coating the entire mitoribosome and stabilizing the fragmented rRNAs (Movie 1). Proteins follow the classical r-protein nomenclature[21], and newly identified proteins are numbered according to the last inventory of mitoribosomal r-proteins[22].

Reconstruction of the LSU (Fig. 1d) revealed eight additional r-proteins, named mL113 to mL119, plus PPR*, a putative PentatricoPeptide Repeat (PPR) protein (Fig. 1, 2, Supplementary Fig. 4 and Supplementary Table 1). They are distributed across the whole LSU, where they extend into the solvent and are anchored to the ribosome by interacting with both conserved r-proteins and rRNA fragments. With the exception of mL119 at the exit of the peptide channel, all these proteins are relatively large RNA binders composed of repeated alpha-helical folds, including a mitochondrial TERmination Factor (mTERF) protein, several OctotricoPeptide Repeat (OPR) proteins and PPR*.

The small subunit (Fig. 1c) reconstruction highlights several distinctive features. Most strikingly, the SSU is shaped by two large protuberances positioned on its beak side, one on the head and one on the body, both formed by helical-rich proteins. The body protuberance, located close to the mRNA entrance, is mainly formed by a specific extension of more than 400 aa in the mitochondria-specific r-protein mS45 (Supplementary Fig. 5), a highly variable r-protein[22]. The head protuberance density could not be assigned due to the low resolution of this area. However, several conserved proteins of the SSU head located nearby, notably uS3m, uS10m and mS35, present large extensions. Therefore, it is likely that these extensions could come together and form the head protuberance, as no other apparent candidates could be identified by MS/MS analyses. On the solvent side of the head, a large torus-shaped domain protrudes in the solvent. This additional domain is a homotrimeric complex formed by three copies of mS105, also called p32 (Supplementary Fig. 5a). This MAM33-family protein is seemingly conserved in all eukaryotes, and has been described to have several functions in mitochondria, some related to mitoribosome assembly[23–26]. However, mS105/p32 was never reported as a core component of a ribosome. Additionally, the head of the SSU is also characterized by its missing beak, which is typically formed by

helix 33 at the junction site of rRNA fragments S3 and S4 (Fig. 3c and Supplementary Fig. 7). The foot of the SSU is reshaped by Chlamydomonas-specific r-proteins. The extension is formed by two super-helical proteins, one PPR (mS106) and one OPR (mS107) identified by MS/MS and confirmed by AlphaFold[27]. The mS106 protein occupies a position similar to mS27 in humans[6,7] and fungi[12], but it does not appear to interact with RNA, nor does it share any sequence identity with mS27 (Supplementary Fig. 5d). On the other hand, the OPR mS107 directly interacts with rRNA fragment S2, where it encapsulates the tip of helix 11 (Supplementary Fig. 5c).

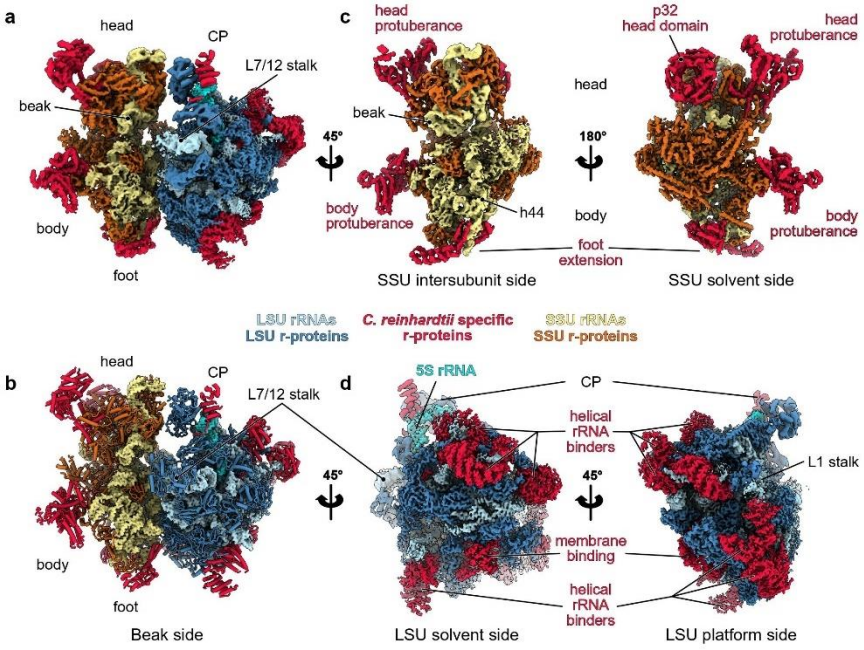

Figure 1. Overall structure of the Chlamydomonas mitochondrial ribosome

a) Composite cryo-EM map of the *Chlamydomonas reinhardtii* mitochondrial ribosome and **b)** the resulting atomic model. The large subunit (LSU) components are depicted in blue shades, the small subunit (SSU) components in yellow shades, and the specific r-proteins and domains are displayed in red. **c-d)** Different views of the cryo-EM reconstructions of the SSU (**c**) and the LSU (**d**).

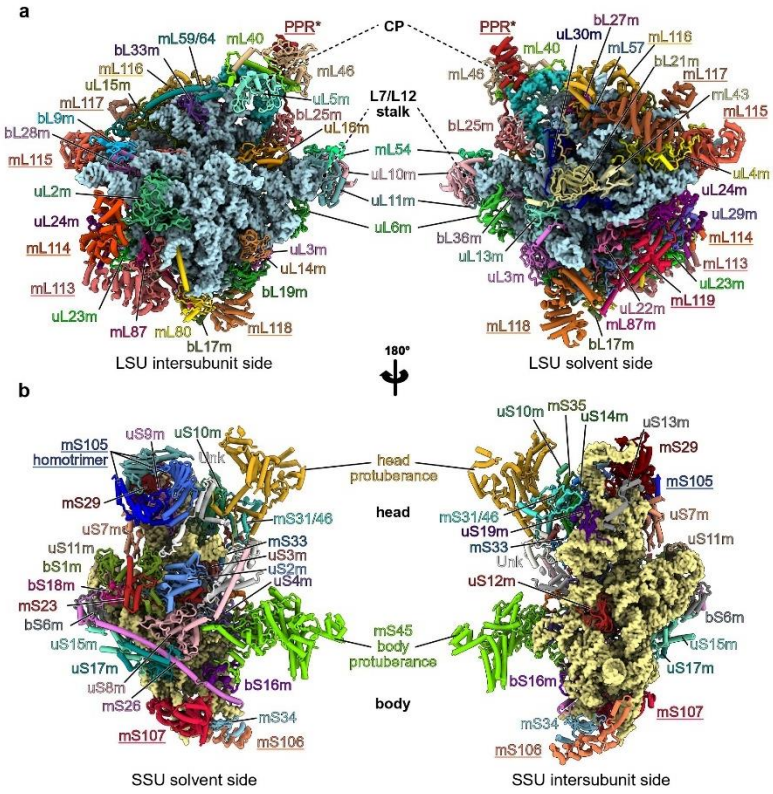

Figure 2. Ribosomal proteins of the Chlamydomonas mitoribosome
a-b) The atomic models of the Chlamydomonas mitoribosome LSU (**a**) and SSU (**b**), with mitoribosomal proteins shown in cartoon representation and individually colored and annotated. rRNAs are shown in surface representation and colored in light blue (LSU) and beige (SSU). Newly identified r-proteins are highlighted with underlined names.

Fragmented ribosomal RNAs are assembled to reconstitute the core of Chlamydomonas mitoribosome

In contrast to flowering plants, where rRNAs are largely expanded, the *C. reinhardtii* mitoribosome is characterized by its reduced and fragmented rRNAs (Fig. 3). These rRNAs are scrambled in the mitochondrial genome (Fig. 3a), where they are expressed as a single polycistron which is then further processed into matured transcripts by currently unknown endonucleases[17]. The “23S” and “16S” rRNAs are respectively split into eight fragments totaling 2035 nt, and four fragments totaling 1200 nt (Fig. 3c, Supplementary Fig. 6 and 7 and Supplementary Movie 1). This corresponds to 30 % and 22 % reductions compared to bacteria (Fig. 3f). Among all the rRNA pieces predicted to be integrated into the mature mitoribosome, all but one (L2b) could be identified in our cryo-EM reconstructions. To

confirm the absence of the L2b fragment, its occurrence was analyzed by comparative RNAseq analyses of mitochondrial and mitoribosomal fractions (Fig. 3b). Consistently, all rRNA fragments could be identified in the mitoribosome fraction except L2b. However, this analysis confirmed that the fragment is indeed expressed and accumulates in the purified mitochondria fraction (Fig. 3b), which is in line with previous transcriptomic analyses[19,28,29]. Additionally, these results were confirmed by RNA blots hybridized against L2b, and an L2a control found in the ribosome and stabilized by the r-protein mL116 (Fig. 3d). Therefore, the L2b RNA is not associated with the mitoribosome, suggesting that this small RNA has an independent function that remains to be elucidated.

In the SSU, the fragmented rRNAs form only a few interactions with the additional r-proteins and are mainly stabilized by base pairing with each other (with the exception the S2 fragment's h11, which is encapsulated by mS107 (Supplementary Fig. 5 and 7). Fragments S1, S2 and a small portion of S3 form the 5' domain, with the rest of S3 making up domain C. The 3' end of S3 and the entirety of S4 constitute domains 3'M and 3'm, with S4 largely contributing to linking the head and body of the SSU, the most conserved part with bacteria being the decoding center, made by h1-2 and h27-28 (Fig. 3, Supplementary Fig. 7).

In contrast to the SSU, the nine rRNA fragments in the LSU are all stabilized by the newly identified Chlamydomonas-specific r-proteins. These fragments reconstitute the different domains of the large subunit. L1 forms the highly reduced domain I of the LSU. L2a, L3b, L4, L5 and part of L6 together form domain II. Portions of L6 and L7 form the highly reduced – almost deleted – domain III. Fragments L7 and L8, the largest of all, make up domains IV, V and VI which form the catalytic core of the ribosome, especially peptidyl transferase center (PTC) formed by H89 to H93 is particularly conserved, compared with bacteria. These three domains are the least altered, with only few helices missing and two expansion segments ES-66 and ES-94 (Fig. 4, Supplementary Fig. 6), which is most likely due to the high selective pressure to conserve the catalytic region of the ribosome[30]. These rRNA fragments are held together by base-pairing with each other, and their extremities are stabilized by base-pairing with other fragments, e.g. L2a, L3b and L4 (Fig. 3e) or with themselves. These results corroborate the initial prediction that were made 30 years ago by Boer and Gray[17]. However, several single stranded rRNA extremities are also stabilized by the Chlamydomonas-specific r-proteins (see below). Surprisingly, while it was anticipated that 5S rRNA should be absent from Chlamydomonas mitoribosome, we identified an RNA density at the typical position of the 5S rRNA in the central protuberance (CP) (Fig. 1 and Supplementary Fig. 8). This rRNA density could be attributed to the L3a rRNA fragment (Supplementary Fig. 8). Its association with the mitoribosome was also confirmed by comparative RNAseq analysis of mitochondrial and mitoribosomal fractions (Fig. 3b). Previous studies of the *C. reinhardtii* mitochondrial genome and rRNAs always failed to

identify this rRNA as a putative 5S[17–19,31]. While L3a likely derives from an ancestral bacterial 5S rRNA, it is highly degenerated; very little of the primary sequence is conserved with other 5S rRNAs (Supplementary Fig. 8d), but a consensus of 6 consecutive nucleotides confirmed its origin. Its overall structure is also weakly conserved, with only the domain γ retaining its characteristic structure to interact with H38. The domain β is angled differently relative to the domain γ stem, which allows the interaction of the terminal loop of the domain β with H87, in contrast to other known ribosome structures. Additionally, the domain α could not be fully resolved, but most likely interacts with the putative PPR protein (labelled "PPR*"), possibly stabilizing its 3' and 5' termini. In conclusion, when compared with the flowering plants mitoribosome[11], the overall structure of the CP appears similar. However, in terms of composition, the Chlamydomonas mitoribosome CP includes a degenerated 5S, lacks the uL18m protein, and an additional protein, PPR*, is present.

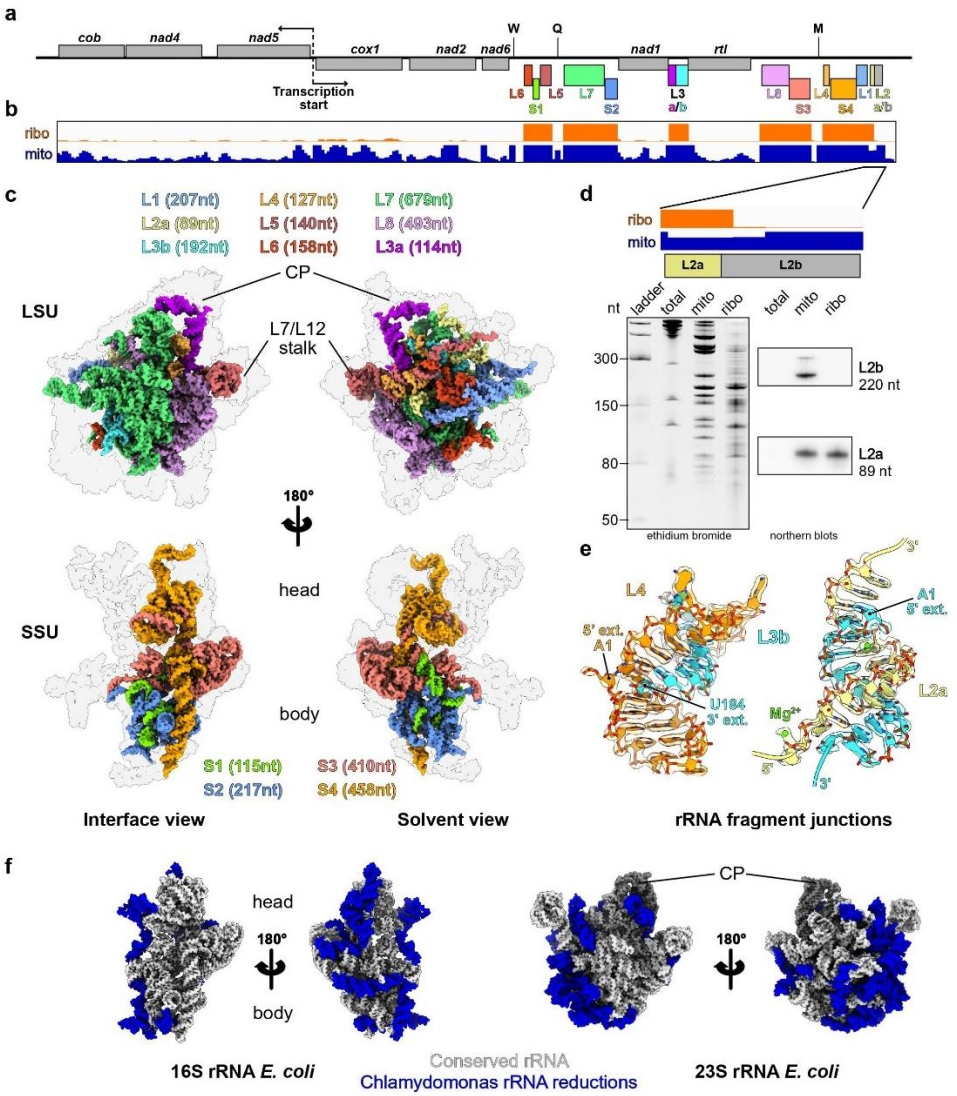

Figure 3. The ribosomal RNAs of the Chlamydomonas mitoribosome are fragmented

a) Schematic representation of the entire *C. reinhardtii* mitochondrial genome. The protein-coding genes are displayed in grey and the rRNA fragments incorporated in the mitoribosome are individually colored. The tRNA genes are indicated by letters. **b)** Browser view of the RNAseq data of libraries built from purified mitochondria (orange) and purified mitoribosome (blue) fractions. Data range is [0-700], mapped to the Chlamydomonas mitochondrial genome in (**a**). **c)** rRNA fragment 3D organization in the LSU and the SSU. The r-proteins are shown as a grey silhouette. The fragment colors match the color code used in (**a**). **d)** Zoomed view of the L2a/b coverage (top). The L2b fragment is absent in the ribosomal fraction in the RNAseq analysis which was confirmed by northern blots (bottom) and the cryo-EM reconstruction. Northern blot was performed for the L2a and L2b fragments on total cell extracts (total), mitochondrial (mito) and mitoribosomal fraction (ribo) on one biological sample. **e)** Detailed view of the rRNA extremities of the L3b fragment and its pairing with the L2a and L4 fragments. The atomic models are shown mapped into the cryo-EM densities. **f)** Comparison of the Chlamydomonas mitoribosome rRNAs with the *E. coli* ribosome. rRNA reductions are shown in blue.

Specific r-proteins stabilize the rRNAs by highly intertwined protein-RNA interactions

In the LSU, with the exception of mL119, all the Chlamydomonas-specific r-proteins belong to families of predicted nucleic-acid binders. mL114 is an mTERF protein, but mL113, mL115, mL116, mL117 and mL118 all appear to belong to the same protein family as they all have similar tertiary structures and resemble ASA2/OPR proteins. These OPR proteins (OctotricoPeptide Repeat), are predicted to fold into repeated pairs of α-helices, forming a super-helical solenoid, similar to PPR (PentatricoPeptide Repeat) and TPR (TetratricoPeptide Repeat) proteins[32,33]. Both PPR and TPR are widespread in eukaryotes and have previously been found in mitoribosomes, notably in the flowering plants mitoribosome which includes 8 PPR proteins (rPPR proteins), that stabilize the numerous rRNA expansions[11]. In Chlamydomonas, OPR proteins were previously described to be involved in gene expression regulation, notably in the chloroplast[32,34–37]. Here, these proteins stabilize the many rRNA fragments by different modes of RNA interaction. This is, to our knowledge, the sole structural description of this kind of protein in interaction with RNA. Proteins mL115, mL116 and mL117 stabilize the 3' extremities of L1, L2a and L5, respectively, by binding the single stranded rRNA fragments in their inner groove (Fig. 4). The stabilization is primarily mediated by positive/negative charge interactions, where the inner grooves of the proteins are largely positively charged, filled with lysine and arginine that interact with the negatively charged phosphate backbone of the RNA (Supplementary Fig. 4). Unlike the rest of the RNA binders, mL113 does not interact with RNA in its inner groove. An inter-repeat domain formed by amino acids 353-397 clamps the tip of H34 from the L3b fragment (Fig. 4c and Supplementary Fig. 4a). Here, the interaction does not stabilize the rRNA itself, but rather constitutes an anchor point between mL113 and the ribosome. mL118 acts similarly to the SSU's OPR mS107, as it binds the 3' extremity of the L8 fragment, which forms a loop inside the inner groove of the protein (Fig. 4a). Additionally, these proteins also interact with RNA *via* the convex side of their super-helical fold. This is the case for mL115 which interacts with H4 and H19 of the L1 fragment. mL116 interacts with H28 of the L2a fragment and H38 formed by the L3b/L4 duplex, and mL118 interacts with ES-94 of the L8 fragment (Supplementary Fig. 4). Moreover, the mTERF protein mL114 stabilizes the ES-66 *via* its C-terminal region, not its inner groove (Supplementary Fig. 4a). All these proteins largely interact with conserved proteins as well as with each other, e.g. mL113 with mL114 and mL116 with mL117 (Fig. 4). Furthermore, mL113, mL114 and mL115 structurally compensate missing rRNA on the backside of the LSU (Fig. 4d). mL113 and mL114 compensate for the almost wholly deleted domain III, while mL115 both stabilizes and compensates for the missing parts of domain I. Interestingly, mL113 and mL114 are

similarly positioned compared to mL101 and mL104, with the mitoribosomes' flowering plants rPPR proteins stabilizing the remodeled domain III[11].

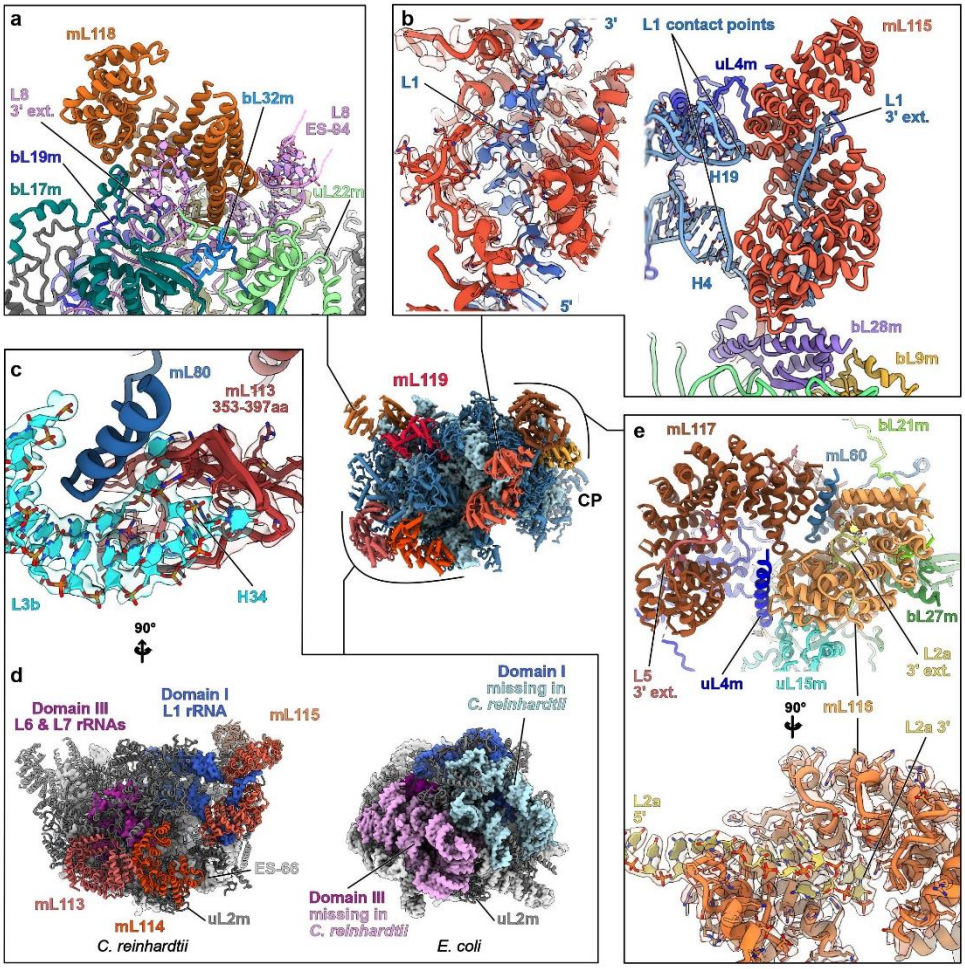

Figure 4. Chlamydomonas-specific proteins stabilize the fragmented rRNAs *via* highly intertwined interactions

Magnified views of the Chlamydomonas-specific r-proteins involved in rRNA stabilization. **a)** mL118 stabilizes the 3' end of the L8 fragment and contacts the expansion segment 94 (L8 ES-94). **b)** mL115 stabilizes the highly reduced domain I, which is formed by the L1 fragment. mL115 binds the 3' end of the L1 fragment and also contacts the L1 fragment at two specific points corresponding to H4 and H19. The single stranded portion of L1 interacting with mL115 is shown in its density. **c)** Detailed view of the mL113 contact with the L3b fragment. An inter-repeat domain of mL113 (red) formed by amino acids 353 to 397 clamps the tip of H34 (cyan). The models are shown in their densities. Contrary to the rest of the r-proteins, this one does not enlace single stranded rRNA. **d)** Structural compensation for the loss of large portions of domain I and III. The missing rRNA regions are depicted on the *E. coli* model in pink and light blue, and the compensating proteins mL113, mL114 and mL115 (red shades) are shown on the Chlamydomonas model. mL113 and mL114 compensate for domain III reduction and mL115 stabilizes and compensates the reduced domain I. **e)** The mL116 and mL117 interact with

each other and with several surrounding proteins. mL117 is involved in stabilizing the 3' end of the L5 rRNA fragment, and mL116 stabilizes the L2a 3' extremity, but also make additional contacts with rRNAs (see Supplementary Fig. 4). The single stranded portion of L2a in mL116 is shown in its density. With the exception of the mTERF protein mL114, the rest of the proteins belong to the same class of ASA2-like/OPR proteins. Further detailed views are shown in Supplementary Fig. 4.

Knock-down of Chlamydomonas-specific r-proteins affects fitness and rRNA stability

Next, we used targeted gene silencing to investigate the importance of the Chlamydomonas-specific r-proteins for ribosome integrity. We explored the CLiP Chlamydomonas mutant library[38], but no mutant strains for the genes of interest could be confirmed. Hence, we generated artificial miRNA (amiRNA) strains for these factors. This method reduces targeted protein expression at the transcript level[39]. Strains were generated for mL113, mL116, mL117, mL118, and mS105 (p32). The physiological phenotype of each amiRNA strain was analyzed, particularly the capacity to grow under heterotrophic conditions (dark + acetate), which is typically defective in Chlamydomonas mutants impaired in mitochondrial respiration[16]. Some transformants revealed growth retardation when cultivated in heterotrophic conditions and the ones presenting the most severe macroscopic phenotypes were selected (Fig. 5a). The expression of targeted mRNAs was monitored by quantitative RT-PCR, revealing down-regulations of 80%, 49%, 82%, 51% and 83% on average for mL113, mL116, mL117, mL118, and mS105, respectively (Fig. 5b).

The levels of rRNA fragments in these down-regulated amiRNA strains were then monitored by quantitative RT-PCR to determine the effect on mitochondrial rRNAs stability. This analysis showed that the overall relative levels of LSU rRNAs decreased by 13%, 40% and 14% in the *mL113, mL117, mL118* knockdown strains respectively, while the level of L2b RNA, which does not occur in mitoribosomes, followed a different behavior (Fig. 5c). In contrast, relative rRNA levels were not significantly affected in the *mL116* and *mS105* knockdown strains, with the exception of L2b which is reduced to about 67% in *mS105.* Altogether, it appears that Chlamydomonas-specific r-proteins, in particular mL113, mL117 and mL118, are required for the proper stability of the LSU rRNAs. In addition, the accumulation of mitochondria-encoded proteins was investigated by protein immunoblots. Two mitochondrial-encoded components of respiratory complex I, Nad4 and Nad6, were analyzed, and two controls used, the nuclear-encoded subunit NUO7 of complex I and the mitochondrial porin VDAC (Fig. 5d). Analysis from 3-4 technical replicates from 2 biological replicates showed that Nad4 and Nad6 levels were decreased in the *mL113, mL117,* and *mS105* mutant strains compared to wild-type; in contrast, NUO7 and VDAC had unchanged levels (Supplementary Fig. 9 and Source Data file). Finally, the accumulation of assembled respiratory complexes, which contain mitochondria-encoded proteins, was investigated by blue native PAGE (BN-PAGE) coupled to in-gel activity assays (Fig. 5e). These tests revealed that the *mL113* strain is impaired in complexes I and IV activity, whereas the *mL117* strain also appears to be affected but to a lesser extent, which correlates with the immunoblot

assays. Collectively, these analyses show different impacts on the knockdown strains, suggesting non-redundant functions for these r-proteins.

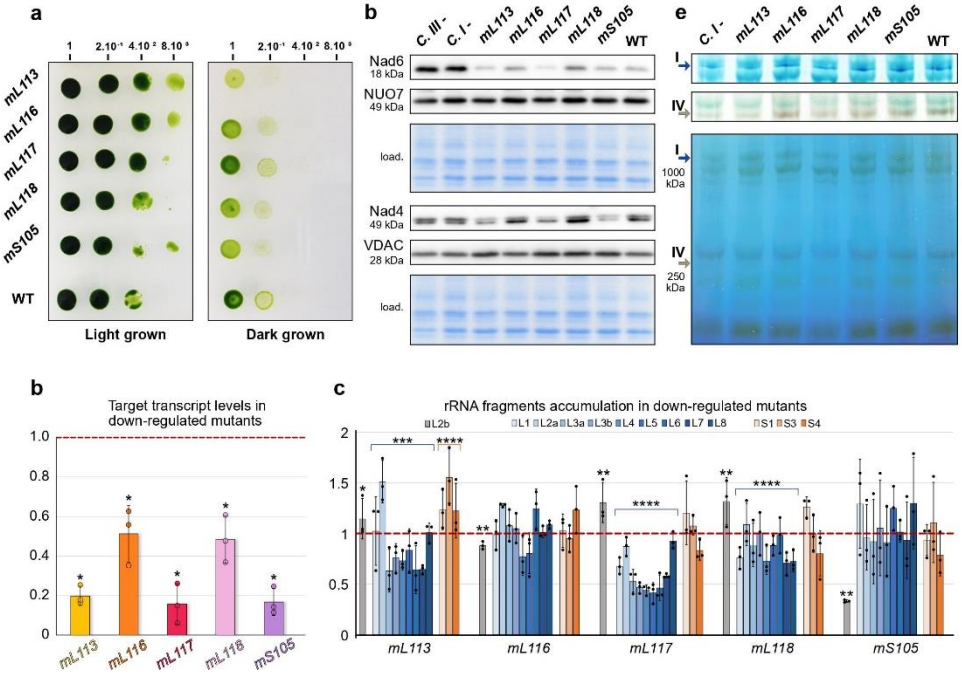

Figure 5. Down regulation of Chlamydomonas-specific r-proteins affect fitness, rRNA accumulation and mitochondrial proteins synthesis

a) Growth phenotype of amiRNA knockdown strains. After a first-round selection, transformants were obtained for *mL113*, *mL116*, *mL117*, *mL118* and *mS105*. Growth phenotypes in the dark were investigated by 5-fold dilution series. Dilutions were spotted on two identical TAP plates, one placed in light and the other in darkness. **b)** Relative levels of amiRNA-targeted mRNAs investigated by RT-qPCR. All strains show clear down-regulation compared to WT. Data are presented as mean values ± SD from *n*=3 biological independent experiments, each analyzed in three technical replicates. The statistical difference between WT and each amiRNA strain for each signal protein was calculated with the two-tailed Mann-Whitney test (*$p < 0.05$). Statistics and the exact *p* values are detailed in the Source Data file. **c)** Relative steady-state levels of rRNA fragments in the different Chlamydomonas-specific r-protein amiRNA strains. rRNA fragments of the LSU are shown in blue shades, rRNA fragments of the SSU are shown in orange shades, and L2b (not present in the ribosome) is grey. Data are presented as mean values ± SD from *n*=3 biological independent experiments, each analyzed in three technical replicates. For statistical analysis, the rRNAs were divided into three groups: the LSU rRNA fragments, the SSU rRNA fragments and the L2b rRNA fragment. The statistical differences between WT and amiRNA strain for each group was calculated with the two-tailed Mann-Whitney test (****$p < 0.0005$; ***$p < 0.005$; **$p < 0.05$; *$p < 0.5$). Statistics and the exact *p* values are detailed in the Source Data file. For (**b**) and (**c**), the WT levels are normalized to 1 on the y-axis. **d)** Steady-state levels of mitochondria-encoded Nad6 and Nad4, as well as nuclear-encoded NUO7 and the mitochondrial porin VDAC, are shown by protein immunoblots corresponding to an example of a typical result from 2 biological replicates performed in 3-4 technical replicates (Supplementary Fig. 9

and Source Data file). **e)** Blue native PAGE and in-gel activity assays for complexes I and IV. Arrows indicate the resulting bands. The activity assay for complex I corresponds to a typical result from two independent experiments. The activity assay for complex IV corresponds to the result of one biological experiment. For (**d**) and (**e**), Wild-type (WT), complex I mutant *dum5* (C I-), and complex III mutant *dum11* (C III-) were used as controls.

The Chlamydomonas mitoribosome is tethered to the inner mitochondrial membrane via two protein contact sites

The LSU reconstruction revealed the presence of a specific r-protein, mL119, precisely located at the exit of the peptide channel (Fig. 6). There, this protein forms several contacts with r-proteins uL22m, uL24m, uL29m and bL32m, and with nucleotides 114-124 of the L6 fragment *via* its C-terminal part, which anchors the protein to the ribosome (Fig. 6e). The N-terminal part of mL119, forming most of the protein's mass, is exposed to the solvent. This protein has no apparent homolog and appears to be restricted to the Chlorophyceae (green alga) lineage. Similar to humans, the Chlamydomonas mitochondrial genome only codes for membrane components of the respiratory chain, except for the *rtl* gene, whose expression and function remain uncertain. In humans and yeast, it was previously shown that mitoribosomes contact the membrane protein insertase Oxa1 *via* r-protein mL45 in human and the linker protein Mba1 in yeast, the two proteins being homologs[40–44]. These two proteins are positioned at the exit of the peptide channel, where they link the ribosome to the membrane by binding Oxa1, allowing direct insertion of nascent proteins into the membrane. Given the position of mL119, one would expect this protein to fulfill a function similar to mL45 and Mba1. To assess the role of mL119 in membrane binding, Chlamydomonas mitoribosomes were directly visualized inside cells using *in situ* cryo-ET (Fig. 6 and Supplementary Movie 2).

Whole *Chlamydomonas reinhardtii* cells were vitrified, thinned by cryo-focused ion beam (FIB) milling, and imaged by cryo-ET. A representative tomogram depicting a section of a native mitochondrion within a *C. reinhardtii* cell is shown in Fig. 6a-d. ATP synthase dimers, cytosolic ribosomes and mitoribosomes were automatically localized by template matching, structurally resolved by subtomogram averaging, and then mapped back into the native cellular environment (Fig. 6b). Contrary to cytosolic ribosomes, which crowd the cytoplasm, mitoribosomes have very low abundance and are localized to the inner mitochondrial membrane. Their low copy number and membrane association highlight the difficulty of purifying these complexes compared to cytosolic ribosomes. Alignment of subtomograms containing mitoribosomes yielded a structure of the native membrane-bound mitoribosome at 31.5 Å resolution (Supplementary Fig. 3). With the exception of dynamic flexible regions (e.g. L7/L12 and L1 stalks), the *in situ* subtomogram average is

highly similar to our single-particle reconstructions, as revealed by molecular fitting. This structural agreement confirms that the single-particle reconstructions very likely correspond to mature forms of the mitoribosome subunits (Fig. 6f). The *in situ* subtomogram average had one additional density located at the mitoribosomes's mRNA exit channel. Although we do not know the identity of this density, we speculate that it may correspond to exiting mRNAs or the recruitment of additional factors during active translation (Fig. 6g).

The *in situ* subtomogram average reveals how the mitoribosome is tethered to the inner mitochondrial membrane. Membrane-bound mitoribosomes were previously described by cryo-ET of mitochondria isolated from yeast[45] and humans[46]. Similar to yeast, but not humans, the Chlamydomonas mitoribosome makes two distinct contacts with the membrane. Superposition with the atomic model reveals that one contact is located at the precise position of mL119, supporting the hypothesis that this protein could directly interact with the ribosome binding domain of Oxa1 *in vivo*. Therefore, it appears that mL119 constitutes a functional analog of mL45 and Mba1. However, mL119 and mL45/Mba1 are not evolutionary related, but rather appear to have convergently evolved to fulfil the same function. The mitoribosome's second membrane contact is mediated via the C-terminal part of mL113 (Fig. 6f). This region of mL113 had poorly resolved density in our cryo-EM map and was thus not modeled, but we could still observe its position at low resolution (Supplementary Fig. 4a). The mL113 contact mimics the rRNA expansion segment ES-96 that forms the second contact site with the membrane in yeast[45].

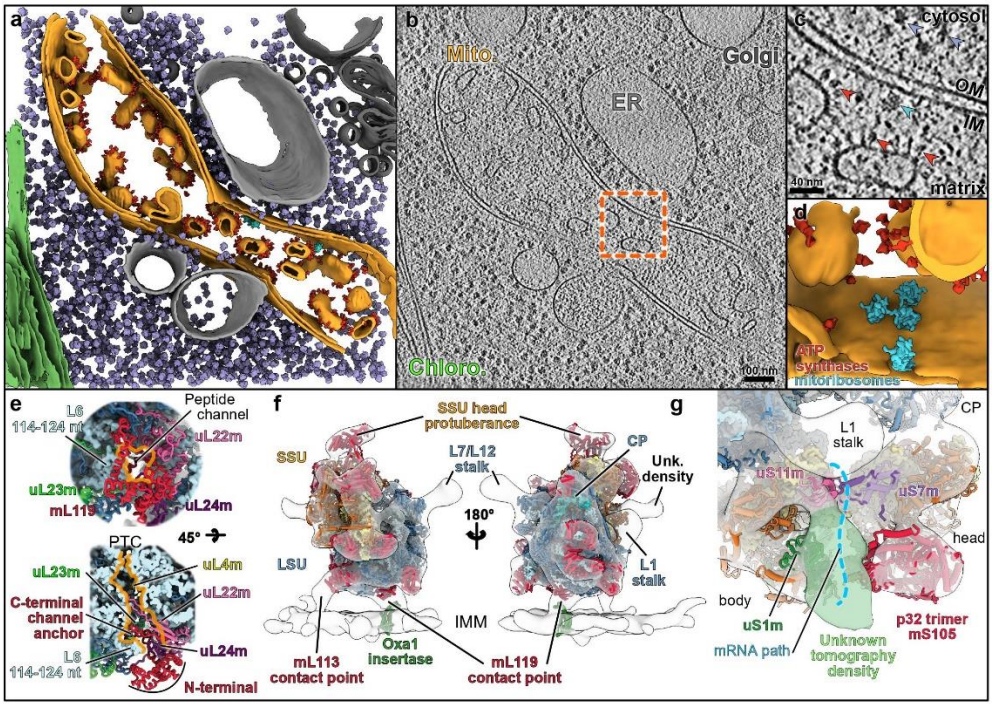

Figure 6. The mitoribosome is attached to the mitochondrial inner membrane *via* specific proteins
a) Segmentation of an *in situ* tomogram, depicting a mitochondrion within a native *C. reinhardtii* cell. The mitochondrion is shown in orange, chloroplast in green, ER and lysosome in light gray and Golgi in dark gray. Subtomogram averages of ATP synthase dimers (red), cytosolic ribosomes (purple) and mitoribosomes (cyan) are mapped into the volume. **b)** A slice through the corresponding raw tomogram (one representative tomogram from n=47 in total). **c)** Close-up view of a membrane-bound mitoribosome at the inner membrane (IM), boxed in (**b**). Arrowheads point to ATP synthase, cytosolic ribosomes and a mitoribosome. **d)** Close-up view of the segmented area presented in (**c**), highlighting a cluster of three mitoribosomes that possibly form a polysome. Scale bar are indicated on (**b**) and (**c**). **e)** The peptide channel of the Chlamydomonas LSU from a solvent view (top) and as well as a cut view (bottom). The mL119 protein is located at the exit of the peptide channel. The C-terminal part of mL119 anchors the protein to the ribosome, while the N-terminal part is exposed to the solvent where it could interact with Oxa1. Orange lines delimit the peptide channel. Ribosomal proteins are depicted as cartoons, and rRNAs are depicted in surface representations in light blue. **f)** The atomic model of the mitoribosome is fitted into the subtomogram average density of the native membrane-bound mitoribosome. The mitoribosome contacts the inner mitochondrial membrane (IMM) at two specific points. These contacts are mediated by two Chlamydomonas-specific proteins, mL113 and mL119, the latter of which is located at the exit of the peptide channel, adjacent to the Oxa1 insertase. The model of the bacterial homolog of Oxa1 is shown for illustration purposes. **g)** Close-up view of the mRNA exit channel. The molecular model is fitted into the subtomogram average, highlighting the presence of an additional unknown density (green) located close to uS1m.

Discussion

Our study describes the structure and composition of the Chlamydomonas mitochondrial ribosome. The cryo-EM reconstructions show that this green alga mitoribosome differs significantly from prokaryotic ribosomes as well as its flowering plant counterpart[47,48]. In both the small and the large subunits, the mitoribosome has acquired several additional r-proteins that significantly reshape this ribosome's architecture. These specific r-proteins combined with the fragmented rRNAs (four pieces in the SSU and nine pieces in the LSU) constitute an extreme case of ribosome divergence, even among the exceptionally diverse mitoribosomes.

One striking feature of the SSU is the presence of two large protuberances on the head and the body. The body protuberance could be assigned to a large insertion in the mitoribosome-specific protein mS45 (Supplementary Fig. 5b), which shows high structural variability between mitoribosomes in different species despite the conservation of its core domain[22]. The head protuberance was poorly resolved in our density map but is most likely composed of long extensions of the head's conserved r-proteins (uS3m, uS10m, mS35). In vascular plant mitoribosomes, the uS3m r-protein was shown to form a similar large protuberance on the SSU head, suggesting a common origin of these protrusions[11]. The roles of these two protuberances is unknown. The position of the body protuberance, close to the mRNA entry channel, might suggest a species-specific mechanism of mRNA recruitment, similar to that in humans mediated by mS39[4,41,46,49]. This protuberance, in conjunction with the additional density observed in the subtomogram average next to bS1m at the mRNA exit channel (Fig. 6g), might point to the existence of specific translation processes in Chlamydomonas. Translation initiation in Chlamydomonas mitochondria shares some features with that of human mitochondria, as the mRNAs lack 5' untranslated regions in both organisms. However, Chlamydomonas most probably has a specific mechanism for translation initiation, as its mitochondrial mRNAs do not have the U-rich motif downstream of the AUG that was proposed to interact with mS39 in humans. Furthermore, mature Chlamydomonas mRNAs have poly-C rich 3' tails that might be required for translation initiation[19].

Another key feature of the SSU is the homotrimeric mS105 (p32) protein forming a torus-shaped protuberance on the back of the SSU head, reminiscent of RACK1 on the cytosolic ribosome[50]. This protein belongs to the MAM33 family, which appears to be eukaryote-specific and is characterized by its quaternary structure: a doughnut-shaped trimer that is highly negatively charged[26,51]. The p32 protein has been the subject of many studies, as its mutations result in severe diseases in humans[25,52–54]. However, despite decades of research, its precise functions remain elusive. Recent studies suggest that MAM33-family proteins might be involved in mitoribosome biogenesis. Indeed, they are linked to the LSU biogenesis in yeast[24], in Trypanosoma, the recent structure of the SSU

"assemblosome" includes a heterotrimeric p22, directly highlighting its role in mitoribosome biogenesis[55,56] and in humans, the protein YBEY forms a complex with p32 and is involved in the SSU biogenesis[23]. We observed that p32 is an integral component of the Chlamydomonas mitoribosome. However, it does not appear to have an obvious function related to the translation process, as it does not bind rRNA and only makes a few contacts with the adjacent r-proteins. Likewise, its downregulation does not impair the accumulation of mitochondrial rRNAs. Taking these results together with the above-mentioned studies, it seems that p32 could act in mitoribosome maturation. Given its overall negative charge, it might serve as a binding platform that scaffolds other factors during ribosome biogenesis. It is unclear why p32 would be kept as a constitutive ribosomal protein in Chlamydomonas and not in other eukaryotes, but this may point to species-specific functions.

One of the most prominent features of Chlamydomonas mitoribosome is its extensively fragmented rRNAs, with four pieces in the SSU and nine pieces in the LSU. It is interesting to mention that Kinetoplastida and Euglenozoa also have fragmented rRNA in their cytosolic ribosomes[57–62]. However, only the LSU rRNA is fragmented, and the fragments are continuous in the genome. Among mitoribosomes, the ciliate mitoribosome also contains LSU and SSU rRNAs that are each split into two pieces, contrasting with the extensive fragmentation observed here with Chlamydomonas[63–65].

It has been proposed that the fragmentation and scrambling of the Chlamydomonas rRNA genes are the result of several mitochondrial genome recombination events between short repeated sequences[31]. We assigned all the previously identified rRNA fragments in the mitoribosome except one, L2b. This fragment is not incorporated into the mature mitoribosome and is thus not an rRNA. Nevertheless, its transcript has reproducibly been found in the total mitochondrial fraction[19,28]. Its function is unclear, but it might be involved in mitochondrial genome maintenance, which involves telomere-like structures in Chlamydomonas, as the L2b sequence is highly similar to both ends of the linear Chlamydomonas mitochondrial genome[66,67]. Alternatively, the observation that the L2b RNA level is decreased in the *mS105* mutant strain as compared to wild-type might point out a function that could be related to mS105 and thus possibly to the mitoribosome or the SSU biogenesis. Conversely, we cannot exclude the possibility that the mS105 protein plays a role outside the mitoribosome and is implicated in mitochondrial genome maintenance *via* an interaction with L2b.

Importantly, we reveal that the L3a rRNA fragment is a degenerated 5S rRNA, which escaped identification because of its highly divergent primary sequence. Even compared to closely related Chlorophytes and Chlorophyceae species, Chlamydomonas L3a is particularly different at the sequence level (Supplementary Fig. 8d). L3a occupies the same position as a classical 5S, but its overall structure, notably the domain α and β

structures, are quite different from other known 5S structures, rendering it one of the most divergent 5S rRNA described to date. Putative highly divergent mitochondrial 5S rRNAs have also been previously identified in various amoebozoan species[68,69]. Given the high divergence of the 5S rRNA in Chlamydomonas, together with the aforementioned studies, a wider phylogenetic distribution of mitochondrial 5S rRNA might be suggested.

The rest of the rRNA fragments form the core of the mitoribosome and are globally conserved, yet reduced. In the ribosome core, these fragments are stabilized by base-pairing with each other. In contrast, on the outer shell of the ribosome, especially in the LSU, the rRNA fragments are stabilized by the Chlamydomonas-specific r-proteins. These proteins are all alpha-helical repeats belonging to nucleic-acid binder families PPR, OPR and mTERF. In our structures, they form highly intertwined interfaces with single- and double-stranded RNA, all involving positive/negative charge interactions. These proteins stabilize the 3' end of rRNA fragments L1, L2a, L5 and L8 by enlacing their single stranded extremities and also contact and stabilize additional rRNA helices via their convex surfaces.

The function of these proteins was investigated by analyzing down-regulation mutants (Fig. 5). All mutants for r-proteins of the large subunit, except the *mL116* mutant, show a diminution of the abundance of rRNA fragments of the LSU, indicating that these r-proteins are important for the stability of the rRNAs, and thus integrity of the mitoribosome. They seem to play a role of chaperones, stabilizing and perhaps contributing to the recognition and recruitment of the different rRNA pieces during assembly. In *mS105,* where the protein does not directly interact with rRNAs, the rRNA levels are almost unaffected. Additionally, in downregulation mutants *mL113* and *mL117* steady-state levels of mitochondria-encoded proteins and active respiratory complexes is decreased, highlighting their importance in translation and impact on mitochondrial metabolism.

Our cryo-ET analysis reveals that Chlamydomonas mitoribosomes are bound to the inner mitochondrial membrane. In animals and most eukaryotes, the mitochondrial genome encodes almost only components of the respiratory chain, which are all membrane-embedded proteins. These proteins are co-translationally inserted into the inner mitochondrial membrane to reduce the probability of inefficient protein aggregation during transport[70]. To facilitate this process, mitoribosomes are consistently found attached to the inner membrane[45,46]. In mammals, the mitoribosome attachment is mediated by a specific r-protein, mL45, located at exit of the peptide channel, which links the ribosome to the main insertase of the inner membrane, Oxa1[42,43]. In yeast, where one of the mitochondria-encoded proteins is soluble[71], the association is mediated by an mL45 homolog, Mba1, which is not an integral constituent of the mitoribosome, and an expansion segment of H96 directly contacting the membrane[13,40,44]. This is most likely also the case in the fungi *N. crassa*[12]. In Chlamydomonas, similarly to mammals, all proteins encoded in the mitochondrial genome are components of the respiratory chain. Therefore, it is not

surprising that the Chlamydomonas mitoribosome would have acquired a specific r-protein to tether translation to Oxa1. Interestingly, the membrane interaction in Chlamydomonas is mediated via two contact points. mL119 forms one contact, and mL113 create a second contact point, directly with the membrane similarly to ES-H96 in yeast. Notably, despite the similar location of the mL113 and ES-H96 contact sites, they are of different molecular nature (protein vs. rRNA) and have been acquired via different evolutionary mechanisms: an expansion of the nuclear genome in case of mL113 vs. the expansion of the mitochondrial gene coding for 23S rRNA in yeast. In light of recent literature suggesting an early expansion of mitoribosomal proteins in eukaryotes[72], this raises the question whether the second contact site displays an isolated case of convergent evolution between green algae and yeast, or whether is a more universal feature of mitoribosomes that was either replaced (yeast) or lost (mammalian mitoribosome) throughout evolution. The fact that membrane association is mediated by different proteins in each organism, yet the Oxa1 contact is conserved, indicates that this interface is particularly critical[40]. In flowering plant mitochondria, which still encode a large number of soluble proteins, accessory factors might recruit mitoribosomes to the membrane, similar to Mba1 in yeast. However, in Tetrahymena, the mitochondrial genome encodes numerous soluble proteins, but the mitoribosome has still acquired a probable permanent anchor to Oxa1, the r-protein mL105[65]. Finally, contrary to mammals where mL45 blocks the peptide channel until the mitoribosome association with the membrane[41,43], or the assembly factor mL71 in kinetoplastids[9], here the peptide channel is not blocked by mL119, which does not suggest an inhibition of translation until the mitoribosome is membrane tethered.

In conclusion, our structural and functional characterization of Chlamydomonas mitoribosome provides a new perspective on mitoribosome evolution and membrane binding. It delivers essential information to the broader questioning of the function and evolution of rRNA and the ribosome. This paves the way for future investigations of mitoribosomes in other species, in particular Apicomplexa such as Plasmodium and Toxoplasma, where fragmented mitochondrial rRNAs also occur[3,73]. Indeed, the structure of the Chlamydomonas mitoribosome demonstrates that despite the extreme fragmentation of rRNAs, the functionally important regions are well preserved. Moreover, it indicates that rRNAs do not have to be covalently continuous if the 3D ribosome structure can be recreated *via* RNA-RNA and RNA-protein interactions. Interestingly, Gray *et al.* proposed that long, covalently continuous conventional rRNAs might derive from short, non-covalently interacting ancestors[20]. The Chlamydomonas mitoribosome might thus represent a relic from an ancestral form of ribosomal RNA organisation.

Overall, the structure reported here provides further insights into the evolution of mitoribosomes and the elaboration of independent strategies to accomplish and regulate translation. Recent work together with this report show how the mitoribosome is truly one

of nature's most eclectic playgrounds for evolving diverse strategies to regulate a fundamental cellular process.

Methods

Chlamydomonas reinhardtii **mitochondria and mitoribosome purification**

Chlamydomonas reinhardtii cell wall-less strain CC-4351 (*cw15–325 arg7–8* mt+) was used for mitochondria purification and transformation. The mitochondrial mutants *dum5*[77] and *dum11*[78] were used as a control for the phenotypic growth analysis in the dark, kindly provided by Dr. Remacle (University of Liège) and respectively annotated on figures as CI- and CIII-. The strains were grown on Tris-Acetate Phosphate (TAP) solid or liquid medium[14], supplemented with 100 µg/ml of arginine when necessary, under continuous white light (50 µE m−2 s−1), or in the dark. Mitochondria were isolated from liquid cell cultures grown up to the exponential phase. Cells were harvested by centrifugation 10 minutes 1000 g, and resuspended in 10 ml ice-cold 25 mM phosphate buffer pH 6.5 containing 6 % PEG 6000, 0.4 % (w/v) bovine serum albumin (BSA), and 0.016 % (w/v) digitonin to a final concentration of $3x10^8$ cells/ml. The suspension was warmed rapidly to 30°C, kept at this temperature for 30 seconds, and cooled to 4°C. Then the broken cells were pelleted at 2500 g and washed with 40 ml of ice-cold 20 mM Hepes-KOH pH 7.2 containing 0.15 M mannitol, 2 mM EDTA, 0.1% (w/v) BSA, and 1 mM $MgCl_2$. After a 2 minutes 1000 g centrifugation, the pellet was resuspended in 2 ml of the same solution, stirred vigorously for 45 seconds, and then 6 ml of 20 mM Hepes-KOH buffer pH 7.2 containing 0.15 M mannitol, 0.8 mM EDTA, and 4 mM $MgCl_2$ were added. Mitochondria were collected at 12000 g for 10 minutes, resuspended in the same last buffer and then loaded on a discontinuous Percoll gradient (13 %/21 %/45 %) in MET buffer (280 mM Mannitol, 10 mM Tris-HCl pH 6.8, 0.5 mM EDTA, and 0.1 % BSA) and centrifuged for 60 minutes at 40000 g. Purified mitochondria were recovered at the 45/21 interface and washed two times in MET buffer by centrifugation at 12000 g for 10 minutes and stored at -80°C.

Mitoribosome purification was conducted as previously[10,11]. In brief, purified mitochondria were re-suspended in Lysis buffer (20 mM HEPES-KOH, pH 7.6, 100 mM KCl, 30 mM $MgCl_2$, 1 mM DTT, 1.6 % Triton X-100, 0.5% n-DDM, supplemented with proteases inhibitors (C0mplete EDTA-free)) to a 1 mg/ml concentration and incubated for 15 min in 4°C. Lysate was clarified by centrifugation at 25.000 *g*, 20 min at 4°C. The supernatant was loaded on a 40% sucrose cushion in Monosome buffer (Lysis buffer without Triton X-100 and 0.1% n-DDM) and centrifuged at 235.000 g, 3h, 4°C. The crude ribosomes pellet was re-suspended in Monosome buffer and loaded on a 10-30 % sucrose gradient in the same buffer and run for 16 h at 65000 g. Fractions corresponding to mitoribosomes were collected, pelleted and

re-suspended in Monosome buffer and analyzed by nanoLC-ESI-MS/MS and cryo-EM (Supplementary Fig. 1).

Grid preparation

For the single particle analyses, 4 µL of the samples at a protein concentration of 1.5 µg/µl was applied onto Quantifoil R2/2 300-mesh holey carbon grid, coated with thin home-made continuous carbon film and glow-discharged (2.5 mA for 20 sec). The sample was incubated on the grid for 30 sec and then blotted with filter paper for 2 sec in a temperature and humidity controlled Vitrobot Mark IV (T = 4°C, humidity 100 %, blot force 5) followed by vitrification in liquid ethane.

Cryo-electron microscopy data collection

The single particle data collection was performed on a Talos Arctica instrument (Thermofisher Company) at 200 kV using the SerialEM software for automated data acquisition. Data were collected at a nominal underfocus of -0.5 to -2.5 µm at a magnification of 36,000 X yielding a pixel size of 1.13 Å for the SSU and 45,000 X yielding a pixel size of 0.9 Å for the LSU. Micrographs were recorded as movie stack on a K2 direct electron detector (GATAN Company), each movie stack were fractionated into 65 frames for a total exposure of 6.5 sec corresponding to an electron dose of 45 $\bar{e}/Å^2$.

Electron microscopy image processing

Drift and gain correction and dose weighting were performed using MotionCorr2[80]. A dose weighted average image of the whole stack was used to determine the contrast transfer function with the software Gctf[81]. The following process has been achieved using RELION 3.0[75]. Initial analyses were performed in CryoSPARC[82] to asses sample composition and to generate *ab-initio* cryo-EM map. After reference-free 2D classification, for the LSU 346,994 particles were extracted and used for 3D classification into 6 classes (Supplementary Fig. 2). *Ab-initio* cryo-EM reconstruction generated in CryoSPARC was low-pass filtered to 30 Å, and used as an initial reference for 3D classification. 2 subclass depicting high-resolution features was selected for refinement with 101,291 particles. After Bayesian polishing, the LSU reconstruction reached 3.00 Å resolution. For the SSU reconstruction a similar workflow was applied. After 2D classification 445,469 particles were extracted and used for 3D classification into 6 classes. 1 subclass depicting high-resolution features was selected for refinement with 40,131 particles. After focus refinement using masks for the head and body of the small subunit, the SSU reconstruction reached a resolution of 4.19 Å for the body and 4.47 Å for the head. Determination of the local resolution of the final density map was performed using ResMap[74].

Structure building and model refinement

The atomic model of the LSU of *C. reinhardtii* was built into the high-resolution maps using Coot, Phenix and Chimera. Atomic models from *E. coli* (PDB: 5KCR [https://www.rcsb.org/structure/5KCR]) and *A. thaliana* mitoribosome (PDB: 6XYW [https://www.rcsb.org/structure/6XYW]) were used as starting points for protein identification and modelisation as well as rRNA modelisation. The online SWISS-MODEL[83] as well as AlphaFold[27] through the ColabFold service[84] were used to generate initial models for bacterial and mitochondria conserved r-proteins. Models were then rigid body fitted to the density in Chimera[85] and all subsequent modeling was done in Coot[86]. Extensions were built has polyalanine and mutated to the adequate sequences. Chlamydomonas-specific proteins for which no model could be generated were first built entirely as polyalanine, then the sequence-from-map PHENIX tool[76] was used to identify each of the proteins, and the correct sequences were placed in the densities. For the SSU, due to the lower resolution in comparison to the LSU, all extensions of the homology models were built as polyalanine and unknown densities were built as Ala residues. For refinement, a combination of regularization and real-space refine was performed in Coot for each proteins. The global atomic model was then subjected to real space refinement cycles using *phenix.real_space_refine* PHENIX[76] function, during which protein secondary structures, Ramachandran and side chain rotamer restraints were applied. Several rounds of refinement (manual in Coot and automated using the *phenix.real_space_refine*) were performed to obtain the final models, which were validated using the built-in validation tool of PHENIX, based on MolProbity. Refinement and validation statistics are summarized in Supplementary Table 2.

Cell Vitrification and Cryo-FIB Milling

For FIB-milling, *Chlamydomonas reinhardtii* mat3-4cells (strain CC-3994)[87], which exhibit superior vitrification due to their small size, were used. They were acquired from the Chlamydomonas Resource Center, University of Minnesota, St. Paul. Cells were grown until mid-log phase in Tris-acetate-phosphate (TAP) medium under constant light exposure and bubbling with normal atmosphere. Vitrification and FIB sample preparation were performed as previously described[88,89]. Using a Vitrobot Mark 4 (FEI), cells in suspension (4 µl of ~1,000 cells per µl) were blotted onto R2/1 carbon-coated 200-mesh copper grids (Quantifoil Micro Tools) and plunge frozen in a liquid ethane/propane mixture. Grids were then mounted into Autogrid supports (FEI) and transferred into either a FEI Scios or FEI Quanta dual-beam FIB/SEM instrument. The grids were coated with an organometallic platinum layer by the gas injection system (FEI), and cells were thinned from both sides with a gallium ion beam to a final thickness of ~100–200 nm.

Cryo-electron tomography data acquisition

Cellular tomograms were acquired on a 300 kV Titan Krios microscope (FEI), equipped with a Gatan post-column energy filter (968 Quantum) and a direct detector camera (K2 summit, Gatan) operated in movie mode at 12 frames per second. Tilt series were recorded using SerialEM software[90] with 2° tilt increments from −60° to +60° (in two halves separated at either 0° or −20°), an object pixel size of 3.42 Å, a defocus of −4 to −5.5 µm, and a total accumulated dose of <100 e−/Å.

Cryo-electron tomography data processing

Movies from the K2 detector were motion corrected with MotionCor2[80]. Using IMOD software, tilt series were aligned with patch-tracking, and tomograms were reconstructed with weighted back projection. Out of ~130 tomograms, 47 tomograms containing mitochondria were selected. The following workflow is described in Supplementary Fig. 3. An initial structure of the *C. reinhardtii* mitoribosome was obtained by manually picking 103 mitoribosomes from 27 tomograms following template-free alignment by spherical harmonics[91]. The initial map was then used as a template for automated template matching on 47 tomograms with a voxel size of 2.1 nm using PyTOM[92]. To reduce-false positives, the highest correlation peaks of the resulting 6-D cross-correlation function localized in the mitochondrial matrix were manually inspected in UCSF Chimera[85], and a set of 222 subvolumes from 27 tomograms was obtained. The subvolumes were reconstructed at a voxel size of 6.84 Å, aligned using PyTOM's real-space refinement, and subjected to 1 round of classification with a mask encompassing the membrane region. This yielded a class of 73 mitoribosomes with a clear membrane-density that was subjected to one more round of real-space refinement in PyTOM. For the resulting average, a resolution of 31.6 Å (large ribosomal subunit) and 31.5 Å (small ribosomal subunit) was determined by fourier-shell cross-resolution of the two map against the maps obtained by single particle analysis (FSC = 0.33). For the localization of ATP synthases, an initial structure of the *C. reinhardtii* ATP synthase was obtained by manually picking 417 subvolumes from four tomograms and aligning them using spherical harmonics. The obtained map was used as template for automated template-matching on tomograms with a voxel size of 2.1 nm using Pytom, and the highest correlation-peaks were then manually inspected in Chimera to remove false-positives. Cytosolic 80S ribosomes were localized in one tomogram by filtering EMDB-1780[93] to 40 Å and using it as a template for template matching on the deconvolved tomogram (tom_deconv; https://github.com/dtegunov/tom_deconv) using Pytom. Subvolumes were extracted for the 2,100 highest correlation peaks, of which 1,700 subvolumes were classified as ribosomes by unsupervised, autofocused 3D classification[94].

Proteomic analyses of *C. reinhardtii* mitoribosome composition

Mass spectrometry analyses of the total, mitochondrial and ribosomal fractions of *C. reinhardtii* were done at the Strasbourg-Esplanade proteomic platform and performed as previously[10]. In brief, proteins were trypsin digested, mass spectrometry analyses and quantitative proteomics were carried out by nanoLC-ESI-MS/MS analysis on a QExactive+ (Thermo) mass spectrometer. Data were searched against the UniProtKB (Swissprot+trEMBL) database restricted to the *C. reinhardtii* taxonomy with a target-decoy strategy (UniProtKB release 2020_03, taxon 3055, 31246 forward protein sequences), Proteins were validated respecting FDR<1% (False Discovery Rate) and quantitative label-free analysis was performed through in-house bioinformatics pipelines.

Artificial miRNA *C. reinhardtii* strain generation and analyses

Artificial microRNAs constructs were created according to Molnar, A. *et al.* [39] as follow: The oligonucleotides were designed using the WMD3 Web MicroRNA Designer software v3.2 [http://wmd3.weigelworld.org/cgi-bin/webapp.cgi] and genome release Chlamydomonas CDS reinhardtii 281 v5.6.cds (Phytozome) (Supplementary Table 3). The oligonucleotides were annealed, phosphorylated, and ligated into a *SpeI*-digested pChlamiRNA2 containing the ARG7 gene as a selection marker. The resulting plasmids were linearized and transformed into Chlamydomonas CC-4351 strain by the Neon® Transfection System (LifeTechnologies) according to the GeneArt® MAX Efficiency® Transformation protocol for Algae (LifeTechnologies Cat#A24229). Cells with integrated plasmid were selected on TAP plates without arginine. Colonies (16 to 48 depending on the transformation) were picked to grown to logarithmic phase on liquid TAP medium. They were then spotted on two identical TAP plates to test their capacity to grow in the dark. One plate was placed in a mixotrophic condition (light + acetate) for 5-7 days, and the other one in a heterotrophic condition (dark + acetate), for 10-15 days. For the dilution series, cells were grown for 3-4 days on TAP plates and were resuspended in 2 ml of liquid TAP medium. The cell density was measured spectrophotometrically at OD750 and diluted to an OD750 = 1.5. This normalized suspension was used as the starting material (set to 1) for making three serial 5-fold dilutions (2.10^{-1}, 4.10^{-2}, and 8.10^{-3}). A volume of 10 µl for each dilution was then spotted on two identical TAP plates.

rRNA analysis by RNA sequencing

The RNAs were prepared from cells using TRI Reagent® (Molecular Research Center) according to the manufacturer's instructions.

For northern blots, 1 µg of total, mitochondrial and mitoribosome fraction RNA, were separated on 7M Urea - 8% polyacrylamide gel, transferred onto Amersham Hybond™-N+

membrane (GE Healthcare Cat#RPN203B) and hybridized to radiolabelled oligonucleotide probes (Supplementary Table 3) in 6 x SSC, 0.5 % SDS at 45°C. Washing conditions were: 2 times 10 min in 2 x SSC and 1 time 30 min in 2 x SSC, 0.1 % SDS at the hybridization temperature. For each specific probe, the signal was detected with the Amersham Typhoon laser scanner (Amersham).

For the quantitative real-time RT-PCR analyses, RNAs were treated with RQ1 RNase-Free DNase (Promega Cat#M6101) according to Promega's protocol, using 0.2 U/µg of RNA. To obtain cDNA, reverse transcription assays were performed according to the manufacturer's instructions with 2,5 µg of total RNA in the presence of 5 µM of oligo(dT) primer (Supplementary Table 3) and 25 ng/µl of Random Primers (Promega Cat#C118A) using the SuperScript™ IV Reverse Transcriptase (Invitrogen Cat#18090010). The RT-qPCR amplification was carried out with the dsDNA-specific dye Takyon™ SYBR® 2X qPCR Mastermix Blue (Eurogentec Cat#UF-FSMT-B0701) and monitored in real-time with a LightCycler 480 instrument (Roche). The primers used are listed in (Supplementary Table 3). The delta-delta Ct method was used to calculate the relative RNA abundance with respect to the geometric mean of two RNA references *MAA7* and *CYN19-3*[95].

For the RNA sequencing, the p204 library was built with total mitochondrial RNA. The RNA was first chemically fragmented (4 min) and then enzymatically treated with Antarctic Phosphatase (NEB#M0289S) and T4 Polynucleotide Kinase (NEB#M0201S). Library preparation was done according to the TruSeq Small RNA Sample Preparation Guide #15004197 Rev. F February 2014. The library was sequenced on the Illumina MiSeq sequencer in a paired-end mode of 2X75 nt reads. The NGS192-small library was built with the mitoribosome fraction. The RNA was also enzymatically treated with Antarctic Phosphatase and T4 Polynucleotide Kinase. The library was then constructed with the NEBNext multiplex small RNA Library set for Illumina reference E7580 following the manufacturer's instructions. Following PCR amplification, a size selection was performed on a 6 % TBE gel to recover the 160-350 bp PCR fragments for sequencing. The NGS192-total library was prepared according to the Truseq Stranded Total RNA with Ribozero Plant kit, starting from the first-strand cDNA synthesis step and omitting the two first depletion and fragmentation steps. The library was sequenced on the Illumina MiSeq sequencer in a paired-end mode of 2X110 nt reads. Both libraries were sequenced at the IBMP platform. The reads were mapped to the Chlamydomonas mitochondrial genome (EU306622) using Bowtie2 version 2.4.1 with the following options --end-to-end --very-sensitive -N 0 -L 22. Alignments were displayed with the Integrative Genomics Viewer (IGV) with the bigWig format.

Protein analyses

The Chlamydomonas crude total membrane fractions were obtained according to Remacle, C. *et al*[96] as follow: Chlamydomonas cells TAP liquid cultures were collected and resuspended to 2-1.6x10^8 cells/ml in MET buffer (280 mM mannitol, 0.5 mM EDTA, 10 mM Tris-HCl pH 7) with 1x cOmplete™ Protease Inhibitor Cocktail and then disrupted by sonication (four times 30 sec of sonication and 30 sec of pause; Bioruptor® Pico, Diagenode). The suspension was centrifugated 10 min at 500 g, followed by 4 min at 3000 g) and the protein content of the supernatant was determined by the Bradford method. Equal amounts of protein were separated using 15% SDS−polyacrylamide gel electrophoresis (PAGE), and transferred to a 0.45 µm PVDF membrane (Immobilon®-P Transfer Membrane; Merck Millipore Cat.#IPVH00010). Specific antibodies were used in immunoblotting and were detected using chemiluminescence (Clarity Western ECL Substrate, Bio-Rad). We used rabbit sera obtained against *Chlamydomonas reinhardtii* mitochondrial-encoded subunits complex I, Nad4 (1:1000) and Nad6 (1:100), nuclear-encoded sub-unit complex I, NUO7 (1:2000), and the nuclear-encoded mitochondrial protein VDACI (1:25000). The expected / apparent molecular weight are as follow: 49 kDa/50-55 kDa for Nad4, 18 kDa/18 kDa for Nad6, 49 kDa/38 kDa for NUO7 and 28 kDa/28 kDa for VDACI. Blue native polyacrylamide gel electrophoresis (BN-PAGE) analyses were conducted according to Schägger et *al.* [97] as follow: the crude total membrane fractions were prepared as above with an additional centrifugation at high speed (27000 *g* for 15 min) and the final pellet was suspended in ACA buffer (375 mM 6-aminohexanoic acid, 25 mM Bis-Tris, pH 7, and, 250 mM EDTA). 0.5 mg of crude total membrane were first solubilized in the presence of 1,5 % (w/v) n-dodecyl-β-D-maltoside and then centrifuged for 40 min 14200 g at 4°C to remove insoluble matters. 0.65 % (w/v) of coomassie serva blue G was then added to the supernatant prior to separation by electrophoresis on a 5% to 12% polyacrylamide gradient BN gel. In-gel detection of Complex I (NADH dehydrogenase) activity was performed using a 100 mM Tris-HCl pH 7.4 buffer containing 200 µM NADH and 0.2 % nitro blue tetrazolium (NBT). In-gel detection of Complex IV (cytochrome *c* oxydase) activity was performed using a 10 mM MOPS-KOH pH 7.4 buffer containing 7.5 % saccharose, 19 U/ml catalase from bovine liver, 0.1 % cytochrome *c* and 0.01 % 3,3'-diaminobenzidine (DAB).

Figure preparation and data visualization

For the tomography reconstruction, segmentation of ER, mitochondrial and chloroplast membranes was done using EMAN's convolutional neural network for automated annotation[98]. Using the TOM toolbox in matlab[99], the averages of the cytoribosomes, mitoribosomes and ATP synthases were pasted into the tomogram at the refined coordinates and angles determined by subtomogram analysis. Figures featuring cryo-EM densities as well as atomic models were visualized with UCSF ChimeraX[100] and Chimera[85].

Statistical information

Data are presented as mean values ± SD (standard deviation), calculated using Microsoft Excel version 16.43 and GraphPad Prism 8 version 8.4. The *p-value* < 0.05 was considered the threshold for statistical significance. The *p-value* significance intervals (*) are provided within each figure legend, together with the statistical test performed for each experiment: the two-tailed Mann-Whitney. For Fig. 5b-c, derived statistics correspond to the analysis of mean values of n=3 biological replicates. Statistics detailed data (means, standard deviation, n values, exact p values) are provided in the Source Data file.

Data Availability

The cryo-EM maps of *C. reinhardtii* mitoribosome have been deposited at the Electron Microscopy Data Bank (EMDB): EMD-13480 [https://www.emdataresource.org/EMD-13480] for the LSU, EMD-13481[https://www.emdataresource.org/EMD-13481] for the head of the SSU, EMD-13477 [https://www.emdataresource.org/EMD-13477] for the body of the SSU and EMD-13578 [https://www.emdataresource.org/EMD-13578] for the subtomogram averaging of the whole ribosome. The corresponding atomic models have been deposited in the Protein Data Bank (PDB) under the accession 7PKT [https://www.rcsb.org/structure/7PKT] for the LSU and 7PKQ [https://www.rcsb.org/structure/7PKQ] for the SSU. Mass spectrometric data have been deposited to the ProteomeXchange Consortium via the PRIDE partner repository with the dataset identifier PXD024708 and 10.6019/PXD024708 [https://www.ebi.ac.uk/pride/archive/projects/PXD024708] . RNAseq data were deposited in the NCBI Gene Expression Omnibus under accession number GSE171125 [https://www.ncbi.nlm.nih.gov/geo/query/acc.cgi?acc=GSE171125]. The raw data underlying figures on this study are provided as a Source Data file.

References

1. Eme, L., Spang, A., Lombard, J., Stairs, C. W. & Ettema, T. J. G. Archaea and the origin of eukaryotes. *Nat. Rev. Microbiol.* **15**, 711–723 (2017).
2. Gray, M. W. Mitochondrial Evolution. *Cold Spring Harb. Perspect. Biol.* **4**, a011403 (2012).
3. Waltz, F. & Giegé, P. Striking Diversity of Mitochondria-Specific Translation Processes across Eukaryotes. *Trends Biochem. Sci.* **45**, 149–162 (2020).
4. Kummer, E. & Ban, N. Mechanisms and regulation of protein synthesis in mitochondria. *Nat. Rev. Mol. Cell Biol.* 1–19 (2021) doi:10.1038/s41580-021-00332-2.
5. Martijn, J., Vosseberg, J., Guy, L., Offre, P. & Ettema, T. J. G. Deep mitochondrial origin

outside the sampled alphaproteobacteria. *Nature* **557**, 101–105 (2018).
6. Amunts, A., Brown, A., Toots, J., Scheres, S. H. W. & Ramakrishnan, V. The structure of the human mitochondrial ribosome. *Science (80-.).* **348**, 95–98 (2015).
7. Greber, B. J. *et al.* The complete structure of the 55S mammalian mitochondrial ribosome. *Science (80-.).* **348**, 303–308 (2015).
8. Ramrath, D. J. F. *et al.* Evolutionary shift toward protein-based architecture in trypanosomal mitochondrial ribosomes. *Science (80-.).* **362**, eaau7735 (2018).
9. Soufari, H. *et al.* Structure of the mature kinetoplastids mitoribosome and insights into its large subunit biogenesis. *Proc. Natl. Acad. Sci.* **117**, 29851–29861 (2020).
10. Waltz, F. *et al.* Small is big in Arabidopsis mitochondrial ribosome. *Nat. Plants* **5**, 106–117 (2019).
11. Waltz, F., Soufari, H., Bochler, A., Giegé, P. & Hashem, Y. Cryo-EM structure of the RNA-rich plant mitochondrial ribosome. *Nat. Plants* **6**, 377–383 (2020).
12. Itoh, Y., Naschberger, A., Mortezaei, N., Herrmann, J. M. & Amunts, A. Analysis of translating mitoribosome reveals functional characteristics of translation in mitochondria of fungi. *Nat. Commun.* **11**, 5187 (2020).
13. Desai, N., Brown, A., Amunts, A. & Ramakrishnan, V. The structure of the yeast mitochondrial ribosome. *Science (80-.).* **355**, 528–531 (2017).
14. Harris, E. H., Stern, D. B. & Witman, G. B. The Chlamydomonas Sourcebook. in *The Chlamydomonas Sourcebook* vols 1–3 iii (Elsevier, 2009).
15. Remacle, C., Cardol, P., Coosemans, N., Gaisne, M. & Bonnefoy, N. High-efficiency biolistic transformation of Chlamydomonas mitochondria can be used to insert mutations in complex I genes. *Proc. Natl. Acad. Sci.* **103**, 4771–4776 (2006).
16. Salinas, T., Larosa, V., Cardol, P., Maréchal-Drouard, L. & Remacle, C. Respiratory-deficient mutants of the unicellular green alga Chlamydomonas: A review. *Biochimie* **100**, 207–218 (2014).
17. Boer, P. H. & Gray, M. W. Scrambled ribosomal RNA gene pieces in *Chlamydomonas reinhardtii* mitochondrial DNA. *Cell* **55**, 399–411 (1988).
18. Denovan-Wright, E. M. & Lee, R. W. Evidence that the fragmented ribosomal RNAs of Chlamydomonas mitochondria are associated with ribosomes. *FEBS Lett.* **370**, 222–226 (1995).
19. Salinas-Giegé, T. *et al.* Polycytidylation of mitochondrial mRNAs in *Chlamydomonas reinhardtii*. *Nucleic Acids Res.* **45**, 12963–12973 (2017).
20. Gray, M. W. & Gopalan, V. Piece by piece: Building a ribozyme. *J. Biol. Chem.* **295**, 2313–2323 (2020).
21. Ban, N. *et al.* A new system for naming ribosomal proteins. *Current Opinion in Structural Biology* (2014) doi:10.1016/j.sbi.2014.01.002.
22. Valach, M. *et al.* An Unexpectedly Complex Mitoribosome in Andalucia godoyi , a Protist with the Most Bacteria-like Mitochondrial Genome. *Mol. Biol. Evol.* **38**, 788–804 (2021).
23. Summer, S. *et al.* YBEY is an essential biogenesis factor for mitochondrial ribosomes. *Nucleic Acids Res.* **48**, 9762–9786 (2020).
24. Hillman, G. A. & Henry, M. F. The yeast protein Mam33 functions in the assembly of the mitochondrial ribosome. *J. Biol. Chem.* **294**, 9813–9829 (2019).
25. Yagi, M. *et al.* p32/gC1qR is indispensable for fetal development and mitochondrial translation: importance of its RNA-binding ability. *Nucleic Acids Res.* **40**, 9717–9737 (2012).
26. Jiang, J., Zhang, Y., Krainer, A. R. & Xu, R.-M. Crystal structure of human p32, a doughnut-shaped acidic mitochondrial matrix protein. *Proc. Natl. Acad. Sci.* **96**, 3572–3577 (1999).
27. Jumper, J. *et al.* Highly accurate protein structure prediction with AlphaFold. *Nature* **596**, 583–589 (2021).
28. Wobbe, L. & Nixon, P. J. The mTERF protein MOC1 terminates mitochondrial DNA transcription in the unicellular green alga *Chlamydomonas reinhardtii*. *Nucleic Acids Res.* **41**,

6553–6567 (2013).
29. Gallaher, S. D. *et al.* High-throughput sequencing of the chloroplast and mitochondrion of *Chlamydomonas reinhardtii* to generate improved de novo assemblies, analyze expression patterns and transcript speciation, and evaluate diversity among laboratory strains and wild isolates. *Plant J.* **93**, 545–565 (2018).
30. Petrov, A. S. *et al.* Structural Patching Fosters Divergence of Mitochondrial Ribosomes. *Mol. Biol. Evol.* **36**, 207–219 (2019).
31. Nedelcu, A. M. Fragmented and scrambled mitochondrial ribosomal RNA coding regions among green algae: a model for their origin and evolution. *Mol. Biol. Evol.* **14**, 506–17 (1997).
32. Hammani, K. *et al.* Helical repeats modular proteins are major players for organelle gene expression. *Biochimie* **100**, 141–150 (2014).
33. Barkan, A. & Small, I. Pentatricopeptide repeat proteins in plants. *Annu. Rev. Plant Biol.* **65**, 415–42 (2014).
34. Rahire, M., Laroche, F., Cerutti, L. & Rochaix, J.-D. Identification of an OPR protein involved in the translation initiation of the PsaB subunit of photosystem I. *Plant J.* **72**, 652–661 (2012).
35. Eberhard, S. *et al.* Dual functions of the nucleus-encoded factor TDA1 in trapping and translation activation of atpA transcripts in *Chlamydomonas reinhardtii* chloroplasts. *Plant J.* **67**, 1055–1066 (2011).
36. Wang, F. *et al.* Two Chlamydomonas OPR proteins stabilize chloroplast mRNAs encoding small subunits of photosystem II and cytochrome b 6 f. *Plant J.* **82**, 861–873 (2015).
37. Boulouis, A. *et al.* Spontaneous Dominant Mutations in Chlamydomonas Highlight Ongoing Evolution by Gene Diversification. *Plant Cell* **27**, 984–1001 (2015).
38. Li, X. *et al.* A genome-wide algal mutant library and functional screen identifies genes required for eukaryotic photosynthesis. *Nat. Genet.* **51**, 627–635 (2019).
39. Molnar, A. *et al.* Highly specific gene silencing by artificial microRNAs in the unicellular alga *Chlamydomonas reinhardtii*. *Plant J.* **58**, 165–174 (2009).
40. Ott, M. & Herrmann, J. M. Co-translational membrane insertion of mitochondrially encoded proteins. *Biochim. Biophys. Acta - Mol. Cell Res.* **1803**, 767–775 (2010).
41. Kummer, E. *et al.* Unique features of mammalian mitochondrial translation initiation revealed by cryo-EM. *Nature* **560**, 263–267 (2018).
42. Desai, N. *et al.* Elongational stalling activates mitoribosome-associated quality control. *Science (80-.).* **370**, 1105–1110 (2020).
43. Itoh, Y. *et al.* Mechanism of membrane-tethered mitochondrial protein synthesis. *Science (80-.).* **371**, 846–849 (2021).
44. Ott, M. *et al.* Mba1, a membrane-associated ribosome receptor in mitochondria. *EMBO J.* **25**, 1603–1610 (2006).
45. Pfeffer, S., Woellhaf, M. W., Herrmann, J. M. & Förster, F. Organization of the mitochondrial translation machinery studied in situ by cryoelectron tomography. *Nat. Commun.* **6**, 6019 (2015).
46. Englmeier, R., Pfeffer, S. & Förster, F. Structure of the Human Mitochondrial Ribosome Studied In Situ by Cryoelectron Tomography. *Structure* **25**, 1574-1581.e2 (2017).
47. Waltz, F., Corre, N., Hashem, Y. & Giegé, P. Specificities of the plant mitochondrial translation apparatus. *Mitochondrion* **53**, 30–37 (2020).
48. Tomal, A., Kwasniak-Owczarek, M. & Janska, H. An Update on Mitochondrial Ribosome Biology: The Plant Mitoribosome in the Spotlight. *Cells* **8**, 1562 (2019).
49. Aibara, S., Singh, V., Modelska, A. & Amunts, A. Structural basis of mitochondrial translation. *Elife* **9**, 1–17 (2020).
50. Johnson, A. G. *et al.* RACK1 on and off the ribosome. *RNA* **25**, 881–895 (2019).
51. Seytter, T., Lottspeich, F., Neupert, W. & Schwarz, E. Mam33p, an oligomeric, acidic protein

in the mitochondrial matrix of Saccharomyces cerevisiae is related to the human complement receptor gC1q-R. *Yeast* **14**, 303–310 (1998).
52. Saha, P. & Datta, K. Multi-functional, multicompartmental hyaluronan-binding protein 1 (HABP1/p32/gC1qR): implication in cancer progression and metastasis. *Oncotarget* **9**, 10784–10807 (2018).
53. Hu, M. *et al.* p32 protein levels are integral to mitochondrial and endoplasmic reticulum morphology, cell metabolism and survival. *Biochem. J.* **453**, 381–391 (2013).
54. Fogal, V. *et al.* Mitochondrial p32 Protein Is a Critical Regulator of Tumor Metabolism via Maintenance of Oxidative Phosphorylation. *Mol. Cell. Biol.* **30**, 1303–1318 (2010).
55. Saurer, M. *et al.* Mitoribosomal small subunit biogenesis in trypanosomes involves an extensive assembly machinery. *Science (80-.).* **365**, 1144–1149 (2019).
56. Sprehe, M., Fisk, J. C., McEvoy, S. M., Read, L. K. & Schumacher, M. A. Structure of the Trypanosoma brucei p22 Protein, a Cytochrome Oxidase Subunit II-specific RNA-editing Accessory Factor*. *J. Biol. Chem.* **285**, 18899–18908 (2010).
57. Matzov, D. *et al.* Cryo-EM structure of the highly atypical cytoplasmic ribosome of Euglena gracilis. *Nucleic Acids Res.* **48**, 11750–11761 (2020).
58. Hashem, Y. *et al.* High-resolution cryo-electron microscopy structure of the Trypanosoma brucei ribosome. *Nature* **494**, 385–389 (2013).
59. Greenwood, S. J. & Gray, M. W. Processing of precursor rRNA in Euglena gracilis: Identification of intermediates in the pathway to a highly fragmented large subunit rRNA. *Biochim. Biophys. Acta - Gene Struct. Expr.* **1443**, 128–138 (1998).
60. Schnare, M. N. & Gray, M. W. Sixteen discrete RNA components in the cytoplasmic ribosome of Euglena gracilis. *J. Mol. Biol.* **215**, 73–83 (1990).
61. Gray, M. W. Unusual pattern of ribonucleic acid components in the ribosome of Crithidia fasciculata, a trypanosomatid protozoan. *Mol. Cell. Biol.* **1**, 347–357 (1981).
62. Spencer, D. F., Collings, J. C., Schnare, M. N. & Gray, M. W. Multiple spacer sequences in the nuclear large subunit ribosomal RNA gene of Crithidia fasciculata. *EMBO J.* **6**, 1063–1071 (1987).
63. Schnare, M. N., Heinonen, T. Y. K., Young, P. G. & Gray, M. W. A discontinuous small subunit ribosomal RNA in Tetrahymena pyriformis mitochondria. *J. Biol. Chem.* **261**, 5187–5193 (1986).
64. Heinonen, T. Y., Schnare, M. N., Young, P. G. & Gray, M. W. Rearranged coding segments, separated by a transfer RNA gene, specify the two parts of a discontinuous large subunit ribosomal RNA in Tetrahymena pyriformis mitochondria. *J. Biol. Chem.* **262**, 2879–2887 (1987).
65. Tobiasson, V. & Amunts, A. Ciliate mitoribosome illuminates evolutionary steps of mitochondrial translation. *Elife* **9**, (2020).
66. Smith, D. R. & Craig, R. J. Does mitochondrial DNA replication in Chlamydomonas require a reverse transcriptase? *New Phytol.* **229**, 1192–1195 (2021).
67. Smith, D. R., Hua, J. & Lee, R. W. Evolution of linear mitochondrial DNA in three known lineages of Polytomella. *Curr. Genet.* **56**, 427–438 (2010).
68. Bullerwell, C. E., Schnare, M. N. & Gray, M. W. Discovery and characterization of Acanthamoeba castellanii mitochondrial 5S rRNA. *RNA* **9**, 287–92 (2003).
69. Bullerwell, C. E. *et al.* Abundant 5S rRNA-Like Transcripts Encoded by the Mitochondrial Genome in Amoebozoa. *Eukaryot. Cell* **9**, 762–773 (2010).
70. Ott, M., Amunts, A. & Brown, A. Organization and Regulation of Mitochondrial Protein Synthesis. *Annu. Rev. Biochem.* **85**, 77–101 (2016).
71. Freel, K. C., Friedrich, A. & Schacherer, J. Mitochondrial genome evolution in yeasts: an all-encompassing view. *FEMS Yeast Res.* **15**, 23 (2015).
72. Gray, M. W. *et al.* The draft nuclear genome sequence and predicted mitochondrial proteome of Andalucia godoyi, a protist with the most gene-rich and bacteria-like

mitochondrial genome. *BMC Biol.* **18**, 1–35 (2020).
73. Feagin, J. E. *et al.* The Fragmented Mitochondrial Ribosomal RNAs of Plasmodium falciparum. *PLoS One* **7**, e38320 (2012).
74. Kucukelbir, A., Sigworth, F. J. & Tagare, H. D. Quantifying the local resolution of cryo-EM density maps. *Nat. Methods* **11**, 63–65 (2014).
75. Zivanov, J. *et al.* New tools for automated high-resolution cryo-EM structure determination in RELION-3. *Elife* **7**, (2018).
76. Liebschner, D. *et al.* Macromolecular structure determination using X-rays, neutrons and electrons: recent developments in Phenix. *Acta Crystallogr. Sect. D Struct. Biol.* **75**, 861–877 (2019).
77. Cardol, P. *et al.* Photosynthesis and State Transitions in Mitochondrial Mutants of *Chlamydomonas reinhardtii* Affected in Respiration. *Plant Physiol.* **133**, 2010–2020 (2003).
78. Dorthu, M.-P. *et al.* Biochemical, genetic and molecular characterization of new respiratory-deficient mutants in *Chlamydomonas reinhardtii*. *Plant Mol. Biol.* **18**, 759–772 (1992).
79. Salinas, T. *et al.* Co-Evolution of Mitochondrial tRNA Import and Codon Usage Determines Translational Efficiency in the Green Alga Chlamydomonas. *PLoS Genet.* **8**, e1002946 (2012).
80. Zheng, S. Q. *et al.* MotionCor2: anisotropic correction of beam-induced motion for improved cryo-electron microscopy. *Nat. Methods* **14**, 331–332 (2017).
81. Zhang, K. Gctf: Real-time CTF determination and correction. *J. Struct. Biol.* **193**, 1–12 (2016).
82. Punjani, A., Rubinstein, J. L., Fleet, D. J. & Brubaker, M. A. cryoSPARC: algorithms for rapid unsupervised cryo-EM structure determination. *Nat. Methods* **14**, 290–296 (2017).
83. Waterhouse, A. *et al.* SWISS-MODEL: homology modelling of protein structures and complexes. *Nucleic Acids Res.* **46**, W296–W303 (2018).
84. Mirdita, M., Ovchinnikov, S. & Steinegger, M. ColabFold - Making protein folding accessible to all. *bioRxiv* 2021.08.15.456425 (2021) doi:10.1101/2021.08.15.456425.
85. Pettersen, E. F. *et al.* UCSF Chimera--a visualization system for exploratory research and analysis. *J. Comput. Chem.* **25**, 1605–12 (2004).
86. Emsley, P., Lohkamp, B., Scott, W. G. & Cowtan, K. Features and development of Coot. *Acta Crystallogr. Sect. D Biol. Crystallogr.* **66**, 486–501 (2010).
87. Umen, J. G. & Goodenough, U. W. Control of cell division by a retinoblastoma protein homolog in Chlamydomonas. *Genes Dev.* **15**, 1652–1661 (2001).
88. Schaffer, M. *et al.* Optimized cryo-focused ion beam sample preparation aimed at in situ structural studies of membrane proteins. *J. Struct. Biol.* **197**, 73–82 (2017).
89. Schaffer, M. *et al.* Cryo-focused Ion Beam Sample Preparation for Imaging Vitreous Cells by Cryo-electron Tomography. *BIO-PROTOCOL* **5**, (2015).
90. Mastronarde, D. N. Automated electron microscope tomography using robust prediction of specimen movements. *J. Struct. Biol.* **152**, 36–51 (2005).
91. Chen, Y., Pfeffer, S., Hrabe, T., Schuller, J. M. & Förster, F. Fast and accurate reference-free alignment of subtomograms. *J. Struct. Biol.* **182**, 235–245 (2013).
92. Hrabe, T. *et al.* PyTom: A python-based toolbox for localization of macromolecules in cryo-electron tomograms and subtomogram analysis. *J. Struct. Biol.* **178**, 177–188 (2012).
93. Armache, J.-P. *et al.* Localization of eukaryote-specific ribosomal proteins in a 5.5-A cryo-EM map of the 80S eukaryotic ribosome. *Proc. Natl. Acad. Sci.* **107**, 19754–19759 (2010).
94. Chen, Y., Pfeffer, S., Fernández, J. J., Sorzano, C. O. S. & Förster, F. Autofocused 3D Classification of Cryoelectron Subtomograms. *Structure* **22**, 1528–1537 (2014).
95. Livak, K. J. & Schmittgen, T. D. Analysis of Relative Gene Expression Data Using Real-Time Quantitative PCR and the 2−ΔΔCT Method. *Methods* **25**, 402–408 (2001).
96. Remacle, C., Duby, F., Cardol, P. & Matagne, R. F. Mutations inactivating mitochondrial genes in *Chlamydomonas reinhardtii*. *Biochem. Soc. Trans.* **29**, 442–446 (2001).
97. Schägger, H. & von Jagow, G. Blue native electrophoresis for isolation of membrane protein complexes in enzymatically active form. *Anal. Biochem.* **199**, 223–231 (1991).

98. Chen, M. *et al.* Convolutional neural networks for automated annotation of cellular cryo-electron tomograms. *Nat. Methods* **14**, 983–985 (2017).
99. Nickell, S. *et al.* TOM software toolbox: acquisition and analysis for electron tomography. *J. Struct. Biol.* **149**, 227–234 (2005).
100. Goddard, T. D. *et al.* UCSF ChimeraX: Meeting modern challenges in visualization and analysis. *Protein Sci.* **27**, 14–25 (2018).

Acknowledgments

We are grateful to Pr. Claire Remacle (University of Liège) for her kind gifts of strains and antibodies. We also thank, J. Chicher and P. Hamman of the Strasbourg Esplanade proteomic analysis for the proteomic analysis. We thank Miroslava Schaffer for help with FIB milling and cryo-ET acquisition, as well as Wojciech Wietrzynski. We thank Jürgen Plitzko and Wolfgang Baumeister for access to cryo-EM instrumentation and support. This work has benefitted from the facilities and expertise of the Biophysical and Structural Chemistry platform (BPCS) at IECB, CNRS UMS3033, Inserm US001, University of Bordeaux. The mass spectrometry instrumentation was funded by the University of Strasbourg, IdEx "Equipement mi-lourd" 2015. This work was supported by a European Research Council Starting Grant (TransTryp ID:759120) to YH, by the LabEx consortium 'MitoCross' (ANR-11-LABX-0057_MITOCROSS), by the ITI 2021-2028 program of the University of Strasbourg, CNRS and Inserm supported by IdEx Unistra (ANR-10-IDEX-0002), and EUR IMCBio (ANR-17-EURE-0023) under the framework of the French Investments for the Future Program to PG and LD, and by the Agence Nationale de la Recherche (ANR) grants [MITRA, ANR-16-CE11-0024-02], [DAMIA, ANR-20-CE11-0021] and [ARAMIS, ANR-21-CE12] to YH, PG and LD. Additional funding was provided by the Max Planck Society and the Helmholtz Zentrum München to FW and BE, and the Nederlandse Organisatie voor Wetenschappelijke Onderzoek (Vici 724.016.001) to FF, as well as by an Alexander von Humboldt Postdoctoral Fellowship to FW.

Author Contributions

FW, LD, PG and YH designed and coordinated the experiments. HM and TSG generated the amiRNA strains and analyzed them. TSG purified mitochondria. FW purified the mitochondrial ribosomes. HS and FW acquired the cryo-EM data and performed the single particle analysis. RE, SP, FF and BE collected and analyzed the cryo-ET data, including subtomogram averaging. FW built the atomic models and interpreted the structures. LK performed the mass-spectrometry experiments. FW prepared and assembled the figures. FW wrote the manuscript, which was edited by TSG, RE, HS, HM, LK, SP, FF, BE, PG, LD and YH.

Competing interest

The authors declare no financial competing interest.

Supplementary Files

a

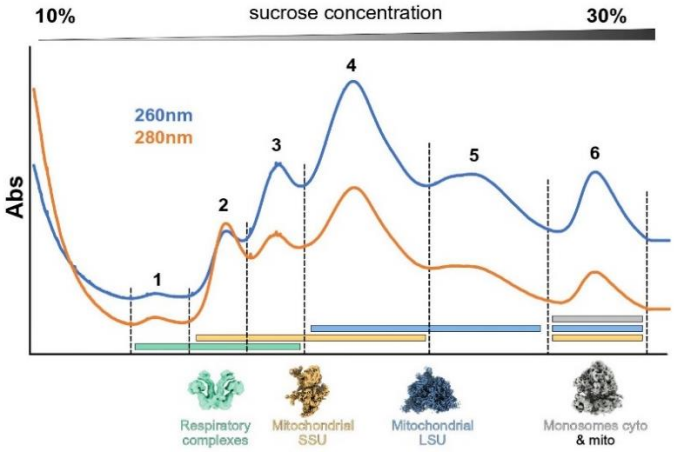

b

Protein	Uniprot ID	Total	Mito	Fractions 1	2	3	4	5	6
ATP Synthase (subunit 19.5 kDa)	Q6QAY3	16	95	180	154	106	65	20	13
ATP Synthase (subunit 5)	A8J3U9	7	84	165	158	95	50	8	9
ATP Synthase (subunit 36.3 kDa)	A8JCE9	23	85	146	169	90	50	20	17
Complex I (subunit 39 kDa)	Q6V506	12	77	35	141	66	18	4	0
Complex I (subunit 24 kDa)	Q6V9B3	14	36	21	60	35	14	2	0
Complex I (subunit 49 kDa)	Q6V9A8	10	66	29	106	61	13	2	0
bS1m	A8IB56	0	3	0	15	51	29	14	7
uS2m	A0A2K3CXL0	0	5	0	22	83	43	32	16
uS4m	A0A2K3E198	0	13	5	37	83	51	50	19
uS9m	A0A2K3E2Q3	0	15	0	30	90	45	41	10
bTHXm	A8J1A6	0	0	0	0	16	11	8	0
mS26	A8J4B1	0	4	0	8	30	11	14	6
uL3m	A0A2K3E681	0	4	1	8	50	95	58	34
uL13m	A8J810	0	1	0	0	11	26	23	5
uL15m	A0A2K3D8F3	0	4	0	3	23	47	40	12
bL33m	A8J9C3	0	0	0	0	5	11	11	4
mL64/L59	A8HPK3	0	0	0	0	11	38	35	9
mL46	A8IWI1	0	3	0	0	6	43	33	13
SSU Cyto (uS2)	A8IB25	22	0	0	0	2	0	0	10
SSU Cyto (eS6)	A8J1G8	25	0	0	0	6	2	5	26
SSU Cyto (uS15)	A8J493	19	0	3	1	2	3	1	10
LSU Cyto (uL15)	A8I2T0	21	0	0	0	0	0	2	13
LSU Cyto (uL24)	A8HMG7	26	0	0	0	0	0	5	14
LSU Cyto (eL28)	A0A2K3D7C4	14	0	0	0	0	0	0	13
Newly identified *C. reinhardtii* specific mitoribosome proteins									
mS105	A0A2K3DAY3	1	42	4	20	65	35	22	12
mS106	A0A2K3DZV7	0	10	0	1	75	15	6	1
mS107	A0A2K3CRX4	1	5	6	43	119	58	50	31
Uncharacterized protein	A8HUB6	0	12	2	21	47	23	22	15
Uncharacterized protein	A0A2K3DVI2	0	26	7	77	190	112	81	28
mL113	A0A2K3DVD3	0	15	9	25	93	166	127	65
mL114	A0A2K3DR53	0	1	0	4	39	80	49	31
mL115	A8J070	0	5	8	0	36	93	39	11
mL116	A0A2K3DXQ3	0	13	10	18	79	132	76	38
mL117	A0A2K3CXJ4	0	20	6	4	67	112	76	44
mL118	A0A2K3DTE5	0	4	4	14	70	133	73	31
mL119	A0A2K3D424	0	4	0	2	39	66	63	31
Uncharacterized protein	A0A2K3CVT3	0	0	0	0	7	31	15	4
Uncharacterized protein	A0A2K3DBX4	0	8	0	5	21	62	39	12
AAA domain-containing protein	A0A2K3CZG9	1	32	2	0	3	44	78	18

Supplementary Fig. 1. C. reinhardtii mitoribosome purificatio and identificatio of novel ribosomal components.

a) Continuous sucrose gradient profil (260 and 280 nm absorbance). 6 peaks were analyzed by proteomics and screened by cryo-EM. Repartition and reconstructions of the complexes identifie are shown below the chromatogram. b) Summary of the proteomic analysis of the corresponding fractions presented in a, that allowed the identificatio of novel r-proteins. Total

cell (Total) and purifie mitochondria (Mito) fraction MS analyses are also shown here. The abundance of the respective proteins is represented as absolute spectra values colored such that higher spectra values are red and lower are blue. The upper part of the table presents known components of the complexes identifie that were used as references to identify novel components of the LSU and SSU of C. reinhardtii mitoribosome. The novel components are presented in the lower part of the table. Proteins that were confirme by cryo-EM are shown in bold

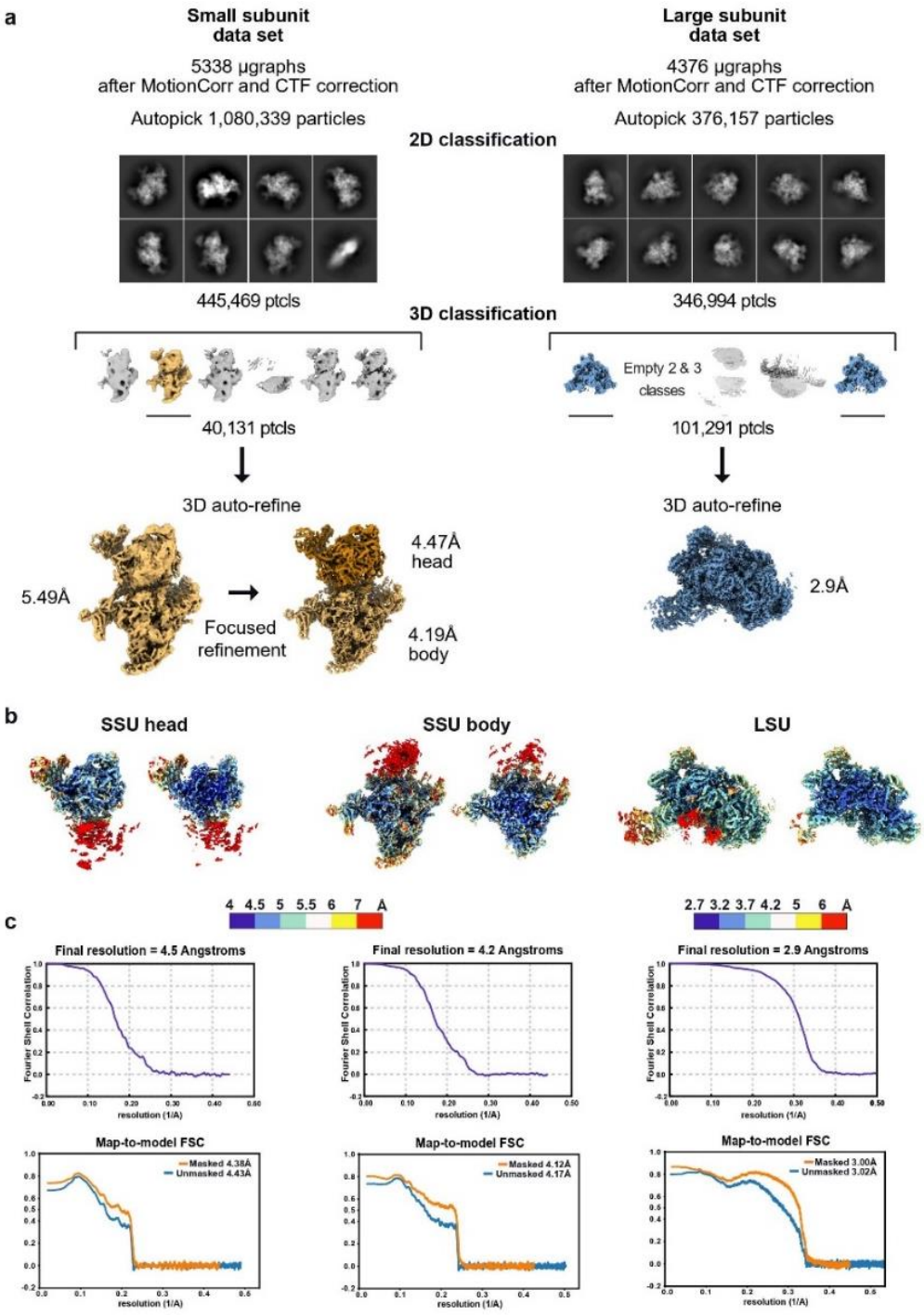

Supplementary Fig. 2. Single-particle data processing workflow.

a) Graphical summary of the processing workflo described in Methods, with 2D and 3D classes, processing and refinement b) Local resolutions of both the LSU and each focused SSU arepresented. The maps are colored by resolution, generated usingResMap74. Maps are also shown incut view. c) For each reconstructions FSC plots (output from RELION75) are displayed for resolution estimation. Map to model FSC are also shown (output from PHENIX76 validation), for the SSU, the head part of the SSU model was used against the head map and thebody part of the model against the body map. The maps resolution were calculated at the 0.143 threshold.

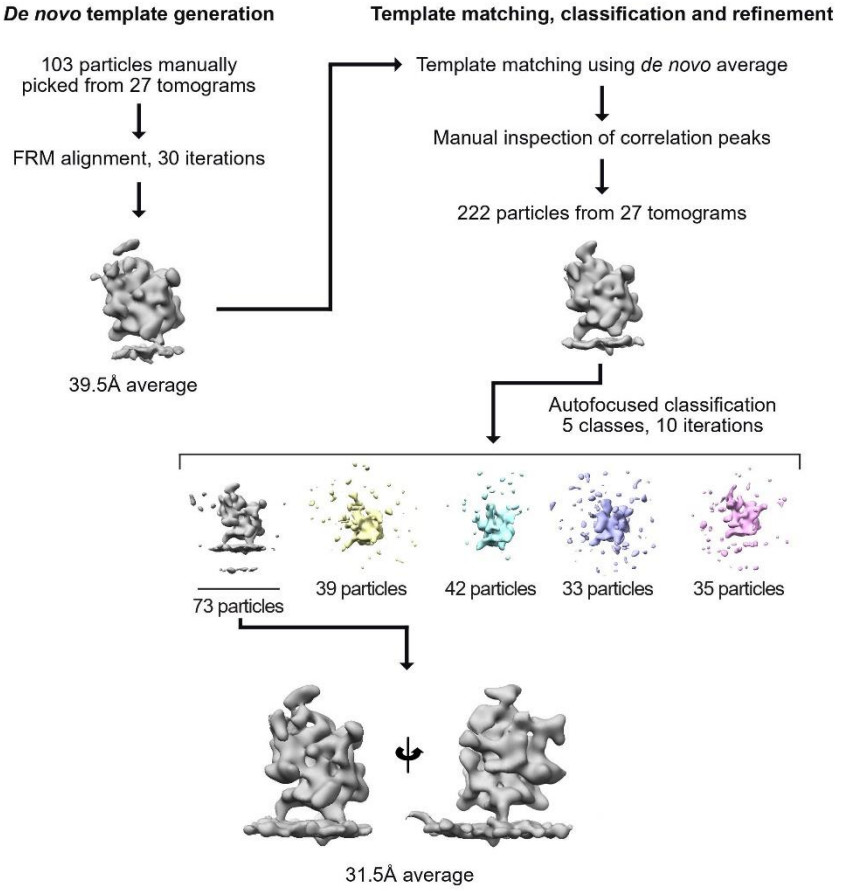

Supplementary Fig. 3. Subtomogram averaging workflow

To create an initial mitoribosome reference, 103 particles were manually picked and subjected to 30 iterations of FRM alignment resulting in an average of 39.5 Å (top left). This was used as a reference volume for Template matching, followed by manual inspection of the top correlation peaks and resulting in a set of 222 particles from 27 tomograms. The 222 particles were aligned and subjected to autofocused classification resulting in one class of 73 particles that showed distinct ribosomal features. 3D refinemen of that class resulted in an average of 31.5 Å. A similar workflo , detailed in the methods section, was adopted for the STA of cytoribosomes and ATP synthases.

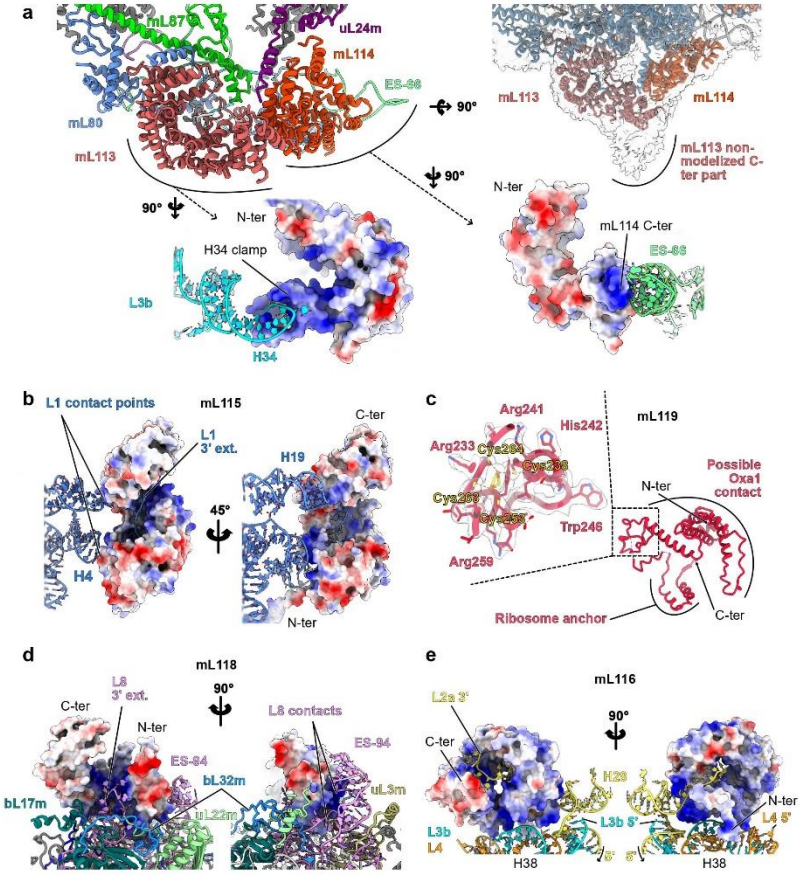

Supplementary Fig. 4. Detailed analyses and views of the specifi LSU proteins Focused views of the differen Chlamydomonas-specifi r-proteins of the LSU. a) View of the mL113 – mL114 area. Both proteins interact together and with the surrounding proteins. The non-modelized C-terminal part of mL113, interacting with the membrane, is shown. It interacts with H34 of the L3b fragment. mL114 interacts with ES-66 of the L7 fragment. Electrostatic coloration (blue coloration corresponds to positive patches and red to negative patches) of the proteins correlate with their rRNA binding site. b) Electrostatic coloration of the mL115 protein reveal that its inner groove is mostly positively charged similarly to the two contact points made with H4 and H19. c) Detailed view of mL119. Part of the protein coordinate an iron-sulfur cluster via four cysteine residues. The model is shown in its density. d) Electrostatic coloration of the mL118 protein showing the positive charge of the inner groove and the two contact points made with ES-94. e) Similarly mL116 by electrostatic potential revealing the largely positive surfaces both in its inner groove and exterior to interact with rRNAs.

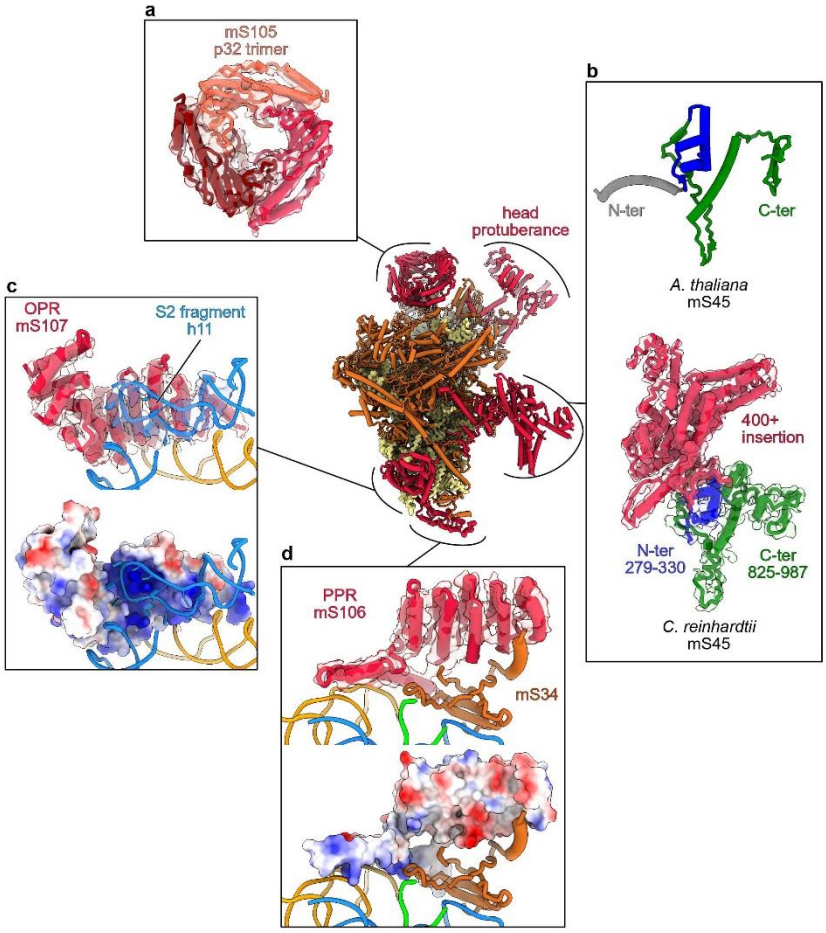

Supplementary Fig. 5. Detailed analyses and views of the specifi SSU proteins

The small subunit model is presented from the solvent view which allows to see the major structural features, highlighted in red, of the SSU. Two Y-shaped protuberances are observed on the head and the body. a) The body protuberance is formed by a large insertion in the conserved mS45 protein. A comparison between the Arabidopsis and Chlamydomonas mS45 proteins are shown. The head protuberance components, could not be clearly identifie and was thus entirely build as poly-alanine. However, several conserved proteins of the SSU head, notably uS3m, uS10m and mS35, have large parts that could not be modelized. These extensions could come together and form this large head protuberance. The foot extension is formed by two helical proteins, one PPR (mS106) (b) and one OPR (mS107) (c). The electrostatic potential of the proteins (blue coloration corresponds to positive patches and red to negative patches) which models were generated using AlphaFold are also presented27. The PPR occupies a position similar to mS27 in human6,7 and fungi12, but does not appear to interact with RNA, which seems consistent with the charge of the inner groove of the protein. (c) The OPR encapsulates the tip of helix 11. d) On the back of the SSU head, the homotrimeric torus-shaped domain formed by three copies of mS105 (p32) is present.

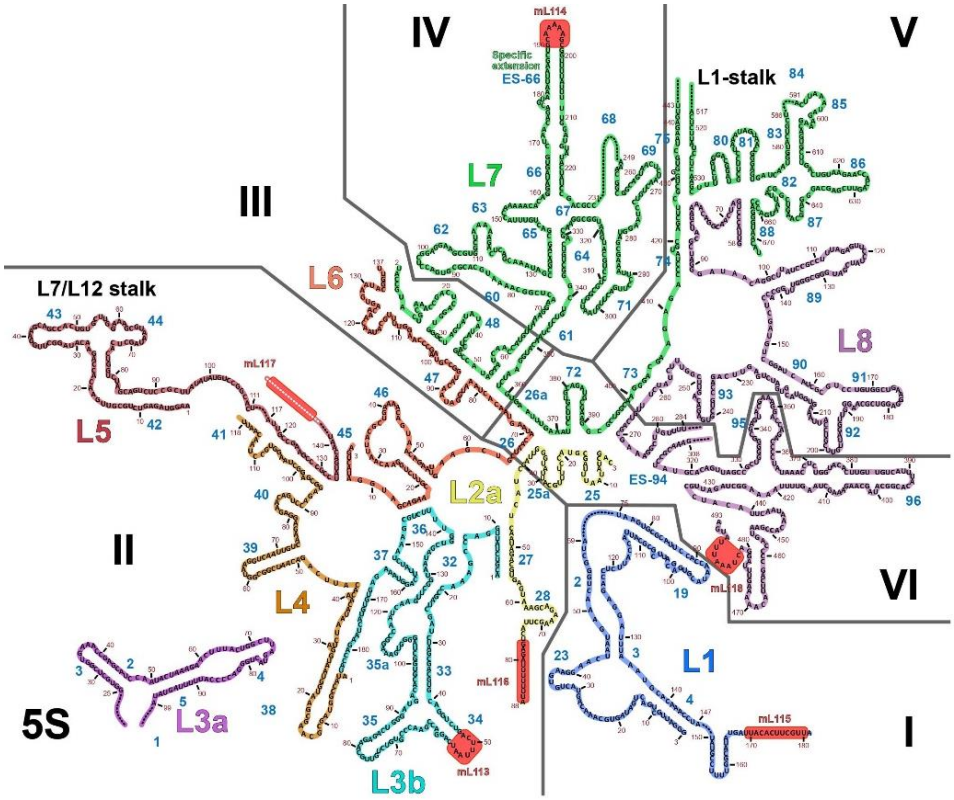

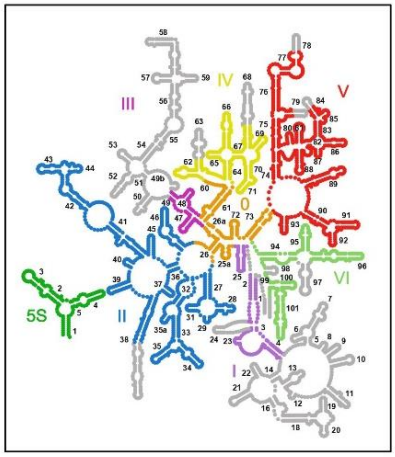

E. coli 2D diagram

Supplementary Fig. 6. 2D diagram of the C. reinhardtii LSU rRNAs 2D representation of the LSU rRNAs of Chlamydomonas mitoribosome. Each 9 rRNA fragments are colored differentl and match the color code of Figure 3. The rRNA expansions (ES-94 and ES-66) are indicated on the diagram. RNA portions that could not be modelled are indicated by dark dashed lines, e.g the L1 stalk could not be built due its motion. White dashed lines indicated regions that were built as polyU/A. Contact points of Chlamydomonas-specifi r-proteins are also highlighted by red boxes. Simplifie secondary structure diagram of the E. coli 23S rRNA is also shown in theblack frame, this time colored by domain. Helices absent in Chlamydomonas mitoribosome are shown in gray, which highlight the strong reduction of domain I and III. Secondary structure templates were obtained from the RiboVision suite (http://apollo.chemistry.gatech.edu/RiboVision).

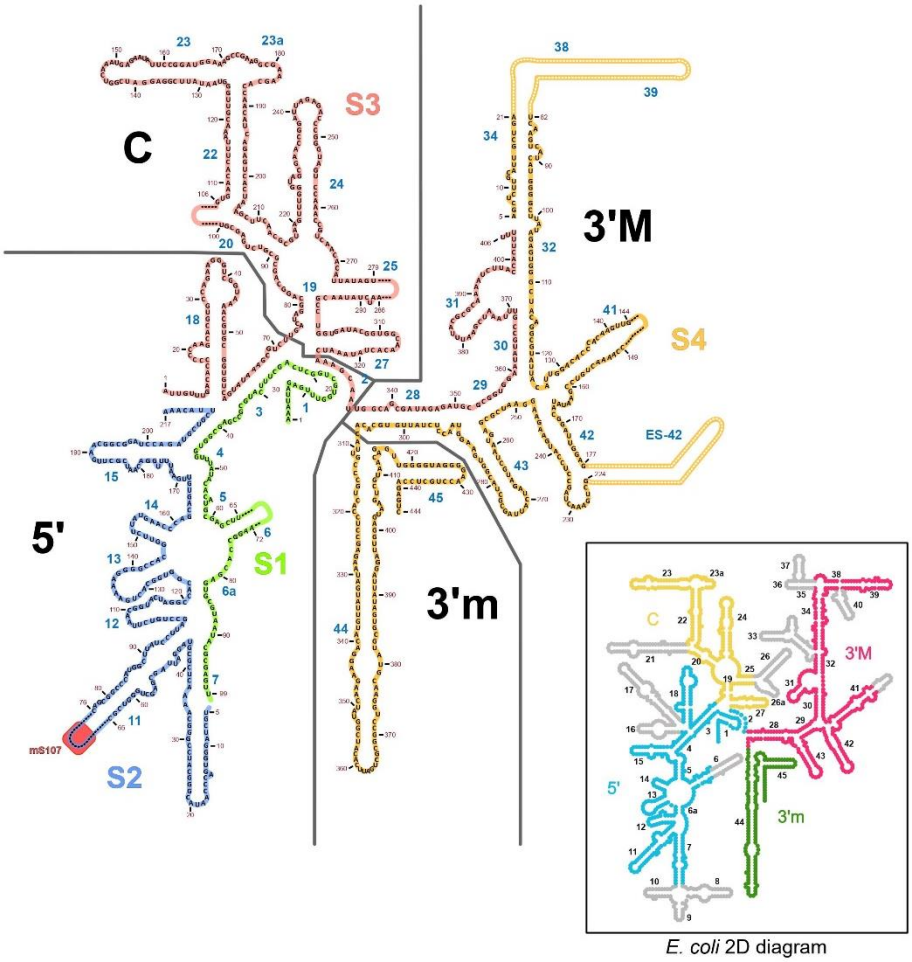

Supplementary Fig. 7. 2D diagram of the C. reinhardtii SSU.

rRNAs 2D representation of the SSU rRNAs of Chlamydomonas mitoribosome. Each 4 rRNA fragments are colored differentl and match the color code of Figure 3. The rRNA expansions are indicated on the diagram. Extensions that could not be modelled are indicated by dashed lines. White dashed lines indicated regions that were built as polyU/A. Contact points of Chlamydomonas-specifi r-proteins are also highlighted by a red box. Simplifie secondary structure diagram of the E. coli 16S rRNA is also shown in the black frame, this time colored by domain. Helices absent in Chlamydomonas mitoribosome are shown in gray. Secondary structure templates were obtained from the RiboVision suite (http://apollo.chemistry.gatech.edu/RiboVision).

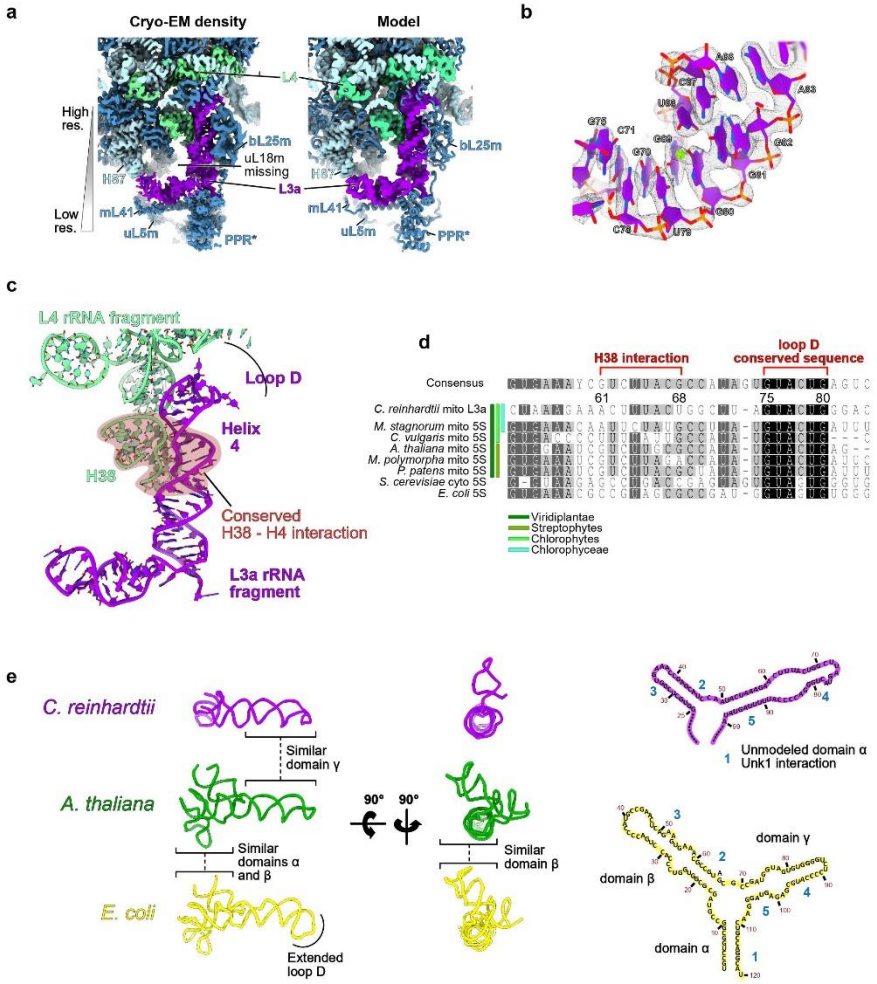

Supplementary Fig. 8. Analysis of the central protuberance, the L3a rRNA fragment is a divergent 5S a) Comparison of the cryo-EM map of the central protuberance (CP) with the corresponding atomic model. Resolution is lower at the outer extremity of the CP due to the CP general motion. rRNAs are shown in light blue, aquamarine (L4) and purple (L3a) and proteins in blue. For the atomic model, rRNAs are shown in surface and proteins in cartoon representation. Compared to classical CP structures, the uL18 protein is missing, which is normally involved in domain α stabilization. b) L3a atomic model in its respective density that allowed identificatio of the rRNA fragment. c) The structurally conserved helix 4 area, interacting with helix 38 of the L7 fragment is highlighted and sequence alignment of the area is shown in d. Conservation is observed from bacteria to eukaryotes, especially at the sequence level for the pre-loop D area. The L3a fragment is particularly divergent even with member of the Chlorophytes. e) shows structural comparison between bacterial, mitochondrial higher plants and Chlamydomonas 5S rRNAs. Domain γ, especially helix 4 and the D loop are more similar between A. thaliana and C. reinhardtii compared to bacteria, whereas domain β is completely differ nt in C. reinhardtii compared to both bacteria and A. thaliana. Chlamydomonas domain β is angled differ ntly which allows the interaction of the fina loop of the domain with H87

which is not the case in other ribosomes. The unmodeled domain α of Chlamydomonas L3a most likely interacts with the unidentifie alpha helical protein, resembling a PPR protein, PPR*.

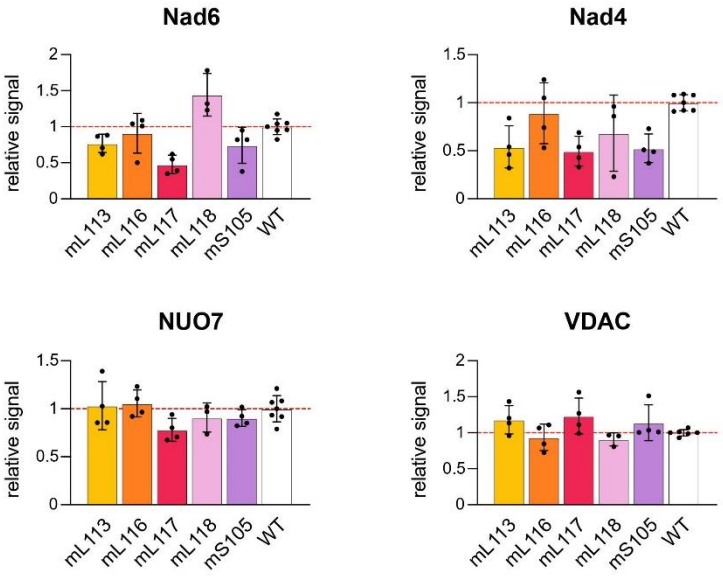

Supplementary Fig. 9. Quantification for Nad6, Nad4, NUO7, and VDAC immunoblot experiments. Histograms correspond to relative signals of 3-4 technical replicates of immunoblot experiments from 2 biological replicates (see SI Table 3 and SI File). The stained blots and immunoblot signals were quantifie with ImageJ 1.52s software. The statistical difference between WT and each amiRNA strains test sdfdfgfor each signal protein as derived from the Mann-Whitney test are indicated (**p < 0.01; *p <0.05).

Proteins of the Chlamydomonas mitoribosome

Proteins of the Large subunit						
MRP	**Uniprot ID**	**Phytozome**	**Chain ID**	**Size (aa)**	**Modeled residues**	**Comments**
uL2m	A0A2K3DL58	Cre07.g348850.t1.2	a	383	69-349	
uL3m	A0A2K3E681	Cre01.g022250.t1.1	b	417	90-393	
uL4m	A0A2K3D422	Cre12.g520400.t1.2	c	427	85-424	Contacts mL115, mL116 and mL117
uL5m	A0A2K3DYN2	Cre03.g196150.t1.2	d	216	12-195	Scant density due to moving CP
uL6m	A8J503	Cre09.g415950.t1.2	e	207	32-195	Scant density but visible close de L7/L12 stalk
bL9m	A0A2K3DRF9	Cre06.g307950.t1.1	f	304	104-163	Scant density due to L1 stalk motion
uL10m	A8HVP7	Cre06.g272850.t1.2	-	235		Very scant density due to L7/L12 stalk motion in LSU reconstruction but visible in the STA data
uL11m	A8J6G9	Cre17.g722200.t1.2	-	153		Very scant density due to L7/L12 stalk motion in LSU reconstruction but visible in the STA data
uL13m	A8J810	Cre09.g405200.t1.2	i	277	6-157	
uL14m	A8IYH4	Cre12.g550650.t1.2	j	120	1-120	
uL15m	A0A2K3D8F3	Cre11.g476800.t1.1	k	337	107-316	
uL16m	A0A2K3DP67	Cre06.g278224.t1.1	l	270	135-270	
bL17m	A0A2K3DXS2	Cre03.g181350.t1.1	m	-	2-178	The protein is a mix of A0A2K3DXS2 and A8JH49
bL19m	A8I7A8	Cre07.g322500.t1.2	n	312	134-306	N-ter part stabilizes mL118
bL20m	A8HNL1	Cre01.g052350.t1.1	o	115	2-111	
bL21m	A0A2K3DDN8	Cre09.g388550.t1.2	p	370	119-341	
uL22m	A0A2K3DSG6	Cre05.g242950.t1.1	q	377	194-354	
uL23m	A8J6R9	Cre17.g727350.t1.2	r	226	30-201	
uL24m	A0A2K3DJU3	Cre07.g330450.t1.2	s	309	2-221	
bL25m	A0A2K3E0K7	Cre02.g081450.t1.2	t	366	117-361	Close to CP, scant density, contacts PPR*
bL27m	A0A2K3E880	Cre01.g053600.t1.2	u	167	-5-131	C-ter interacts with mL116. Extends in N-ter, before the first amino-acid of the reference sequence
bL28m	A0A2K3D077	Cre13.g579150.t1.2	v	153	4-123	Beta sheets stacking with the beta sheet of the N-ter of mL115
uL29m	A8HUW1	Cre13.g588310.t1.1	w	127	4-123	
uL30m	A0A2K3DSP9	Cre05.g234659.t1.1	x	214	8-213	
bL32m	A8JGW4	Cre12.g558750.t1.2	y	123	48-118	
bL33m	A8J9C3	Cre16.g653601.t1.1	z	59	5-57	
bL34m	A0A2K3CX36	Cre14.g608970.t1.1	A	280	231-280	
bL35m	A0A2K3DKX8	Cre07.g345850.t1.2	B	151	22-149	Long C-ter extension
bL36m	-	-	C	-	2-37	Present but no sequence identified
mL40	A0A2K3D9N2	Cre10.g428350.t1.2	D	172	25-118	
mL41	A8J2J1	Cre06.g291300.t1.2	E	112	25-103	
mL43	A8HW20	Cre06.g270650.t1.2	F	141	2-130	
mL46	A8IWI1	Cre03.g193550.t1.1	G	259	37-257	
mL54	A8IY84	Cre12.g546000.t1.2	-	127		Very scant density due to L7/L12 stalk motion in LSU reconstruction but visible in the STA data
mL63/S7/60	A8IS96	Cre16.g684950.t1.2	I	132	10-106	C-ter extension interacts with both mL116 and mL117
mL59/64	A8HPK3	-	J	134	18-133	
mL80	A0A2K3DBX4	Cre10.g461650.t1.2	K	249	35-248	Long C-ter extension stabilize mL113
mL87	A8J535	Cre09.g417100.t1.1	L	206	59-195	N-ter additional domain contacts mL113 and domain III of reduced rRNA
mL113	A0A2K3DVD3	Cre03.g145867.t1.1	M	876	63-587	OPR (ASA2-like), contacts mLXX2. Contacts H34. Unmodeled C-ter part interacts with the membrane
mL114	A0A2K3DR53	Cre06.g303850.t1.1	N	455	139-424	mTERF, contacts mL113 and the specific extension ES-66
mL115	A8J070	Cre09.g392579.t1.1	O	688	75-670	OPR10, presence of Trp in several repeats. Stabilize 3' end of the L1 fragment
mL116	A0A2K3DXQ3	Cre03.g179901.t1.1	P	530	34-526	OPR (ASA2-like), contacts mLXX5. Stabilize 3' end of the L2a fragment
mL117	A0A2K3CXJ4	Cre14.g615450.t1.2	Q	820	130-786	OPR, contacts mLXX4. Stabilize the 3' end of the L5 fragment. Mostly build as polyA due to scant densi
mL118	A0A2K3DTE5	Cre04.g217904.t1.1	R	653	152-598	OPR. Stabilizes the 3' end of the L8 fragment.
mL119	A0A2K3D424	Cre12.g521050.t1.2	S	334	71-334	At the channel exit. Presence of a FeS cluster. Involved in membrane contact, probably with Oxa1
PPR*	??		Y	??	1-172	PPR-like on CP
Unk1	??		X	??	1-31	Peptide encapsulated by mL113
Unk2	??		Z	??	1-49	Next to uL25m

Proteins of the Small subunit						
MRP	**Uniprot ID**	**Phytozome**	**Chain ID**	**Size (aa)**	**Modeled residues**	**Comments**
bS1m	A8IB56	Cre10.g432200.t1.2	a	253	40-253	Clearly visible
uS2m	A0A2K3CXL0	Cre14.g614950.t1.2	b	530	118-440	
uS3m	A0A2K3D7R0	Cre11.g467702.t1.1	c	490	126-260	Unmodelled residues are most likely part of the unknown proteins of the head
uS4m	A0A2K3E198	Cre02.g091450.t1.1	d	415	257-385	
uS5m	A0A2K3DFB5	Cre09.g407100.t1.1	e	368	175-350	
bS6m	A8JGX6	Cre12.g558000.t1.1	f	122	2-104	
uS7m	A0A2K3CXT8	Cre14.g618700.t1.1	g	281	144-281	
uS8m	A0A2K3CNM3	Cre17.g696550.t1.2	h	412	10-371	
uS9m	A0A2K3E2Q3	Cre02.g106750.t1.2	i	446	284-437	
uS10m	A0A2K3CN25	Cre24.g755297.t1.1	j	580	112-290	Unmodelled residues are most likely part of the unknown proteins of the head
uS11m	A0A2K3DQ48	Cre06.g288400.t1.1	k	233	121-219	Very scant density of the platform area
uS12m	A0A2K3E3V0	Cre02.g144400.t1.1	l	128	13-122	
uS13m	A8J3J1	Cre16.g674350.t1.2	m	124	18-116	
uS14m	A8J6P9	Cre17.g726300.t1.1	n	112	15-111	
uS15m	A0A2K3CQY8	Cre17.g731250.t1.2	o	300	107-287	
bS16m	A0A2K3D9S4	Cre10.g429550.t1.2	p	88	1-79	
uS17m	A0A2K3DKB4	Cre07.g337800.t1.2	q	220	5-184	
bS18m	A0A2K3DDW6	Cre09.g388282.t1.1	r	356	238-293	
uS19m	A0A2K3DHN0	Cre08.g375250.t1.1	s	116	4-94	
bTHXm	A8J1A6	Cre09.g391208.t1.1	u	136	66-89	
mS23	A8IW03	Cre12.g530500.t1.2	v	190	9-136	
mS26	A8J4B1	Cre08.g361500.t1.2	w	193	34-188	
mS29	A0A2K3DXG4	Cre03.g176700.t1.1	x	485	63-479	
mS33	A8JI15	Cre17.g747697.t1.1	y	209	125-185	
mS34	A8J254	Cre06.g283350.t1.1	z	133	22-115	
mS35	A0A2K3CST5	Cre16.g650700.t1.1	B	883	818-870	Unmodelled residues are most likely part of the unknown proteins of the head
mS45	A0A2K3DM91	Cre06.g254600.t1.1	C	999	280-600/853-980	Large insertion and N-terminal could not be modeled and likely form most of the body protuberance
mS45-In	A0A2K3DM91	Cre06.g254600.t1.1	D	-		Probable insertion and N-terminal part of mS45 modeled as a separate block
mS31/46	-	-	K	-	1-186	Present but no sequence identified
			L			
mS105	A0A2K3DAY3	Cre10.g447100.t1.2	M	253	69-251	p32 trimer
			N			
mS106	A0A2K3DZV7	Cre03.g211409.t1.1	O	516	271-513	PPR at the foot. Similar to mS27 (human and yeast) or mS90 in tetrahymena. AlphaFold modelization
mS107	A0A2K3CRX4	Cre17.g743597.t1.1	P	416	1-413	OPR SSU, contact h11. AlphaFold modelization
Unk1	??		U	??	1-22	Unknown body protein
Unk2	??		V	??	1-218	Unknown helical protein(s) bundle on the body
Unk3	??		W	??	1-54	Unknown peptide in the body protuberance
Unk4	??		X	??	1-91	Unknown helical bundle on the head
Unk5	??		Y	??	1-92	Unknown peptide linking head and body and contacting mS105
Unk6	??		Z	??	1-695	Unknown head protuberance, most likely formed by extensions of conserved proteins

Supplementary Table 1. List of proteins identified as constituent C. reinhardtii mitoribosome, for the LSU and SSU.

List of the r-proteins constituting the C. reinhardtii mitoribosome, the table is divided between LSU and SSU r-proteins. The proteins are colored by conservation with the bacterial ribosome (blue) other mitochondrial ribosomes (yellow) or specifi to C. reinhardtii mitoribosome (red). Due to the L7/L12 stalk motion, proteins uL10m, uL11m and mL54 were not visualized and are presentedonly in the illustration figures not the deposited fina model. Similarly, bL12m was observed in the subtomogram averaging reconstruction but is not present in the fina model. Due to the overall lower resolution of the SSU compared to the LSU, the totality of visible extensions and insertion were modelled as polyA. bS21m, mS37 and mS38 are most likely present but could not be observed in our reconstruction. Full list of proteins identified is provided in Supplementary information.

Table S2. Cryo-EM data collection, refinement and validation statistics

	#1 LSU (EMD-13480)	#2 SSU body (EMD-13477)	#3 SSU head (EMD-13481)
	(PDB 7PKT)	(PDB 7PKQ)	
Data collection and processing			
Magnification	45,000X	36,000X	
Voltage (kV)	200	200	
Electron exposure (e–/Å^2)	45	45	
Defocus range (μm)	-0.5 to -2.5	-0.5 to -2.5	
Pixel size (Å)	0.9	1.13	
Symmetry imposed	C1	C1	
Initial particle images (no.)	346,994	445,469	
Final particle images (no.)	101,291	40,131	
Map resolution (Å) FSC threshold	2.93 0.143	4.19 0.143	4.47 0.143
Map resolution range (Å)	2.7 - 7	3.8 - 10	
Refinement			
Initial model used (PDB code)	5KCR, 6GAW, 6XYW, 5MRC		
Map sharpening *B* factor (Å^2)	-50.6	-169.5	-174.3
Model composition Non-hydrogen atoms Protein residues Nucleotide residues Ligands	57 chains 103,142 8300 1901 Zn:1 Mg:69 FES:1	44 chains 70,328 6690 1114 -	
FSC (model) = 0.143 (Å) = 0.5 (Å) CC	3.00 3.18 0.75	4.12 4.35 0.73	4.38 5.01 0.75
B factors (Å^2) (mean) Protein Nucleotide Ligand	 27.87 36.85 19.13	 101.52 143.00 -	
R.m.s. deviations Bond lengths (Å) Bond angles (°)	 0.010 1.228	 0.007 1.223	
Validation MolProbity score Clashscore Poor rotamers (%)	 1.72 5.50 0.26	 1.88 8.12 0.21	
Ramachandran plot Favored (%) Allowed (%) Disallowed (%)	 93.56 6.19 0.25	 93.27 6.57 0.15	
RNA validation Sugar pucker outliers (%) RNA backbone	 1% 0.46	 1% 0.38	

Supplementary Table 2. Cryo-EM data collection, refinement and validation statistics.

Gene	Genome	Gene ID	Experiment	Forward primer (5' -> 3')	Reverse primer (5' -> 3')
CYN19-3	Nucleus	*Cre13.g588100.t1.2*	qPCR	CAAGACTGCGGAGAACTTCC	CACATGAAGGAGGGGATGAC
MAA7	Nucleus	*Cre03.g161400.t1.2*	qPCR	GTTCGGCGGCAAGTACGT	CGCAATCGCCTCGTTGTAGT
mL113	Nucleus	*Cre03.g145867.t1.1*	qPCR	GACAGCTATCTCTGTCTTTGTTAGCTC	ACTCCTCTCCCGACAGCAC
mL113	Nucleus	*Cre03.g145867.t1.1*	amiRNA	ctagtTCGCATCAGTATAACTAGATAtctcgctgatcggcaccatgggggtggtggtgatcagcgctaTATCAAGTTATACTGATGCGAg	ctagcTCGCATCAGTATAACTTGATAtagcgctgatcaccaccaccccccatggtgccgatcagcgagaTATCTAGTTATACTGATGCGAa
mL116	Nucleus	*Cre03.g179901.t1.1*	qPCR	CTCAGACCGGCCAACATC	TGAACTCTCAGCGCGTAGG
mL116	Nucleus	*Cre03.g179901.t1.1*	amiRNA	ctagtAAGATCAACACCTCTGTAAGAtctcgctgatcggcaccatgggggtggtggtgatcagcgctaTCTTTCAGAGGTGTTGATCTTg	ctagcAAGATCAACACCTCTGAAAGAtagcgctgatcaccaccaccccccatggtgccgatcagcgagaTCTTACAGAGGTGTTGATCTTa
mL117	Nucleus	*Cre14.g615450.t1.2*	qPCR	CAGCTGCAGCAACACCAG	CGACACGTTGGACTGGAAC
mL117	Nucleus	*Cre14.g615450.t1.2*	amiRNA	ctagtCAGGCTGAACAAACTTGAACAtctcgctgatcggcaccatgggggtggtggtgatcagcgctaTGTTTGAGTTTGTTCAGCCTGg	ctagcCAGGCTGAACAAACTCAAACAtagcgctgatcaccaccaccccccatggtgccgatcagcgagaTGTTCAAGTTTGTTCAGCCTGa
mL118	Nucleus	*Cre04.g217904.t1.1*	qPCR	ATCCCCAGCGTCCAATCT	TTCGGAGCTGTTGGTGGT
mL118	Nucleus	*Cre04.g217904.t1.1*	amiRNA	ctagtCCGAAAGGAGGTCTGTGATTAtctcgctgatcggcaccatgggggtggtggtgatcagcgctaTAATGACAGACCTCCTTTCGGg	ctagcCCGAAAGGAGGTCTGTCATTAtagcgctgatcaccaccaccccccatggtgccgatcagcgagaTAATCACAGACCTCCTTTCGGa
mS105	Nucleus	*Cre10.g447100.t1.2*	qPCR	TGATGAGCTGGATGACAACCT	GAGGAAGCGCAGGTACTCC
mS105	Nucleus	*Cre10.g447100.t1.2*	amiRNA	ctagtGTGATCGCGTATTGCTCTTTAtctcgctgatcggcaccatgggggtggtggtgatcagcgctaTAAACAGCAATACGCGATCACg	ctagcGTGATCGCGTATTGCTGTTTTAtagcgctgatcaccaccaccccccatggtgccgatcagcgagaTAAAGAGCAATACGCGATCACa
rrnL1	Mitochondria		qPCR	AGGGATTGCTGACTGATAGTGC	ATGCGCGAATGCTCACGTATTG
rrnL2a	Mitochondria		qPCR	GCTTTCTGCTTAACTCACG	GCGTACCTTTTGCATTATGG
rrnL2b	Mitochondria		qPCR	GCGTGCAACAACACACTAAAGGG	TGTGAGAGTGTGGGTTGAACCAG
rrnL3a	Mitochondria		qPCR	ACTCAATTTCGGTGCTCGGTGA	GGGTCCCAGTACTAAGCCAGTAA
rrnL3b	Mitochondria		qPCR	AACCGATCGATCTAGCGACGTG	TCTTGCAACAGACACGGGTTCG
rrnL4	Mitochondria		qPCR	ATACCGGTAGCGCAAGCGAATG	TGACCTTACCGCCGATTGTCTG
rrnL5	Mitochondria		qPCR	AAGGTAGAGTCTGCGTTGAACACC	TTCCAAGCACAGTGGCTGCTTC
rrnL6	Mitochondria		qPCR	ACGTTCTGGAACAATTACGCTGA	GGGCTTACGGCCATGTTATCCA
rrnL7	Mitochondria		qPCR	ACGTTTAATTGGCGTCCTTG	AGCTGCATAGGGTCTCTTCG
rrnL8	Mitochondria		qPCR	CGCCTATGCACAGTTAGCC	TGACAACAAGTGTACCAGAGGTTT
rrnS1	Mitochondria		qPCR	GTTTGGTGCTGGCTCAGCTTTC	ATTACGCACTCGTGCGCTTAATC
rrnS3	Mitochondria		qPCR	TTCAAATCTATAACGCCTGGTG	GCTGCCAATTGCTTTGATTT
rrnS4	Mitochondria		qPCR	ACGGTCGAGCAAGTCATCATGG	TGGTATCCAACTTGTGGGTGTCC
rtl	Mitochondria		qPCR	TACGCCGACAGTACATCCAG	TACCAAAACCAGGACGGAAG
dT			RT		TTTTTTTTTTTTTTTTTTTTTTT

Supplementary Table 3. List of oligonucleotides used in this study

Chapter 7

Sucrose binds to a conserved ribosomal pocket to induce translational stalling of bZIP11-uORF2

Robert Englmeier[1*], Sjors van der Horst[2*], Johannes Hanson[3], Sjef Smeekens[2], Friedrich Förster[1]

[1] Structural Biochemistry group, Bijvoet Centre for Biomolecular Research, Utrecht University, Padualaan 8, 3584 CG Utrecht, The Netherlands

[2]Molecular Plant Physiology, Institute of Environmental Biology, Utrecht University, 3584CH Utrecht, The Netherlands

[3]Umeå Plant Science Center, Department of Plant Physiology, Umeå University, SE-90187 Umeå,
Sweden

[*]Authors contributed equally

Abstract

Metabolites can control the synthesis of specific proteins by stalling ribosomal translation of their upstream open reading frames (uORFs). In plants, sucrose stalls ribosomes translating the uORF2 of the transcription factor *bZIP11* mRNA in a concentration-dependent manner. Despite the high abundance of uORFs in eukaryotic mRNAs the structural mechanisms of metabolite-dependent control in eukaryotes remain elusive. Here, we use cryoEM single particle analysis to determine the structures of stalled ribosomes engaged with bZIP11-uORF2 in the presence of sucrose. The structures show that sucrose locks the ribosome in two translational states and binds to a conserved binding pocket in the peptide exit tunnel to stall the ribosome. Its binding site parallels that of tryptophan and the drug PF846, which were shown to exhibit transcript-specific stalling in the *Escherichia coli* and human ribosomes, respectively. Our findings elucidate the mechanism of sucrose-induced stalling of bZIP11-uORF2 and suggests that a >3 billion years-old binding pocket is functionally conserved and exploited across several kingdoms of life.

Introduction

Cells rely on the regulation of gene expression to coordinate cell division and development, maintain homeostasis and respond to changing environments. This control is either achieved by transcriptional regulation, where transcription factors turn genes on or off, or by translational regulation, where the translation of a transcript is either accelerated or stalled before or during the engagement with the ribosome by regulatory elements within the mRNA[1]. Translational regulation operates independent of transcription control an delivers an immediate modulation of protein availability to the cell. A specific form of translational regulation is metabolite-induced translational regulation, where the ribosome acts as a metabolite sensor to stall or release translation of a specific transcript in a concentration-dependent manner[2].

One of the mechanistically best understood examples of metabolite-induced translational stalling is the tryptophan-induced stalling of the tryptophanase leader peptide C (TnaC) in *E. coli*[3–6]. Cryogenic electron microcopy (cryo-EM) single particle analysis (SPA) revealed the mechanism of TnaC mediated ribosome stalling: the TnaC peptide forms two short α-helices close to the peptidyltransferase center (PTC) when the ribosome reaches the stop codon and contribute to the formation of a ligand-binding site that accommodates a single tryptophan molecule[6]. Translation termination is prevented by the two ultimate residues of TnaC, which preclude the formation of the GGQ loop of release factor 2 (RF2) and inhibit hydrolysis of the TnaC-peptidyl-tRNA[4,6], thereby inducing termination arrest. Another structurally explored example of sequence-specific translational stalling is the cholesterol lowering drug candidate PF846, which selectively stalls synthesis of Proprotein convertase subtilisin/kexin type 9 (PCSK9), Cadherin1 (CDH1) and general vesicular transport factor p115 (USO1) [7–9]. PF846 binds to a small cavity in the peptide exit tunnel above the uL4/uL22 constriction site and is in close contact with the nascent chain. PF846 locks the ribosome in two different states, a rotated pre- and an unrotated post-translocation state, resulting in both elongation and termination arrest, respectively[8,9].

Mechanistic insights into translational stalling of widespread regulatory upstream open reading frames (uORFs) that are encoded in the 5'-untranslated region (UTR) of mRNAs is limited[10,11]. An estimated 20 - 50% of all eukaryotic mRNAs contain such uORFs[12]. Many of those uORFs have conserved amino acid sequences across the plant kingdom, and referred to as conserved peptide uORFs (CPuORFS)[10,13], with the species *Arabidopsis thaliana* alone containing more than 69 CPuORFs[14]. CPuORFs have been well characterized in plants, which contain several uORFs that exhibit metabolite-induced regulation and are sensitive to different molecules such as sucrose, polyamines or ascorbate[10]. Prominent examples are the CPuORFs of the five S1-group basic region leucine zipper (bZIP) transcription factors, which control growth, amino acid and sugar metabolism[15,16]. bZIP11-uORF2, was shown to

stall translation on the stop codon in the presence of sucrose in a concentration-dependent manner[16]. Single substitutions of 10 out of the 14 most C-terminal amino acids into alanine residues abolished the ability of sucrose to induce ribosome stalling[17]. However, the detailed mechanism of sucrose-induced stalling, i.e., where the sucrose binds and how it interacts with the nascent peptide, remains unresolved. In this study we applied cryoEM to resolve the structure of a wheat ribosome stalled by sucrose on *bZIP11*-uORF2.

Results

Optimizing bzip11-uORF2 mediated stalling for structural studies by cryoEM

We performed *in vitro* translation (IVT) reactions using wheat germ extract with three different bZIP-uORF2 constructs containing different N-terminal tags in the presence or absence of sucrose to assess the translation and stalling efficiency. We tested two short constructs containing either a Hexahistidine- (HH) and a hemagglutinin (HA)-tag (HH)or a Hexahistidine- and HA-tag followed by a 3x Flag (HHF) tag upstream of the bZIP11-uORF2, as well as a longer construct with an HHF-tag followed by a 75 amino acid linker (HHF-DP75) which has previously been used [17] (Figure 1A). In *our* IVT assay, all three constructs resulted in stalling in the presence of 540 mM sucrose, as indicated by a clear band for the peptidyl-tRNA detected by western blot (Fig 1B). A previously reported lower peptidyl-tRNA band for the HHF-DP75-uORF2 in the absence of sucrose was also observed[17], which is also present for the HHF-transcript, but at a lower concentration. This sucrose-independent stalling results in a lower peptidyl-tRNA band in the absence of sucrose. For the HH-transcript no such lower band is observed (Figure 1B).

High sucrose concentrations such as the 540 mM used in the assay pose a challenge for the structural investigation by cryo-EM for two reasons: (i) with increasing sucrose concentration, the contrast between particles and solvent decreases, (ii) organic additives such as sugars tend to increase radiolysis limiting the electron dose that can be applied to the sample. Thus, SNR of images decreases due to reduced intrinsic contrast and due to a lower tolerable electron dose. Typically, the concentration of glycerol and sugar do not exceed 5 % w/v in cryo-EM studies.

To determine a cryo-compatible sucrose concentration with sufficient stalling efficiency, IVT reactions were performed using HH-uORF2 and HHF-uORF2 transcripts at different sucrose concentrations ranging from 20 mM to 540 mM (Figure 1C). We observe a dose-dependent response for both the HH- and HHF-uORF2 transcripts, with a faint band already appearing at a concentration as low as 20 mM, and only a very moderate increase for the peptidyl-tRNA band for concentrations higher than 150 mM (Figure 1C). Next, we wanted to compare

the translation efficiency between the HH- and the HHF- transcripts. IVT reactions for both transcripts performed in parallel showed that both the amount of free peptide as well as of ribosome nascent-chain complexes (RNC) are considerably higher for the HHF transcript than for the HH-uORF2 transcript (Figure 1D). In conclusion, the results indicate that strong *in vitro* stalling of the HHF transcript can already be achieved at cryo-EM compatible sucrose concentrations of 150 mM.

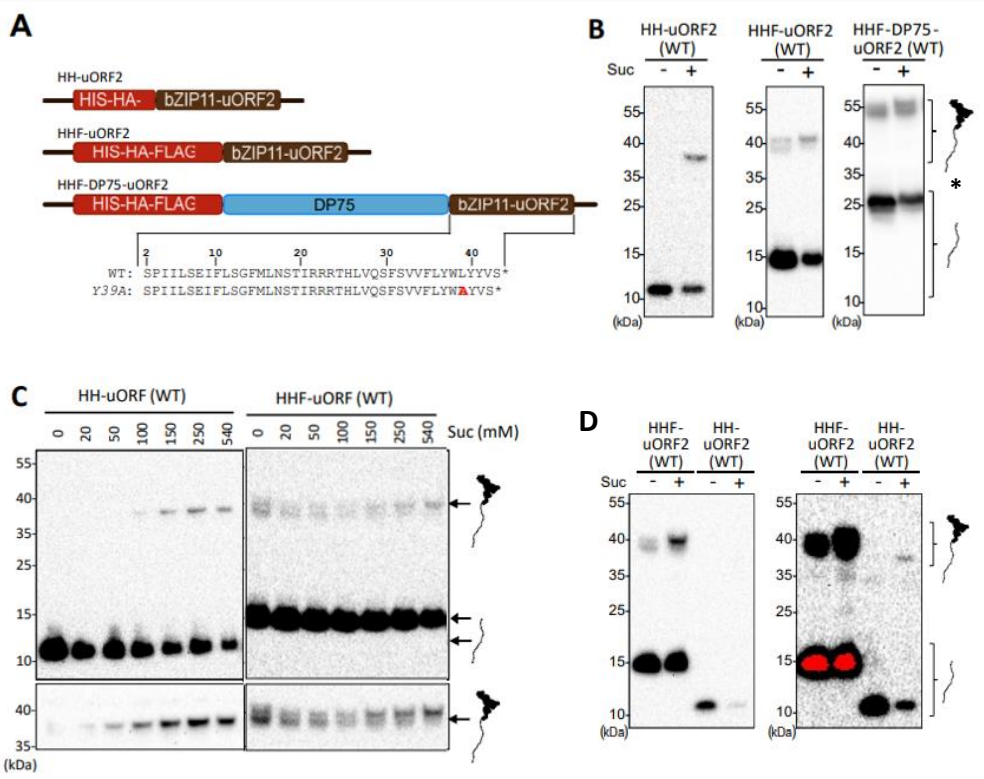

Figure 1: uORF2-bZIP11 induces stalling of WG ribosome in a sucrose dependent manner and is affected by the upstream sequences. A) The constructs that were used for the in vitro translation (IVT) reactions contain different sequences upstream of uORF2: a Hexa-Histidin (HH), Hexa-Histidin-HA-3xFlag (HHF) or Hexa-Histidin-HA-3xFlag followed by a 75 amino acid linker (HHF-DP75) as described[17]. Wild type and mutant uORF amino acid sequences are shown below. B) Western blot of IVT reactions in the presence or absence of 540 mM Sucrose shows stalling for the HH transcript and a shift from the peptidyl-tRNA band observed in the absence of sucrose (*) to a higher molecular weight for the HHF and HHF-DP75 transcripts. C) and D) Western blot of IVT reactions with the HH (left) and HHF-transcript (right) at increasing sucrose concentrations shows translational stalling for the HH-transcript, and a shift from the sucrose-independent peptidyl tRNA to a higher-molecular weight with increasing sucrose concentrations. D) Western blot of IVT reactions with ribosomes translating either the HHF- or the HH- uORF2 transcript, in otherwise identical conditions, in the absence (-) or presence of 540 mM sucrose (+). Both the amount of free peptide (bottom) and the

peptidyl tRNA (top) is higher for the HHF transcript. The image on the right is a longer exposure of the left image (red area indicates overexposure).

Sucrose-mediated stalling of bZIP-uORF2 locks the ribosome into a rotated and unrotated state

To investigate the molecular mechanism behind sucrose-induced ribosome stalling on bZIP11 uORF2, we determined the structure of sucrose-stalled wheat germ ribosome by cryoEM. For this, ribosomes translating HHF-uORF2 in the presence of 540 mM sucrose were subjected to affinity purification targeting the N-terminal Hexa-Histidin affinity tag of the nascent peptide, followed by ultracentrifugation and pellet resuspension in buffer containing 150 mM of sucrose to provide an increased contrast for cryoEM imaging. Since our own (Figure 1C) as well as previous IVT reactions[17] show that the majority of peptide is fully synthesized and released from the ribosome even in the presence of sucrose, this affinity step was conducted to enrich the amount of stalled ribosome nascent-chain complexes (RNC) and separate them from translationally terminated or non-initiated ribosomes. The resulting sample shows an increased ratio RNC's to fully synthesized peptide (Figure S1), which was used for cryoEM data acquisition.

To obtain a high-resolution structure of stalled ribosomes and separate the different translational states, we subjected the obtained ribosome particle images to several rounds of 3D classification using different masks: a first round focusing on the small subunit (SSU) to separate rotated from unrotated states, followed by two rounds of classification focusing on the tRNAs (Figure S2). Using this classification protocol, we obtained two main states: 33 % of the particles are in unrotated post-translocation state containing a P-site tRNA, and 17% in a rotated pre-translocation state containing a tRNA in the A/P and the P/E-site (Figure 2A & S2). The other two classes comprising 11 % each were discarded as they contained either a weak density for the P-tRNA or the P- and E-site tRNAs (Figure S2), and likely represent intermediate states. Comparison of the maps of the rotated and unrotated state clearly visualizes a rotation of the SSU in the rotated state as well as only partial transition of the A-site tRNA towards the P-site (Figure 2B). To resolve the structural details of the two states, we refined both classes to a resolution of 3.7 Å (unrotated) and 4.0 Å (rotated). We used the better-resolved map of the unrotated state to build an atomic model of the *T. aestivum* ribosome, starting from a previous model based on a lower resolution map[18].

We interpreted densities corresponding to amino-acyl-tRNAs, nascent peptide and sucrose in the context of the atomic models for LSU and SSU. Both, unrotated and rotated structures show a clear density for the tRNAs (Figure 2 & 3), as well as a continuous density for the nascent peptide, which extends into the exit tunnel (Figure 3A). The resolution obtained is

insufficient to unambiguously assign sidechains but allowed for approximate tracing of the nascent peptide backbone (Figure 3A & S4A). The rotated state reconstruction is a pre-translocation configuration and exhibits tRNAs in the A/P- and P/E-sites, suggesting that translation elongation is inhibited. In the unrotated state, only the P-site tRNA is occupied, consistent with stalling during termination.

Rotated pre-translocation and termination states have also been recently described for peptide-specific stalling induced by the compound PF846 [8] as well as in trailing, collided ribosomes within the same polysome[19]**.** To rule out that the A/ P transition state occurs due to ribosome collision[19,20], linear gradient ultracentrifugation was conducted, revealing only residual amounts of di or trisomes in the assay (Figure S3). Consistent with the gradient profile, the Western blot analysis only shows a single peptide length (Figure S3B). While we cannot fully rule out ribosome collisions, it is unlikely that they significantly contribute to the observed stalling. Previously, incomplete pairing of the CCA end with the P-loop was contributed to result in the observed elongation arrest[21]. A close-up of the P-tRNA CCA-ends of the two sucrose-stalled structured shows that there is complete base pairing between the CCA and P-loop nucleobases for both the rotated as well as the unrotated state (Figure S4B). The elongation pause depicted by the rotated state can therefore not be attributed to incomplete CCA-P-loop basepairing of the P-tRNA.

For the unrotated, pre-termination state, we could not separate a class with the bound termination factor eRF1. Previously, for both the bacterial and eukaryotic ribosome structures stalled transcript-specifically by a small molecule, complex structures with bound release factors were i) not observed[22], ii) obtained at extremely low abundances (2.5 %) from much larger datasets[23], or iii) determined after modification of the wild type peptide that resulted in stronger stalling[6,9]. Interestingly, the nucleobase U2956 that forms part of the PTC, which is conserved between the *E. coli* (Ec U2585), human (Hs) and the *T.aestivum* (Ta) ribosome, is in an upward conformation in both the unrotated and rotated states of the stalled ribosome (Figure 3B, S4C). This upward conformation of U2956 would result in a clash with the second glycine of the GGQ loop of eRF1 when compared to the structure of the human ribosome with bound eRF1 (Figure 3B), where respective nucleobase is flipped by 90 degrees to allow binding of eRF1 and the formation of the GGQ loop (Figure 3B). Compared to our structure, the C-terminal end of the nascent peptide is also located closer towards U4501 (EC2585) in the PF846-stalled human ribosome, which was previously argued to push U4501 into the downward state (Figure 3B). In our structure, the peptide is located further away from the PTC and allows for accommodation of U2956 in an upward state (Figure 3B, S4C). Instead, U2955 overlaps with the position of the U4501 in the downward conformation of the human structure (Figure S4C). In case of the ornithine- as well as tryptophan-induced stalling of the *E.coli* (Ec) ribosome[6,22], the U2585 was also

reported in upward conformation preventing the binding of RF2[6], or the formation of the GGQ loop in the complex structure where RF2 could be resolved despite its low abundance[23]. Therefore, sucrose-induced termination arrest of bZIP11-uORF2 potentially functions via a flipped nucleobase at the PTC that prevents the binding of eRF1, similar to the ornithine- and tryptophan-induced mechanism of anti-termination[6,22].

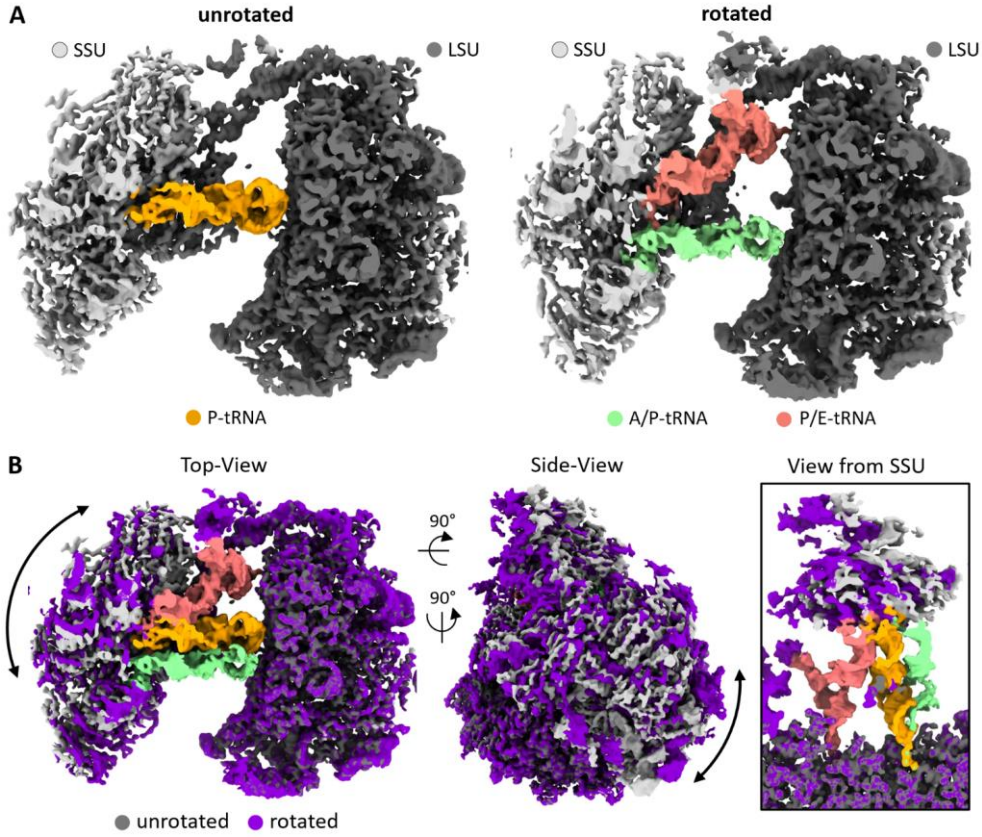

Figure 2: Sucrose-mediated stalling of bZIP-uORF2 results a rotated and unrotated state of the ribosome. A) Cryo-EM maps of the unrotated and rotated state, with the P-tRNA (yellow) and A/P- (green) and P/E-tRNAs (red) highlighted respectively. C) Overlap of unrotated and rotated state visualizing the motion on the small subunit (SSU), and close-up view of the tRNA cleft viewed from the SSU.

Sucrose binds to a conserved binding pocket during bZIP-uORF2 ribosome stalling

The mechanism of sucrose-induced stalling previously remained elusive, but other mechanisms of transcript-specific, metabolite-induced stalling have shown an interaction of the metabolite with the peptide inside the exit tunnel [6,21]. For the unrotated state, we observe a density inside a pocket of the 28S rRNA, which is not explained by the atomic models of the ribosome and nascent chain (Figure 3A & 3C). The observed density is located

approximately 24 Å from the PTC, which corresponds to approximately 12 amino acids in the traced peptide backbone. Further towards the tunnel exit, the peptide density starts to fade. The observed length of the structured region of the first 12 amino acids coincides with the length of the C-terminal stretch that was previously shown to be essential for stalling of the bZIP11-uORF2 peptide[17]. The density positions close to a constriction-site formed by uL22 and uL4 that was previously shown to be involved in stalling[6,19,24]. It contacts the peptide as well as a pocket formed by rRNA nucleotides (Figure 3A), and its overall mass is consistent with that of sucrose (Figure 3C). The density is not present in the rotated state, where instead a longer density connected to the nascent peptide density reaches into the binding pocket. Importantly, the density is absent in a control dataset of idle wheat-germ ribosomes in 150 mM sucrose without added mRNA (Figure S5). Due to the agreement in size of the density with sucrose and its absence in the control dataset, we conclude that the density we observe for the unrotated state represents sucrose. It is absent in the rotated state potentially due to a sidechain of the peptide that occupies the pocket. Local fitting of sucrose into the density positions it close to the rRNA nucleotides C880, A885, G883 and the Histidine 90 of uL22 (Figure S6). The hydroxy groups of sucrose are positioned 2- 5.6 Å from the adjacent nitrogen atoms of the rRNA and the imidazole of His90, and there is no clash between position of the locally fitted sucrose and the neighboring atoms. For the two closest contacts between sucrose and the rRNA, which are positioned to each other at a distance of 2 and 2.8 Å (Glucose C2 – G883, Fructose C3 – G883, respectively), we can identify two connecting densities in the cryoEM density map (Figure S6C).

The binding site of sucrose overlaps with the binding site of the small heterocyclic molecule PF846 which was previously shown to induce transcript-specific stalling[9,21] (Figure 3D). Similar to the two translational arrest states we observe for the bZIP11-uORF2 stalling, PF846 was also shown to mediate both elongation and termination arrest[8,9]. Comparison of our unrotated structure to the structure of the tryptophan-stalled *E. coli* ribosome translating TnaC shows that tryptophan binds to a site in the *E. coli* ribosome that corresponds to that of sucrose in the wheat-germ ribosome. Furthermore, all rRNA nucleobases involved in the ternary complex are conserved between the *T. aestivum*, *H. sapiens* and *E. coli* ribosomes (Figure S6D), indicating that the binding pocket is structurally conserved across those three kingdoms and functionally exploited.

Comparing the sucrose, PF864- and tryptophan molecules shows that these molecules share a negatively charged carboxy, hydroxy or carbonyl group in proximity to G883, indicating the formation of a hydrogen bond (Figure S6B & S6D). For all three molecules, additional density can be observed between the respective atoms (Figure S6C, S7B). For TnaC-mediated stalling, sidechain specificity is mediated by the shape, size and properties of the binding pocket rather than with the peptide[6]. While we cannot resolve the individual

sidechains for bZIP-uORF2 to address their contribution to stalling, we do observe a connective density between the peptide and sucrose (Figure 3C) which potentially stabilizes sucrose. Since nearly all C-terminal residues upstream of sucrose are essential for stalling [17], peptide-specificity is likely mediated by multiple sidechains that form interactions with the tunnel wall nucleotides- similar to the TnaC peptide, which is supported by multiple connecting densities that we observe (Figure 3C & S4A). In conclusion, our results identify the binding site of sucrose and indicate that the rRNA binding pocket is conserved across kingdoms, for which specific molecules can lead to stalling in concert with the peptide.

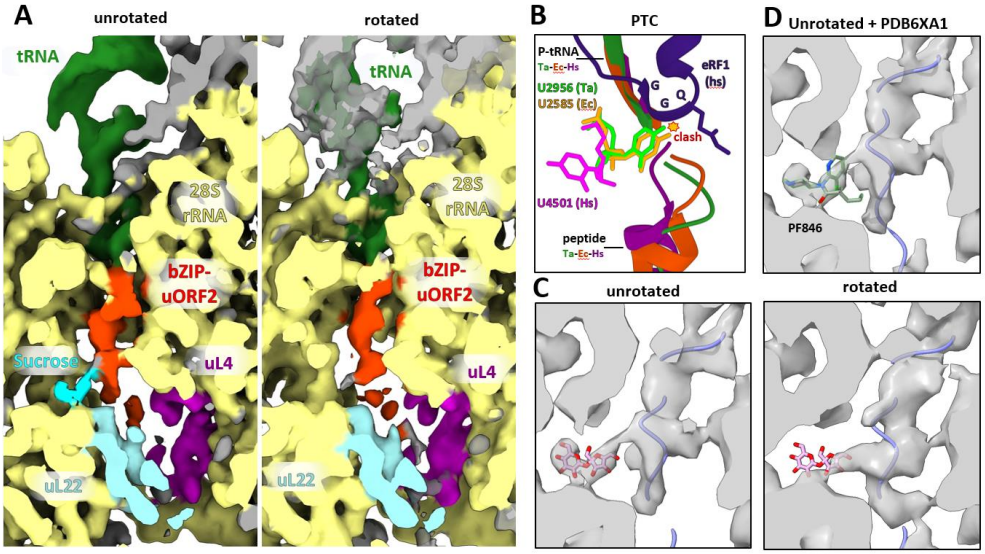

Figure 3: Characterization of Sucrose binding pocket and inhibition of eRF1 binding. A) Maps of stalled ribosomes in the unrotated and the rotated state. B) PTC region of the atomic model of the stalled unrotated state (Ta, shades of green) overlapped with the PF846-stalled structure of the human ribosome with bound eRF1 (hs, PDB 6xa1, shades of purple) and the tryptophan-stalled structure of the *E. coli* ribosome (Ec, orange, PDB7O19). The clash of U2956 with eRF1 in the accommodated state is indicated in red. C) Maps of stalled ribosomes in the unrotated and rotated state overlapped with the peptide backbone (blue) and fitted sucrose molecule (pink). D) PF846 overlapped with the map of the unrotated state after rigid body fitting of the structure of the PF846-stalled human ribosome (PDB 6xa1).

Stop codon is essential for uORF mediated stalling in angiosperms but not in gymnosperms

In the sucrose-stalled, unrotated state of the bZIP-uORF2 translating ribosome the stop codon resides in the A-site tRNA. Previous studies highlighted the importance of the stop codon for the metabolite-induced stalling of bZIP-uORFs in *A.thaliana* and TnaC in *E.coli*[5], which presumably aid stalling due to a reduced hydrolyzation rate[25]. In contrast the stop-

codon position is not essential for other metabolite-induced stalling mechanisms, for example the AAP attenuator peptide in fungi[26]. For the bZIP11-uORF2 transcript, translation regulation was shown to be abolished when the stop codon was shifted by 13 codons[27], but a detailed analysis on the reliance of the stop codon position was lacking. To further investigate the stop codon reliance of bZIP11-uORF2, we performed IVT reactions of transcripts where the stop codon was changed into an alanine and introduced 1, 2, 5 and 10 codons downstream (Figure 4A). For all the transcripts stalling was abolished, with a shift by one codon already fully abolishing stalling (Figure 4B). Therefore, the stop codon is essential for the sucrose-induced stalling of bZIP11-uORF2.

Accordingly, the stop codon position of bZIP-uORFs is highly conserved amongst angiosperms such as *A.thaliana*. However, this is not the case for gymnosperms[28] (Figure 4C). Previous research revealed that the CPuORFs of the bZIP11 homologues in *Picea abies* (Norway spruce) and *Pinus taeda* (loblolly pine) are capable of the sucrose dependent regulation of translation, despite the lack of a conserved stop codon[28]. To explore the functional conservation of sucrose- induced ribosome stalling throughout angiosperms and gymnosperms, capped RNA was produced similar to bZIP-11-uORF2, but with the CPuORF of *A. thaliana* replaced by the CPuORF of the monocotyledon *Oryza sativa* bZIP78 or bZIP77 (uORF(Osa78), and uORF(Osa77), respectively) or of the gymnosperm species Picea abies (HH-uORF(Pab)) or Pinus taeda (uORF(Pta)) (Figure 4C). IVT of these transcripts revealed that all transcripts induced a sucrose-dependent appearance of a PtR and inhibition of FP production, except for uORF(Osa77) (Figure 4D). Interestingly, the CPuORF of O. sativa bZIP77 lost the conserved position of the stop codon (Figure 4C).

To explore whether ribosome stalling can be restored by correct positioning of the stop codon, the valine at position 40 of *O. sativa* bZIP77 was mutated into a stop codon (ORF(Osa77_ES)). In addition, the serine codon at position 27 of *P. abies* S1-bZIP CPuORF was also mutated into a stop codon (uORF(Pab_ES)) (Figure 4C). Interestingly, presence of sucrose in the IVT reaction of uORF(Osa77_ES) RNA reduced production of the FP, moreover the presence of a faint PtR was observed indicating restoration of the stalling mechanism (Figure 4D). In contrast, altering the Ser27 of *P. abies* S1-bZIP CPuORF into a stop codon abolished sucrose-induced ribosome stalling. The stop codon of the CPuORF of *P. abies* S1-bZIP, is 14 codons downstream of the conserved stretch of amino acids and the conserved position of the stop codon in angiosperms. It is to be expected that the ribosome stalls at a similar position on the CPuORF of gymnosperms and angiosperms. Therefore, if the CPuORF of S1-bZIP *P. abies* stalls on the same position, the PtR- peptide will be 14 amino acids shorter than the FP, a difference separable by SDS-PAGE. Indeed, treatment of the IVT mixtures of HH-uORF(Pab) RNA with RNAse A revealed an additional band with a lower apparent molecular weight, but only in the sucrose treated sample (Figure 4E, lower panel).

These results show that the stop codon is crucial for stalling of angiosperm S1-bZIP CPuORFs, but not for gymnosperm S1-bZIP.

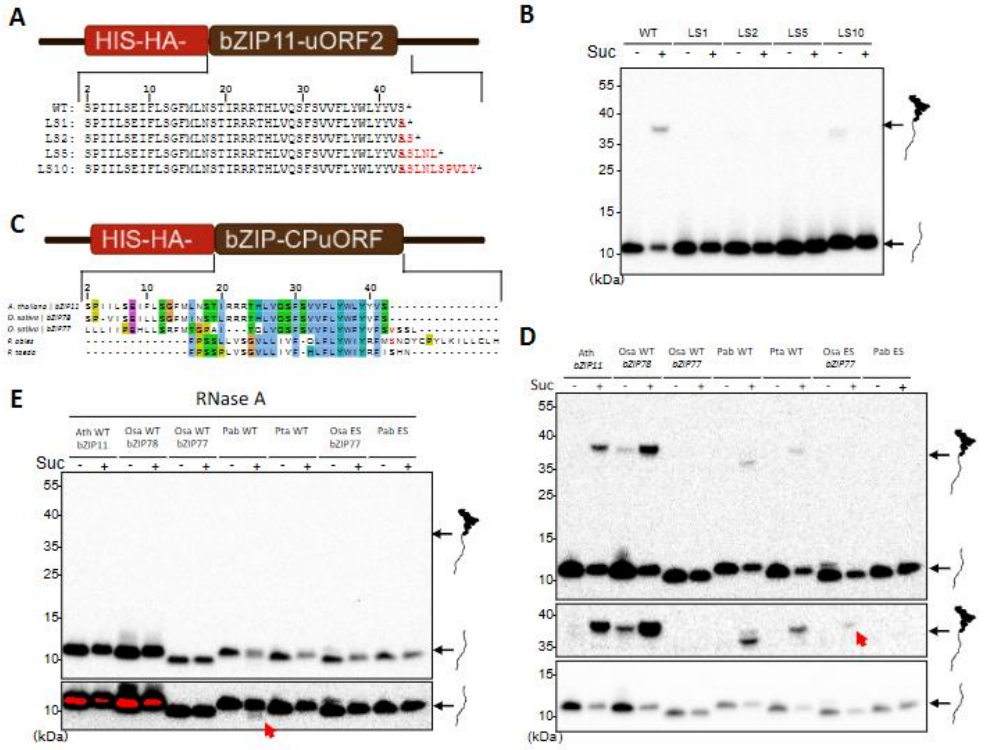

Figure 4: bZip-uORF sucrose-mediated stalling is maintained across evolutionary divergent plants requiring a stop codon in angiosperms, but not in gymnosperms. (A) The stop codon of HH-uORF2(WT) was mutated into an alanine codon and inserted as a late stop codon (LS) one, two, five or ten codons downstream (LS1, LS2, LS5 or LS10, respectively). (B) RNA of the constructs shown in (A) were translated in vitro in the presence (+) or absence (-) of 540 mMsucrose (Suc) and analyzed using SDS-PAGE and immunoblot detection using anti-HA antibody. (C) Schematic representation of RNA used in (D) and (E). The Arabidopsis thaliana (Ath) bZIP11-uORF2 was replaced by the CPuORF of an orthologues S1-group bZIP of Oryza sativa (Osa), Picea abies (Pab) or Pinus taeda (Pta). The V and S amino acids marked in red were changed into an early stop (ES) codon in the Pab_ES and Osa_ES_bZIP77 RNAs. The alignment was adapted from Peviani et al. (2016) (D) Transcripts mentioned in (C) were translated and analyzed similarly as in (B). (E) Samples of (D) were treated with RNase A before analysis. Red arrows indicate restored PtR (D) or released PtR peptide after RNase A treatment (E). The middle and lower panel in (D) shows the PtR or FP of the upper panel but with a longer or shorter exposure time, respectively. The lower panel in (E) shows the FP of the upper panel with a longer exposure time. The peptidyl-tRNA and full peptide are indicated. Red regions on the blot indicate overexposure.

Discussion

In this study, using cryoEM we determined two different translational arrest states of stalled ribosomes translating bZIP11-uORF2 in the presence of sucrose. The structures reveal that sucrose, together with the bZIP11-uORF2 peptide, locks the ribosomes in an unrotated, post-translocation state with the Ser42-tRNA in its P-site. The second observed state is a rotated, pre-translocation state with the tRNA in the A/P-site, which notably does not contain sucrose in the identified binding pocket. For the unrotated state, termination arrest is potentially mediated by the conserved nucleobase U2956, which is in an upward conformation and prevents binding of eRF1. This would depict the same mechanism of termination inhibition which was described by the tryptophan-induced stalling of the TnaC peptide and the ornithine-induced stalling of the SpeFL peptide[6,22]. Unlike previously reported for a stalled pre-translocation state[21], we do observe complete base-pairing of the CCA end to the P-loop, indicating a different mode of elongation arrest. But, the detailed mechanism of how the rotated, intermediate state is stabilized and translocation is inhibited could not be resolved.

The presence of the two stalling intermediates, together with the data on the stop codon reliance, allows to hypothesize a sequence of actions for sucrose-induced stalling of bZIP11-uORF2. First, translation of the uORF2 peptide leads to elongational slow-down and arrest, mediated by the interaction of multiple nascent chain sidechains with the exit tunnel (Figure 3C & Yamashita et al.[17]), which results in the rotated state with incomplete translocation of the peptidyl-tRNA into the P-site of the decoding center. This is followed by translocation of the tRNA into the P-site, and the rearrangement of the peptide exposing the sucrose binding site. Conversely, translocation might be preceded or require a conformational change of the peptide in the tunnel to allow for translocation. Finally, binding of sucrose retains the upward conformation of U2956 at the PTC, which prevents the binding of eRF1 - similar to the binding of tryptophan in the TnaC mediated stalling[6]. The binding of sucrose is dependent on complete accommodation of the tRNA in the P-site and formation of the peptide – indicated by the absence of sucrose in the control dataset without mRNA, which is again similar to the tryptophan/ TnaC stalling mechanism. The reliance on complete formation of the peptide for sucrose to bind also explains the transcript specificity, as it does not bind to the ribosome and interfere with translation in the absence of the bZIP-uORF2 peptide.

The stop codon also plays an essential role for the termination arrest, as we have shown by mutational analysis where a shift by single codon abolishes stalling. The stalling contribution of the stop codon is possibly due to a necessary slow-down for translational elongation, resulting from reduced reaction kinetics of eRF1 hydrolysis[25]. This is another commonality between the sucrose and tryptophan induced stalling, where the stop codon is essential[5].

While the detailed interactions of the bZIP11-uORF2 peptide remain to be determined, our structural data contributes additional insight into the concerted mechanism of sucrose-stalling that is reliant on the peptide, metabolite and the stop codon. Notably, it was shown for other composite stalling mechanisms that slight variations in the peptide sequence can reduce the requirement on the other contributing factor, such as was shown for the TnaC peptide, where a mutation of the penultimate residue drastically reduced the IC50 of tryptophan and increased the stalling in absence of tryptophan[6]. Another example which we illustrate here is the sucrose-induced bZIP-uORF stalling in gymnosperms, with its changed bZIP-uORF sequence and the reliance on the stop codon for stalling abolished. It will be interesting to unravel the requirements of the individual contributary factors and their evolutionary implications.

In previous structural studies on the PF846- and tryptophan-induced stalling the common binding site for both molecules[6,21] was not mentioned. Here, we present evidence that in eukaryotes this binding pocket is also targeted by sucrose, a naturally synthesized small molecule for the translational regulation of a highly conserved group of CP-uORFs present in flowering plants. The big evolutionary gap of 3 billion years between pro- and eukaryotes, and the abundance of other CP-uORFs raises the possibility that many other metabolites may potentially exploit the same binding pocket for translational control in eukaryotes. In addition, there might be other conserved binding sites that are exploited for translational regulation, for example the binding site of ornithine in the context of SpeFL mediated stalling[22], which is structurally conserved between prokaryotes and eukaryotes. This urges for the structural characterization of other characterized metabolites shown to inhibit eukaryotic translation[30,31]. In addition to the characterization of native metabolite-induced translational regulation, the identification of new binding sites might present interesting targets for novel therapeutics as it was shown for PF846[21] and present novel opportunities for modulating plant traits.

References

1. Gebauer, F., Preiss, T. & Hentze, M. W. From cis-regulatory elements to complex RNPs and back. *Cold Spring Harb. Perspect. Biol.* **4**, 1–14 (2012).
2. Seip, B. & Innis, C. A. How Widespread is Metabolite Sensing by Ribosome-Arresting Nascent Peptides? *Journal of Molecular Biology* vol. 428 2217–2227 (2016).
3. Stewart, V. & Yanofsky, C. Evidence for transcription antitermination control of tryptophanase operon expression in Escherichia coli K-12. *J. Bacteriol.* **164**, 731–740 (1985).
4. Gong, F., Ito, K., Nakamura, Y. & Yanofsky, C. The mechanism of tryptophan induction of tryptophanase operon expression: Tryptophan inhibits release factor-mediated cleavage of TnaC-peptidyl-tRNAPro. *Proc. Natl. Acad. Sci. U. S. A.* **98**, 8997–9001 (2001).
5. Konan, K. V. & Yanofsky, C. Regulation of the Escherichia coli tna operon: Nascent leader peptide control at the tnaC stop codon. *J. Bacteriol.* **179**, 1774–1779 (1997).
6. van der Stel, A. X. *et al.* Structural basis for the tryptophan sensitivity of TnaC-mediated ribosome stalling. *Nat. Commun.* **12**, (2021).
7. Lintner, N. G. *et al.* Selective stalling of human translation through small-molecule engagement of the ribosome nascent chain. *PLOS Biol.* **15**, e2001882 (2017).
8. Li, W. *et al.* Structural basis for selective stalling of human ribosome nascent chain complexes by a drug-like molecule. *NSMB* (2019).
9. Li, W., Chang, S. T., Ward, F. R. & Cate, J. H. D. Selective inhibition of human translation termination by a drug-like compound. *Nat. Commun.* 3–11 (2020) doi:10.1038/s41467-020-18765-2.
10. Van Der Horst, S., Filipovska, T., Hanson, J. & Smeekens, S. Metabolite control of translation by conserved peptide uORFs: The ribosome as a metabolite multisensor. *Plant Physiol.* **182**, 110–122 (2020).
11. Takahashi, H. *et al.* Exhaustive identification of conserved upstream open reading frames with potential translational regulatory functions from animal genomes. *Sci. Rep.* **10**, 16289 (2020).
12. Kochetov, A. V. Alternative translation start sites and hidden coding potential of eukaryotic mRNAs. *BioEssays* **30**, 683–691 (2008).
13. Vaughn, J. N., Ellingson, S. R., Mignone, F. & Von Arnim, A. Known and novel post-transcriptional regulatory sequences are conserved across plant families. *RNA* **18**, 368–384 (2012).
14. Takahashi, H. *et al.* Comprehensive genome-wide identification of angiosperm upstream ORFs with peptide sequences conserved in various taxonomic ranges using a novel pipeline, ESUCA. *BMC Genomics* **21**, (2020).
15. Dröge-Laser, W. & Weiste, C. The C/S1 bZIP Network: A Regulatory Hub Orchestrating Plant Energy Homeostasis. *Trends in Plant Science* vol. 23 422–433 (2018).
16. Hanson, J., Hanssen, M., Wiese, A., Hendriks, M. M. W. B. & Smeekens, S. The sucrose regulated transcription factor bZIP11 affects amino acid

metabolism by regulating the expression of ASPARAGINE SYNTHETASE1 and PROLINE DEHYDROGENASE2. *Plant J.* **53**, 935–949 (2008).
17. Yamashita, Y. *et al.* Sucrose sensing through nascent peptide-meditated ribosome stalling at the stop codon of Arabidopsis bZIP11. **591**, 1266–1277 (2017).
18. Gogala, M. *et al.* Structures of the Sec61 complex engaged in nascent peptide translocation or membrane insertion. *Nature* **506**, 107–10 (2014).
19. Matsuo, Y. *et al.* RQT complex dissociates ribosomes collided on endogenous RQC substrate SDD1. *Nat. Struct. Mol. Biol.* **27**, 323–332 (2020).
20. Juszkiewicz, S. *et al.* ZNF598 Is a Quality Control Sensor of Collided Ribosomes Correspondence. *Mol. Cell* **72**, 469–481 (2018).
21. Li, W. *et al.* Structural basis for selective stalling of human ribosome nascent chain complexes by a drug-like molecule. *Nat. Struct. Mol. Biol.* **26**, (2019).
22. Herrero del Valle, A. *et al.* Ornithine capture by a translating ribosome controls bacterial polyamine synthesis. *Nat. Microbiol.* **5**, 554–561 (2020).
23. Su, T. *et al.* Structural basis of L-tryptophan-dependent inhibition of release factor 2 by the TnaC arrest peptide. *Nucleic Acids Res.* **49**, (2021).
24. Takamatsu, S. *et al.* Reverse genetics-based biochemical studies of the ribosomal exit tunnel constriction region in eukaryotic ribosome stalling: Spatial allocation of the regulatory nascent peptide at the constriction. *Nucleic Acids Res.* **48**, 1985–1999 (2020).
25. Schuller, A. P. & Green, R. Roadblocks and resolutions in eukaryotic translation. *Nat. Rev. Mol. Cell Biol.* **19**, 526–541 (2018).
26. Fang, P., Wang, Z. & Sachs, M. S. Evolutionarily Conserved Features of the Arginine Attenuator Peptide Provide the Necessary Requirements for Its Function in Translational Regulation. *J. Biol. Chem.* **275**, 26710–26719 (2000).
27. Weltmeier, F. *et al.* Expression patterns within the Arabidopsis C/S1 bZIP transcription factor network: Availability of heterodimerization partners controls gene expression during stress response and development. *Plant Mol. Biol.* **69**, 107–119 (2009).
28. Peviani, A., Lastdrager, J., Hanson, J. & Snel, B. The phylogeny of C/S1 bZIP transcription factors reveals a shared algal ancestry and the pre-angiosperm translational regulation of S1 transcripts. *Sci. Rep.* **6**, 1–11 (2016).
29. Wang, T. *et al.* Dynamics of transcription–translation coordination tune bacterial indole signaling. *Nat. Chem. Biol.* **16**, 440–449 (2020).
30. Onoue, N. *et al.* S-adenosyl-L-methionine induces compaction of nascent peptide chain inside the ribosomal exit tunnel upon translation arrest in the Arabidopsis CGS1 gene. *J. Biol. Chem.* **286**, 14903–14912 (2011).
31. Bhushan, S. *et al.* Structural basis for translational stalling by human cytomegalovirus and fungal arginine attenuator peptide. *Mol. Cell* **40**, 138–146 (2010).
32. Mastronarde, D. N. Automated electron microscope tomography using robust prediction of specimen movements. *J. Struct. Biol.* **152**, 36–51

(2005).
33. Scheres, S. H. W. RELION: Implementation of a Bayesian approach to cryo-EM structure determination. *J. Struct. Biol.* **180**, 519–530 (2012).
34. Zheng, S. Q. *et al.* MotionCor2: anisotropic correction of beam-induced motion for improved cryo-electron microscopy. *Nat. Methods* **14**, 331–332 (2017).
35. Zhang, K. Gctf: Real-time CTF determination and correction. *J. Struct. Biol.* **193**, 1–12 (2016).
36. Liebschner, D. *et al.* Macromolecular structure determination using X-rays, neutrons and electrons: Recent developments in Phenix. *Acta Crystallogr. Sect. D Struct. Biol.* **75**, 861–877 (2019).
37. Emsley, P., Lohkamp, B., Scott, W. G. & Cowtan, K. Biological Crystallography Features and development of Coot. (2010) doi:10.1107/S0907444910007493.

Material & Methods

In vitro translation assay

Twenty µl of control in vitro translation (IVT) reaction was performed in the absence of sucrose using 10µl wheat germ extract (Promega, L4380), 1.6 µl complete amino acid mixture (Promega, L4461), 0.4 µlRibolock nuclease inhibitor (ThermoFisher Scientific, EO0382), 6 µl water and 2 µl 125 nM HHF-uORF2RNA. For cryo-EM analysis of HH-uORF2 mRNAs, 200 µl IVT reactions were briefly spun (5 min at 15,000 xg) and loaded onto a 1M sucrose cushion (50 mM Tris-HCl (pH 7.0), 250 mM Potassium acetate (KOAc),25 mM Magnesium acetate (Mg(OAc) 2), 2 mM 1,4-dithiothreitol (DTT) and 1M sucrose) followed byultracentrifugation at 91,000 RPM for 45 minutes in a precooled Beckman Optima TLX with TLA-100.2rotor. The pellet was resuspended in 50 µl resuspension buffer (20 mM Tris-HCl (pH 7.0), 50 mM KOAc,10 mM Mg(OAc) 2, 1 mM DTT and 150 mM sucrose) and used for cryo-EM analysis.

For affinity purification of stalled ribosomes on HHF-uORF2 mRNA in the presence of sucrose, the IVT was scaled up to 2 x 500 µl reaction in the presence of 540 mM sucrose. Next, the IVT reaction was ultracentrifuged over a 1M sucrose cushion as described above. The pellets were resuspended in 250 µl RNC buffer (50 mM Tris-HCl (pH 7.0), 250 mM KOAc, 25 mM Mg(OAc) 2, 5 mM 2-mercaptoethanol and 540mM sucrose), combined and incubated with 60 µl cobalt-based magnetic beads (ThermoFisher Scientific,10103D) for 10 minutes at 4°C, followed by thorough washing with RNC buffer and RNC buffer supplemented with 0.5% Triton-X100. Stalled ribosomes were eluted using RNC buffer with 200 mM imidazole and the eluate was pelleted again through a 1M sucrose cushion. The pelleted ribosomes wereresuspended in 30 µl resuspension buffer and stored on ice until they were loaded onto the cryo-EM grid.

Western Blot analysis

SDS-PAGE loading buffer (premixed 4 µl Laemmli sample buffer (Bio-Rad) and 1.6 µl Bolt reducing agent(Thermo Fisher Scientific)) was added to the samples followed by separation on 8% Bolt Bis-Tris gel in MESbuffer (Thermo Fisher Scientific), followed by transfer onto a 0.45 µm PVDF Immobilon-P membrane (Bio-Chapter 691Rad). The blots were probed with Anti-HA-peroxidase, high affinity antibody (Roche) andchemiluminescence was visualized using a ChemiDoc gel system (Bio-Rad).

Cryo-EM grid preparation

Cryo-EM grids were prepared by applying 3ul of sample at a concentration of 2- 4mg/ ml to freshly glow discharged Quantifoil Cu200 R1.2/ 1.3 (HHF-bZIP11-uORF2 + Sucrose) or R2/1 (control datasets) holey carbon. The grids were flash-frozen using a Vitrobot Mark IV

(Thermo Fisher Scientific) with 595 blotting paper (Ted Pella) set to 4 ˚C, 100% humidity and a blot force of 0 for 4 s, and plunged into a liquid ethane/ propane mixture.

Cryo-electron microscopy data acquisition and processing

The dataset of the sucrose-stalled, HHF-bZIP11-uORF2 translating Wheat germ ribosomes was acquired on a 200 kV Talos Arctica (Thermo Fisher Scientific) equipped with a post-column energy filter and a K2 Summit direct-electron detector (Gatan) at Utrecht University. Movies containing 70 frames were acquired with SerialEM [32] at varying defocus of 0.8 - 1.8 µm, at a pixel size of 1.015 Å/ pixel, a dose rate of 4 e^-/ pix/ sec and a total dose of 56 e^-/ Å. Control datasets of empty were acquired on a 300 kV Titan Krios (Thermo Fischer Scientific) equipped with a post-column energy filter and K3 at the Netherlands Centre for Electron Nanoscopy (NeCEN). Movies containing 42 frames were acquired with SerialEM [32] at varying defocus of 0.8 - 2.2 µm, a pixel size of 0.86 Å/ pixel, a dose rate of 15 e^-/ pix/ sec and a total dose of 54 e^-/ $Å^2$. Datasets were processed using Relion 3.1 [33]. Micrographs were motion-corrected using MotionCor2 [34] and CTF-corrected using gCTF [35]. Ribosomes were picked using Relion's Laplacian-of-Gaussian auto-picking, and false-positive particles were removed by 2 rounds of 2D classification and one round of 3D classification. A high-resolution map of all ribosomes was obtained by alignment using Refine3D. For the separation of the different t-RNA states, masks encompassing the A-, P- and E-tRNA site or just the P-tRNA site were employed using Relion's background subtraction followed by 3D classification. High-resolution maps of the three translating states were obtained using Relion's Refine3D, followed by one round of CTF refinement, Bayesian polishing and a final alignment using Refine3D and a total dose of xx e^-/ Å. The maps were sharpened using Phenix's auto-sharpen [36].

Model Building

An initial model of the wheat germ ribosome was build using Coot 0.9 [37] by placing and refining the individual subunits of PDB 4v7e[18] into the sharpened cryo-EM map of the ribosome containing a P- and E-tRNA.

Analytical Ultracentrifugation

Linear gradients of 10- 50% buffered sucrose (50mM Tris pH 7.6, 150mM KCl, 7 mM MgCl, 500 µg/ml Heparin, 1mM Spermidine, 1mM DTT) were prepared by layering a 50% buffered sucrose solution under a 10% buffered sucrose cushion in Sw41 tubes using a syringe, followed by mixing using a Gradient Fractionator/ Master Combo (BioComp Instruments). The gradients were centrifuged for 90min at 90.000 rpm (260,000 g_{max}) and 4 °C using a TH-641 rotor (Thermo Fisher Scientific) and an Optima-MAX Ultracentrifuge (Beckmann Coultier). The gradients were fractionated and a continuous UV-absorption profile (A260 and A280) was measured using a Gradient Fractionator/ Master Combo (BioComp Instruments).

Acknowledgements

We would like to thank Chris Schneijdenberg and Stuart Howes for their support of the Utrecht University CryoEM facility, and Mihajlo Vanevic for his support of the computational infrastructure. We thank NeCEN in Leiden for their support in acquiring the 300 kV dataset. This research was funded by the Dutch Research Council (NWW) (grant no. Vici 724.016.001 to F.F. and ALWOP.2015.115 to S.S.) and the Netherlands Electron Microscopy Infrastructure, project number 184.034.014 of the National Roadmap for Large-Scale Research Infrastructure of the Dutch Research Council (NWO).

Author Contributions

R.E., S.v.d.H., F.F. and S.S. designed experiments. R.E. and S.v.d.H. conducted experiments and analysed the data. S.v.d.H conducted in vitro translation assays, affinity purification and, together with R.E., analytical ultracentrifugation. R.E. prepared cryoEM grids, acquired the cryo-EM data, performed the single-particle analysis and build the atomic models. R.E. wrote the initial draft of the manuscript, which was edited by F.F., S.v.d.H and S.S.

Supplementary Material

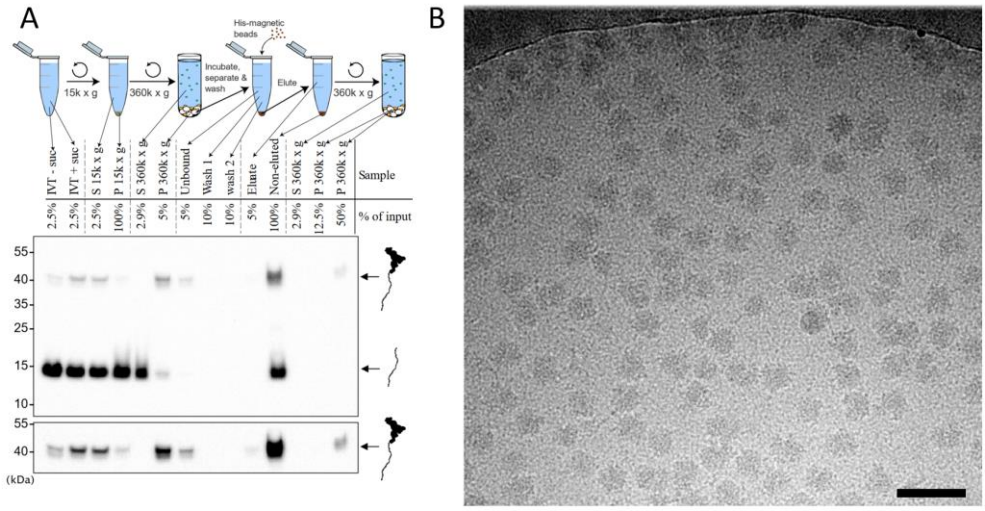

Figure S1: Enrichment of stalled RNC's by affinity purification. A) Following in vitro translation of HHF-bZIP11-uORF2(IVT) transcript in the presence of 540mM sucrose, ribosome-nascent chain complexes (RNC's) were purified by ultracentrifugation followed by affinity purification using His-magnetic beads. Samples of intermediate steps were analyzed using western blot with anti-HA antibodies. Bottom panel shows the PtR region of the top panel, but with a longer exposure time. Positions of the peptide and PtR bands are indicated. S = Supernatant, P = Pellet. B) CryoEM micrograph of affinity purified RNC's. Scalebar 50 nm.

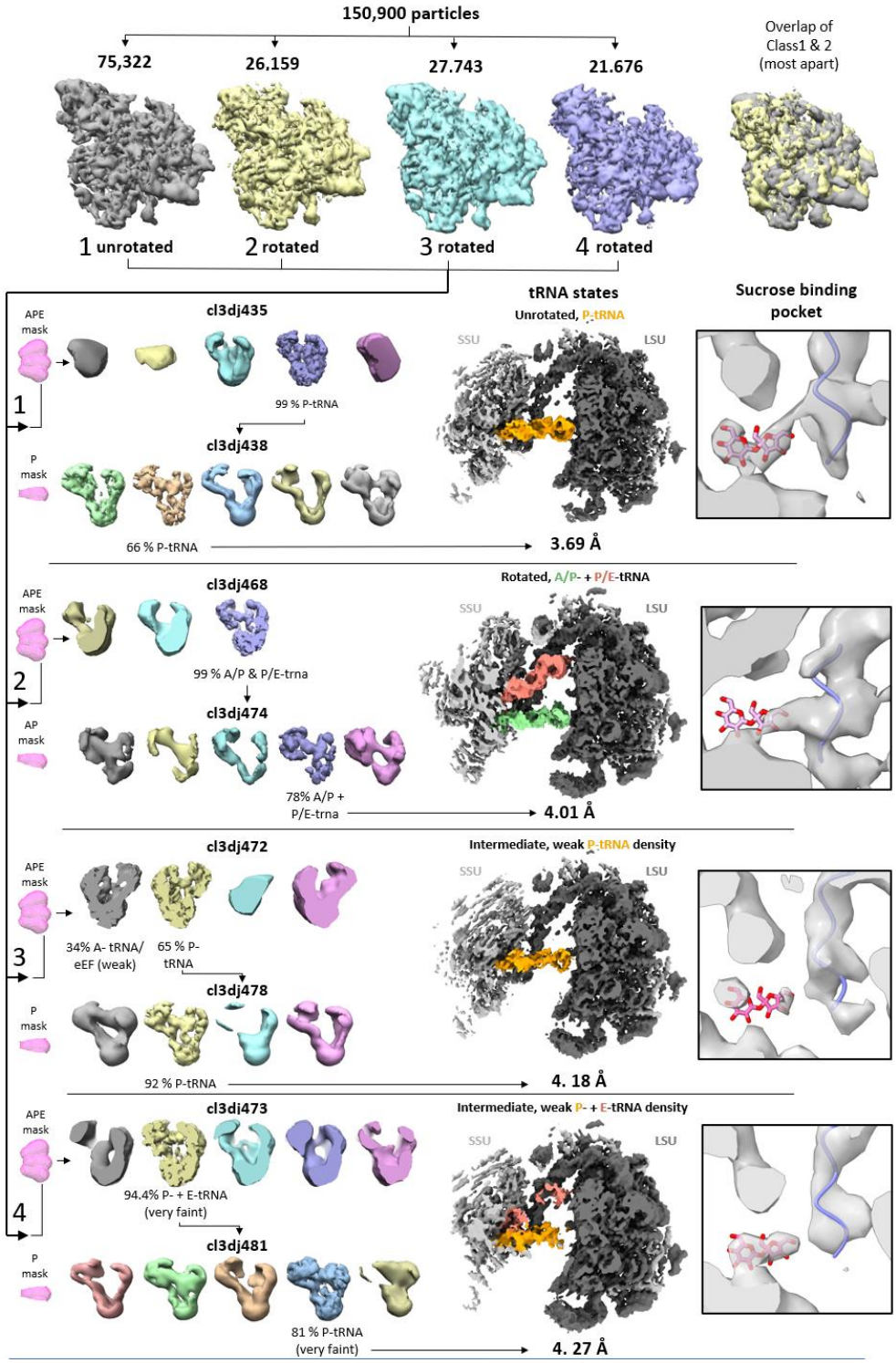
150,900 particles
75,322
26,159
27.743
21.676
Overlap of Class1 & 2 (most apart)
1 unrotated
2 rotated
3 rotated
4 rotated
tRNA states
Sucrose binding pocket
cl3dj435
APE mask
1
99 % P-tRNA
cl3dj438
P mask
66 % P-tRNA
Unrotated, P-tRNA
SSU
LSU
3.69 Å
cl3dj468
APE mask
2
99 % A/P & P/E-trna
cl3dj474
AP mask
78% A/P + P/E-trna
Rotated, A/P- + P/E-tRNA
4.01 Å
cl3dj472
APE mask
3
34% A- tRNA/ eEF (weak)
65 % P-tRNA
cl3dj478
P mask
92 % P-tRNA
Intermediate, weak P-tRNA density
4. 18 Å
cl3dj473
APE mask
4
94.4% P- + E-tRNA (very faint)
cl3dj481
P mask
81 % P-tRNA (very faint)
Intermediate, weak P- + E-tRNA density
4. 27 Å

Fig S2: Classification of affinity purified wheat germ ribosomes translating HHF-uORF2 in the presence of sucrose. After initial 2D classification, 3D classification, and 3D refinement 150,900 ribosome were obtained and subjected to 3 rounds of classification using masks focusing on the SSU (top), the ribosome cleft (encompassing the A-,P- and E-trna site) and the P-site (classes 1, 3,4) or A/P-site t-RNA (class 2). Maps of the cleft viewed from top or the sucrose binding site are shown on the right.

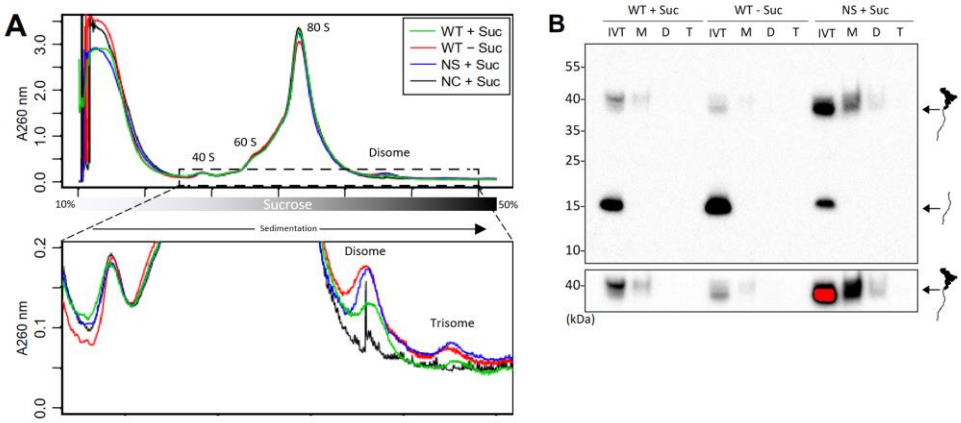

Fig S3: Ribosomes translating HHF-uORF2 are largely present as monosomes. A) Sucrose gradient profile of ribosomes translating HHF in the presence (WT+), absence (WT-) shows a strong monosome peak (top) and small di- and trisome peaks (bottom). IVT reactions of transcripts lacking the stop codon (NS) or without transcripts (NC) were loaded as controls. B) Western blot analysis of the complete IVT mix (IVT), monosome (M), disome (D) and trisome fractions (T) shows that peptidyl tRNA is only present in the monosome fraction for HHF transcripts (bottom), as well as the mono- and disome fraction for the HHF transcript without the stop codon (NS).

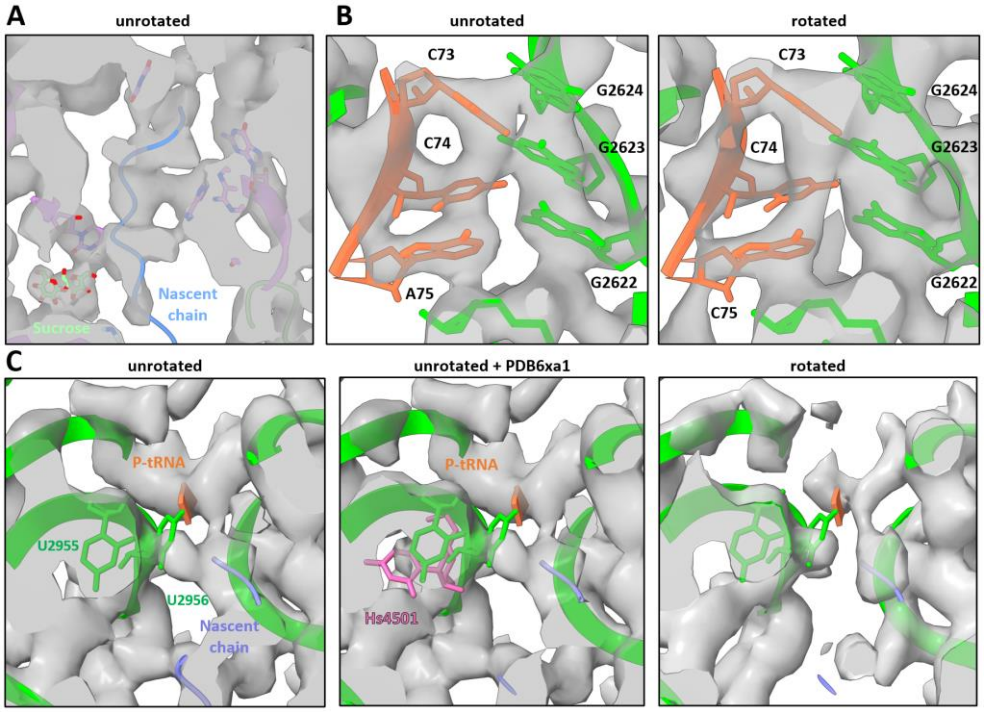

Figure S4: Details of the nascent chain, the P-loop and the PTC regions. A) Density observed adjacent to the tRNA of the stalled ribosome allowed for tracing of the nascent chain. B) The CCA end of the P-tRNA shown for the unrotated (left) and rotated state (right). C) PTC region showing the U2956 in an upward state for the unrotated and rotated state (left and right). The position where the human U4501 is located is occupied by U2955 in our structure (middle).

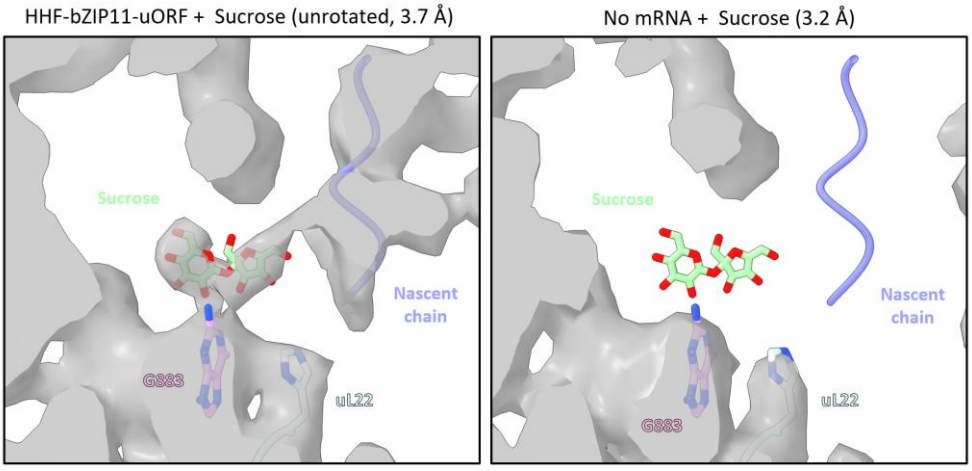

Fig S5: Sucrose does not bind to ribosome in the absence of the nascent peptide. Map of stalled ribosomes (unrotated state) as well as idle, non-translating ribosomes purified from IVT assays where no mRNA was added (right). Resolution of maps is indicated in brackets.

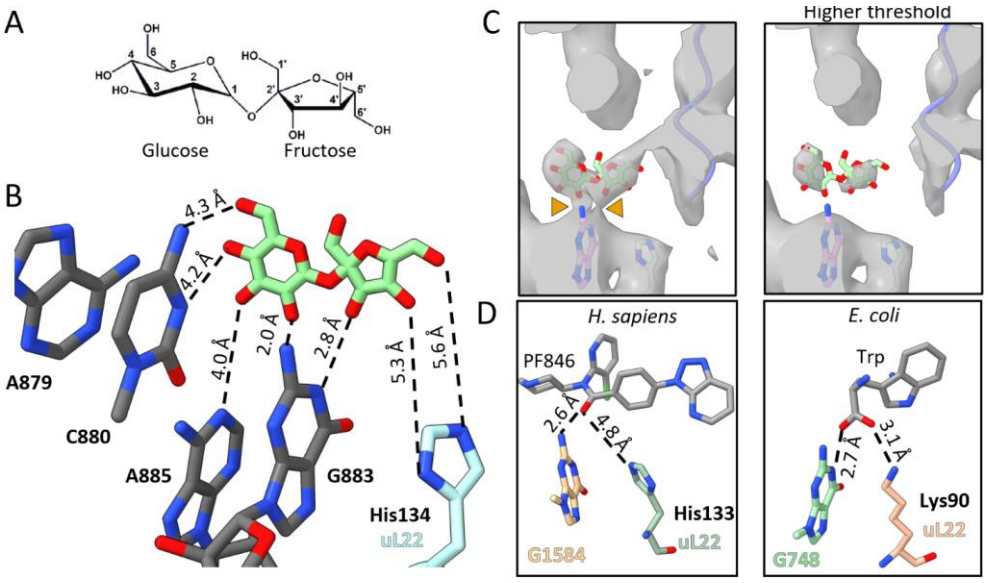

Figure S6: Interaction of fitted sucrose with rRNA nucleotides and uL22. A) Skeletal model of sucrose with indexed C-atoms. B) Details of interaction of Sucrose with rRNA nucleotides and His90. Dashed line indicates distance between respective atoms. C) Close-up of the density of the unrotated state overlapped with the sucrose and G883 at two different threshold levels. Orange arrows indicate densities between sucrose and G883. D). Interactions of PF846 and Tryptophan with the human and *E.coli* ribosome ,respectively, previously observed for stalled states.

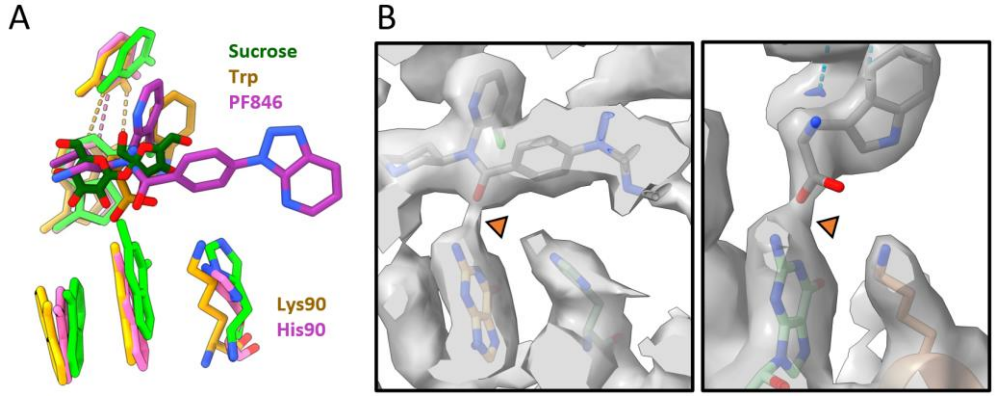

Figure S7: Conservation of rRNA binding pocket between *T.aestivum*, *H.sapiens and E.coli.* A) Structures of the human (pink, 6xa1), *E.coli* (orange, 7o19) and *T.aestivum* ribosome (green) in the molecule-induced stalled state. Small molecules are coloured in darker shades. **B**) Previous electron density maps for the human (left) and E.coli (right) ribosomes stalled by PF846 and Tryptophan respectively. Orange arrow highlights connective density of the hydrogen bonds between Gxx and the carbonyl/ carboxy group of PF846 and Trp respectively.

Chapter 8

General discussion

Robert Englmeier

Structural Biochemistry, Bijvoet Center for Biomolecular Research, Utrecht University, 3584 CG Utrecht, The Netherlands

In this thesis, I have investigated the translational machinery of three organisms from three different kingdoms of life across different scales, using cryo-electron microscopy. In order to investigate the native structure of the mitoribosome, we have used whole cell sections of the algae *C. reinhardtii* (**chapter 6**) and isolated mitochondrial vesicles derived from human cells **(chapters 2 and 4)**. In addition, using purified, cytosolic wheat germ ribosomes, we also studied the metabolite-induced translational regulation of the abundant disaccharide sucrose, commonly referred to as table sugar, at near atomic resolution (**chapter 7**).

Evolution of mitoribosomes

Mitochondria maintained their own genome and translation machinery of bacterial origin, the mitoribosome. As well as encoding those membrane-embedded oxidative phosphorylation complex (OxPhos) subunits that are synthesized by the mitoribosome, the mitochondrial genome also encodes the ribosomal RNA (rRNA) of the mitoribosome and tRNAs. Throughout evolution, mitoribosomes have been subjected to drastic modifications such as the acquisition of novel rRNA expansion segments, deletions of ancestral rRNA stretches and the acquisition of novel mitoribosomal proteins encoded in the nucleus[1,2]. One particularly striking case of mitoribosomal evolution is that of the green algae *Chlamydomonas reinhardtii*. Its mitoribosomal rRNA is fragmented into 12 rRNAs scattered across the mitochondrial genome. When initially characterized, it was not clear how the rRNA fragments are assembled and stabilized to constitute a single functional mitoribosome[3,4].

In **chapter 6**, we determined the structure of the *C. reinhardtii* mitoribosome by combining cryoEM SPA and cryoET. The structures reveal the organization of the rRNA fragments, which form overlapping base-pairs and are stabilized by highly intertwined, algae-specific mitoribosomal proteins. To determine the complex structure of the *C. reinhardtii* mitoribosome, applying focused ion beam milling under cryogenic conditions (cryoFIB) to obtain thin sections for subsequent cryoET was essential, since the isolation of intact mitoribosomes proved to be challenging and resulted. Using cryoET, the obtained subtomogram average allowed us to fit the high-resolution structures of the individual ribosome subunits obtained by SPA.

The subtomogram average revealed the membrane association of the *C. reinhardtii* mitoribosome, which shows striking differences to the only other available *in organello* structures of the human and yeast mitoribosomes[5,6]. Similar to yeast, the membrane association of the algae mitoribosome is mediated by a second contact site in addition to that near the exit tunnel associated with the conserved insertase Oxa1. However, unlike in yeast where this secondary contact site is mediated by the rRNA expansion segment ES-96, in *C. reinhardtii* the second contact site is formed by the algae-specific protein mL113. Notably, the protein mediating the membrane association for the primary contact site, mL119, does not show structural similarity to the human or yeast analogues mL45/ Mba1, indicating a case of convergent evolution[7]. The fact that both the yeast and algae mitoribosomes independently evolved a secondary contact site containing different molecules (rRNA in yeast & protein in *Chlamydomonas*), while this second contact site is absent in mammals, highlights the importance of mitoribosomal membrane association and

exemplifies that membrane association is achieved by different evolutionary routes (Figure 1).

Recently, a study identified the mitoribosome of the jakobid *Andalucia godoyi* to be the closest to the mitoribosome of the last eukaryotic common ancestor (LECA)[8]. *A. godoyi* exhibits the mitochondrial genome most similar to bacteria identified to date, with the rRNA being nearly identical to that of α-proteobacteria, the closest suggested sister-group of the mitochondrial progenitor[9]. While the mitoribosomal rRNA of *A. godoyi* is mostly preserved compared to α-proteobacteria, it already shows an expanded mitoribosomal proteome[10]. Comparison of the composition of *A. godoyi* with existing mitoribosome structures suggests that mitoribosomal evolution is characterized by an early expansive phase of mitoribosomal proteins (mtRPs)[10], followed by continuous mtRP expansion and different rRNA phases depending on the phylum (Figure 1)[1]. Regarding membrane association, *A. godoyi*, similar to α-proteobacteria[11], already lost the rRNA helix 59, which constitutes a secondary membrane contact site during co-translation insertion in *E. coli*[12,13]. This raises the question of whether *A. godoyi* compensated for the absence of helix 59 by another protein, or whether it contained a single membrane contact site similar to humans, which was later complemented in yeast and *C. reinhardtii* with a secondary contact site obtained via different evolutionary routes. To address this question, *in situ* structures of the *A. godoyi* mitoribosome and of α-proteobacterial ribosomes would be extremely valuable and would potentially help to identify the sequence of events and driving factors of the evolution of mitoribosomal membrane association.

Chapter 6 highlights the value of cryoET in obtaining context-specific information, which is particularly important for the mitoribosome and was critical for identifying the strikingly unique membrane association of the *C. reinhardtii* mitoribosome.

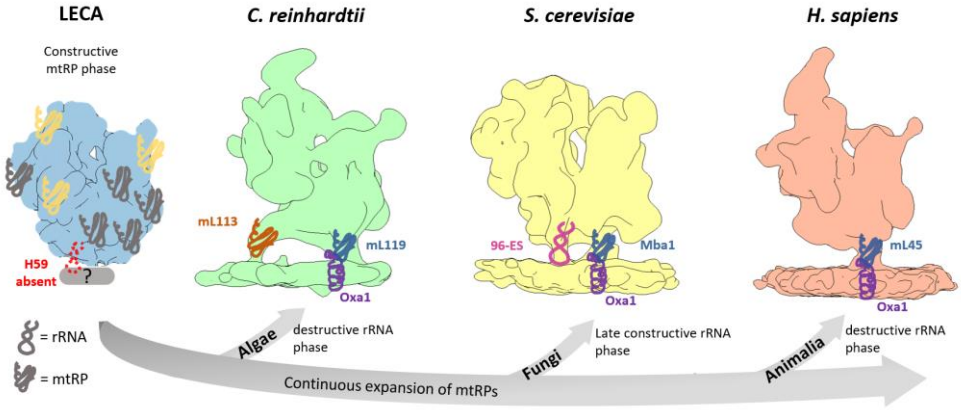

Figure 1: The mitoribosome-membrane interface is a critical hub that was vastly remodelled throughout evolution. *In organello* structures of the mitoribosomes from humans, *C.reinhardtii* and yeast, as determined in **chapters 2 and 7** or by Pfeffer et al. using cryo-electron tomography[6], as well as a hypothetical model of the LECA mitoribosome based on a bacterial ribosome[13]. The LECA mitoribosome already contained a largely expanded set of mitoribosomal proteins (mtRPs), but lacks the rRNA helix 59 (H59) which mediates membrane association in *E. coli*. Mitoribosomal protein expansion continued throughout evolution, while the mitochondrial genome was subjected to different phases of rRNA expansion (yeast) or deletion (algae and human). This resulted in striking

differences regarding the number and composition of secondary mitoribosomal membrane contact sites, while the primary contact site aligning the exit tunnel with the insertase Oxa1 via mL45/ Mba1/ mL119 has been preserved in all mitoribosome structures known to date.

In organello structures of the human mitoribosome

In **chapters 2 and 4**, we have investigated the human mitoribosome inside intact mitochondria by cryo-electron tomography. The structure of the human mitoribosome was previously only studied by applying cryoEM single particle analysis (SPA) to purified mitoribosomes. The initial structure which was only solved in 2015[14], and revealed a highly reduced rRNA components, the arrangement of compensatory mitoribosomal proteins and a canonical peptide exit tunnel (PET) – in contrast to the altered PET previously shown for the yeast mitoribosome[15]. However, due to the disruptive nature of membrane solubilization and mitoribosome purification, the membrane association of the human mitoribosome remained elusive. In particular, the previous cryoET study of the yeast mitoribosome, which showed that its membrane association is mediated by two contact sites of which one is an rRNA expansion segment missing in human mitoribosomes[6], raised the question of how mitochondrial membrane association is mediated and whether the second contact site is missing in humans or has been compensated for.

Our *in organello* subtomogram average in **chapter 2** revealed that only one contact site formed by mL45 mediates the membrane association of the human mitoribosome, as opposed to two contact sites in yeast. The second contact site, comprised of an rRNA expansion segment in yeast, is missing in humans and has not been compensated for. Despite this difference, the major contact site is mediated by the same homolog in both species (mL45 in humans, Mba1 in yeast), which aligns the peptide exit tunnel with the membrane (Figure 1). In addition, our study revealed that mitoribosomes are predominantly associated to the membrane and form polysomes – aspects that could not be previously structurally addressed due to mitoribosome isolation after mitochondrial disruption, and give important insight into the native distribution of mitoribosomes. Their predominant membrane association is in agreement with the fact that all proteins synthesized by mitoribosomes are highly hydrophobic OxPhos subunits. Mitoribosome membrane association may also be closely linked to their biogenesis. This is supported by a study that showed in yeast that mitoribosome assembly occurs on mitochondrial membranes[16]. A similar study of the human mitoribosome showed that the membrane anchor mL45 is incorporated early on in mitoribosome biogenesis[17], but could not address the membrane context due to the absence of membrane-tethered mitoribosomal protein in humans as opposed to yeast. An early assembly of the human mitoribosome on the membrane, in a manner similar to mitoribosome biogenesis in yeast, seems likely, and cryoET could be potentially used to localize and structurally characterize different assembly intermediates *in situ* – something that has previously only been investigated upon mitoribosome isolation rather than *in organello*[18,19].

Another finding of **chapter 2** was an additional density on the head of the small subunit (SSU) that was previously not observed by SPA, presumably due to the weak association of the involved proteins, resulting in disruption upon mitoribosome isolation. Interestingly, in a later studies employing SPA, this density could be observed and were attributed to a complex formed by SLIRP-LRPPRC[20,21], which was previously shown to be involved in mitochondrial translation[22]. However, the exclusive binding of the SLIRP-LRPPRC complex

does not explain the tissue-specific effects of the LRPPRC founder mutation[23], as well the role of the mitoribosome-associated and mRNA binding protein TACO1, a knockdown of which was shown to result in age-specific mitochondrial dysfunction and late-onset Leigh-Syndrom[24,25]. Therefore, potentially different mRNA binding compolexes might be associated to the mitoribosome, as is the case in yeast[26]. To conclusively address the identity of the complex, or set of protein complexes, high-resolution structures, ideally *in situ*, will be required.

The protocols for grid preparation, data acquisition and analyses that were applied in **chapter 2** were published as a separate methods chapter and are presented in detail in **chapter 3**.

Towards a 'high' resolution *in organello* structure of the mitoribosome

While **chapter 2** gave important first insights into the native structure and distribution of the human mitoribosome, its limited resolution of 25 Å did not allow for a more detailed structural characterization. In particular the structure of the associated membrane insertase Oxa1L is of high interest due to its critical role for the insertion of the mitochondrially encoded hydrophobic respiratory chain subunits. Aside from a short stretch of its CTD[27], there was also no previous structural data for Oxa1L.

The shortcoming of limited resolution was addressed in **chapter 4,** where we provide structural insights to the human mitoribosome at subnanometer resolution. One main limitation that prevented a higher resolution structure in **chapter 2** was the relatively small dataset size, limited by a relatively low amount of intact mitochondria in the sample. In **chapter 4**, we have optimized the isolation protocol of mitochondria by screening different parameters of all involved steps, namely cell lysis, differential centrifugation and cryoEM grid prepartion. Our results indicate that commonly used isolation protocols lead to the disruption of mitochondria. Interestingly, the lower centrifugation speed, which we identified as critical to preserve the structural integrity of mitochondria, coincides with protocols that were initially used in the 1940s for pioneering studies of resin-embedded mitochondria by conventional electron microscopy[28]. Our improved isolation protocol, also described separately in **chapter 5**, resulted in a sample with a high concentration of mitochondria and enabled the acquisition of a larger dataset, permitting the achievement of a subtomogram average at subnanometer resolution.

Aside from sample optimizations, improved data analysis was critical to achieve this higher resolution. We improved workflows for unsupervised tilt series alignment, particle localization and 3D classification resulting in a set of 32.000 mitoribosomes from an initial set of nearly half a million subtomograms - nearly two orders of magnitude higher than the subtomogram set used in **chapter 2,** which went through labour-intensive manual curation. The combination of this large dataset with state-of-the art software for subtomogram alignment[29] allowed for the characterization of a previously unknown insertase complex, as well as the characterization of the mitoribosome-Oxa1 binding interface.

An alternative mitoribosome-insertase complex

Surprisingly, classification of the subtomograms focusing on the membrane region of the human mitoribosome in **chapter 4** revealed not one, but two defined mitoribosome insertase complexes. This contrasts with the current model where Oxa1 is characterized as

the main insertase responsible for co-translational protein insertion of mitochondria-encoded proteins[27]. However, an exclusive role of Oxa1 for co-translational insertion has been debated for a long time based on the fact that several mitochondrial subunits are barely affected by Oxa1 knockout[30–32]. In particular, Oxa1 knockdown in HEK cells indicated that Oxa1 is only required for 9 out of the 13 mitochondrially encoded subunits, although results were slightly varied between the two studies[32,33]. Similarly, in yeast, 3 out of 7 mitochondrial-encoded subunits were only partially impaired in an Oxa1-temperature-sensitive mutant[31]. Interestingly, a recent study also observed tissue-specific phenotypes for an Oxa1 mutation in humans, further stressing the possibility of an as-yet unidentified insertase[33].

Potential candidate proteins for an alternative insertase that have both been identified to be involved in the insertion of mitochondrial encoded proteins and are localized to the IMM are limited to Cox18, MPV17L2 and Mdm38/ LetM1 (homologues in yeast and human respectively). Of these candidates, the best characterized is Cox18, a homologue of Oxa1 which was initially identified in yeast and is required for the translocation of the N-terminal domain of Cox2p into the IMS[34,35]. The same function was recently confirmed for its human homologue Cox18[36]. Notably, Oxa1 is still required for the translocation of the N-terminal domain of Cox2[36]. This clearly defined role of Cox18 and the reliance on Oxa1 for initial insertion of Cox2 likely exclude Cox18 as a potential alternative insertase.

MPV17L2 was identified as an integral membrane protein involved in both the assembly of the mitoribosomal large subunit (mtLSU) as well protein synthesis[37]. A role in co-translational insertion has been proposed based on the reduced expression levels of mitochondrial proteins upon MPV17L2 knockdown, but in the single available study there is no clear evidence that separates its role in ribosome biogenesis from co-translational insertion[37]. Therefore, the latter might just be a consequence of reduced levels of mitoribosomes. The scarcity of available literature leaves an unclear picture of MPV17l2's role in protein synthesis, and stresses the need for further research.

The last proposed candidate for Oxa1-independent insertion, LETM1, was initially identified in patients with Wolf-Hirschhorn syndrome (WHS). WHS is a rare disease resulting in mental disability and developmental delays with nearly all WHS patients carrying a deletion of LETM1[38]. A variety of studies showed that LETM1 is overexpressed in cancer cells, interacts with mitoribosomes, affects mitochondrial mass and physiology, and is involved in Ca^{2+} homeostasis[39–42]. Insights on the role of human LETM1 in the context of mitochondrial translation is however limited to one study, which showed that levels of assembled complexes I, III and IV were significantly reduced upon LETM1 knockdown[43]. However, aside from these assembled respiratory complexes, only one individual mitochondrial-encoded subunit, mt-ND2, was quantified, and its levels were not affected by the LETM1 knockdown. Interestingly, a study on its yeast homologue, Mdm38, gave more detailed insights into its role for protein synthesis[44]. It showed that Mdm38 is required for complete membrane insertion of the mitochondrial encoded Atp6 and CytB subunits, as demonstrated by proteinase assays. This is particularly interesting, because these two subunits were only partially affected in initial studies of Oxa1 knockout strains[31], which suggests an Oxa1 independent insertion of Atp6 and cytB[30,31]. However, levels of all subunits (including Atp6 and CytB) were not reduced in Mdm38 knockout strains, indicating that it is not essential for their synthesis but rather their membrane insertion. Therefore, it remains unclear

whether Mdm38 is solely required for post-translational insertion of Atp6 and CytB, or whether it acts co-translationally but its deletion can partially compensated for, e.g. by a complementary insertase or the self-insertion of proteins - similar to the observed phenotype after knockdown of the Oxa1-associated Mba1 protein[6] or the self-insertion of certain YidC substrates in in vitro assays[45].

Lastly, an alternative mitochondrial insertase might potentially be more closely related to the multisubunit ER membrane complex (EMC) rather than to Oxa1/ YidC, and thereby have evaded detection. EMC is a recently characterized protein insertase of the ER, and descendant of the archaeal DUF106 protein family [46–52]. A recent study showed that a mitochondria-targeted fusion-protein of EMC3-EMC6 can restore the insertion of mitochondrial encoded proteins in Oxa1 deletion mutants in yeast[47]. The ability of EMC-EMC6 to functionally complement Oxa1 highlights a high degree of conservation between these proteins and further highlights that the Oxa1 superfamily is not limited to the bacterial lineage of Oxa1/Yidc/Alb3[53], but shares both ancestry and a conserved mechanism for protein insertion with the archaeal DUF106 family [46,47,52]. If the alternative insertase is indeed related to an archaeal ancestor, it would provide an exciting example of an archaeal protein complementing the ancestral prokaryotic translation machinery of the mitochondria upon the endosymbiotic event.

Clearly, there is more complexity to mitochondrial co-translational insertion, despite a recent study attributing it exclusively to Oxa1[27]. The literature discussed above indicates complex, substrate-specific insertion routes for the set of mitochondrial proteins. To identify those routes further research will be required. The subtomogram average presented in **chapter 4** provides the first structural evidence for an alternative insertase and shows that it accounts for 50% of mitoribosome complexes, highlighting its relevance and calling for its further investigation.

Mechanism of co-translational protein insertion by Oxa1

The other central finding of **chapter 4** is a subtomogram average of the Mitoribosome-Oxa1 complex, which allowed for the structural characterization of the binding interface between the two complexes. Previous structural data was limited to the c-terminal domain (CTD) of Oxa1[27], which was previously shown to bind to the mitoribosome and ensure efficient co-translational protein insertion[54–56]. However, it remained unclear how the nascent peptide would be reliably guided across the relatively large gap from the peptide exit tunnel into the membrane. In addition, the peripheral binding of the CTD to the mitoribosome, together with the flexible nature of the extended CTD, indicates the necessity for an additional binding site in order to align the mitoribosome with the Oxa1 membrane-embedded insertase core.

Indeed, our results from **chapter 4** identify an additional binding site between Oxa1 and the mitoribosome. A model of Oxa1 generated by Alphafold[57] showed excellent agreement with our subtomogram average of the Mitoribosome-Oxa1 complex, and in addition to the CTD of Oxa1, we observe a density overlapping with the helical hairpin domain of Oxa1 formed by the helices h3 and h4. This helical domain contacts the mitoribosomal exit tunnel and

the nascent peptide, bridging the gap between mitoribosome and membrane, and is closely located to the mitoribosomal tunnel exit proteins mL45 and uL23m. Based on this, we propose a central role of the helical hairpin domain for co-translational insertion by aligning the mitoribosome with Oxa1, providing a hydrophobic environment for the nascent peptide and facilitating membrane insertion by guiding the nascent chain into the membrane.

Notably, Oxa1's helical hairpin domain is conserved across all domains of live, from bacterial YidC, across archaeal, ER-resident EMC/ GET/ TMCO1 proteins to the mitochondrial Oxa1 insertase [47,52,58], highlighting its importance. A recent study identified for the first time a patient with a congenital Oxa1 mutation, which was located within or adjacent to the helical hairpin domain and comprised of two point mutations[33], showing the relevance of this domain for the proper functioning of Oxa1. To our knowledge, mutagenesis studies of the helical hairpin domain are currently limited to this single patient study of Oxa1, and two studies in yeast and bacteria[45,59]. In yeast, deletion of either the helical hairpin or the CTD domain of Oxa1 did not reduce the level of mitochondrial OxPhos subunits, but a combination of these deletions completely abolished translation[59]. In *E. coli*, deletions of YidC's helical hairpin domain strongly reduced growth under aerobic conditions, while viability was only completely abolished for deletions adjacent to the N-terminus of the domain[60]. The fact that deletions of a stretch of residues of Oxa1/ YidC can be partially compensated in yeast and *E. coli* contrasts with the case for human Oxa1, where severe defects were observed upon two point mutations, indicating a different dependance on the helical hairpin domain between fungal/ bacterial and human Oxa1/YidC. This differing dependance can likely be explained by two aspects: i) both the yeast mitoribosome and *E. coli* ribosome are located closer to the membrane and have multiple contact sites to it as compared to human mitoribosomes which exhibit a larger gap between the exit tunnel and the membrane and contains a single membrane contact site, and ii) YidC/ yeast Oxa1 interact with other membrane components such as SecYEG and Mba1[61,62], while our subtomogram average and previous studies indicate that human Oxa1 does not seem to interact with complexes other than the mitoribosomes during co-translational insertion. In addition, as compared to human mL45, the yeast homologue Mba1 shows a stronger membrane-association and was shown to partially complement for Oxa1 mutations[61,62]. This again indicates an important role for the helical hairpin domain in aligning the mitoribosome with Oxa1 and facilitating co-translational insertion.

Importantly, the conserved helical hairpin has previously not been visualized in the substrate-bound state for any of the Oxa1 homologues. Previous studies of the mitoribosome-Oxa1 or the bacterial ribosome-YidC complex failed to resolve this critical domain[13,27], likely due purification-induced disruption and the inherent flexibility of the domain[63]. While structures of more distant Oxa1 relatives such as the EMC complex or TMCO1 confirmed the conserved Oxa1 fold of 5 TMDs and the helical hairpin domain, they were either determined upon isolation of the ribosome or in absence of their substrate[49,64]. Therefore, our structure provides a valuable model for co-translational insertion by Oxa1 insertases. Our proposed functional model is in excellent agreement with, and

complements the suggested mechanism for co-translational insertion by YidC[45,65]. In this hypothesized mechanism, a 'greasy slide' formed by YidC/Oxa1 TM2-3, which is positioned directly under the flexible helical hairpin, guides the nascent chain into the membrane and laterally releases it[65].

One main limitation of our cryoET study is the relatively low resolution inside the inner mitochondrial membrane, which does not permit modelling of the transmembrane domains of Oxa1. Our model is therefore limited to the matrix-exposed domains of Oxa1 and the initial steps of mitoribosome binding and nascent peptide delivery towards the core. A high-resolution structure of the Oxa1 core, providing at least secondary structure resolution, could give valuable further insights into nascent chain membrane insertion and folding. Major challenges for obtaining a high-resolution structure of the Oxa1 transmembrane helices by cryoET are the sample thickness, the crowded mitochondrial matrix and the inner-mitochondrial membrane with its high protein to lipid ratio[66]. Structure determination by SPA on the other hand, would benefit from a reconstituted system that allows programming and stalling of mitoribosomes to stabilize mitoribosome-insertase complexes. The establishment of such a mitochondrial *in vitro* translation system would prove extremely valuable for further studies, as it would allow to study synthesis and folding of each individual mitochondrially encoded protein subunit. However, the approach might be an equally or even more challenging route than cryoET due to the complexity of mitochondrial translation and mitochondrial membrane composition[66]. Arguably the closest to such a IVT system is an vitro system for co-translational insertion by YidC[45], where YidC was reconstituted into proteoliposomes which allowed for studying co-translation membrane insertion of defined protein susbtrates by prokaryotic ribosomes.

Metabolite-induced translational regulation in eukaryotes

In **chapter 7**, we identified the ribosomal binding site of sucrose, which stalls translation of the bZIP11-uORF2 transcript in a concentration-dependent manner in *Arabidopsis thaliana*. Transcript-specific, metabolite-induced translational regulation has been previously studied for different metabolites in prokaryotes[67,68]. Despite the abundance of upstream open reading frames (uORFs) in eukaryotes and their potential role in metabolite-induced translational regulation[69,70], this is the first structure of a stalled eukaryotic ribosome nascent chain complex bound to its regulating metabolite.

Our results show that ribosomes translating bZIP11-uORF2 are enriched in two translational states in the presence of sucrose, which stalls ongoing translation by binding to the ribosomal exit tunnel. One main limitation of our study is the low resolution for the peptide, which did not permit modelling of the peptide sidechains. The resolution was likely limited by the relatively weak stalling efficiency of sucrose that results in flexibility of the nascent peptide. Future studies will ideally resolve the detailed mechanism and provide insights into the role of the individual side chains. However, this might require the mutation of residues to increase the stalling efficiency, as was done in previous studies[67,71]. The wild-type sequence of bZIP11-uORF2 likely provides an optimized sensitivity for a physiologically relevant range of sucrose concentrations, and increased stalling efficiency might completely prevent the expression of the gene.Such a complete translational shutdown would be

desirable for structural studies, but likely not for its physiological function. It would be interesting to investigate whether slightly altered uORF sequences in related species result in different sucrose sensitivities, and whether those changes are a result of adaptations to different environments.

One key finding of our study is that sucrose occupies the same binding site as tryptophan during translational stalling of the TnaC peptide in *E. coli*, as well as the drug PF846 which was shown to stall translation of two specific proteins in humans – a connection which has not been shown before[67,71,72]. Our results therefore reveal that this 3-billion-year-old binding site is functionally exploited across three different kingdoms. These findings raise the question of whether the binding site has been exploited in other species, and whether endogenous, as well as exogenous compounds[71], exploit this site in human ribosomes. Due to its broad conservation, the same binding site might possibly be used in other kingdoms such as archaea, algae, fungi; this binding site could potentially date back to LUCA and the first ribozyme complexes. In light of our findings, one could also ask if ribosomal binding sites of other metabolites that have been shown to regulate translation for specific peptides, such as the ornithine binding site in *E.coli*[73], might be functional across different clades. To address these questions, a combination of bioinformatic screens, functional assays and structure determination by cryoEM would be a valuable approach for further characterization of conserved ribosomal binding sites.

Future perspectives

The regulation of protein synthesis is essential for life and ensures cellular growth, homeostasis and division. Mitochondria play a particularly interesting role in these processes. They maintained their own genome, regulate their own gene expression and co-ordinate protein import and synthesis[74] in order to produce membrane-embedded respiratory chain complexes of dual-genetic origin in a process heavily shaped by evolution. Many diseases are linked to defects of these complexes[75], highlighting their importance and providing an explanation for the evolutionary preservation of the mitochondrial genome - as mutations often result in deleterious consequences. While recent studies have investigated a variety of techniques to treat mitochondria-related diseases, such as the delivery of mRNA to mitchondria[76], genetic modification of mitochondrial DNA by CRISPR/Cas9[77] or mitochondrial replacement[78], a detailed understanding of the fundamental processes that govern mitochondrial membrane protein synthesis and insertion will be essential for realizing their full therapeutic potential.

The findings presented in this thesis contribute to our understanding of mitochondrial co-translational protein synthesis by providing insights into the mitoribosomal membrane association and its interaction with protein insertases. Future studies will hopefully uncover the mechanisms of the downstream processes of nascent peptide insertion, release into the membrane and assembly into functional respiratory chain complexes. In uncovering these convoluted processes, cryoET will play a valuable role. Historically, the choice between cryoET and SPA was an exclusive choice between contextual information or high resolution. However, recent advances have been challenging this long-standing dogma and are pushing the boundaries of cryoET[29,79]. The results in this thesis also highlight the potential of cryoET, in resolving the previously uncharacterized binding interface of the small 42 kDa membrane protein Oxa1 inside mitochondria. In combination with cryoFIB milling, the advances in cryoET pave the way for the future of cellular structure biology[29]. With improved techniques

for sample preparation, data acquisition[80] and image analysis, structural studies will be ideally conducted in the native environment of the cell. For complexes of low abundance, such as the mitoribosome, structural studies in the cellular context will likely remain challenging in the foreseeable future. As seen in **chapter 6**, the combination of low mitoribosome density with thin cellular sections cumbersomely prepared by cryoFIB-milling result in very few mitoribosomes per tomogram – two orders of magnitude lower than their cytosolic counterpart. This limits the resolution for structural studies but also the quantities for statistical analysis. Until this throughput issue is resolved, e.g., by preventing the loss of 98% of the cellular volume during cryoFIB-milling, the improved protocols for mitochondrial isolation presented in this thesis will provide a useful tool for the structural investigation of mitochondrial complexes. For investigating different conditions, e.g. relevant mutations or the effect of drugs, enrichment of mitochondria by isolation can be critical to achieve the quantities required for structural studies.

Regarding cytosolic protein synthesis, the central dogma has been historically viewed as a simplified mechanism where a main open reading frame (mORF) is translated into amino acid chain, but findings from the last three decades show that a plethora of regulatory elements can act up- or downstream of the mORF to post-transcriptionally modulate translation[81–84]. Recent studies[67,71] and our findings from **chapter 7** highlight the importance and potential of small molecules for peptide-specific translational regulation. The fact that the sucrose binding site identified by us is functionally exploited across several kingdoms of life invites for the further investigation of potential molecules targeting translational regulation of specific peptides in bacteria, plants and humans, as it was shown for the compound PF846[71] acting on the human ribosome. CryoEM will play an essential role in identifying the detailed stalling mechanisms and potentially contribute to the design of improved therapeutics or molecules for agricultural use.

Structural biology is key to understanding the detailed mechanisms that orchestrate the play of life. In the last decade, cryoEM has drastically accelerated protein structure determination and resulted in an exponential increase in the deposition of protein structures – a trend that will likely continue[85]. Recent breakthroughs in protein structure prediction contribute to this development[57]. Easy access to these structures and tools enable the interpretation of protein machinery at atomic level and can greatly enhance the design of new studies or complement existing results. With increasing access to cryoEM and ongoing technological developments, protein structure determination will likely become a routine technique that will allow scientists to study proteins at molecular detail in a variety of contexts.

References

1. Waltz, F. & Giegé, P. Striking Diversity of Mitochondria-Specific Translation Processes across Eukaryotes. *Trends in Biochemical Sciences* vol. 45 149–162 (2020).

2. Scaltsoyiannes, V., Corre, N., Waltz, F. & Giegé, P. Types and Functions of Mitoribosome-Specific Ribosomal Proteins across Eukaryotes. *International Journal of Molecular Sciences* vol. 23 (2022).

3. Denovan-Wright, E. M. & Lee, R. W. Comparative structure and genomic organization of the discontinuous mitochondrial ribosomal RNA genes of Chlamydomonas eugametos and Chlamydomonas reinhardtii. *J. Mol. Biol.* **241**, 298–311 (1994).

4. Denovan-Wright, E. M. & Lee, R. W. Evidence that the fragmented ribosomal RNAs of Chlamydomonas mitochondria are associated with ribosomes. *FEBS Lett.* **370**, 222–6 (1995).

5. Englmeier, R., Pfeffer, S. & Förster, F. Structure of the Human Mitochondrial Ribosome Studied In Situ by Cryoelectron Tomography. *Structure* **25**, 1574-1581.e2 (2017).

6. Pfeffer, S., Woellhaf, M. W., Herrmann, J. M. & Förster, F. Organization of the mitochondrial translation machinery studied in situ by cryoelectron tomography. *Nat. Commun.* **6**, 6019 (2015).

7. Waltz, F. *et al.* How to build a ribosome from RNA fragments in Chlamydomonas mitochondria. *Nat. Commun.* **12**, 1–15 (2021).

8. Gray, M. W. *et al.* The draft nuclear genome sequence and predicted mitochondrial proteome of Andalucia godoyi, a protist with the most gene-rich and bacteria-like mitochondrial genome. *BMC Biol.* **18**, 1–35 (2020).

9. Martijn, J., Vosseberg, J., Guy, L., Offre, P. & Ettema, T. J. G. Deep mitochondrial origin outside the sampled alphaproteobacteria. *Nature* **557**, 101–105 (2018).

10. Valach, M. *et al.* An Unexpectedly Complex Mitoribosome in *Andalucia godoyi* , a Protist with the Most Bacteria-like Mitochondrial Genome. *Mol. Biol. Evol.* **38**, 788–804 (2021).

11. Petrov, A. S. *et al.* Structural Patching Fosters Divergence of Mitochondrial Ribosomes. *Mol. Biol. Evol.* **36**, 207–219 (2019).

12. Frauenfeld, J. *et al.* Cryo-EM structure of the ribosome-SecYE complex in the membrane environment. *Nat. Struct. Mol. Biol.* **18**, 614–621 (2011).

13. Kedrov, A. *et al.* Structural Dynamics of the YidC:Ribosome Complex during Membrane Protein Biogenesis. *Cell Rep.* **17**, 2943–2954 (2016).

14. Amunts, A., Brown, A., Toots, J., Scheres, S. H. W. & Ramakrishnan, V. The structure of the human mitochondrial ribosome. *Science (80-.).* **348**, 95–98 (2015).

15. Amunts, A. *et al.* Structure of the yeast mitochondrial large ribosomal subunit. *Science* **343**, 1485–9 (2014).

16. Zeng, R., Smith, E. & Barrientos, A. Yeast Mitoribosome Large Subunit Assembly Proceeds by Hierarchical Incorporation of Protein Clusters and Modules on the Inner Membrane. *Cell Metab.* **27**, 645-656.e7 (2018).

17. Bogenhagen, D. F., Ostermeyer-Fay, A. G., Haley, J. D. & Garcia-Diaz, M. Kinetics and

Mechanism of Mammalian Mitochondrial Ribosome Assembly. *Cell Rep.* **22**, 1935–1944 (2018).

18. Hillen, H. S. *et al.* Structural basis of GTPase-mediated mitochondrial ribosome biogenesis and recycling. *Nat. Commun.* **12**, 1–10 (2021).

19. Itoh, Y. *et al.* Mechanism of mitoribosomal small subunit biogenesis and preinitiation. **606**, (2022).

20. Aibara, S., Singh, V., Modelska, A. & Amunts, A. Structural basis of mitochondrial translation. *Elife* **9**, 1–17 (2020).

21. Singh, V., Itoh, Y., Huynen, M. A. & Amunts, A. Activation mechanism of mitochondrial translation by LRPPRC-SLIRP. *bioRxiv* 2022.06.20.496763 (2022) doi:10.1101/2022.06.20.496763.

22. Spåhr, H. *et al.* SLIRP stabilizes LRPPRC via an RRM-PPR protein interface. *Nucleic Acids Res.* (2016) doi:10.1093/nar/gkw575.

23. Sasarman, F. *et al.* Tissue-specific responses to the LRPPRC founder mutation in French Canadian Leigh Syndrome. *Hum. Mol. Genet.* **24**, 480–491 (2015).

24. Richman, T. R. *et al.* Loss of the RNA-binding protein TACO1 causes late-onset mitochondrial dysfunction in mice. *Nat. Commun.* **7**, 11884 (2016).

25. Weraarpachai, W. *et al.* Mutation in TACO1, encoding a translational activator of COX I, results in cytochrome c oxidase deficiency and late-onset Leigh syndrome. *Nat. Genet.* **41**, 833–7 (2009).

26. Herrmann, J. M., Woellhaf, M. W. & Bonnefoy, N. Control of protein synthesis in yeast mitochondria: The concept of translational activators. *Biochim. Biophys. Acta - Mol. Cell Res.* **1833**, 286–294 (2013).

27. Itoh, Y. *et al.* Mechanism of membrane-tethered mitochondrial protein synthesis. *Science (80-.).* **371**, 846–849 (2021).

28. Claude, A. The constitution of mitochondria and microsomes, and the distribution of nucleic acid in the cytoplasm of a leukemic cell. *J. Exp. Med.* **80**, 19–29 (1944).

29. Tegunov, D., Xue, L., Dienemann, C., Cramer, P. & Mahamid, J. Multi-particle cryo-EM refinement with M visualizes ribosome-antibiotic complex at 3.5 Å in cells. *Nat. Methods* **18**, 186–193 (2021).

30. Stuart, R. A. Insertion of proteins into the inner membrane of mitochondria: the role of the Oxa1 complex. *Biochim. Biophys. Acta - Mol. Cell Res.* **1592**, 79–87 (2002).

31. Hell, K., Neupert, W. & Stuart, R. A. Oxa1p acts as a general membrane insertion machinery for proteins encoded by mitochondrial DNA. *EMBO J.* **20**, 1281–8 (2001).

32. Stiburek, L. *et al.* Knockdown of human Oxa1l impairs the biogenesis of F1Fo-ATP synthase and NADH:ubiquinone oxidoreductase. *J. Mol. Biol.* **374**, 506–16 (2007).

33. Thompson, K. *et al.* OXA1L mutations cause mitochondrial encephalopathy and a combined oxidative phosphorylation defect. *EMBO Mol Med* **10**, 9060 (2018).

34. Saracco, S. A. & Fox, T. D. Cox18p is required for export of the mitochondrially encoded

Saccharomyces cerevisiae Cox2p C-tail and interacts with Pnt1p and Mss2p in the inner membrane. *Mol. Biol. Cell* **13**, 1122–1131 (2002).

35. Fiumera, H. L., Broadley, S. A. & Fox, T. D. Translocation of Mitochondrially Synthesized Cox2 Domains from the Matrix to the Intermembrane Space. *Mol. Cell. Biol.* **27**, 4664–4673 (2007).

36. Bourens, M. & Barrientos, A. Human mitochondrial cytochrome c oxidase assembly factor COX18 acts transiently as a membrane insertase within the subunit 2 maturation module. *J. Biol. Chem.* **292**, 7774–7783 (2017).

37. Dalla Rosa, I. *et al.* MPV17L2 is required for ribosome assembly in mitochondria. *Nucleic Acids Res.* **42**, 8500–15 (2014).

38. Endele, S., Fuhry, M., Pak, S. J., Zabel, B. U. & Winterpacht, A. LETM1, a novel gene encoding a putative EF-hand Ca2+-binding protein, flanks the Wolf-Hirschhorn syndrome (WHS) critical region and is deleted in most WHS patients. *Genomics* **60**, 218–225 (1999).

39. Nakamura, S. *et al.* The mitochondrial inner membrane protein LETM1 modulates cristae organization through its LETM domain. *Commun. Biol.* **3**, (2020).

40. Doonan, P. J. *et al.* LETM1-dependent mitochondrial Ca2+ flux modulates cellular bioenergetics and proliferation. *FASEB J.* **28**, 4936–4949 (2014).

41. Dimmer, K. S. *et al.* LETM1, deleted in Wolf-Hirschhorn syndrome is required for normal mitochondrial morphology and cellular viability. *Hum. Mol. Genet.* **17**, 201–214 (2008).

42. Lin, Q. T. & Stathopulos, P. B. Molecular mechanisms of leucine zipper EF-hand containing transmembrane protein-1 function in health and disease. *International Journal of Molecular Sciences* vol. 20 (2019).

43. Tamai, S. *et al.* Characterization of the mitochondrial protein LETM1, which maintains the mitochondrial tubular shapes and interacts with the AAA-ATPase BCS1L. *J. Cell Sci.* **121**, 2588–2600 (2008).

44. Frazier, A. E. *et al.* Mdm38 interacts with ribosomes and is a component of the mitochondrial protein export machinery. *J. Cell Biol.* **172**, 553–64 (2006).

45. Geng, Y. *et al.* Role of the Cytosolic Loop C2 and the C Terminus of YidC in Ribosome Binding and Insertion Activity. *J. Biol. Chem.* **290**, 17250–61 (2015).

46. Borowska, M. T., Dominik, P. K., Anghel, S. A., Kossiakoff, A. A. & Keenan, R. J. A YidC-like Protein in the Archaeal Plasma Membrane. *Structure* **23**, 1715–24 (2015).

47. Güngör, B., Flohr, T., Garg, S. G. & Herrmann, J. M. The ER membrane complex (EMC) can functionally replace the Oxa1 insertase in mitochondria. *PLOS Biol.* **20**, e3001380 (2022).

48. Guna, A., Volkmar, N., Christianson, J. C. & Hegde, R. S. The ER membrane protein complex is a transmembrane domain insertase. *Science (80-.).* **359**, 470–473 (2018).

49. Bai, L., You, Q., Feng, X., Kovach, A. & Li, H. Structure of the ER membrane complex, a transmembrane-domain insertase. *Nature* **584**, 475–478 (2020).

50. Chitwood, P. J., Juszkiewicz, S., Guna, A., Shao, S. & Hegde, R. S. EMC Is Required to Initiate Accurate Membrane Protein Topogenesis. *Cell* **175**, 1507-1519.e16 (2018).

51. Shurtleff, M. J. *et al.* The ER membrane protein complex interacts cotranslationally to enable biogenesis of multipass membrane proteins. *Elife* **7**, (2018).

52. Anghel, S. A., McGilvray, P. T., Hegde, R. S. & Keenan, R. J. Identification of Oxa1 Homologs Operating in the Eukaryotic Endoplasmic Reticulum. *Cell Rep.* **21**, 3708–3716 (2017).

53. Hennon, S. W., Soman, R., Zhu, L. & Dalbey, R. E. YidC/Alb3/Oxa1 family of insertases. *Journal of Biological Chemistry* vol. 290 14866–14874 (2015).

54. Szyrach, G., Ott, M., Bonnefoy, N., Neupert, W. & Herrmann, J. M. Ribosome binding to the Oxa1 complex facilitates co-translational protein insertion in mitochondria. *EMBO J.* **22**, 6448–6457 (2003).

55. Haque, M. E. *et al.* Properties of the C-terminal tail of human mitochondrial inner membrane protein Oxa1L and its interactions with mammalian mitochondrial ribosomes. *J. Biol. Chem.* **285**, 28353–62 (2010).

56. Jia, L. *et al.* Yeast Oxa1 interacts with mitochondrial ribosomes: the importance of the C-terminal region of Oxa1. *EMBO J.* **22**, 6438–47 (2003).

57. Jumper, J. *et al.* Highly accurate protein structure prediction with AlphaFold. *Nature* **596**, 583–589 (2021).

58. McDowell, M. A., Heimes, M. & Sinning, I. Structural and molecular mechanisms for membrane protein biogenesis by the Oxa1 superfamily. *Nat. Struct. Mol. Biol.* doi:10.1038/s41594-021-00567-9.

59. Lemaire, C., Guibet-Grandmougin, F., Angles, D., Dujardin, G. & Bonnefoy, N. A yeast mitochondrial membrane methyltransferase-like protein can compensate for oxa1 mutations. *J. Biol. Chem.* **279**, 47464–47472 (2004).

60. Wang, G. *et al.* PNPASE regulates RNA import into mitochondria. *Cell* **142**, 456–67 (2010).

61. Ott, M. *et al.* Mba1, a membrane-associated ribosome receptor in mitochondria. *EMBO J.* **25**, 1603–10 (2006).

62. Preuss, M. *et al.* Mba1, a novel component of the mitochondrial protein export machinery of the yeast Saccharomyces cerevisiae. *J. Cell Biol.* **153**, 1085–96 (2001).

63. Wickles, S. *et al.* A structural model of the active ribosome-bound membrane protein insertase YidC. *Elife* **3**, e03035 (2014).

64. McGilvray, P. T. *et al.* An ER translocon for multi-pass membrane protein biogenesis. *Elife* **9**, 1–43 (2020).

65. He, H., Kuhn, A. & Dalbey, R. E. Tracking the Stepwise Movement of a Membrane-inserting Protein In Vivo. *J. Mol. Biol.* **432**, 484–496 (2020).

66. Daum, G. Lipids of mitochondria. *Biochim. Biophys. Acta - Rev. Biomembr.* **822**, 1–42 (1985).

67. van der Stel, A. X. *et al.* Structural basis for the tryptophan sensitivity of TnaC-mediated ribosome stalling. *Nat. Commun.* **12**, (2021).

68. Herrero del Valle, A. *et al.* Ornithine capture by a translating ribosome controls bacterial polyamine synthesis. *Nat. Microbiol.* **5**, 554–561 (2020).

69. Dever, T. E., Ivanov, I. P. & Sachs, M. S. Conserved Upstream Open Reading Frame Nascent Peptides That Control Translation. *Annu. Rev. Genet.* **54**, 237–264 (2020).

70. Van Der Horst, S., Filipovska, T., Hanson, J. & Smeekens, S. Metabolite control of translation by conserved peptide uORFs: The ribosome as a metabolite multisensor. *Plant Physiol.* **182**, 110–122 (2020).

71. Li, W., Chang, S. T., Ward, F. R. & Cate, J. H. D. Selective inhibition of human translation termination by a drug-like compound. *Nat. Commun.* 3–11 (2020) doi:10.1038/s41467-020-18765-2.

72. Li, W. *et al.* Structural basis for selective stalling of human ribosome nascent chain complexes by a drug-like molecule. *Nat. Struct. Mol. Biol.* **26**, (2019).

73. Herrero del Valle, A. *et al.* Ornithine capture by a translating ribosome controls bacterial polyamine synthesis. *Nat. Microbiol.* **5**, 554–561 (2020).

74. Couvillion, M. T., Soto, I. C., Shipkovenska, G. & Churchman, L. S. Synchronized mitochondrial and cytosolic translation programs. *Nature* **533**, 1–17 (2016).

75. Smits, P., Smeitink, J. & van den Heuvel, L. Mitochondrial translation and beyond: processes implicated in combined oxidative phosphorylation deficiencies. *J. Biomed. Biotechnol.* **2010**, 737385 (2010).

76. Yamada, Y., Somiya, K., Miyauchi, A., Osaka, H. & Harashima, H. Validation of a mitochondrial RNA therapeutic strategy using fibroblasts from a Leigh syndrome patient with a mutation in the mitochondrial ND3 gene. *Sci. Rep.* **10**, 1–13 (2020).

77. Hussain, S.-R., Yalvac, M., Khoo, B., Eckardt, S. & McLaughlin, K. J. Adapting CRISPR/Cas9 System for Targeting Mitochondrial Genome. *bioRxiv* 2020.02.11.944819 (2020) doi:10.1101/2020.02.11.944819.

78. Zhang, J. *et al.* Live birth derived from oocyte spindle transfer to prevent mitochondrial disease. *Reprod. Biomed. Online* **34**, 361–368 (2017).

79. Schur, F. K. M. *et al.* An atomic model of HIV-1 capsid-SP1 reveals structures regulating assembly and maturation. *Science (80-.).* **353**, 506–508 (2016).

80. Eisenstein, F. *et al.* Parallel cryo electron tomography on in situ lamellae. *bioRxiv* 2022.04.07.487557 (2022) doi:10.1101/2022.04.07.487557.

81. Seip, B. & Innis, C. A. How Widespread is Metabolite Sensing by Ribosome-Arresting Nascent Peptides? *Journal of Molecular Biology* vol. 428 2217–2227 (2016).

82. Rendleman, J. *et al.* Title: Regulatory start-stop elements in 5' untranslated regions pervasively modulate translation. *bioRxiv* 2021.07.26.453809 (2021) doi:10.1101/2021.07.26.453809.

83. Li, J. J., Chew, G. L. & Biggin, M. D. Quantitative principles of cis-translational control by general mRNA sequence features in eukaryotes. *Genome Biol.* **20**, 162 (2019).

84. Otsuka, H., Fukao, A., Funakami, Y., Duncan, K. E. & Fujiwara, T. Emerging evidence of translational control by AU-rich element-binding proteins. *Frontiers in Genetics* vol. 10 332 (2019).

85. Chiu, W., Schmid, M. F., Pintilie, G. D. & Lawson, C. L. Evolution of standardization and dissemination of cryo-EM structures and data jointly by the community, PDB, and EMDB. *J. Biol. Chem.* **296**, 100560 (2021).

Summary

All cellular processes such as nutrient uptake, energy conversion and cell division are executed and regulated by molecular machines consisting of RNA and proteins. All proteins are synthesized by the ribosome, the cellular protein factory which is itself composed of proteins and RNA. The instruction set for proteins are encoded in the DNA of cells which is transcribed into RNA and translated into proteins by ribosomes in a process called translation. Around 2.5 billion years ago, the endosymbiotic event occurred, in which a bacterium was engulfed by an archaeon, giving rise to a stable organism and a new domain of life: the eukaryote. As far as we know, this unique endosymbiotic event only happened once, and gave rise to organelles and multicellular organisms. Therefore, all eukaryotes from us humans to bakers' yeast date back to the last eukaryotic common ancestor (LECA) in which this endosymbiotic event occurred. The engulfed bacterium developed into a new organelle: the mitochondrion, also known as the powerhouse of the cell. Mitochondria are central to metabolism and health, but notably also kept their own genome and ribosomes, the mitoribosomes, which represent remnants of their bacterial progenitor. As a result, there are two translation machineries inside eukaryotic cells: the cytosolic ribosome and the mitoribosome. In humans, only 13 proteins are encoded in the mitochondrial genome, and all are membrane-embedded proteins required for cellular respiration.

Many aspects of mitochondrial translation remain elusive. In particular, the process of membrane insertion of newly synthesized proteins by the mitochondrial protein insertase, which guides proteins from mitoribosomes into the membrane during translation, is poorly understood. Another peculiar aspect of mitoribosomes is their structural variety across different species, as both the mitochondrial genome and the composition of the mitoribosomes were heavily shaped by evolution. One main goal of this thesis was to investigate mitoribosomes in their native environment in order to elucidate their membrane association across different species and gain insights into the mechanism of protein insertion. Studying the mitoribosome in its native environment was central to adress these questions, as previous studies failed to stably isolate mitoribosome-insertase complexes.

Another topic investigated in this thesis is the translational regulation of cytosolic ribosomes by metabolites. Here the ribosome acts as a molecular switch to enable or disable the translation of specific proteins depending on the cellular concentration of the metabolite. This is useful if the protein is involved in a pathway associated with the metabolite, e.g. if the pathway requires the presence of certain nutrients. While metabolite-induced translation is well studied in prokaryotes, the mechanisms in eukaryotes remain elusive. One example for metabolite-induced translational regulation is the translational regulation of bZIP transcription factors by the table sugar sucrose. This mechanism is conserved in all plants, but it remained unclear how sucrose is detected during translation of the bZIP transcription factors.

In this thesis, cryogenic electron microscopy (cryoEM) was applied to study mitochondrial translation and sucrose-dependent translational regulation in plants. CryoEM is a method that allows determination of three-dimensional (3D) protein structures at near atomic resolution by imaging frozen hydrated biological samples. Protein structures serve as molecular maps that are extremely valuable for understanding the mechanism of proteins,

as they help us to identify relevant protein domains and inform us on their roles. There are two main applications of cryoEM: cryo-electron tomography (cryoET) and single particle analysis (SPA). In cryoET the sample is imaged from multiple angles by tilting it during acquisition, which allows reconstruction of a 3D volume of the sample and retrieval of contextual information. In a process called subtomogram averaging, multiple subvolumes of a protein complex of interest can be aligned and averaged to obtain a 3D structure at sub-nanometer resolution. cryoET is particularly suited for investigating proteins in their native environments, e.g. cell organelles or intact cells. In SPA, 2D images of a sample are acquired in rapid succession without tilting the samples. The angular sampling required for the 3D reconstruction of the protein structures is instead obtained by getting views from hundreds of thousands of copies of randomly oriented complexes. It allows for a high throughput of images and is applied to purified, homogenous protein complexes, for which near-atomic resolution can be achieved.

In this thesis, we employ cryoET to investigate mitoribosomes inside isolated human mitochondria and cell sections of green algae. The findings shed light on the molecular evolution of mitoribosomes and visualize the structure of the human mitoribosome inside intact mitochondria at unprecedented resolution. This allowed us to resolve a previously unidentified binding interface of the mitochondrial protein insertase and identify the presence of a hitherto uncharacterized alternative insertase-complex. In addition, the structure of the sucrose-arrested plant ribosome was determined by SPA. The structure allowed for the identification of the sucrose binding site, depicting the first case of a metabolite-binding site for a eukaryotic ribosome. Surprisingly, the binding site is functionally conserved across humans, plants and bacteria. The findings in this thesis provide novel insights into mitochondrial protein synthesis and metabolite-induced translational regulation of eukaryotes.

Samenvatting

Alle cellulaire processen zoals de opname van voedingsstoffen, energieomzetting en celdeling worden uitgevoerd en gereguleerd door moleculaire machines die bestaan uit RNA en eiwitten. Alle eiwitten worden gesynthetiseerd door ribosomen. Dit zijn de eiwitfabrieken van de cel enzij bestaan zelf ook uit eiwitten en RNA. De instructies voor eiwitproductiezijn gecodeerd in het DNA van de cellen, die instructies worden omgezet in RNA en door ribosomen vertaald in eiwitten in een proces dat translatie wordt genoemd. Ongeveer 2,5 miljard jaar geleden vond de endosymbiotische gebeurtenis plaats, waarbij een bacterie werd opgeslokt door een archaeon. Door deze gebeurtenis ontstond een stabiel organisme en een nieuw levensdomein : de eukaryoot. Voor zover wij weten is deze unieke endosymbiotische gebeurtenis slechts één keer voorgekomen, en zijn er organellen en meercellige organismen uit voortgekomen. Daarom stammen alle eukaryoten, van wij mensen tot bakkersgist, af van de laatste eukaryotische gemeenschappelijke voorouder (LECA) waarin deze endosymbiotische gebeurtenis plaatsvond. De opgeslokte bacterie ontwikkelde zich tot een nieuw organel: het mitochondrium, ook bekend als de energiecentrale van de cel. Mitochondriën staan centraal in het metabolisme en de gezondheid van de cel. Opmerkelijk genoeg hebben ze hun eigen DNA en ribosomen, de mitoribosomen, behouden. Dit zijn de overblijfselen van hun bacteriële voorloper. Als gevolg hiervan zijn er twee vertaalmachines in eukaryote cellen: het cytosolische ribosoom en het mitoribosoom. Bij de mens zijn slechts 13 eiwitten gecodeerd in het mitochondriale DNA, en dat zijn allemaal in het membraan ingebouwde eiwitten die nodig zijn voor de celademhaling.

Veel aspecten van mitochondriale translatie zijn moeilijk te onderzoeken . Met name het proces van membraaninsertie door het mitochondriale eiwitinsertase, waarbij eiwitten gesynthetiseerd door mitoribosomen het membraan in worden geleidt tijdens translatie, wordt slecht begrepen. Een ander eigenaardig aspect van mitoribosomen zijn de verschillen in hun structuur tussen verschillende soorten eukaryoten, aangezien zowel het mitochondriaal DNA als de samenstelling van de mitoribosomen sterk gevormd zijn door de evolutie. Een belangrijk doel van dit proefschrift was het onderzoeken van mitoribosomen van verschillende soorten eukaryoten, in hun natuurlijke omgeving, om de membraanassociatie op te helderen en inzicht te krijgen in het mechanisme van eiwitinsertie. Het bestuderen van het mitoribosoom in zijn natuurlijke omgeving stond centraal bij het beantwoorden van deze vragen, aangezien eerdere studies er niet in slaagden mitoribosoom-insertase complexen stabiel te isoleren.

Een ander onderwerp dat in dit proefschrift wordt onderzocht is de translationele regulatie van cytosolische ribosomen door metabolieten. Hierbij werkthet ribosoom als een moleculaire schakelaar die de translatie van specifieke eiwitten in- of uitschakelt, afhankelijk van de cellulaire concentratie van het metaboliet. Dit is nuttig als het eiwit betrokken is bij een proces dat met het metaboliet samenhangt, bijvoorbeeld als het proces de aanwezigheid van bepaalde voedingsstoffen vereist. Hoewel metaboliet-geïnduceerde translatie bij prokaryoten goed onderzocht is, blijven de mechanismen bij eukaryoten onduidelijk. Een voorbeeld van metaboliet-geïnduceerde translatieregulatie is de translatieregulatie van bZIP-transcriptiefactoren door hetsuiker sucrose. Dit mechanism wordt gebruikt in alle planten, maar het is nog onduidelijk hoe sucrose wordt gedetecteerd tijdens translatie van de bZIP transcriptiefactoren.

In dit proefschrift werd cryogene elektronenmicroscopie (cryoEM) toegepast om mitochondriale translatie en sucrose-afhankelijke translatieregulatie in planten te bestuderen. CryoEM is een methode waarmee driedimensionale (3D) eiwitstructuren met bijna atomaire resolutie kunnen worden bepaald door bevroren gehydrateerde biologische samples in beeld te brengen. Eiwitstructuren dienen als moleculaire kaarten die zeer waardevol zijn voor het begrijpen van het mechanisme van eiwitten, omdat ze ons helpen relevante eiwitdomeinen te identificeren en ze ons informeren over hun functie. Er zijn twee belangrijke toepassingen van cryoEM: cryo-elektronentomografie (cryoET) en single particle analysis (SPA). Bij cryoET wordt het sample vanuit meerdere hoeken in beeld gebracht door het tijdens de acquisitie te kantelen, waardoor een 3D-volume van het sample kan worden gereconstrueerd en contextuele informatie kan worden verkregen. In een proces dat subtomogram averaging wordt genoemd, kunnen meerdere subvolumes van een relevant eiwitcomplex worden uitgelijnd en gemiddeld om zo een 3D-structuur met sub-nanometerresolutie te verkrijgen. CryoET is bijzonder geschikt voor het onderzoeken van eiwitten in hun natuurlijke omgeving, zoals celorganellen of intacte cellen. Bij SPA worden 2D-beelden van een sample snel achter elkaar verkregen zonder het sample te kantelen. De voor de 3D-reconstructie van de eiwitstructuren vereiste beelden van het eiwit vanuit alle hoeken,wordt bij SPA verkregen door het verzamelen van beelden van honderdduizenden exemplaren van willekeurig georiënteerde eiwitcomplexen. Dit maakt een snelle productie van beelden mogelijk en dit wordt toegepast op gezuiverde, homogene eiwitcomplexen, waarvoor een bijna-atomaire resolutie kan worden bereikt.

In dit proefschrift is cryoET gebruikt om mitoribosomen in geïsoleerde menselijke mitochondriën en celsecties van groene algen te onderzoeken. De bevindingen werpen licht op de moleculaire evolutie van mitoribosomen en visualiseren de structuur van het menselijke mitoribosoom in intacte mitochondriën met een ongekend hoge resolutie. Dit heeft ons in staat gesteld om een voorheen ongeïdentificeerde bindingsinterface van het mitochondriale eiwit insertase te bepalen en de aanwezigheid van een tot nu toe ongekarakteriseerd alternatief insertase-complex te identificeren. Bovendien werd de structuur van het sucrose-arrest plantenribosoom bepaald met SPA. De structuur maakte de identificatie mogelijk van de sucrosebindingsplaats, wat de eerste keer is voor een metabolietbindingsplaats van een eukaryotisch ribosoom. Verrassend genoeg is de bindingsplaats functioneel geconserveerd bij mensen, planten en bacteriën. De bevindingen in dit proefschrift geven nieuwe inzichten in mitochondriale eiwitsynthese en metaboliet-geïnduceerde translatieregulatie van eukaryoten.

Acknowledgements

Many people contributed to the work described in this thesis as great scientists, colleagues, and friends. I would like to thank them here.

Friedrich, thank you for giving me the opportunity to do the PhD in your group. Being your first PhD student in Utrecht and part of a small and growing nucleus was challenging, but I enjoyed it very much. I learned a lot from it and am grateful for the time and effort you spend on supervising me. I look forward to reading about your future discoveries!

I would like to thank all past and present colleagues of the Structural Biochemistry department. I had a great time working with all of you and appreciate all your help, feedback and efforts to keep the labs running. I have already been missing the joint group meetings, labuitjes and Sinterklaas parties.

I would like to thank all collaborators and students that worked with me on shared projects over the last years. **Stefan**, thank you for teaching me the principles of cryo-electron tomography and Matlab scripting. I learned a lot and it saved me a lot of time on my PhD. **Ben and Florent**, thank you for getting me on board with the Chlamy project and entrusting me with your precious FIB milled data. I am looking forward to more exciting algal cryoET! **Sjors and Sjef,** thank you for reaching out to us with the sucrose project. It evolved a lot from our initial ideas, and I enjoyed the collaboration very much. I hope we can publish it soon and wish you good luck with your future career Sjors! **Fan**, thank you for the great crosslinks that you've identified.

Lena, you were the first student I supervised. I learned a lot and enjoyed supervising you. I am very glad you decided to join the group. Despite exploding phones, it was lots of fun to share the office, work alongside of you and share a passion for mitochondria. Good luck finishing your PhD! **Douwe and Daan**, thank you for your hard work on the mitoribosome purification. Unfortunately, the project didn't make it into the thesis, but I appreciate your hard work and am sure you learned a lot. Douwe, keep up your table tennis skills!

Matthieu, my neighbor, colleague and dear friend, thank you for having me over for coffee 6 years ago, and all the great times together. I'm glad that we always managed to stay within 10 minutes from each other and look forward to many more great times together in Utrecht with you and **Danielle**! **Manu & Susi,** thank you for all the great times, adventures and weeks of cooking together. I'm very happy that both of you found your way back to beloved Swabia. I'm looking forward to hearing about your future contributions Manu, and good luck with finishing your thesis Susi! **Max,** my fellow german PhD student and bench mate, I always enjoyed our discussions on organelle and ribosome purifications and wish you good luck finishing! **Juliette & Gonzalo**, the yoga sessions with you were lots of fun – good luck with your projects and don't work too hard! **Gijs**, thanks again for your massages and our silly office chats. **Mihajlo**, thank you for your help and support with data transfers, software requests and running jobs. I also enjoyed our discussions in the old office a lot! **Marten**, I enjoyed the long bike rides with you. I look forward to hearing about your first 300k ride and bikepacking tours! **Rodrigo**, your will to continue despite your challenging projects is impressive! **Wenfei,** your mysterious protein cages stuck with me – good luck with your projects and your future academic career! **Dimitrios**, our overlap was brief but fun. Good luck juggling all your projects, and I'm looking forward to visiting beautiful Crete after all

your stories. **Lucas**, I have great memories of partying with you. I wish you good luck with your academic career, and hope you keep up your great climbing shape! **Wout**, I cannot imagine a borrel without you. It's been lots of fun to work and party with you, but take it easier with alcohol at graduation parties! **Karla** de La O, your love for food, fun and chatting is only surpassed by your appetite for Ramen. It's been a blast, and I can only give you the same advice as to Wout. **Ramon**, your jokes were equally predictive as they were bordering with the acceptable. **Dounia** thanks for your great humour and all the laughs. **Wouter**, thank you for being the best hulpsinterklaas. **Jitse**, I'm very impressed by your cycle endurance on old dutch omafiets! **Joke**, thank you for keeping the labs running and being so patient and kind whenever I needed something! **Arie**, thank you for ordering chemicals quickly and being patient with me whenever I forgot to put the empty containers at the right spot. **Mariska**, thank you for keeping the cell culture room running & stocked! **Miguel**, your knowledge on both technical as well as biological aspects is impressive. I enjoyed the discussions with you a lot and look forward to your future publications! **Leanne**, I enjoyed the shared shifts & chats in the cell culture lab a lot. Thanks again for reviewing my dutch summary, and good luck with finishing! **Ravi**, thank you for showing me your egg cells, and good luck with your challenging projects. Oh hi **Marc! Jo**, you are a strong addition to the fading german fraction and it is admirable how relaxed you remain despite the PhD challenges (I hope this is still the case). **Louris**, my almost bedmate on my 2nd night in Utrecht, thanks for all shared laughter and borrels. **Menno, Franziska, Nicoleta and Elisa,** our overlap was short and interrupted by COVID, the move to DdW and my remote work since, but I would like to thank you for your help, discussions and the shared time in the lab. **Bert, Eric, Loes, Martin, Piet, Stuart and Tzviya**, I would like to thank you for critical feedback in group meetings and helpful discussions. **Stuart**, I also want to thank you for your continuous support and efforts with many things at the EM facility and at NeCEN. **Chris and Hans**, thank you for helping to troubleshoot the microscopes whenever there was a problem at the EM facility.

Boy and Ilja, thank you for being such great co-founders and believing in me and my idea. Working together with you was a great motivation to finish the thesis.

I would like to thank my family, my brother, mother, and wonderful parents-in-law, for their support and reminding me that there are more important things in life than research.

In case I forgot somebody: my apologies, and thanks to everybody who crossed paths with me in the last six years and helped making it a good time.

I would like to finish with thanking my better half and greatest support during my PhD studies: **Alex**, we met in the second month that I started my PhD. Thank you so much for all your patience and support during the last 6 years. Whether it was long nights in the lab, at the microscope or in front of my screen - you were always understanding, supportive and helped me to stay happy and healthy. You were my greatest motivation on days that I could hardly motivate myself, and I could not wish for a better partner. I look forward to sharing many more years with you!